# Assessment of Chronic Wounds Using In Vivo Diffuse Near Infrared Spectroscopy

A Thesis

Submitted to the Faculty

of

Drexel University

by

Michael T. Neidrauer

in partial fulfillment of the

requirements for the degree

of

Doctor of Philosophy

October 2010

## Acknowledgments

First I would like to thank Dr. Elisabeth Papazoglou, my advisor, for the many years of energetic guidance, encouragement, and motivation she has given me, and for assembling such a great team to work with.

Special thanks to Dr. Leonid Zubkov for sharing his expertise in opto-electronics, physics, and data analysis; he has been invaluable to all aspects of this research.

I would like to thank Dr. Michael Weingarten for all of his help with the clinical aspects of this research – especially providing access to his wound clinic each week, operating on our animal subjects, and sharing his medical/wound healing expertise. Thanks also to Lisa Flowers, Jane McDaniel, and Lori Jenkins for their help with research patients each week.

I would like to thank Dr. Kambiz Pourrezaei, Dr. Som Tyagi, and Dr. Rami Seliktar for the advice and suggestions they have provided, and for agreeing to serve on my committee.

Thanks to Dr. Linda Zhu for helping to get me started when I joined this research team, to Richard Sensenig for his ideas and suggestions on possible paths forward with this research, Dr. Rick Huneke and Janet Schulenberg from Drexel's animal facility for all of their help with our animal studies, and to Maryann Fitzpatrick and Wolf Nadler for their help with hardware and tools.

I want to acknowledge and thank the current and past members of this research team for their many hours of help with animal measurements, human measurements, and data analysis, including Xiang Mao, Joshua Samuels, Chetana Sunkari, David Diaz, Varshana Gurusamy, Usha Kumar, Sarah Kralovic, Meredith Harrison, Guy Savir, Kim Peace, and Kim Tustison.

Finally, I would like to thank my wife Lisa for all of her patience and support throughout this entire process.

This research was made possible by the generous support of the Wallace H. Coulter Foundation and the U.S. Army Medical Research Acquisition Activity.  This research was funded by The U.S. Army Medical Research Acquisition Activity, 820 Chandler Street, Fort Detrick, MD 21702-5014 is the awarding and administering acquisition office. This investigation was funded under a U.S. Army Medical Research Acquisition Activity; Cooperative Agreement W81XWH 04-1-0419. The content of the information herein does not necessarily reflect the position or the policy of the U.S. Government or the U.S. Army and no official endorsement should be inferred.

## TABLE OF CONTENTS

# LIST OF TABLES

## LIST OF FIGURES

# ABSTRACT

Assessment of Chronic Wounds Using In Vivo Diffuse Near Infrared Spectroscopy
Michael T. Neidrauer
Elisabeth S. Papazoglou, Ph.D.

Chronic wounds are an increasing challenge as the population ages and the prevalence of obesity and diabetes increase in the U.S. and throughout the world. As the number and cost of treatments for chronic wounds increases, the importance of assessing the effectiveness of new therapies becomes critical. Current clinical methods for wound assessment rely on qualitative assessment of wound surface appearance and measurements of wound surface dimensions, but do not take the health of underlying tissue into account. The goal of this research is to develop a non-invasive method of assessing and predicting chronic wound healing using in vivo frequency-domain diffuse near infrared spectroscopy (DNIRS). The main hypothesis behind this research is that changes in blood vessel density and oxygen delivery beneath the surface of a wound can be measured using DNIRS. Furthermore, these changes could be used to quantitatively assess the healing status of a chronic wound and predict faster and more accurately than current clinical methods whether a wound treatment is working.

The results of a study of twenty-eight human diabetic foot ulcers shows that changes in oxy- and total hemoglobin concentration measured with DNIRS can be used to differentiate healing from non-healing wounds, and the capability of DNIRS wound monitoring to predict healing in diabetic foot ulcers is examined. Additionally, data obtained from a study of impaired wound healing in obese rats demonstrate that DNIRS can be used to assess wound healing in an animal model, and a model for expected changes in DNIRS measurements of oxy- and deoxy-hemoglobin concentration during wound healing is proposed. Wound size data obtained from

this animal study show that obese rats may provide a better model of impaired healing than the chemically-induced diabetic rats which are often used by researchers when assessing novel wound therapies.

# CHAPTER 1: INTRODUCTION

## 1.1 Problem Statement

Chronic wounds such as pressure sores, ischemic-, venous leg-, and diabetic foot ulcers constitute a major challenge in clinical practice. Over 5-7 million Americans are, especially among the growing elderly population are afflicted with these types of wounds, with an annual treatment cost of more than 20 billion dollars (Samson, Lefevre et al. 2004). It is estimated that approximately 1% of the total health care costs in the western world are likely to be used for management of chronic leg ulcers (Nelzen 2000). It is expected that these costs will grow rapidly as the population ages and the prevalence of obesity and diabetes increases in the U.S. and throughout the world.

A wide variety of advanced chronic wound treatments such as topical growth factors, bioengineered skin equivalents, negative pressure wound therapy, and hyperbaric oxygen therapy are commercially available and clinical studies of these products have shown some evidence of improved healing compared to standard of care (Sibbald, Orsted et al. 2007). However, the effectiveness of each treatment is not the same in all patients. For example, there is evidence that growth factors and cell therapies improve healing in diabetic neuropathic foot ulcers compared to standard care; however, only 30-50% of patients who received these treatments healed by 12-20 weeks of care (Margolis, Allen-Taylor et al. 2002). Clinicians often need to try several different treatment options before finding one that is effective for a particular wound. During the prolonged healing process of a chronic wound, rapid and accurate evaluation of healing progress is critical so that unsuccessful treatments can be discontinued and alternate treatments initiated as soon as possible (Goldman and Salcido 2002; Jessup 2006).

Hence, there is a need to develop non-invasive technologies that would enable improved diagnosis of chronic wounds and reduction of the current high cost of their treatment.

Traditionally, wounds have been evaluated using qualitative measures of appearance (color) and quantitative measures of wound length, width, and depth (Goldman and Salcido 2002). The main limitation of these wound evaluations is that they can give information mostly from the surface of the wound. Such surface characteristics of a wound do not take into account the health of the wound environment beneath the surface and provide inadequate information regarding the wound healing status of a wound. Therefore, misdiagnosis may occur or treatment may not be altered as early as possible, with direct implications on the quality and cost of care for chronic wounds (Cullum, Nelson et al. 2001; Mustoe March 17-18, 2005). Non-invasive analysis of the full depth of the chronic wound bed could provide the clinician with a more complete picture of wound health, allowing better prediction of wound closure and probability of wound recurrence than can be achieved by surface measurements alone. Diffuse Near Infrared Spectroscopy (DNIRS) may be able to meet this need by providing quantitative information about blood vessel density and oxygen delivery beneath the surface of a wound at depths of up to several centimeters.

## 1.2 Objectives

The **overall goal** of this research is to develop a non-invasive method of assessing and predicting chronic wound healing using *in-vivo* frequency-domain diffuse near infrared spectroscopy (DNIRS).

The main **hypothesis** enabling the use of NIR to differentiate healing from non-healing wounds and to predict treatment outcome is that changes in blood vessel density and oxygen delivery beneath the surface of a wound can be measured using DNIRS. These changes may be used to quantitatively assess the healing status of a chronic wound, and may be able to predict faster and more accurately than current clinical practices (size measurement and visual observation) whether a wound treatment is working.

Accordingly, the aims of this research are:

**Aim 1:** Demonstrate that diffuse NIR spectroscopy (DNIRS) can be used to assess wound healing in an obese rat animal model, which may be a better model of impaired healing than chemically-induced lean diabetic rats.

**Aim 2:** Conduct a study of human diabetic foot ulcers to demonstrate the ability of the DNIRS methodology to quantify changes in chronic wounds and to predict wound outcomes in a clinical environment.

# CHAPTER 2: OVERVIEW OF WOUND HEALING

The purpose of this chapter is to provide a brief summary of the wound healing process and its impairment in diabetic and obese patients. A more detailed review of wound healing literature can be found in (Zhu 2008).

## 2.1 Normal Healing

Great strides have been made in recent years in understanding the physiology of tissue healing, yet the process is not fully understood. The process of soft tissue healing can be divided into three overlapping phases: hemostasis/inflammation, fibroplasia/proliferation, and maturation/ remodeling (Ueno, Hunt et al. 2006). As Figure 1 illustrates, there is significant overlap between the phases (Singer and Clark 1999; Lamorte 2002).

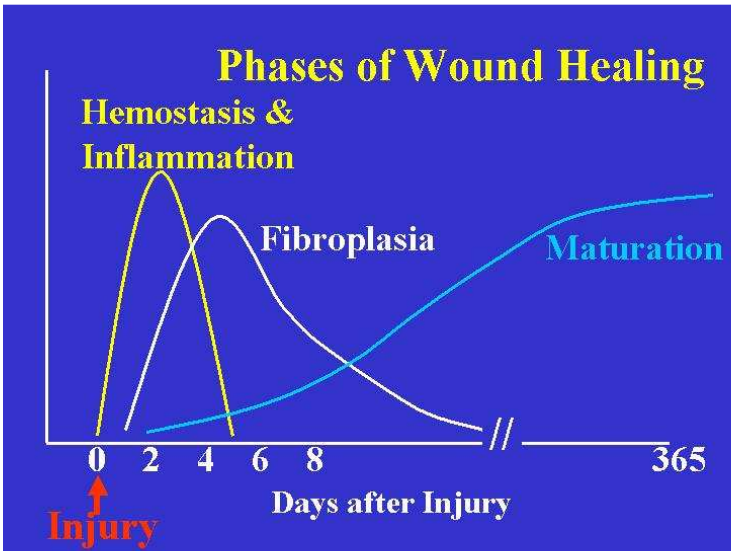

**Figure 1: The three overlapping phases of the wound healing process Reprinted from (Lamorte 2002).**

Hemostasis is the body's initial response to a wound, and begins when a blood vessel breaks and platelets are exposed to collagen beneath the endothelial lining of the vessels. The purpose of hemostasis is to stop blood loss as soon as possible, and this typically happens within a few hours or even minutes of the injury (Silverthorn, Ober et al. 2004). Inflammation begins a few minutes after the injury is sustained, can last for several days, and is characterized by erythema, edema, heat, and pain. These macroscopic characteristics of inflammation are the result of vasodilation and increased capillary permeability, which allows the release of chemical messengers that attract neutrophils and macrophages to the site of the wound (Baum and Arpey 2005). These cells have three major functions: 1) to attack pathogens that may have entered the body through the wound, 2) to remove dead tissue from the wound area in preparation for tissue regeneration, and 3) to release chemical messengers that attract the endothelial cells and fibroblasts that are responsible for the cell migration/proliferation that occurs during the second phase of tissue healing (Martin 1997; Diegelmann and Evans 2004; Ueno, Hunt et al. 2006).

The fibroplasia or cell proliferation phase of tissue healing begins with angiogenesis, or the establishment of new blood vessels at the wound site. The creation of new tissue is energy intensive and therefore requires a steady supply of oxygen and nutrients. The events in the hemostasis phase reduce the blood supply to the wounded tissue, so angiogenesis is needed to restore oxygen and nutrient delivery to the healing tissue. A steady blood supply allows fibroblasts in the wound site to form granulation tissue. Fibroblasts form granulation tissue by synthesizing a network of collagen fibers (primarily type III collagen) and fluid that fills the wound. The collagen fibers shorten and myofibroblasts within the granulation tissue undergo contraction to reduce the size of the wound. As granulation tissue forms, epithelial cells migrate across the surface of the wound from its edges. After the wound is filled with granulation tissue and the surface of the wound has been completely epithelialized, the fibroplasia/proliferation phase is complete. The epithelialized granulation tissue that forms during this phase is scar tissue (Muncaster 2001; Diegelmann and Evans 2004; Ueno, Hunt et al. 2006).

The final phase of cutaneous wound healing is the tissue maturation or remodeling phase, which begins before a wound is completely closed and can last for years. During remodeling, gelatinous type III collagen fibers in the extracellular matrix of the scar are replaced with stronger type I collagen fibers and arranged into a more organized pattern. This increases the tensile strength of the scar tissue. Then fibroblasts leave the wound site and the vascularization of the scar tissue is reduced. This shrinks the scar and causes its color to pale (Singer and Clark 1999; Diegelmann and Evans 2004; Ueno, Hunt et al. 2006).

## 2.2 Diabetic Foot Ulcers

Diabetes affects 13 million people every year (5.2% of the U.S. population) with approximately 650,000 new cases diagnosed annually (Skyler and Oddo 2002). Worldwide, diabetes is estimated to affect more than 150 million adults, and this number is expected to double in the next 25 years (King 1998). Vascular disease and neuropathy in the lower limbs of diabetic patients lead to the formation of chronic ulcers from what is often initially a minor trauma. It is estimated that 15% of diabetic patients will develop an ulcer of the feet or ankles at some time during their disease course, and approximately 14% of diabetic ulcers lead to amputation (Reiber, Lipsky et al. 1998). It is estimated that diabetic foot ulcers are the underlying cause of 85% of all non-traumatic amputations (Singh, Armstrong et al. 2005). Mortality during the 5-year period following amputation ranges from 39%-80% (Singh, Armstrong et al. 2005), and the health-related quality of life (HRQoL) of patients with chronic neuropathic foot ulcers is poor and comparable with the quality of life of patients with recurrent cancer (Nabuurs-Franssen, Huijberts et al. 2005). Because diabetes is strongly associated with both obesity and age, the incidence of diabetic foot ulcers is expected to increase in the future.

Multi-organ complications of diabetes include neuropathy and vascular disease, both of which lead to an increased risk of foot ulceration in diabetic patients (Jeffcoate and Harding 2003). Diabetes leads to both macrocirculatory and microcirculatory deficiencies in the extremities of diabetic patients. Microvascular disease may include a reduction in the size of capillaries and a thickening of the basement membrane of microvessels, which impairs exchange between blood and the tissue surrounding the vasculature (Falanga 2005). Microvascular disease in the diabetic foot leads to neuropathy, which can futher impair microcirculatory regulation by the nervous system and impair vasodilation (Veves, Akbari et al. 1998). Autonomic sympathetic neuropathy can cause reduced sweating, which leads to warm, dry feet with skin that is likely to crack. These effects are compounded by sensory neuropathy that reduces a patient’s ability to feel pressure, heat, or pain (Brem, Sheehan et al. 2004) and motor neuropathy that can result in foot deformities such as Charcot foot and clawed toes that cause localized regions of pressure from footwear (Bader 2008). The combination of microvascular disease with autonomic, sensory, and motor neuropathy often results in unperceived trauma (such as rubbing from ill-fitting footwear) to a foot that has already weakened skin, and this is how many diabetic foot ulcers are initially sustained.

Once a wound has formed on the foot of a diabetic patient, there are many complications from diabetes that may cause delayed healing. One of the most common complications from diabetes is foot infection, which can include abscesses, cellulitis, and osteomyletis. Vascular insufficiency may cause chronic hypoxia in the limbs of diabetic patients, which impairs the function of neutrophils and macrophages that are critical to the body's immune response (Falanga 2005; Bader 2008). Additionally, fibroblast cells cultured from diabetic foot ulcers show a reduced mitogenic response to growth factors compared to non-diabetic ulcers, indicating that impaired fibroblast function may contribute to delayed healing (Loots, Kenter et al. 2002). High levels of matrix metalloproteinases (MMPs) such as MMP-9 are present in the diabetic wound tissue. These enzymes break down extracellular matrix proteins and growth factors, and excessive amounts of MMPs can impair cell migration (Falanga 2005). The release of MMPs is natural part of the inflammatory phase of wound healing, and it has been hypothesized that non-healing diabetic foot ulcers get “stuck” in the inflammatory phase, which inhibits the later phases of healing (Loots, Lamme et al. 1998; Falanga 2005).

## 2.3 Obesity and Wound Healing

Obesity has been linked to delayed wound healing in acute post-surgical wounds due to increased incidence of infection, reduced cutaneous vascularization, increased tension on wound edges, and reduced tissue oxygenation (Wilson and Clark 2004). Several factors contribute to poor tissue oxygenation in obese patients: (1) subcutaneous adipose tissue is poorly vascularized which may lead to insufficient perfusion and oxygenation of a wound bed, (2) impaired pulmonary function due to the weight of the chest and restricted movement of the diaphragm, (3) subcutaneous fluid accumulation (Wilson and Clark 2004; Baugh, Zuelzer et al. 2007).

Although most research involving obesity as a risk factor for impaired wound healing has involved surgical wounds, obesity has also been shown to increase the risk of chronic wounds. Specifically, obesity has been shown to be a risk factor for the development of venous leg ulcers when poor vascularization of adipose tissue is combined with venous hypertension (Wilson and Clark 2003). Another study showed that high body mass index (BMI) is an independent predictor of poor venous leg ulcer outcome (Meaume, Couilliet et al. 2005). In addition, edema and the poor vascularity of adipose tissue increase the risk of pressure ulcers in obese patients (Wilson and Clark 2003).

Recent estimates suggest that two thirds of adults in the United States are overweight and one third of adults are obese. The number of obese adults has doubled in the past 40 years, and the number of overweight teenagers has tripled (Gallagher and Gates 2003). These data indicate the likely continued growth of wound healing complications due to obesity in the near future.

# CHAPTER 3: REVIEW OF OPTICAL NON-INVASIVE CHARACTERIZATION OF CHRONIC WOUNDS

## 3.1 Introduction

The rapid development of opto-electronic and semiconductor components has led to an increasing interest in optical technologies for non-invasive medical diagnostics. A significant disadvantage of optical methods compared to other non-invasive medical diagnostic modalities like ultrasound, x-ray, and magnetic resonance imaging is that optical methods cannot penetrate tissue beyond several centimeters. However, this issue is less of a concern when working with cutaneous chronic wounds, and in recent years several optical technologies have been applied to the characterization of chronic wounds in research and clinical environments.

This chapter is a summary of progress made toward improved characterization of chronic wounds (diabetic foot ulcers, venous leg ulcers, pressure ulcers) using non-invasive optical methods. Technologies covered include: laser Doppler perfusion imaging for monitoring cutaneous blood flow, optical coherence tomography for structural imaging of wound tissue, orthogonal polarization spectral imaging for visualizing cutaneous microcirculation, thermal imaging for visualizing cutaneous temperature distributions, spectroscopic methods for monitoring metabolic status at both superficial (less than 1 millimeter) and deep (up to several centimeters) penetration depths, hyperspectral imaging for creating spatial maps of spectroscopic data,.

## 3.2 Laser Doppler Perfusion Monitoring and Imaging

Laser Doppler perfusion monitoring (LDPM) relies on frequency shifts of an incident light beam to determine a quantitative index that is related to microvascular blood flow or perfusion (Humeau, Steenbergen et al. 2007). Coherent laser light at near infrared wavelengths is delivered to the skin by an optical fiber (see Figure 2a). Photons that are scattered by moving particles undergo shifts in frequency (Doppler shifts) that are proportional to the velocity of the scattering particles. Light that is backscattered to the surface is transported by a second optical fiber to a photodetector, where a spectrum of frequency shifts is detected. It is assumed that the primary source of moving particles within tissue is red blood cell circulation. Algorithms have been developed to determine Laser Doppler Flux (LDF) indices that are proportional to the average velocity and number of red blood cells within the probed tissue volume (Rajan, Varghese et al. 2009). The calculated values of LDF reflect the movement of cells in any direction, so that the signals originating from cells moving in opposing directions do not cancel each other out (Khan and Newton 2003). The volume of tissue that is measured with LDPM depends on the wavelength of light used, the optical properties of tissue, and the separation distance between the source fiber and detector fiber. Typically, LDPM probes have a source-detector separation of 0.25 mm, wavelengths ranging from 630-830nm, and measure tissue depths of roughly 0.5-1.0 mm and volumes of about 1 mm$^3$ (Rajan, Varghese et al. 2009).

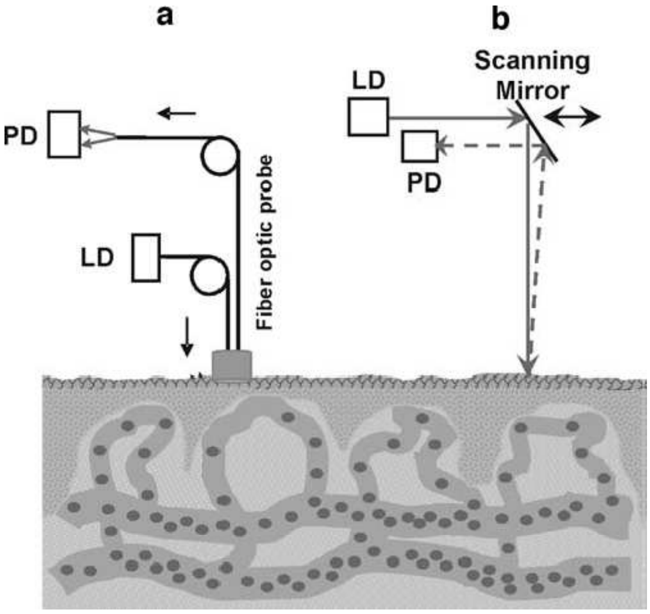

**Figure 2: Schematic of the optical systems used for (a) laser Doppler perfusion monitoring and (b) laser Doppler perfusion imaging. LD = laser diode, PD = photodetector. Reprinted from (Rajan, Varghese et al. 2009).**

Laser Doppler perfusion imaging (LDPI) systems operate on the same principle as LDPM, except that light is delivered to and from the tissue using lenses and mirrors rather than optical fibers (see Figure 2b). As a result, LDPI systems are non-contact and two-dimensional maps of LDF can be generated by scanning the laser over a region of tissue. Commercially available LDPI systems can create a 256x256-pixel blood flow image in 4-5 minutes with a spatial resolution of approximately 1 mm (Rajan, Varghese et al. 2009).

Jünger et al. 1996 used a laser Doppler perfusion monitoring (LDPM) device with a 633nm light source to measure changes in laser Doppler flow (LDF) at the center of 12 venous leg ulcers while the legs of the patients underwent elevation and arterial occlusion. Similar tests were performed on the intact skin of the ankles of 12 healthy control subjects. Changes in LDF during leg elevation and arterial occlusion were significantly reduced in patients with leg ulcers compared to controls, indicating that LDPM could be used to distinguish healthy microcirculatory responses from diseased responses (Jünger, Klyscz et al. 1996).

A series of studies were published over the past decade by Gschwandtner and Ambrozy (Gschwandtner, Ambrozy et al. 1999; Gschwandtner, Ambrózy et al. 1999; Gschwandtner, Ambrózy et al. 2001; Ambrozy, Waczulikova et al. 2009) in which LDPI with a 632 nm laser was used to quantify microcirculatory disturbances in venous and arterial ulcers at depths of 1-2 mm. Groups of patients were recruited having venous leg ulcers, ischemic leg ulcers, and ulcers caused by a combination of peripheral arterial disease and chronic venous insufficiency. An LDF image was created for each ulcer and image analysis was used to calculate the mean LDF of four locations: granulation tissue within the ulcer, non-granulation tissue within the ulcer, intact skin adjacent to the ulcer, and intact skin distant from the ulcer. As expected, ischemic leg ulcers overall showed less LDF than venous leg ulcers. In venous leg ulcers (n=15), mean LDF in granulation tissue was significantly greater than mean LDF in the non-granulation tissue and the skin adjacent to the ulcer. However, in ischemic leg ulcers (n=15), LDF was greater in intact skin compared to either granulation or non-granulation tissue within the ulcers (Gschwandtner, Ambrozy et al. 1999; Gschwandtner, Ambrózy et al. 1999; Gschwandtner, Ambrózy et al. 2001). In combination venous/arterial ulcers (n=17), significantly greater values of LDF were found in both the granulation tissue and in the intact skin adjacent to the ulcer than in the non-granulation tissue within the ulcer. An example of a laser Doppler perfusion image of a mixed arterial/venous ulcer is shown in Figure 3 (Ambrozy, Waczulikova et al. 2009). These studies indicate that insufficient blood flow to localized areas of the wound may be preventing the formation of granulation tissue. Based on these results, one could envision the possibility of using LDPI measurements to quantify the formation of granulation tissue in venous and arterial leg ulcers, and the authors (Ambrozy, Waczulikova et al. 2009) point out that a longitudinal study is needed to monitor changes in perfusion during the healing process.

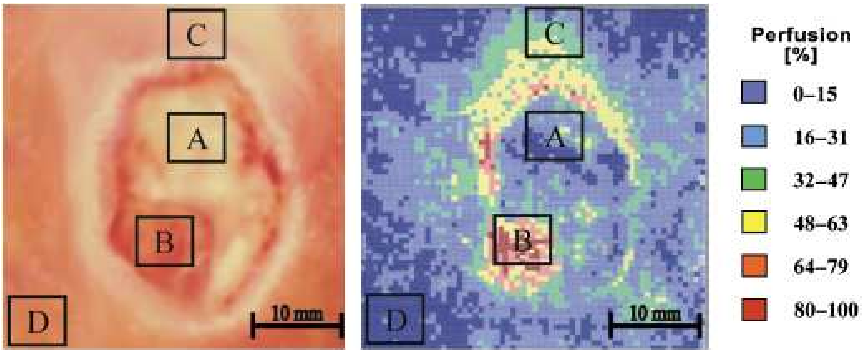

**Figure 3: Macroscopic photograph and corresponding laser Doppler perfusion image of a mixed arterial/venous ulcer. Four areas of interest are marked with capital letters: A, nongranulation tissue area; B, granulation tissue area; C, adjacent skin area; D, a more distant skin area. Reprinted from (Ambrozy, Waczulikova et al. 2009).**

A longitudinal study was published in 2005 by Mlacak et al. that compared changes in LDF measured before and after healing in venous leg ulcers. Nine subjects with venous leg ulcers and nine healthy control subjects participated in this study. Laser Doppler perfusion monitoring probes were fastened to the intact skin adjacent to venous leg ulcers, and values of LDF were recorded at rest, after arterial occlusion, during heating to 44°C, and during venous occlusion. The same tests were repeated after each ulcer has healed, and control subjects were also measured twice at comparable time intervals. The values of LDF measured at rest in subjects with venous leg ulcers were approximate six times greater than those measured in healthy subjects. Changes in LDF during leg elevation and arterial occlusion were significantly reduced ($p<0.008$) in patients with leg ulcers compared to controls, which is in agreement with the findings of Junger et al. 1996. However, within the group of patients with venous leg ulcers, no significant differences were observed between the tests conducted before and after healing. This suggests that blood perfusion in the skin adjacent to venous leg ulcers does not change in a manner that can be detected by LDPM, and indicates that while LDPM may be an appropriate tool for quantifying microcirculatory pathology near venous leg ulcers, it might not be a good tool for monitoring changes that occur during the healing process of the ulcers themselves.

Laser Doppler perfusion measurements have been conducted in chronic wound types other than venous and arterial leg ulcers. Timar-Banu et al. 2001 used LDPM with a 785nm diode laser to assess perfusion in chronic wounds of mixed etiology (4 diabetic foot ulcers, 10 venous leg ulcers, and 1 pressure ulcer). The authors found increased values of LDF in granulation tissue compared to intact skin, similar to the results reported by Gschwandtner and Ambrozy (Gschwandtner, Ambrozy et al. 1999; Gschwandtner, Ambrózy et al. 1999; Gschwandtner, Ambrózy et al. 2001; Ambrozy, Waczulikova et al. 2009) in venous and arterial leg ulcers (Timar-Banu, Beauregard et al. 2001). In a study published by Newton et al. 2001, 13 diabetic foot ulcers were scanned with an LDPI system having a 633nm light source. Intact skin on the contralateral limbs of the same subjects was used as a control. Average LDF values at the periphery of the diabetic foot ulcers were approximately 50% greater than those of control skin; however, the difference was not significant because of large inter-subject variance within each group of subjects. The high variability may have been related to heterogeneity of diabetic foot ulcers, as some were full-thickness wounds while others were partial thickness wounds, 5 of the 13 limbs were neuropathic, and there was considerable variation in the size and duration of the ulcers studied (Newton, Leese et al. 2001). It would be interesting to see if limb elevation, heating, or arterial occlusion tests similar to those used in venous leg ulcers by Jünger (Jünger, Klyscz et al. 1996) and Mlacak (Mlacak, Blinc et al. 2005) would lead to significant differences in LDF between diabetic foot ulcers and control skin.

There are some potential limitations of using Laser Doppler to assess wound healing in a clinical environment. Manufacturers of LDPM and LDPI systems use their own proprietary algorithms for calculating relative perfusion indices. The values of LDF are not calculated in absolute units but in arbitrary units, so it is difficult to compare results obtained with different systems. In LDPI systems, specular reflection of the light beam may occur due to curvature of the feet and presence of moisture on the surface of the wound, resulting in a loss of signal (Khan and Newton 2003). Furthermore, the patient is required to remain motionless for the duration of each LDPI measurement in order to avoid motion artifacts. The image acquisition time of 4-5 minutes may make this difficult for some patients and result in non-reliable data.

### 3.3 Optical Coherence Tomography

Optical Coherence Tomography (OCT) is a non-invasive imaging modality that uses low coherence interferometry to create high resolution cross-sectional images of structural features in skin at depths of up to 1-2 mm. In most OCT systems, light of low coherence length is delivered to the skin through one arm of a fiber optic Michelson interferometer that terminates with a lens assembly that focuses light onto the skin (see Figure 4). As a result, OCT imaging is completely non-invasive and requires no contact to be made between the skin and the optical system, although some OCT systems do require light contact to be made between the skin and a window at the end of the probe. Light that is reflected and backscattered to the surface of the skin is combined with light from the reference arm of the interferometer and registered by a photodetector. The reference arm of the interferometer contains a mirror that is moved mechanically to control the axial scan depth. Multiple axial scans are combined to form two or three dimensional images of scattering objects within the skin. The wavelength of the light source is typically in the near infrared region (800-1800nm), with wavelengths between 1300nm and 1800nm providing the best penetration depth (Schmitt 1999). The resolution of the images is typically on the order of 10-20 microns, but recent advances have led to resolutions approaching 1 micron (Schmitt 1999; Gambichler, Moussa et al. 2005).

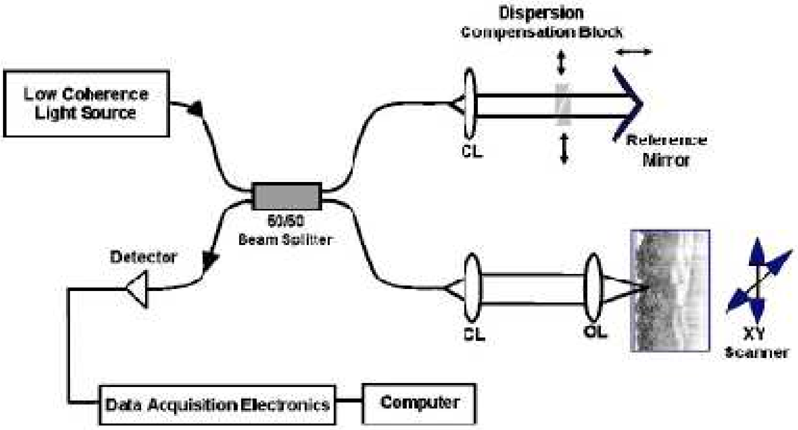

**Figure 4: Schematic of the OCT system described in Cobb et al. 2006. CL = collimating lens; OL = objective lens. Reprinted from (Cobb, Chen et al. 2006).**

Imaging of human chronic wounds with OCT has not yet been reported, but several studies of experimentally-created animal wounds have been conducted (Cobb, Chen et al. 2006; Singer, Wang et al. 2007; Wang, Pan et al. 2008). Structures visible in OCT images of acute murine wounds such as the epithelial layer, granulation tissue, blisters, collagen matrix, and regions of high inflammatory response have been qualitatively validated against histological micrographs from the same wound beds. In particular, the superficial layer of epithelial cells in a healing wound exhibits high scattering and appears very bright in OCT images, allowing researchers to monitor the migration and development of epithelium over time (Cobb, Chen et al. 2006; Wang, Pan et al. 2008). Serial imaging of full-thickness wounds allowed changes in wound morphology to be followed throughout the healing process, and in one study the integration of collagen implants into healing wound tissue could be visualized using OCT (Wang, Pan et al. 2008). Algorithms for automated analysis of OCT images have been developed and they can calculate the size of a wound and identify the location of the dermal-epidermal junction, the formation of which may be used as an indicator of epithelialization in a healing wound (Cobb, Chen et al. 2006). In a study of partial-thickness wounds in porcine skin, which is more similar to human skin than rodent skin, OCT was used to visualize and measure the thickness of re-epithelialized skin (Singer, Wang et al. 2007).

Polarization-sensitive optical coherence tomography (PS-OCT) is a variation of OCT that provides not only structural images, but also information regarding polarization changes due to tissue birefringence (Schmitt 1999; Park, Saxer et al. 2001; Gambichler, Moussa et al. 2005; Oh, Lee et al. 2006). Normal skin exhibits birefringence due to the interlaced structure of collagen fibers and causes an alteration in the polarization state of light that interacts with it. This alteration in polarization, or phase retardation angle, can be detected and quantified using PS-OCT systems and is indicative of the quantity and structure of collagen within the imaged tissue.

Oh et al. 2006 used a PS-OCT system with a 1310 nm light source to quantify temporal changes in collagen birefringence in rabbit ear skin wounds. There were three groups of wounds: (1) wounds treated with sphingosylphosphorylcholine (SPC) to accelerate healing, (2) wounds treated with tetraacetylphytosphingosine (TAPS) to impair healing, and (3) untreated wounds that underwent normal healing. Birefringence was quantified using the change in phase retardation angle over depths ranging from 0.05 to 0.20 mm. Wounds in the SPC accelerated healing group showed 30% more birefringence than untreated wounds, while wounds in the TAPS impaired healing group showed 50% less birefringence than untreated wounds. The authors compared their OCT images with histological micrographs, and concluded that the differences in birefringence were due to differences in both the quantity and orientation of collagen fibers within each group of wounds (Oh, Lee et al. 2006). PS-OCT has also been used to quantify collagen damage *ex vivo* in burned human skin by measuring the loss of birefringence (Pierce, Sheridan et al. 2004). Similar measurements were conducted *in vivo* using burned animal skin, and subsequent histological analysis of the same skin revealed that the magnitude of birefringence loss measured using PC-OCT corresponded to the depth of collagen damage (Park, Saxer et al. 2001; Srinivas, de Boer et al. 2004).

The translation of OCT and PS-OCT to clinical assessment of human chronic wounds is still uncertain due to the lack of published human studies in this area and the size and complexity of human chronic wounds compared to experimental acute wounds in animals. However, OCT technology is rapidly improving and the arrival of real-time, non-contact imaging may make studies of human chronic wounds more feasible in the near future.

### 3.4 Orthogonal Polarization Spectral Imaging

Orthogonal polarization spectral (OPS) imaging is a method used to directly visualize microcirculation *in vivo* without the use of contrast agents or dyes. Monochromatic light (typically with wavelength = 548 nm) is linearly polarized and used to illuminate the tissue through an objective lens, as shown in Figure 5. Light that is reflected and scattered from the tissue is collected by the same objective lens, and the image passes through a polarizer that is oriented orthogonally to the illumination polarization. Light that is specularly reflected from the tissue surface will have the same polarization as the incident light and will be rejected by the second polarizer. Only light that has undergone multiple scattering events within the tissue and has lost is original polarization state passes through the polarizer to a CCD video camera that captures video images in real-time. The illumination spot size is typically around 1 mm, and the penetration depth of *in vivo* measurements is approximately 200 microns (Groner, Winkelman et al. 1999). The wavelength of incident light is usually 548 nm, which is the wavelength at which both oxyhemoglobin and deoxyhemoglobin absorb equally. Therefore, red blood cells appear dark (due to high absorption) on a bright background when they are within the field of view, regardless of the oxygenation state of hemoglobin. The magnification used in OPS systems provides images with a resolution of approximately 1 micron per pixel, which allows individual erythrocytes to be visualized and tracked as they move through the microvasculature (Groner, Winkelman et al. 1999; Milner, Bhat et al. 2005).

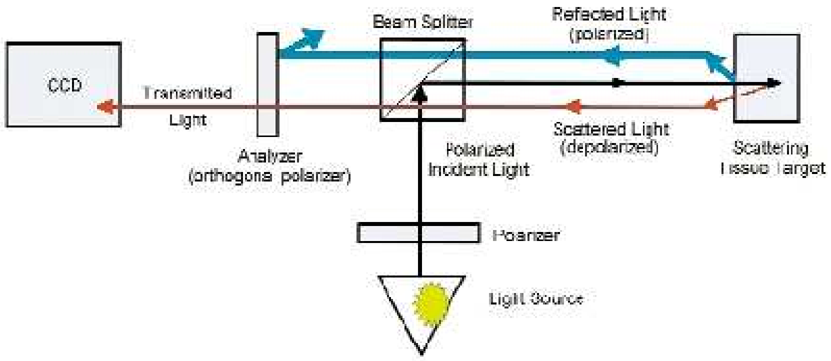

**Figure 5: Schematic of an OPS system. The light source is typically monochromatic with wavelength of 548nm. Reprinted from (Groner, Winkelman et al. 1999).**

A study published in 2002 by Langer et al. showed that OPS imaging could be used to quantify the microvascular characteristics of experimental acute wounds in hairless mice. Wounds with a diameter of 2.5mm were created on the ears of 8 mice, and 20 seconds of OPS video were recorded at three locations on each wound. Measurements were obtained on days

1, 4, 7, 10, and 15 after the wound surgery. Video processing software was used to calculate the diameter of arterioles and venules, red blood cell velocity in arterioles and venules, and the functional capillary density within each field of view. Changes in these parameters were observed over the course of healing. The same OPS system was used to obtain serial measurements from the edge of a single human chronic wound over eight weeks (see Figure 6), showing that the use of OPS in clinical environment may be feasible (Langer, Born et al. 2002).

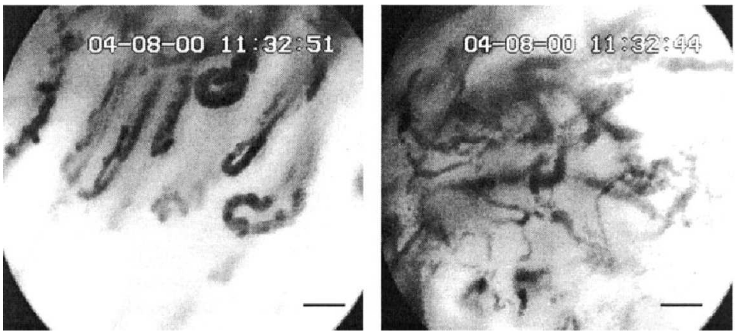

**Figure 6: OPS images from a human chronic wound using a probe equipped with a 5X lens. Scale bar = 50 µm. Reprinted from (Langer, Born et al. 2002).**

OPS was used by Virgini-Magalhães et al. 2006 to image the intact skin of 87 lower limbs of patients having chronic venous insufficiency (CVI), a condition that often leads to the formation of venous ulcers. Morphological and functional microcirculatory parameters were quantified from OPS data and compared to clinical evaluation of CVI severity. In patients with more severe CVI, decreased values of functional capillary density were observed, and increases in the capillary bulk, the dermal papilla diameter, the percentage of irregularly shaped capillaries were observed, indicating a decline in capillary function and an increase in tissue edema. A microcirculatory index was developed by the authors that took into account all of the

OPS derived parameters. This microcirculatory score correlated well with the clinical system currently used to classify CVI patients (CEAP system – based on clinical observations), indicating that it may be possible to use OPS imaging to objectively quantify the progression of CVI and identify those patients most at risk of developing venous ulcers (Virgini-Magalhães, Porto et al. 2006).

Milner et al. 2005 used OPS to image burn damage *in vivo* in 12 human patients, and a quantifiable difference was seen between the dermal microvasculature of superficial vs. deep burns. Large coagulated vessels were visible in deep burns, in contrast to the functioning capillaries that were visible in superficial burns. These results further demonstrate that OPS imaging may be both feasible and valuable in a clinical environment (Milner, Bhat et al. 2005).

There are a few potential limitations of using OPS imaging as a diagnostic tool for chronic wounds in clinical environment. OPS image acquisition is fast (real time), but the analysis of video is time consuming because significant manual input is required to calculate circulatory parameters (Virgini-Magalhães, Porto et al. 2006). However, the automation of analysis could be accelerated with improved image analysis software (Christ, Bauer et al. 2002). Another potential issue is that OPS may not be able to image patients with high melanin content. Virgini-Magalhaes et al. 2006 indicated that patients with dark skin (Fitzpatrick skin phototypes 5 and 6) were excluded from their study owing to limitation of the technique.

## 3.5 Thermal Imaging

Thermal imaging is a method of measuring the thermal energy emitted by any object with a temperature above absolute zero. In contrast to the other optical methods described in this chapter, thermal imaging requires no external source of illumination because the measured radiation is emitted naturally from the skin or wound under examination. The emissive behavior of human skin is similar to a physical black body at wavelengths ranging from 2-14 µm, and the emissive power ($E_b$) of a black body is strongly dependent upon temperature (T) according to the Stefan-Boltzmann law: $E_b = \sigma T^4$, where σ is the Stefan-Boltzmann constant (Jones 1998). The wavelength at which skin (at a temperature of 300 K) exhibits maximum emissive power is approximately 10 µm, and modern thermal imaging systems employ detectors that are sensitive in the 8-10µm wavelength range (Fauci, Breiter et al. 2001). The design of thermal imaging systems is similar to that of CCD cameras in that an array of detectors is placed in the focal plane of a lens. However, glass absorbs strongly at wavelengths near 10µm, so the lenses used in thermal imaging systems must be made from materials such as germanium (Jones 1998). The response of thermal detector elements must be calibrated using objects of known temperature in order for an imaging system to provide absolute measurements of temperature. After calibration, thermal imaging systems can provide maps of temperature values with a spatial resolution of approximately 2-4 mm (Jones and Plassmann 2002) and temperature resolution near 0.1ºC (Jones 1998). Radiation emitted from deep tissue does not reach the skin surface because of the high absorption coefficient of tissue at infrared wavelengths. Therefore, the temperature maps provided by thermal imaging systems are superficial, reflecting the temperatures at the surface of the epidermis (Jones 1998).

The use of thermal imaging in the assessment of chronic wounds has been reported for over 35 years. Verhonick et al. 1972 described the use of infrared thermal imaging to visualize temperature increases in the skin of healthy subjects after applying pressure to bony prominences where pressure ulcers are most likely to occur. Although the temperature changes were not quantified, this study showed that thermal imaging had the potential to identify skin regions most susceptible to developing pressure ulcers (Verhonick, Lewis et al. 1972). Newman and Davis 1981 captured infrared thermal images of the intact sacral skin of 91 patients admitted to a geriatric assessment ward. Eleven of these images showed diffuse regions of increased temperature at the sacrum, and 5 of the 11 patients with increased skin temperatures developed a sacral pressure ulcer within 10 days. None of the 63 patients who had normal thermograms developed pressure ulcers within 10 days, showing that thermography may be capable of providing early indication of sacral pressure sore risk (Newman and Davis 1981).

Armstrong et al. 1997 conducted a retrospective study to determine whether skin temperature measured with infrared thermometry could be correlated with diabetic foot ulceration. The feet of 44 subjects with diabetic neuropathic foot ulcers and 78 subjects with diabetic neuropathy but no foot ulceration were measured using an infrared skin temperature probe. The infrared device functioned in a similar manner to infrared imaging systems; however it measured the mean temperature across a 1 $cm^2$ area of skin rather than creating a temperature map of a wider skin area. No temperature differences were observed between the left and right feet of non-ulcerated neuropathic subjects. On the other hand, significantly increased temperatures (5.6ºF) were observed in the skin of ulcerated feet compared to the non-ulcerated contralateral limbs of the same subjects ($p<0.0001$). Furthermore, after their ulcers had completely healed and temperature differences between feet had resolved, 5 subjects experienced reulceration. Importantly, on the clinical visit immediately prior to reulceration, skin temperature on the pre-ulcerative limbs increased by an average of 7.1ºC. This study provides evidence that skin temperature increases measured with infrared thermometry may be useful in predicting the formation of diabetic foot ulcers (Armstrong, Lavery et al. 1997).

Harding et al. 1998 conducted a study to determine whether thermal imaging could be used to identify patients with soft tissue infection and osteomyelitis (bone infection) adjacent to diabetic foot ulcers. Thermal images of the feet of 49 patients with diabetic foot ulcers were captured using a commercially available thermal imaging camera (Aga Thermovision 782 I-R). The presence of osteomyelitis was determined in each patient using standard clinical radiological methods that included x-ray radiography, magnetic resonance imaging, and isotope bone scans. To analyze the thermal images, the authors classified an image as a "positive thermogram" if the temperature of a diffuse area of skin on the sole of the ulcerated foot was at least 0.5ºC greater than the temperature in the contralateral foot. 21 of the 26 subjects (81%) who has positive thermograms tested positive for osteomyelitis, and all of the 23 subjects (100%) with negative thermograms tested negative for osteomyletis (Harding, Wertheim et al. 1998).

Elevated local skin temperature has been reported in several recently published case studies of venous leg ulcers (Sayre, Kelechi et al. 2007; Bagavathiappan, Saravanan et al. 2008). Sayre et al. 2007 reported a case in which a subject with chronic venous disease was monitoring skin temperature with an infrared thermometer on a daily basis for 46 days. During this period, the subject developed two leg ulcers on sites that were being monitored. In the days immediately preceding ulceration, a sudden drop and then increase in temperature were observed, suggesting the possibility of an ischemic event followed by reperfusion effect that may have caused inflammation and skin damage (i.e. ischemia-reperfusion injury). Bagavathiappan et al. 2008 acquired thermal images of the limbs of two non-diabetic patients with a history of vascular disorders and ulceration using an infrared camera. In both patients, regions having temperatures elevated by 0.7 – 1.0 ºC were identified as regions of abnormal blood flow. Although the number of patients in these studies precludes any statistically conclusions, they show that infrared imaging has the potential to help in the diagnosis and prediction of the location of venous leg ulcers.

## 3.6 Diffuse Reflectance Spectroscopy

Diffuse Reflectance (or Remittance) Spectroscopy (DRS) is an optical method that uses light at visible and near infrared wavelengths (400 to 1500nm) to measure hemoglobin concentration and oxygenation of blood in superficial capillaries (less than 1 mm depth). This method is sometimes referred to as tissue light-guide spectrophotometry. As shown in Figure 7, DRS devices typically use optical fiber bundles to deliver light from a white light source to the skin. When light enters the skin, it can be reflected, scattered, or absorbed. Light that is reflected from the skin surface (specular reflection) and light that interacts with scattering particles within the skin and then returns to the surface (diffuse reflection) is transported to a spectrometer by optical fibers located near the light source fibers. The geometry of the source and detector fibers within the probe varies among different DRS systems. Some probes contain a random mix of source and detector fibers while others have a fixed geometry, often with the source fiber(s) in the center and detector fibers immediately surrounding the source. The spectrometer disperses light into a spectrum, and a photodetector array or CCD chip is used to convert the spectrum to an electronic signal (Mourant and Bigio 2003).

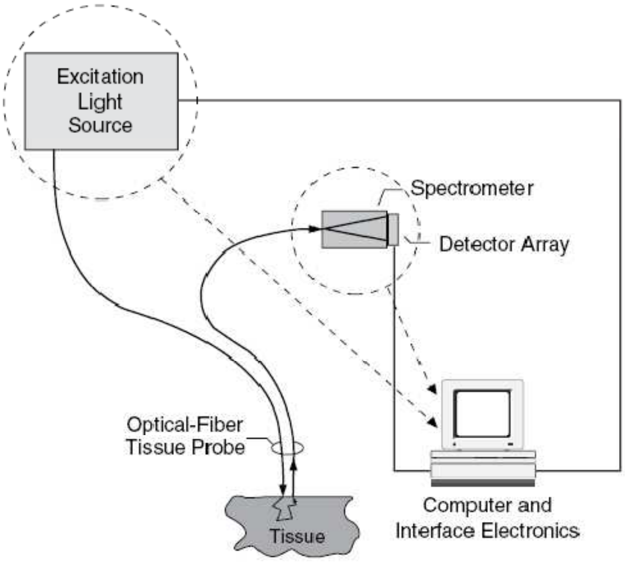

**Figure 7: Schematic of a typical diffuse reflectance spectroscopy system. The excitation light source is typically a bulb or arc-lamp emitting broadband visible and near infrared radiation. Reprinted from (Mourant and Bigio 2003).**

The intensity of the reflectance spectrum is altered by absorbing molecules (chromophores) within the skin. DRS intensity spectra are often converted to absorbance spectra by measuring a white reflectance standard that is defined as having 100% reflectance at all wavelengths. The ratio of the measured intensity signal, $I(\lambda)$, to the reference intensity signal, $I_{ref}(\lambda)$, can be used to calculate an absorbance spectrum using the following equation (Stamatas, Zmudzka et al. 2004):

$$A(\lambda) = -\log_{10}[\ I(\lambda) / I_{ref}(\lambda)\ ] \qquad (1)$$

The main chromophores of interest in wound healing studies are oxyhemoglobin, deoxyhemoglobin, and water; their absorption spectra are shown in Figure 8. The relative contribution of each chromophore to the diffuse reflectance spectrum gathered from a wound or intact skin can be found by fitting the measured DRS spectrum to a reference spectrum from each chromophore (Stamatas, Zmudzka et al. 2004). This provides the relative concentration of each molecule within the volume of tissue probed. Alternatively, specific wavelength bands associated with a molecule of interest can be analyzed directly from DRS spectra. For example, changes in reflectance or absorbance at 550-575nm may be used to identify changes in hemoglobin concentration because these wavelengths are associated with high hemoglobin absorption (see Figure 8) (Wollina, Liebold et al. 2002).

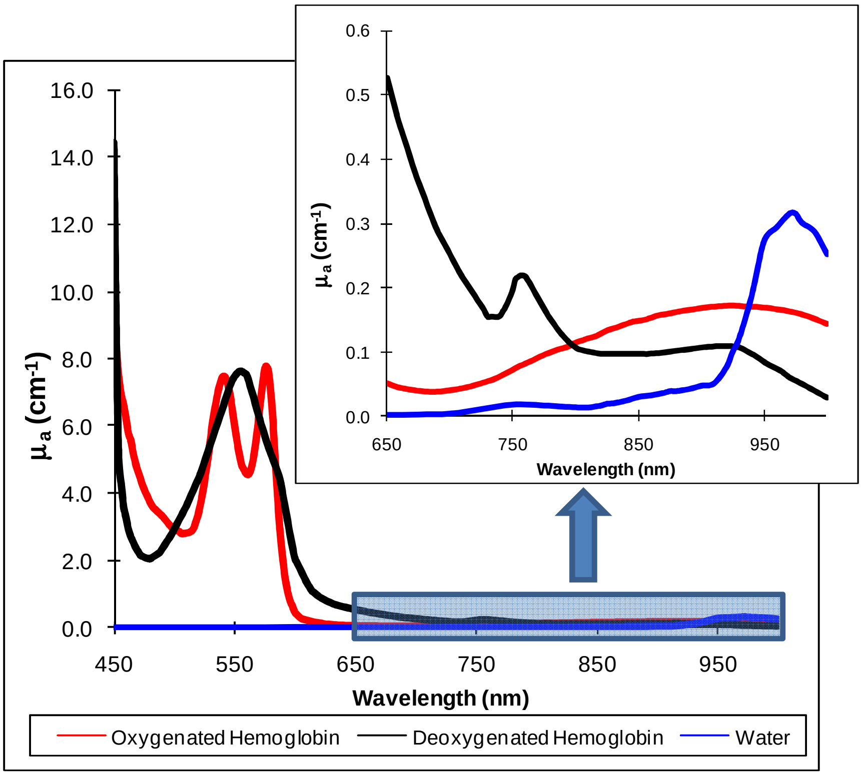

**Figure 8: Absorption of hemoglobin and water in tissue at visible and near infrared wavelengths, assuming 14mM tissue hemoglobin concentration and 70% water. Based on hemoglobin extinction coefficients from (Prahl 1999) and water absorption coefficients from (Querry, Cary et al. 1978).**

In a study by Schmidt et al. 2001, DRS spectra from 29 chronic venous and arterial leg ulcers were obtained at wavelengths in the visible and near infrared range (400-1600nm) using a non-contact fiber optic probe. Non-contact measurements were made by holding the end of the probe at a distance of 1 mm from either the wound surface or the skin immediately adjacent to the wound, eliminating the possibility of contamination or changes in cutaneous microcirculation due to the pressure of the probe. Clinical scores based on the color, consistency, and amount of granulation tissue apparent in each wound were recorded. The authors reported characteristic differences in the spectra of high-scored wounds and low-scored wounds, with high-scored wounds generally having low remittance intensity at wavelengths corresponding to high hemoglobin absorption (450-600 nm). This indicates higher concentrations of hemoglobin in the high-scored wounds compared to the low-scored wounds, perhaps because the high wound scores have better granulation tissue which is highly perfused with blood. However, simple remittance intensity values at wavelengths 450-600 nm did not correlate well with wound score because of high variability among measurements of the same wound (relative standard deviation 5-30%). A more complex multivariate analysis was performed in an attempt to classify the DRS spectra based on clinical wound scores. Cross-validation analysis showed that the DRS spectra could predict the clinical wound scores with an accuracy of 69% (Schmidt, Liebold et al. 2001).

The same research group used DRS to monitor the effect of biosurgical debridement (maggot therapy) on chronic leg or foot ulcers of mixed etiology in 30 patients. These wounds were scanned with a DRS device before and after bio-debridement, which typically lasted 3-4 days. Characteristic differences between the pre- and post-bio-debridement spectra were observed, however these differences were not quantified. Low remittance intensity was observed at wavelengths 548-575nm in post-treatment wounds compared to pre-treatment wounds.  This wavelength range corresponds to maximum hemoglobin absorption, and it was concluded that increased hemoglobin concentration in treated wounds was probably a result of increased granulation tissue formation after bio-debridement (Wollina, Liebold et al. 2002). Although the spectral differences from before and after bio-debridement were not quantified in this paper, one could envision the development of quantifiable index from these data that would be used to measure changes in granulation tissue caused by biosurgical debridement.

Rajbhandari, et. al. 1999 published a study in which serial DRS measurements of 21 neuropathic diabetic foot ulcers were taken over a period of nine months.  The device used in this study operated in the wavelength range 502-628nm, and had a fiber-optic probe that came in contact with the wound through a sterile piece of transparent film.  Whereas the previously described DRS studies used measurements of relative hemoglobin concentration to compare chronic wounds, Rajbhandari et al. report measurements of microvascular oxygen saturation. Oxygen saturation ($SaO_2$) is typically defined as the ratio of oxyhemoglobin to total hemoglobin, where total hemoglobin is defined as the sum of oxygenated and deoxygenated hemoglobin levels.  A curve fitting procedure was used to fit each wound spectrum to reference spectra of oxygenated hemoglobin and deoxygenated hemoglobin, and the mean values of microvascular $SaO_2$ were calculated for each wound at intervals of 2-6 weeks.  Wounds that healed within the 9-month period of the study were compared to wounds that did not heal.  In healed wounds (n=13), values of $SaO_2$ were initially elevated and then decreased significantly ($p=0.018$) over the course of healing.  In non-healing wounds (n=8), values of $SaO_2$ did not change significantly over the course of the study.  Six of the eight non-healing wounds were classified as ischemic by standard clinical diagnostic methodology (ankle-brachial pressure index), and in these wounds the values of $SaO_2$ measured by DRS were significantly lower than in the healed wounds (44 vs. 56%) as would be expected due to poor blood perfusion.  The other two non-healing wounds became infected during the study, and the values of $SaO_2$ became elevated in these wounds prior to clinical recognition of infection. The likely cause of increased $SaO_2$ in infected wounds was increased blood flow to the ulcer due to inflammatory response. Since increased levels of $SaO_2$ were measured using DRS prior to the infections becoming clinically apparent, this technology may have potential clinical utility by providing early warning of infection (Rajbhandari 1999). Furthermore, the decreasing levels of $SaO_2$ observed over time in healing wounds suggest that it may be possible to use DRS to monitor healing progress in diabetic foot ulcers, which could lead to improved evaluation of the effectiveness of treatment efficacy and the prediction of wound closure.

In addition to chronic wounds, DRS operating at wavelengths 500-1100nm has been used to monitor healing of surgical skin flaps in animal models. Blood flow to a group of flaps was temporarily occluded to create a state of ischemia, while a control group flaps remained non-ischemic. Both groups were measured with DRS and laser Doppler perfusion monitoring (LDPM) throughout the procedure. A significant difference in DRS measurements of $SaO_2$ was reported between ischemic and non-ischemic skin flaps, while very little difference was observed in LDPM measurements, indicating that DRS may be more reliable than LDPM in predicting arterial insufficiency (Payette, Kohlenberg et al. 2005). In another study, DRS spectra obtained from 41 human burns were used to predict whether or not healing would occur within 14 days. Rather than calculating relative hemoglobin concentrations and $SaO_2$, an artificial neural network system was developed to predict the time of healing from DRS reflectance spectra. The authors reported sensitivity of 75% and specificity of 97% in predicting whether or not healing would occur within 14 days (Yeong, Hsiao et al. 2005). Although not conducted in chronic wounds, these studies demonstrate that DRS may have clinical value in assessing wound ischemia and in predicting wound closure.

As pointed out by Schmidt et al. 2001, one limitation of using DRS to assess chronic wounds is that there is a high degree of variability among DRS spectra obtained from a single wound. Changes of the surface appearance due to bleeding, dried blood, or wetness from wound dressings will significantly affect the capability of DRS to provide information about the wound status and oxygenation. Another limitation for clinical environments is that ambient light can adversely affect results, so calibrations must be performed in each examination room prior to DRS measurement.

## 3.7 Hyperspectral Imaging

Hyperspectral (or multi-spectral) imaging (HSI) is a spectroscopic method used to obtain two-dimensional maps of cutaneous oxygenation. The principle behind HSI is similar to Diffuse Reflectance Spectroscopy, except that instead of obtaining a spectrum from a point source, many spectra are captured over a wide spatial area (Gillies, Freeman et al. 2003; Vo-Dinh 2004; Khaodhiar, Dinh et al. 2007; Stamatas and Kollias 2007). HSI systems typically consist of a broadband light source with visible and near infrared wavelengths that is used to illuminate the skin and a camera with a tunable optical filter to capture images from the illuminated skin. Tunable optical filters allow the rapid selection of many narrow bands of wavelengths by an electronically controlled tuner. In HSI systems the tunable filter scans a series of wavelengths while a stack of images is gathered by the camera. Software is used to ensure that the images are spatially aligned, and then a reflectance spectrum consisting of the intensity values registered at each pixel for each wavelength can be analyzed (see Figure 9). Relative absorbance spectra can be calculated by comparing the reflectance spectra to white references. Each absorbance spectrum can be fit to reference curves for oxygenated and deoxygenated hemoglobin, and two dimensional maps of hemoglobin oxygen saturation ($SaO_2$) can be generated (Martinez 2002; Gillies, Freeman et al. 2003). Because HSI is a reflectance-based modality, its penetration depth is limited to several hundred microns beneath the surface of the skin. The accuracy of HSI when measuring wounds directly may be compromised if the surface is covered with a reflective fluid, causing a large percentage of the incident light to undergo specular reflection. Light that is specularly reflected from the surface has not propagated through the wound tissue, and therefore does not contain any spectral information about the wound composition. For this reason, some researchers have analyzed the intact skin immediately surrounding the wound rather than the center of the wound (Khaodhiar, Dinh et al. 2007).

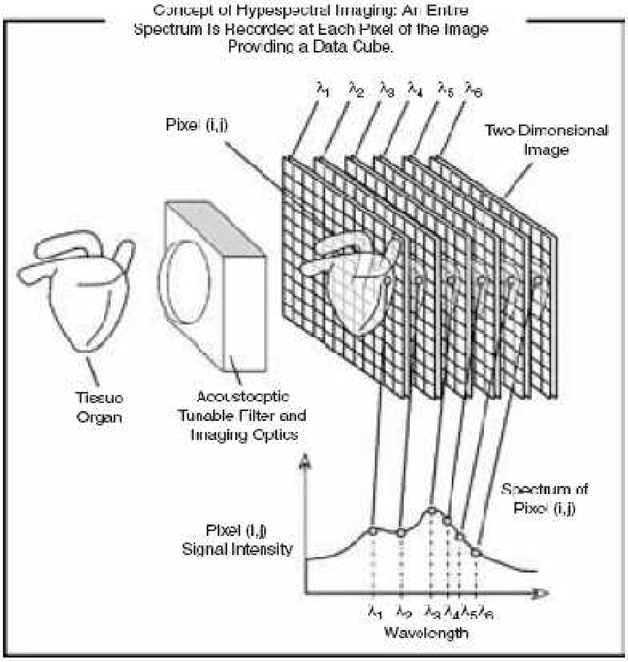

**Figure 9: Hyperspectral data cube. The HSI approach provides a "data cube" of spectral information, which consists of a series of optical images recorded at various wavelengths of interest. Reprinted from (Vo-Dinh 2004).**

Hyperspectral imaging for the analysis of chronic wounds was first reported in 2002 (Martinez 2002). In this proof-of-concept study, oxygen saturation images were generated for one diabetic foot ulcer at several time points during the healing process. Changes in the spatial variability of oxygen saturation were observed over time. In a later study (Greenman, Panasyuk et al. 2005), hyperspectral imaging was used to compare oxy-hemoglobin, deoxy-hemoglobin, and oxygen saturation in diabetic patients with peripheral neuropathy (n=51), diabetic patients without peripheral neuropathy (n=36), and non-diabetic control patients (n=21). Reduced levels of both oxy-hemoglobin and $SaO_2$ were observed in the skin of neuropathic diabetic patients compared to non-neuropathic diabetic patients and non-diabetic patients ($p<0.03$). Deoxy-hemoglobin levels were not significantly different across the three groups. This study demonstrated that HSI has the potential to be used for the early identification of diabetic feet at high risk of ulceration (Greenman, Panasyuk et al. 2005).

In a study published in 2007 (Khaodhiar, Dinh et al. 2007), tissue oxy-hemoglobin and deoxy-hemoglobin were quantified in the skin immediately surrounding 21 foot ulcers in Type I diabetic patients using a commercially available hyperspectral imaging system. Among the subset of ulcers that had healed after 6 months (n=14), it was observed that both oxyhemoglobin and deoxyhemoglobin levels were significantly greater than those observed in non-healing ulcers (n=7). An example of a hyperspectral image of a foot ulcer is shown in Figure 10. A “healing index” based on oxyhemoglobin and deoxyhemoglobin levels was developed to simplify the clinical interpretation of the hyperspectral data. Values of the healing index measured during each subject’s first visit were used to predict whether or a not wound would heal within 6 months with a sensitivity of 93% and a specificity of 86% (Khaodhiar, Dinh et al. 2007), demonstrating the potential of HSI to predict healing of diabetic foot ulcers.

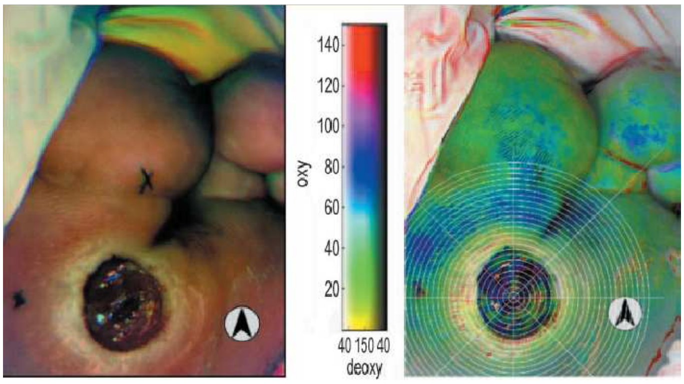

**Figure 10: An example of a diabetic foot ulcer imaged using color photography (left) and hyperspectral technology (left). The color bar indicates oxy-hemoglobin values along the vertical color scale and deoxy-hemoglobin values along the shorter horizontal brightness scale. The radial grid pattern was added to the hyperspectral image to help with quantification of oxy- and deoxy- hemoglobin levels at various locations around the wound. Reprinted from (Khaodhiar, Dinh et al. 2007).**

Hyperspectral imaging has been used to analyze the depth of cutaneous burns in both animal (Sowa, Leonardi et al. 2001) and human studies (Levasseur, Leonardi et al. 2005). Increased levels of oxygenation and hemoglobin were observed in superficial wounds compared to normal skin, while decreased levels were observed in full-thickness wounds compared to normal skin, and it was shown that first, second, and third degree burns could be distinguished using HSI data (Levasseur, Leonardi et al. 2005). HSI was also used in a proof-of-concept study to analyze oxygenation changes in surgical wounds resulting from amputation (Zuzak, Perumanoor et al. 2007).

### 3.8 Deep Tissue Spectroscopy

In spectroscopic devices, the depth of tissue probed depends on the distance between the light source fiber(s) and the detector fiber(s) within the probe, as well as on the wavelength of incident light. As the source-detector separation distance increases, the average depth of penetration increases. The studies described in the Diffuse Reflectance Spectroscopy section were conducted using very small source-detector separations, resulting in penetration depths on the order of several hundred microns. However, some researchers have used larger probes to penetrate tissue up to several millimeters (Beckert, Witte et al. 2004; Cross, Leonardi et al. 2007). The wavelength of light used for illumination can also affect significantly the penetration depth of spectroscopic measurements. As shown in Figure 8, the absorption of light by hemoglobin at near infrared wavelengths (700-1000nm) is roughly an order of magnitude lower than its absorption at visible wavelengths (400-700nm). As a result, near infrared light is able to penetrate up to several centimeters beneath a tissue surface. As with DRS, a measured spectrum can be fitted to reference spectra for oxyhemoglobin, deoxyhemoglobin, and water in order to calculate oxygen saturation ($SaO_2$) and the relative concentration of each chromophore.

Beckert et al. 2004 used a commercially available spectrophotometer (Oxygen to See, LEA Medizintechnik, Germany) to measure $SaO_2$ in diabetic foot ulcers of patients who were clinically ischemic. The authors state that their system used wavelengths ranging from 500-800nm and was capable of measuring $SaO_2$ at depths of 2mm and 6mm. Technical specifications from the device manufacturer indicate that these penetration depths were achieved by using a larger probe size compared to those used by conventional DRS devices. The results from both measurement depths showed significantly increased values of $SaO_2$ and hemoglobin concentration in healed wounds compared to non-healed wounds, indicating that this technology may be helpful in predicting wound healing in diabetic patients with ischemic foot ulcers (Beckert, Witte et al. 2004).

Cross et al. 2007 have developed a spectroscopic device for assessing burn depth. The device detects light in the 500nm to 1100nm wavelength range and has a probe with four detection fibers at distances of 1.5, 3, 4.5 and 6 mm from the source fiber, which provide measurements of $SaO_2$ and relative hemoglobin concentration from four different tissue depths. Significant differences in $SaO_2$ between superficial and full-thickness burns were observed at the 3 deepest locations, and in relative hemoglobin concentration at all 4 detector locations (Cross, Leonardi et al. 2007). The ability to provide spectroscopic data at several depths may prove to be valuable in assessing chronic wound healing as well as burns.

### 3.9 Diffuse Near Infrared Spectroscopy Methodology

Diffuse Near Infrared Spectroscopy (DNIRS), or Diffuse Photon Density Wave (DPDW) methodology at Near Infrared wavelengths, is a variant of deep-tissue spectroscopy that allows the determination of tissue oxyhemoglobin and deoxyhemoglobin concentrations at depths of up to several centimeters. In contrast to the near infrared devices described in the previous section in which the intensity of light illumination was constant, DNIRS methodology uses a near infrared light sources that are intensity-modulated. Because the light intensity in sinusoidally modulated, it is possible to register both the amplitude and phase shift of the detected signals. A diffusion-based model of light propagation in tissue can be used to calculate the absorption and reduced scattering coefficients ($\mu_a$ and $\mu_s'$) from the detected values of amplitude and phase shift (Papazoglou, Weingarten et al. 2006). The absorption coefficients calculated at each wavelength are fitted to the extinction coefficients of oxy- and deoxy-hemoglobin at each wavelength to determine absolute values of the concentration of each chromophore within the volume of tissue investigated. Details of this method will be presented in Chapter 4. One of the main advantages that DNIRS has over the spectroscopic methods discussed in the previous sections is that absolute instead of relative values of hemoglobin concentration can be calculated at depths of several millimeters beneath the surface of a wound.

Previous research on the application of diffuse near infrared methodology to assess wound healing in animal models (Papazoglou, Weingarten et al. 2008; Zhu 2008) showed that changes in the optical properties of wounds could be quantified using DNIRS, and that these changes corresponded to changes in wound vascularization.  In chapter 6 of this thesis, the results of a pilot human study in which chronic diabetic foot ulcers were monitored over the course of several weeks using this methodology are reported.

## 3.10 Comparison of Optical Methods Used to Characterize Chronic Wounds

The above review of the relevant literature of using non-invasive optical methods to assess wound healing reveals that although several technologies exist that could assist in evaluating the status of a wound, the heterogeneity of the population with chronic wounds and the length of time required to properly complete human studies have limited the studies available or make definite conclusions from such studies difficult to reach. It is likely that metabolic information combined with structural details of a wound will be critical to help clinicians evaluate new and / or existing wound treatments and customize such treatments. There is a need for well designed human studies that provide comparative evaluation of some of these technologies. This would encourage their adoption by wound centers which would help to accelerate the rate of data acquisition and further refine the best technologies. The cost of wound care, in the form of active dressings or hyperbaric oxygen therapy or vacuum assisted devices, is significant and application of suboptimal treatment may lead to amputations. Given this cost scenario, commercialization of diagnostic optical devices and their incorporation into the standard of care could help to improve the quality of life for patients and contain costs by giving timely critical information to the clinical decision makers.

Table 1 summarizes the advantages and limitations of each of the optical methods of wound characterization presented in this chapter.

**Table 1: Comparison of optical methods used to characterize chronic wounds**

| Technology | Description | Advantages | Limitations | Published Evidence |
|---|---|---|---|---|
| Frequency domain NIR spectroscopy with Diffuse Photon Density Wave methodology | • Uses optical fibers to transport intensity-modulated near infrared (685-830nm) light to and from tissue and calculates absolute concentrations of oxy- and deoxy-hemoglobin in tissue | • Depth ranges from few millimeters to few centimeters<br>• Provides information on tissue blood vessel density and hemoglobin oxygenation<br>• Non-invasive optical fiber based system<br>• Non-contact measurements are possible<br>• Measures absolute concentration of oxy- and deoxy-hemoglobin in tissue (not relative values)<br>• Not affected by ambient light – minimal calibration is needed<br>• Can be used on skin with high or low levels of melanin<br>• Can separate optical absorption effects from optical scattering effects, which increases the accuracy of hemoglobin measurements compared to non-frequency-domain systems | • Spatial resolution is on the order of several millimeters<br>• Does not measure structural features of wound tissue<br>• Does not measure blood flow | • Papazoglou 2006, 2008, 2009 |
| Continuous-Wave Near Infrared Spectroscopy (Deep tissue spectroscopy) | • Uses broadband light at visible and near infrared wavelengths (500-1100 nm) to measure relative values of oxy-hemoglobin concentration and deoxy-hemoglobin concentration | • Optical fibers deliver light to tissue non-invasively<br>• Measures relative concentrations of oxy- and deoxy-hemoglobin within a localized region of skin.<br>• Penetration depth up to several millimeters | • Cannot measure absolute concentrations of oxy- and dexoxy-hemoglobin (provides relative measurements in arbitrary units)<br>• Cannot separate optical absorption effects from optical scattering effects, and it is expected that optical scattering effects will change significantly during healing.<br>• Calibration may be necessary before each measurement because ambient light may affect the results. | • Increased values of oxygenation in healed ischemic wounds compared to non-healed ischemic wounds (Beckert et al. 2004). (Article has very few technical details).<br>• Measurements at 4 different depths were used to distinguish full-thickness burns from partial-thickness burns (Cross et al. 2007) |

| Technology | Description | Advantages | Limitations | Published Evidence |
|---|---|---|---|---|
| Diffuse Reflectance/Remittance Spectroscopy (DRS)<br>OR<br>Tissue light-guide spectrophotometry | • Uses broadband light at visible and near infrared wavelengths (400 to 1500nm) to measure relative values of oxy-hemoglobin concentration and deoxy-hemoglobin concentration in superficial capillaries | • Optical fibers deliver light to tissue non-invasively<br>• Non-contact measurements are possible<br>• Measures relative concentrations of oxy- and deoxy-hemoglobin within a localized region of superficial skin. | • Penetration depth less than 0.5 mm<br>• Cannot measure absolute concentrations of oxy- and dexoxy-hemoglobin (provides relative measurements in arbitrary units)<br>• Cannot measure directly on wound surface because changes of the surface appearance due to bleeding, dried blood, or wetness from wound dressings will significantly affect the results.<br>• Calibration is necessary before each measurement because ambient light affects the results.<br>• Skin color affects results | • Multivariate analysis was used to correlate DRS spectra from 29 leg ulcers with physician-assessed wound scores with 69% accuracy (Schmidt 2001).<br>• Measured Diabetic Foot Ulcers every 2-6 weeks for 9 months and compared healed wounds to non-healed wounds. Significant changes in oxygen saturation were observed in healing wounds, but not in non-healing wounds. (Rajbhandari, et. al. 1999). However, 75% of non-healing wounds were known to be ischemic at the start of the study. |

| Technology | Description | Advantages | Limitations | Published Evidence |
|---|---|---|---|---|
| Hyperspectral Imaging | • Consists of a broadband light source with visible and near infrared wavelengths that is used to illuminate the skin and a camera with a tunable optical filter to capture images from the illuminated skin. | • Non-contact<br>• Creates two-dimensional maps of superficial cutaneous oxygenation (relative concentrations of oxy- and deoxy-hemoglobin) | • Penetration depth less than 0.5 mm<br>• Cannot measure absolute concentrations of oxy- and dexoxy-hemoglobin (provides relative measurements in arbitrary units)<br>• Cannot measure directly on wound surface because changes of the surface appearance due to bleeding, dried blood, or wetness from wound dressings will significantly affect the results.<br>• Calibration is necessary before each measurement because ambient light affects the results.<br>• Skin Color affects results | • Oxygenation measurements of the intact skin surrounding an ulcer were used to predict whether or a not diabetic foot ulcers would heal within 6 months with a sensitivity of 93% and a specificity of 86% (Khaodhiar et al. 2007) |
| Laser Doppler Perfusion Monitoring (LDPM) and Imaging (LDPI) | • Quantifies red blood cell microcirculation<br>• Measures frequency shifts of an incident coherent light beam to determine a quantitative index (Laser Doppler Flux – LDF) that is related to microvascular blood flow or perfusion | • Non-invasively indicates microvascular blood flow or perfusion within a localized region<br>• Can be used with optical fibers for point measurements or mirrors/lenses to create a spatial map (~1mm spatial resolution) of LDF.<br>• Non-contact measurements are possible | • Penetration depth 0.5-1.0 mm<br>• Results from different devices cannot be compared because LDF is calculated in arbitrary units using proprietary algorithms that differ by device manufacturer.<br>• In imaging systems, specular reflection of the light beam may occur due to curvature of the feet and presence of moisture on the surface of the wound, resulting in a loss of signal<br>• Patient is required to remain motionless for 4-5 minutes during image acquisition in order to avoid motion artifacts.<br>• Trained Professional can use it | • Not used to predict healing outcome or to monitor vascular changes that occur during healing<br>• Used to quantify ischemia in wounded limbs (venous leg ulcers, arterial leg ulcers, diabetic foot ulcers) |

| Technology | Description | Advantages | Limitations | Published Evidence |
|---|---|---|---|---|
| Optical Coherence Tomography (OCT) | • Low coherence interferometry<br>• Typically use near infrared light<br>• High resolution cross-sectional images of structural features in skin | • Non-contact<br>• Resolution ~10 micron<br>• Visualization of superficial epithelialization, granulation tissue, collagen, inflammatory infiltration, skin thickness | • Penetration depth less than 1 mm<br>• No metabolic information – only structural information<br>• Image analysis algorithms are needed to obtain quantitative information | • No published studies of human chronic wounds – only controlled laboratory wounds |
| Polarization-sensitive optical coherence tomography (PS-OCT) | • Variation of OCT that provides information on the quantity and structure of collagen in addition to structural images<br>• Measures polarization changes due to tissue birefringence | • Non-contact<br>• Resolution ~10 micron<br>• Visualization of collagen structure, superficial epithelialization, granulation tissue, collagen, inflammatory infiltration, skin thickness | • Penetration depth less than 1 mm<br>• No metabolic information – only structural information<br>• Image analysis algorithms are needed to obtain quantitative information | • No published studies of human chronic wounds – only controlled laboratory wounds |
| Orthogonal Polarization Spectral (OPS) Imaging | • Illuminate tissue with monochromatic (548nm) polarized light<br>• Detect light using CCD camera with polarization filter and magnifying objective lens<br>• Red blood cells absorb light @ 548nm, so they appear black on a bright background | • Directly visualize microcirculation *in-vivo* without the use of contrast agents or dyes.<br>• Cross-polarization of the camera with respect to illumination prevents specular reflection from affecting results<br>• Spatial resolution ~1 micron per pixel<br>• Can obtain real-time video of RBC movement in skin's microvasculature | • Depth ~200 microns<br>• No information about oxygenation<br>• Video/Image analysis software that requires significant manual user intervention is needed to quantify microcirculatory parameters<br>• High melanin content prevent images from being obtained | • Microcirculatory damage was quantified in patients with chronic venous insufficiency (which often leads to venous ulcers). OPS results correlated with semi-quantitative system of clinical observation (Virgini-Magalhães et al. 2006)<br>• Quantify superficial vs. deep burns (Milner et al. 2005)<br>• Studies excluded patients with dark skin |

| Technology | Description | Advantages | Limitations | Published Evidence |
|---|---|---|---|---|
| Thermal Imaging | • Measure thermal emission from skin using cameras sensitive at the 8-10µm wavelength range<br>• Creates images of skin temperature with spatial resolution ~2-4mm, temperature resolution near 0.1ºC | • Local temperature increases have been correlated with increased risk of pressure ulcer and diabetic foot ulcer development | • Measurements are superficial because superficial tissue absorbs thermal radiation from deep tissue.<br>• Calibration must be done frequently | • Pressure ulcers develop in regions of high temperature (Newman and Davis 1981)<br>• Diabetic foot ulcers develop in regions of high temperature (Armstrong et al. 1997)<br>• Detects osteomyletis in bone underlying foot ulcers (Harding et al. 1998) |

# CHAPTER 4: DIFFUSE NEAR INFRARED SPECTROSCOPY

## 4.1 Background

Diffuse Near Infrared Spectroscopy (DNIRS), or Diffuse Photon Density Wave Methodology (DPDW) at near infrared wavelengths, is a non-invasive method of measuring the optical properties of tissue at depths of up to several centimeters. The geometry of a typical non-invasive DNIRS measurement would involve illuminating a tissue surface (e.g. skin) with a narrow beam of light and then detecting light that propagates through a volume of tissue and returns to the tissue surface at some distance from the light source. As light propagates through tissue, it can be scattered and absorbed, as described below.

Light scattering occurs when photons encounter particles with refractive index mismatch at the interface of the particle and the surrounding medium. The scattering coefficient ($\mu_s$) is a measure of the likelihood that a scattering event will occur, and depends on the size, shape, number density, and refractive indices of physical structures within the tissue, and on the wavelength of incident light. $\mu_s$ is the inverse of the average distance a photon is expected to travel before a scattering event occurs, and is often measured in units of inverse centimeters ($cm^{-1}$). The scattering coefficient of tissue cannot be measured directly using DPDW methodology. Instead, the reduced scattering coefficient ($\mu'_s$) is measured. The reduced scattering coefficient is the inverse of the transport length $l^*$, which is the average distance a photon must travel before its direction of propagation becomes random. $\mu'_s$ is defined as a function of the scattering coefficient $\mu_s$ and the anisotropy of scattering ($g$) according to the equation: $\mu'_s = \mu_s(1-g)$ (Mobley and Vo-Dinh 2003). The anisotropy of scattering is a measure of the forward component of a photon's trajectory after a scattering event, and is defined as the average cosine angle of scattering (see Figure 11). The value of $g$ in tissue is approximately 0.9

for near infrared wavelengths, indicating a strongly forward scattering regime (Mobley and Vo-Dinh 2003). Since *g* is unitless, $\mu'_s$ is often measured in units of inverse centimeters ($cm^{-1}$).

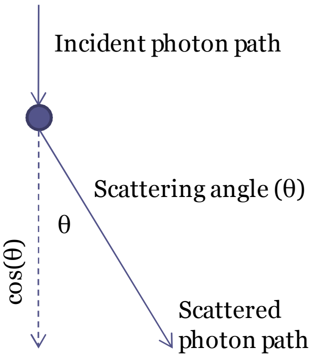

**Figure 11: Diagram of a light scattering event, showing the scattering angle and the forward component of the scattering angle, cos(θ).**

Optical absorption occurs when light encounters chromophores within tissue. The optical absorption coefficient ($\mu_a$) is a measure of the likelihood of an absorption event, and is often measured in units of inverse centimeters ($cm^{-1}$) like $\mu_s$ and $\mu'_s$. The primary absorbing chromophores in wound tissue are oxygenated hemoglobin, deoxygenated hemoglobin, and water. The optical absorption of hemoglobin decreases sharply at red and near infrared wavelengths (600 – 850 nm) when compared to other visible wavelengths (Figure 12). This behavior provides a “diagnostic window” that allows the determination of tissue optical properties at depths of up to several centimeters, which is not possible with visible light. The absorption spectra of oxy-hemoglobin and deoxy-hemoglobin are distinct at near infrared wavelengths (Figure 12 inset), and therefore the absolute concentrations of each chromophore can be determined if the light absorption is known (based on known extinction coefficients).

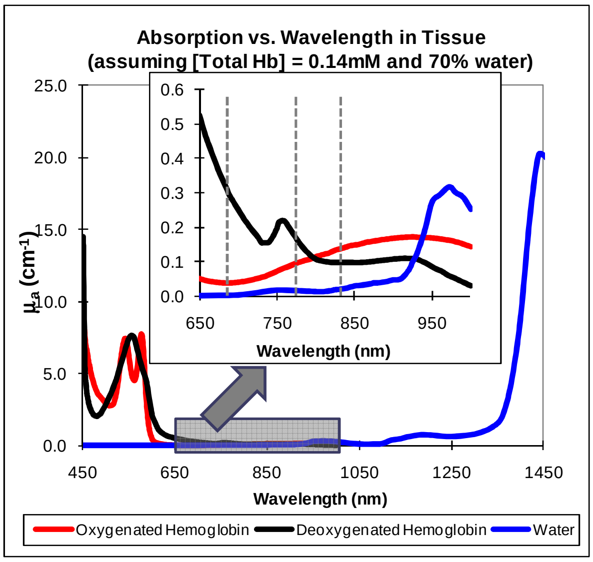

**Figure 12: Absorption of hemoglobin and water in tissue at visible and near infrared wavelengths, assuming 14mM tissue hemoglobin concentration and 70% water. Based on hemoglobin extinction coefficients from Prahl 1999 and water absorption coefficients from Querry et al. 1978.**

There are three experimental methods that can be used to measure the optical properties ($\mu_a$ and $\mu'_s$) of multiply scattering tissues at NIR wavelengths. The main difference between these methods is the source of incident light. Continuous Wave (CW) devices use constant power lasers (Culver 2003; Ntziachristos 1998), time resolution spectroscopy instruments (TRS) use very short light pulses (Fishkin 1997; Patterson 1989; Schmit 1998), and frequency domain systems use lasers that are modulated sinusoidally (Durduran 2002; Fantini 1994). CW devices use the least complicated and least expensive hardware, but can provide only information about changes in the amplitude of scattered light. TRS instruments can provide information about changes in amplitude and the time delay of scattered light, but the pulsed lasers and high-speed detectors can be expensive and difficult to use in a clinical setting. Frequency-domain systems can provide information about the amplitude and time delay (phase shift) of scattered light, but with lower cost and simpler operation compared to TRS devices.

The advantage of obtaining information about changes in both the amplitude and phase shift (or time delay) of scattered light is that analytic solutions allow the independent calculation of the optical absorption and reduced scattering coefficients when amplitude and phase shift are known. In the process of wound healing the tissue structure changes significantly over time, and therefore we expect that optical scattering will also change over time. This necessitates obtaining the absolute values of both the absorption $\mu_a$ and reduced scattering $\mu'_s$ coefficients, in order to be able to fully separate scattering from absorption effects. A frequently used model to describe light propagation in tissue is the one based on the diffusion approximation; closed solutions of the diffusion equation allow determination of tissue optical properties. A brief analytical description of the light propagation by diffusion is provided below.

## 4.2 Diffuse Photon Density Wave Methodology

Light propagation in dense inhomogeneous scattering media is described by the Boltzmann transport equation. In the case of biological tissue the Boltzmann equation can be converted to the time – dependent diffusion equation where the fluence rate $\Phi$ (photons/ [m$^2$*sec]) obeys the following equation:

$$\frac{1}{V}\frac{\partial \Phi}{\partial t} = D * \nabla^2 \Phi(\vec{r}, t) - \mu_a \Phi(\vec{r}, t) + S(\vec{r}, t) \qquad \textbf{(Eq. 1)}$$

where $S(\vec{r}, t) = (S_{dc} + S_{ac} * e^{-i\omega t})$ is the photon source term, $S_{dc}$ and $S_{ac}$ are the DC and AC components of the source radiation, $\omega$ is the source modulation frequency (70 MHz for our device), *V* is the speed of light in the tissue ((3/1.4*10$^8$) m/s), and the photon diffusion coefficient is:

$$D = \frac{1}{3}\left(\mu_a + \mu_s^{'}\right) \qquad \textbf{(Eq. 2)}$$

Propagation of light in tissue can be described by the diffusion approximation only when the following assumptions are met: (1) $\mu_s' >> \mu_a$; (2) the light source is quasi-isotropic; and (3) the modulation frequency is less than the frequency of photon collisions (f < ~500 MHz).

Closed analytical solutions to the diffusion equation can be obtained for special cases of the boundary conditions. For semi – infinite geometries, typical of tissue measurements, sources and detectors are placed on an air –tissue interface. The optical fiber source is modeled as an isotropic, point light source. The so-called extrapolated condition for semi-infinite media provides a good approximation in non-invasive clinical applications where the fluence rate is nonzero at the boundary, but it extrapolates to zero at some distance $z_b$ above the tissue surface (Farrell, Patterson et al. 1992; Haskell, Svaasand et al. 1994). The theory allows derivation of an expression for $\Phi(\vec{r})$ as a function of effective distances $r_b$ and $r_1$, which depend on the Fresnel reflection at the tissue-air interface, the transport length *l** (where $l^*=1/\mu_s'$) and the source – detector separation $\rho$ along the sample surface (Haskell, Svaasand et al. 1994; Pham, Coquoz et al. 2000),

$$\Phi(\rho,t) = S_{ac}\exp(-i\omega t)\left(\frac{\exp(ikr_1)}{r_1} - \frac{\exp(ikr_b)}{r_b}\right) \qquad \textbf{(Eq. 3)}$$

where $k = k_{real} + ik_{imag}$ is a complex diffuse wavenumber.

For measurements on tissue surfaces (semi-infinite geometry), $r_1$ and $r_b$ can be written as:

$$r_1 = \sqrt{\mu_s'^{-2} + \rho^2};$$
$$r_b = \sqrt{\left(\frac{4}{3\mu_s'} * \frac{(1+R_{eff})}{(1-R_{eff})} + \frac{1}{\mu_s}\right)^2 + \rho^2};$$

**(Eq. 4)**

Here, $R_{eff}$ is the effective reflection coefficient, approximately equal to 0.4 – 0.5 in tissue (Haskell, Svaasand et al. 1994) and $\rho$ is the distance between the source and the detector positions. In the semi-infinite geometry, when the detector is at a distance of at least 2 to 3 transport lengths (*l**) from the isotropic point source, the following linear relationship can be used (Boas 1996):

$$\ln[\rho^2 * A_{att}(\rho)] = -k_{real} * \rho + \ln(A_0)$$
$$\Theta_{lag} = k_{imag} * \rho + \Theta_0$$

**(Eq. 5)**

where

$$k_{real} = \sqrt{\frac{3}{2}\mu_a\mu_s'}\sqrt{\left[1+\left(\frac{\omega}{V\mu_a}\right)^2\right]^{1/2} + 1};$$
$$k_{imag} = \sqrt{\frac{3}{2}\mu_a\mu_s'}\sqrt{\left[1+\left(\frac{\omega}{V\mu_a}\right)^2\right]^{1/2} - 1};$$

**(Eq. 6)**

and $A_{att}(\rho)$ is the experimental intensity of scattered light measured in mV (millivolts), $\Theta_{lag}(\rho)$ is the experimentally measured change of phase relative to the phase of the 70MHz generator, and $V$ is the velocity of light in tissue. $k_{real}$ and $k_{imag}$ represent the real and imaginary components of the complex wavenumber of the diffuse photon density wave. Since the modulation frequency ($\omega$) and the speed of light tissue ($V$) are fixed values, the values of $\mu_s'$ and $\mu_a$ in tissue can be determined from measurements of the amplitude and phase shift of sinusoidally modulated light at known distances from the light source.

### 4.3 Calculation of hemoglobin concentration from optical absorption

Oxyhemoglobin concentration ([*HbO$_2$*]) and deoxyhemoglobin concentration ([*Hb*]) can be determined from the measured values of the optical absorption coefficient ($\mu_a$) using the method described by Shah et al. (Shah, Cerussi et al. 2004). When it is assumed that oxyhemoglobin, deoxyhemoglobin, and water are the primary chromophores at near infrared wavelengths (685 - 830 nm), Equation 6 can be used to describe the relationship between measured values of absorption coefficient ( $\mu^{\lambda}_{a,measured}$ ) and the concentrations of hemoglobin and water:

$$\mu^{\lambda}_{a,measured} = \varepsilon^{\lambda}_{Hb}[Hb] + \varepsilon^{\lambda}_{HBO2}[HbO_2] + \mu^{\lambda}_{a,H2O}[\%\ H_2O] \qquad \textbf{(Eq. 7)}$$

where $\varepsilon^{\lambda}_{Hb}$ and $\varepsilon^{\lambda}_{HBO2}$ are the molar extinction coefficients of deoxy- and oxyhemoglobin at each wavelength (λ = 685, 780, and 830 nm) as published in Prahl 1999 (Prahl 1999), $\mu^{\lambda}_{a,H2O}$ is the absorption coefficient of pure water at each wavelength as published in Hale and Querry 1973 (Hale and Querry 1973), and the concentration of water [*% H$_2$O*] was assumed constant at 70%. The choice of a value for [*% H$_2$O*] has little effect on the calculated values of hemoglobin concentration because of the low absorption of water relative to hemoglobin at wavelengths in the range 685-830 nm (Svensson, Andersson-Engels et al. 2007).

Values of [*HbO$_2$*] and [*Hb*] can be derived from the experimental values of $\mu^{\lambda}_{a,measured}$ through a least-squares fitting method. Specifically, the values of [*HbO$_2$*] and [*Hb*] are used as fitting parameters to minimize the following expression:

$$Min\left\{\left[\mu^{\lambda}_{a,measured} - \left(\varepsilon^{\lambda}_{Hb}[Hb] + \varepsilon^{\lambda}_{HBO2}[HbO_2] + \mu^{\lambda}_{a,H2O}[\%\ H_2O]\right)\right]^2\right\} \qquad \textbf{(Eq. 8)}$$

Total hemoglobin concentration [*Tot Hb*] can be calculated as the sum of [*Hb*] and [$HbO_2$].

Oxygen saturation can be calculated as [$HbO_2$] / [*Tot Hb*].

## 4.4 Diffuse Near Infrared Spectroscopy System

### *4.4.1 Hardware*

A schematic of the frequency-domain NIR system is shown in Figure 13. The system includes one source position, four detector channels, and three diode lasers ($\lambda$ = 685, 780, and 830 nm). A 70 MHz RF signal (Wilmanco Corp.) is used to modulate the intensity of the light emitted from each laser diode. One wavelength at a time is directed to the tissue by a 1x4 optical switch (Dicon Fiberoptics), that cycles through all three wavelengths. The optical switch is controlled by digital signals generated by a data acquisition board (National Instruments) and laptop computer. A variable optical attenuator (Oz Optics, Ltd) is connected to the output of the optical switch to provide control over the intensity of light delivered to the tissue. A 62.5/125 µm multimode optical fiber is used to deliver light from the attenuator to the tissue.

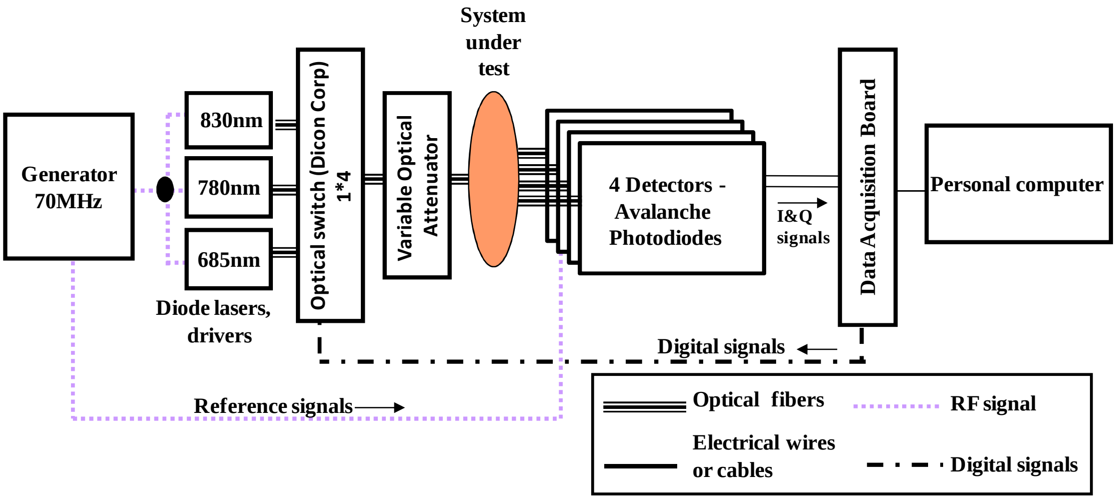

**Figure 13: Schematic of frequency-domain diffuse near infrared system**

Four optical fiber bundles with diameters 0.5 mm (1st and 2nd detectors) and 1.0 mm (3rd  and 4th detectors) are used to deliver backscattered light from the tissue to four avalanche photodiode (APD) detectors (Hamamatsu C5331-03).  The electrical signal from each APD is passed through an amplifier (Mini-Circuits, ZFL-500LN), a band-pass filter (70MHz), and a second amplifier (Mini-Circuits, ZFL-500HLN).  Then the signal is fed to an In-Phase/Quadrature (I/Q) demodulator (MIQY-70D, Mini-Circuits), which compares the detected signal to a reference signal from the RF generator.  The outputs of the I/Q demodulators are the cosine (I) and sine (Q) low frequency components of amplitude and phase shift relative to the reference signal. The I and Q signals are digitized by the data acquisition board (National Instruments), and these data are recorded on a laptop computer.  A photograph of the device and computer is shown in Figure 14.

**Figure 14: Photograph of frequency-domain diffuse near infrared system**

### *4.4.2 Probe*

The optical fiber that delivers light to the tissue from the optical switch (source fiber) and the four optical fibers that delivery light from the tissue to the photodetectors (detector fibers) are immobilized on a Teflon probe. The four detector fibers are fixed at distances of 4, 8, 12, and 16 mm from the source fiber. The distances of the detector fibers from the source fiber determine the measurement depth of the NIR system. A rule of thumb estimate for depth penetration in tissue is between 1/3-1/2 of the source-detector distance (Weiss, Nossal et al. 1989; Fridolin, Hansson et al. 2000); therefore our probe configuration allows the calculation of $\mu_a$ and $\mu'_s$ at depths of approximately 4-6 mm beneath the surface of a wound. A diagram and a photograph of the probe are shown in Figure 15.

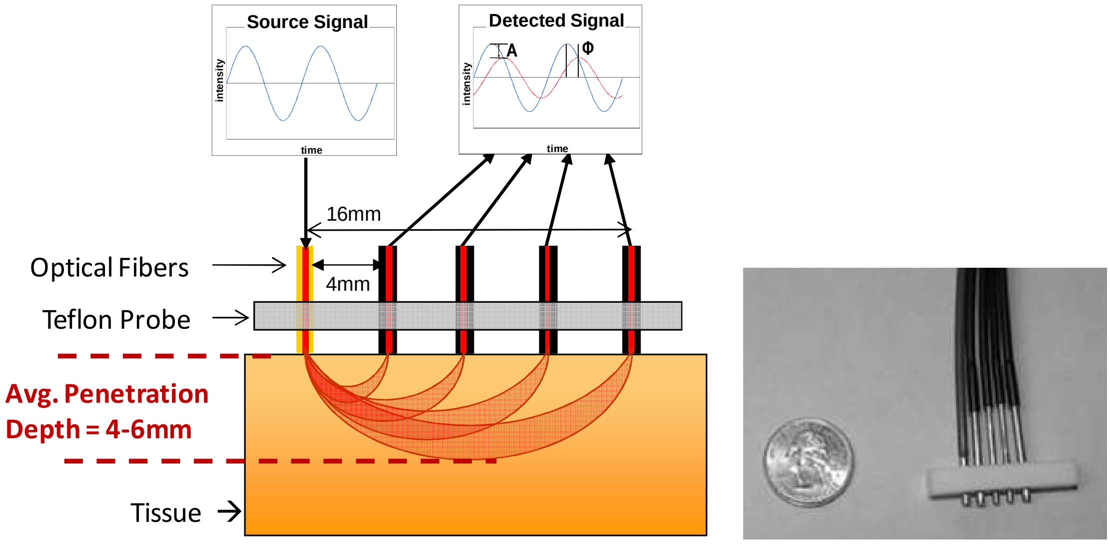

**(a)** **(b)**

**Figure 15: (a) Diagram and (b) photograph of the optical fiber probe used in this research (coin included for size reference). The fiber on the left delivers light from the lasers to the tissue, while the remaining four fibers deliver back-scattered light from the tissue to the photodetectors. Fibers are spaced equidistantly at 4 mm apart. The dimensions of the Teflon probe are 3.6 cm x 0.4 cm x 0.6 cm (length x width x height).**

An important factor that must be considered when designing the geometry of a probe is the minimum distance between the source and detector fibers. The transport length *l** represents the distance of propagation of a collimated beam of light before it becomes effectively isotropic, and can be approximated by $1/\mu_s'$ when $\mu_s' >> \mu_a$ as is the case in tissue. It is possible to use the diffusion approximation to calculate absorption and scattering of tissue from the intensity and phase shift of scattered NIR light using a probe where the minimum distance between source and detector fibers is greater than one to three transport lengths ($\rho > l^*$) (Vo-Dinh 2003; Jacques and Pogue 2008). In particular, after propagating more than one to three transport lengths most photons have undergone multiple light scattering (i.e. they are now at a different orientation from their incident direction) and may be described as diffuse. For most human tissues, $\mu_s'$ is ~10 $cm^{-1}$, therefore the transport length $l^*$ is approximately 1 mm, since $l^*$ is the inverse of the reduced scattering coefficient $\mu_s'$. This suggests that the smallest source-detector distance that can be used in probe design is 2-3 mm for the diffusion approximation to be valid (Dunsby and French 2003). The probe used in this research has a minimum distance between source and detector fibers of 4 mm to be safely within the diffusion approximation regime.

### *4.4.3 Software*

Computer software written with Visual Basic is used to operate the DNIRS system and to record data obtained from the system. The Visual Basic program performs the following tasks:

- Enables the user to start and stop measurements.

- Sends digital signals to the optical switch during each measurement causing the switch to cycle through each wavelength.
- Records the digitized I and Q signals from the I/Q demodulators in each detector block.
- Records the detector offsets, or dark signals, which are the I and Q signals registered at each detector when no light is entering the detector fibers. These offsets are checked at the beginning of every measurement sessions and stored in memory. The recorded offsets are automatically subtracted from all subsequent measurements of I and Q.
- Calculates the amplitude and phase shift at each detector from the adjusted values of I and Q (adjusted by subtracting the offset signals).
    - $Amplitude = sqrt[I^2 + Q^2]$
    - $Phase\ Shift = arctan(Q/I)$
- Automatically writes a text file during each measurement that contains the values of I, Q, Amplitude, and Phase Shift measured at each detector at each wavelength.

When a DNIRS measurement is complete, a second program that was written with Matlab is used to calculate optical absorption and reduced scattering coefficients from the text files that the Visual Basic program writes. The Matlab program performs the following tasks:

- Loads a text file containing the values of I, Q, Amplitude, and Phase Shift measured at each detector at each wavelength.
- Applies calibration coefficients as described in Section 4.5.5 Calibrating multiple detectors using equidistant probe
- Plots and finds the slopes of linear trendlines fitted to log(Amplitude*$\rho^2$) vs. $\rho$, and Phase Shift vs. $\rho$, where $\rho$ is the source-detector separation distance. As shown in Eq. 5 and Eq. 6 from Section 4.2 Diffuse Photon Density Wave Methodology, these slopes are

the real and imaginary components ($k_{real}$ and $k_{imag}$, respectively) of the complex wavenumber.

- Calculates $\mu_a$ and $\mu'_s$ using the values of $k_{real}$ and $k_{ima}$ determined in the previous step, according the following equations (Boas 1996):

$$\mu_a = \frac{\omega}{V}\left[\tan\left(2\tan^{-1}\frac{k_{real}}{k_{imag}}\right)\right]^{-1} \qquad \mu'_s = \frac{k_{imag}{}^2 + k_{real}{}^2}{3\left(\mu_a{}^2 + \frac{\omega^2}{V^2}\right)^{1/2}}$$

where $\omega$ is the modulation frequency in radians (70MHz * 2π) and $V$ is the speed of light in tissue: ($3x10^{10}$ cm/s) / $n$; where $n$ is the index of refraction of tissue. We use $n$=1.33, but the value could range from 1.33 to 1.5 (Mobley and Vo-Dinh 2003).

- Calculates oxyhemoglobin concentration [$HbO_2$], deoxyhemoglobin concentration [*Hb*], total hemoglobin concentration [*Tot Hb*], and oxygen saturation using the methods described in Section 4.3 Calculation of hemoglobin concentration from optical absorption.
- Identifies any data file that does not meet the validation requirements described in Section 6.1.3 Validation of Optical Data.

A new software program was developed using Labview (National Instruments, Austin, TX) in order to improve the clinical utility of the software. The Labview software includes all of the VisualBasic and Matlab the functionality described above, in addition to the following features:

- Calculates and records $\mu_a$, $\mu'_s$, [$HbO_2$], [*Hb*], [*Tot Hb*] in real-time, as measurements are being obtained. This enables the user to see immediately whether the measured optical properties are within a reasonable range of values.

- An improved user-interface for conducting DNIRS measurements, viewing results, and troubleshooting any device issues.
- Automatically identifies (in real-time) measurements that are invalid due to low signal strength or probe movement, allowing the device operator to make adjustments and/or repeat measurements.

The Labview software is intended to replace the VisualBasic and Matlab programs. However, none of the animal or human data reported in this thesis were obtained using the Labview software, because the new software was developed after the animal and human studies were started. We decided not change the software in the middle of these studies, which could potentially introduce unexpected variables into the analysis of our data. However, the Labview software has been successfully used in some recent animal studies and will be used in future human studies.

## 4.5 Calibration and Testing

### *4.5.1 Optical Phantoms*

Many of the calibration and testing procedures used to characterize the performance of the DNIRS system include measurements of the optical properties of various intralipid suspensions. Intralipid is an emulsion of fats that is commonly used as an optical phantom because its light scattering properties are similar to living tissue (Driver, Feather et al. 1989; Van Staveren, Moes et al. 1991; Flock, Jacques et al. 1992). The intralipid used in our phantom experiments (Liposyn 20% from Abbott Laboratories) is usually diluted in deionized water from its original concentration of 20% to concentrations ranging from 0.5-2.0%, which produces phantoms with reduced scattering coefficient ($\mu'_s$) values similar to those measured in human tissue. Placing the probe on the surface of the intralipid suspension allows measurement and calculation of optical properties in a geometric configuration that is similar to an *in-vivo* diagnostic situation. Varying the concentration of intralipid will change the scattering coefficient of the suspension, while the absorption coefficient ($\mu_a$) will remain nearly constant and similar to the optical absorption of water at near infrared wavelengths (Driver, Feather et al. 1989).

Black India Ink (Higgins Corp) can be added to intralipid solutions to alter the optical absorption properties of the phantom. The relative concentration of intralipid to ink is approximately 10,000:1 to resemble properties of human tissue. The low concentrations of ink relative to intralipid are expected to have very little effect on the reduced scattering coefficients ($\mu'_s$) of intralipid / ink phantoms, but can significantly increase the optical absorption coefficient ($\mu_a$) over those of intralipid-only suspensions.

It should be noted that the use of an Intralipid solution as an optical phantom for experiments that span several days is not the best approach, because the solution changes optical properties due to phase separation and degradation. An additional factor that contributes to operator variability when using Intralipid is the repeatability of placing the solid plastic probe exactly on the surface of the solution. Use of the semi-infinite approximation relies on perfect contact between the solid and liquid interface, without any air gap and also without immersing the probe in the liquid. A practical issue with using intralipid phantoms in medical clinics is the inconvenience of transporting a container of liquid. Solid phantoms can overcome many of these challenges: Silicone optical phantoms were the method of choice for testing the stability of the DNIRS device for long-term studies because these phantoms do not change optical properties during the time course of our experiments.

Cylindrical phantoms made of silicone with dispersed particles of titanium dioxide to act as scatters and carbon black to act as an absorber were used (Basu 2007). The amount of scattering and absorbing particles can be varied to match the optical properties of tissue, and the silicone mixtures can be molded into any desired shape or size. Several solid phantoms were created having optical properties similar to tissue ($\mu_a$ : 0.05-0.15 $cm^{-1}$, $\mu_s$' : 5-15$cm^{-1}$) that are suitable for daily calibration/testing of our NIR device in a clinical or field setting. Cylinders with diameter of 90mm and thickness of 45mm were synthesized from silicone with activator (XP565 from Silicones Inc); $TiO_2$ particles with diameter between 0.9 - 1.6 µm simulated tissue scattering and carbon black acetylene, 50% compressed, 99.9+% (metals basis) (diameter = 0.042 µm) simulated light absorption. Both $TiO_2$ and carbon black were obtained from Alfa Aesar. Variables in the preparation of these models include intensity and time of mixing, the order of addition of the components, and the environment in which the crosslinking reaction occurs. These variables were optimized to ensure that phantoms can be consistently produced with the desired optical properties, homogeneity, and without air bubbles.

Details of the phantom manufacturing process are explained in the M.Sc. thesis of Hande Basu (Basu 2007). Briefly, the steps required to produce a cylindrical optical phantom having optical properties similar to tissue ($\mu_a$=0.05-0.10 $cm^{-1}$; $\mu'_s$=10-15 $cm^{-1}$) are as follows:

1. A very small amount of carbon black acetylene particles are needed to achieve optical absorption coefficients similar to human tissue. Furthermore, the density of carbon black acetylene powder is extremely low, making it difficult to accurately measure the amount of carbon black added to the phantom. Therefore, it is necessary to prepare a master batch of silicone and carbon black by thoroughly mixing a “pinch” of carbon

black (approximately 0.5 ml) with 100 g of uncured silicone base (Silicones, Inc. XP-565B). This master batch of carbon black will be used in all phantoms.

2. Measure 105 grams of uncured silicone base in 250ml beaker.
3. Add 5 grams of carbon black / silicone masterbatch to the 250ml beaker. Mix until appearance is homogeneous.
4. In separate beaker, combine 10.5 grams of silicone activator (Silicones, Inc. XP-565) with 0.25g of Titanium (IV) dioxide (Alfa Aesar, 42681). Mix until appearance is homogeneous.
5. Add the silicone activator/$TiO_2$ mixture to the silicone base/carbon black mixture. Mix with a mixing paddle attached to a hand-held drill for 10 minutes or until appearance is homogeneous.
6. Place the mixture (still in 250ml beaker) in vacuum desiccator for one hour or until bubbles have disappeared.
7. Remove mixture from vacuum desiccator and leave for 24 hours to cure.

### 4.5.2 Detector linearity testing

Typical of any device that measures light intensity, the DNIRS instrument has a limited range where the electrical output signal is linearly proportional to the optical power of the input signal. Before using the DNIRS system for any *in-vivo* experiments, a calibration procedure is conducted to define this range of linearity. Then any subsequent human or animal measurements that fall outside of the range of linearity can be immediately discarded, the optical attenuator can be adjusted to increase or decrease the signal amplitudes, and the measurement can be repeated. The procedure for testing the linearity of a detector is as follows:

1. Connect a variable optical attenuator to the output of a laser diode.
2. Connect the variable optical attenuator to the input of an optical splitter having one input and two output fibers.
3. Connect one output end of the splitter to an optical power meter using a multimode optical fiber.
4. Connect the second output connector of the splitter to a multimode optical fiber (source fiber).
5. Make a Teflon probe that allows you place the source fiber at a fixed distance from the detector fiber that leads to the detector you are testing. The fibers should be only a few millimeters apart, because it is important to have a strong signal such that the detector is saturated when the attenuator is set to maximum transmission.
6. Submerge the probe in an intralipid optical phantom. Make sure that the probe and fibers are secure and cannot move during calibration.
7. Turn the variable attenuator clockwise until no light is transmitted. Both the optical power meter and the detector output signal should show signals of zero.
8. Slowly turn the variable attenuator (counter-clockwise) to increase light transmission
9. Record both the optical power shown by the power meter and the amplitude of the detector output signal.
10. Continue increasing light transmission with the attenuator in small increments while recording the power and amplitudes at each increment. Use very small increments at low light levels (amplitude < 5mV). You can use larger increments when the amplitude is greater than 5 mV.
11. When you reach a maximum optical power level, repeat the procedure using decreasing power steps (turn the attenuator clockwise).

12. Plot log(Amplitude) vs. log(Power) and Phase vs. Power.

An example of the amplitude and phase data from a linearity test of one detector is shown in Figure 16. Ideally, the slope of linear trendline fitted to a plot of log(amplitude) vs. log(power) would be 1.0 V/µW, and the slope of a linear trendline fitted to a plot of phase vs. power would be 0.0 radian/µW. Figure 17 shows the same data as Figure 16 after removing points where the detector amplitude was less than 0.001 V or greater than 0.150 V. Linear trendlines fitted to the remaining data points show that the slope of the log(Amplitude) vs. log(power) data is 1.021 and the slope of the phase vs. power data is 0.000, indicating that detector amplitudes between 0.001 V and 0.150 V are within the linear range of the detector. All future measurements made with this detector will be checked to ensure that the amplitude is within this range.

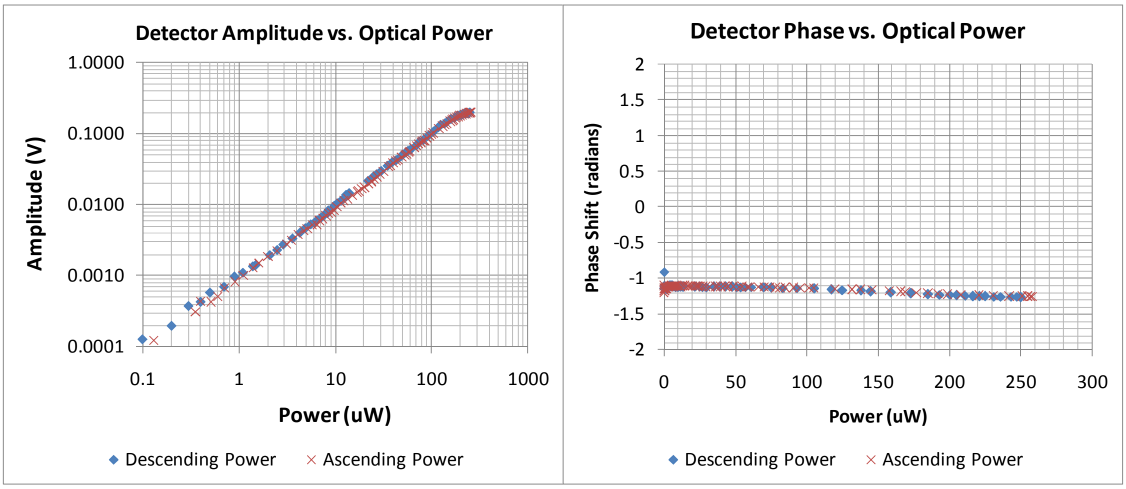

**Figure 16: Raw amplitude and phase data from a detector linearity test. It is apparent from the plot of detector amplitude vs. optical power that linearity of the detector breaks down at amplitudes less than .001 V and greater than 0.15 V.**

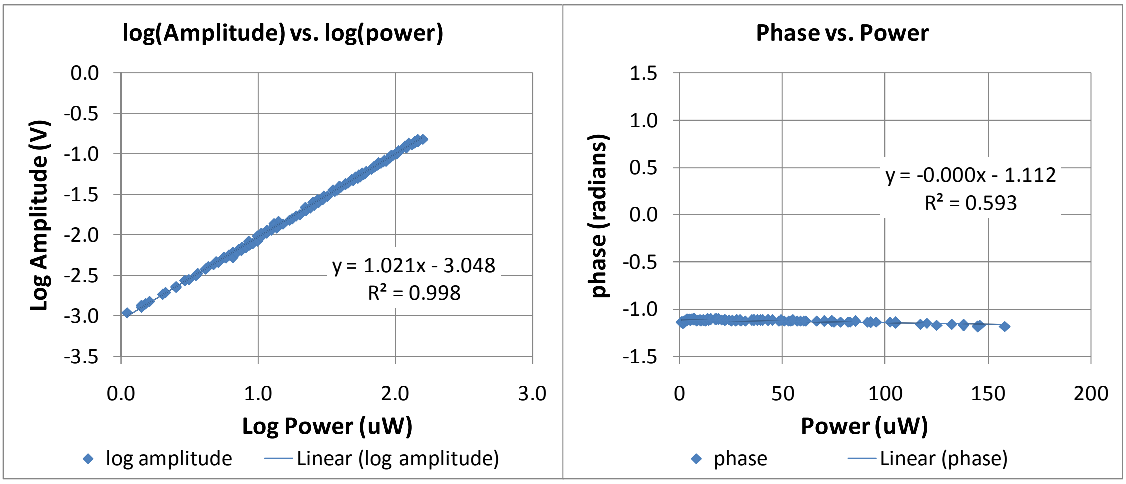

**Figure 17: Plots of log(Amplitude) vs. log(power) and phase vs. power after removing data points having amplitudes less than 0.001 V or greater than 0.150 V. The slope of the linear trendline fitted to the log(amplitude) data is 1.021 and the slope of the linear trendline fitted to the Phase data is 0.000, indicating that amplitudes within 0.001V and 0.150V are within the linear range of the detector.**

### *4.5.3 Stability testing*

It is important to be certain that the DNIRS system can provide consistent measurements throughout a measurement session that could last for several hours during animal and human experiments. To test the stability of the system (all lasers, all detectors, optical switch), the fiber optic probe was placed securely in contact with a silicone optical phantom using a laboratory clamp and measurements were obtained continuously over a period of 11 hours. Plots of amplitude and phase at each of the four detectors are shown in Figure 18. Note that the amplitudes are not stable for the first 15-20 minutes of measurement. This instability is the reason that measurements should not be obtained until the system has had sufficient time to warm up. Excluding the first 20 minutes of data, the percent deviation of each detector / wavelength combination was less than 3%.

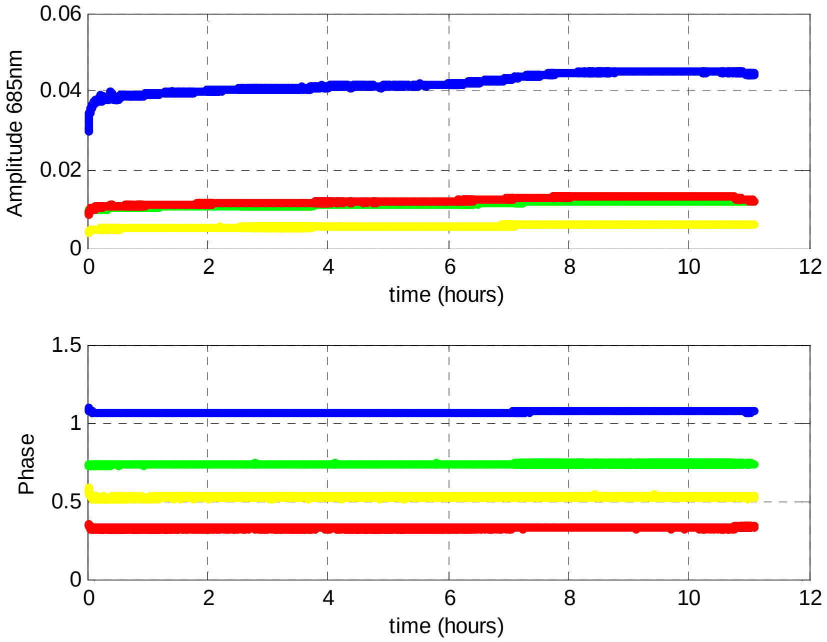

**Figure 18: Amplitude and phase measurements from a silicone optical phantom obtained over an 11-hour period at 685nm. Each color represents one of the four detectors. Similar results were obtained for wavelengths 780nm and 830nm, but are not shown here.**

Chronic wounds may take several months to heal and it was therefore necessary to test the stability of the device during the course of such measurements. Consistent measurements of optical coefficients must be made by the device over long periods of time. To assess the long-term stability of the device, an optical phantom made of silicone (see section 4.5.1 Optical Phantoms) was measured before each patient measurement session. The measured absorption coefficients from the silicone phantom over the course of 61 weeks are shown in Figure 19. Standard error remained at less than 3% throughout the period of the study.

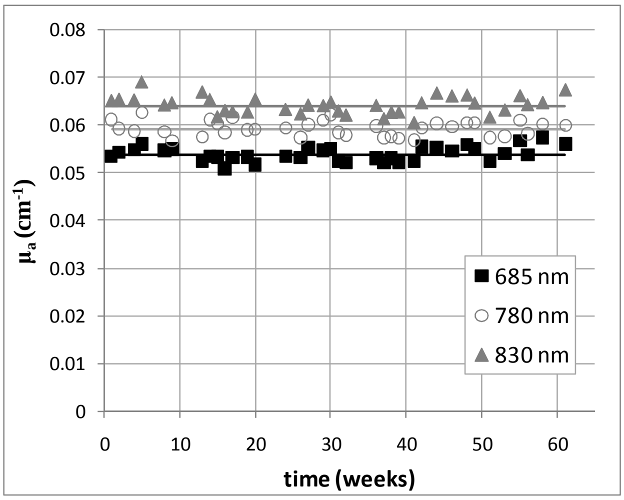

**Figure 19: Measured values of $\mu_a$ in a silicone optical phantom over a 61-week period. Solid lines represent average values for the entire measurement period. Average values of $\mu_a$ (mean ± s.d.) at 685, 780, and 830 nm were 0.054 ± 0.0014, 0.059 ± 0.0016, and 0.064 ± 0.0018 cm$^{-1}$, respectively.**

### *4.5.4 Response of a single detector to changes in distance from source*

It is important to assess the amplitude and phase response of each detector to changes in the source-detector separation distance. The analytic solution to the diffusion equation in an infinite geometry, as described in (Li 1998), predicts that a linear relationship exists between log(Amplitude*ρ) vs. ρ, and Phase Shift vs. ρ, where ρ is the source-detector separation distance. The following procedure was followed to test each detector's response:

1. Partially fill a 10-liter fish tank with approximately five liters of 1% intralipid suspension (See Section 4.5.1 Optical Phantoms).
2. Position the DNIRS source fiber in a fixed location in the tank, just above the intralipid and several centimeters away from any of the tank walls, using optical stands/posts.

3. Attached one detector fiber to a motorized linear stage (Velmex BiSlide) using optical stands/posts. Position the fiber at the same height as the source fiber and aligned parallel to the axis of the linear stage.
4. Wrap the portions of the optical posts and fibers that extended into the tank (except for the tips of the fibers) with white Teflon tape to reduce absorption of light by fibers and holders.
5. Measure the initial distance between source and detector fibers by taking a photograph with a ruler in the same plane as the fibers, and calculating the distance using image processing software (Matlab).
6. Fill the tank with an additional 4 liters of 1% intralipid, submerging the ends of the fibers at a depth of 8-10 cm.
7. Configure the motorized linear stage to move in equal-sized steps of a few millimeters.
8. After each step, record the amplitude and phase registered at the detector at each wavelength (685nm, 780nm, and 830nm).
9. Repeat this process until the signal at all wavelengths is negligible (usually at a source-detector separation distance of about 6 cm).
10. Reverse the direction of the motor and repeat the process.
11. Calculate source-detector separation at each step using: $\rho$ = (initial distance) + (step number X step size).
12. Excluded data where the amplitude falls outside of the linear range of the device (see Section 4.5.2 Detector linearity testing)
13. Plot log(Amp*$\rho$) vs. $\rho$ and Phase vs. $\rho$ for each wavelength

Typical results from this procedure are shown in Figure 20, which demonstrates the linear response of log(Amplitude*$\rho$) and Phase Shift to changes in source-detector separation distance (ρ). The slopes of the linear trendlines fitted to these graphs can be used to calculate the values of $\mu_a$ and $\mu'_s$ of the intralpid solution, using the equations described in Section 4.4.3 Software. The values of $\mu_a$ and $\mu'_s$ obtained from the data shown in Figure 20 are shown in Table 2 and which are in agreement with previously published values of the absorption and reduced scattering coefficients of 1% intralipid (Papazoglou, Weingarten et al. 2006; Papazoglou, Weingarten et al. 2008).

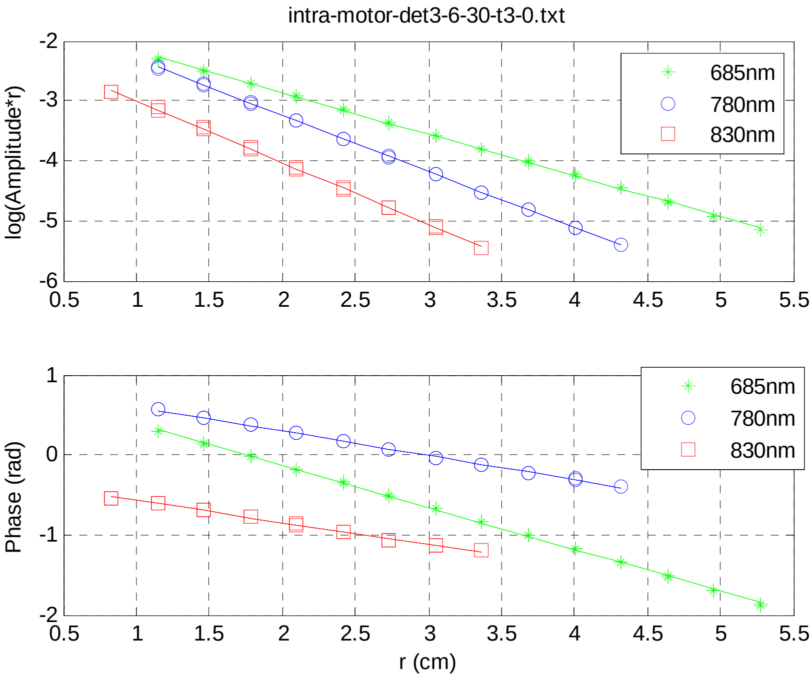

**Figure 20: Plots of (*upper*) log(Amplitude*ρ) vs. ρ and (*lower*) Phase vs. ρ, where ρ is the source-detector separation distance, from a single detector submerged in 1% intralipid at wavelengths 685, 780, and 830 nm.**

**Table 2: $\mu_a$ and $\mu'_s$ calculated from data shown in Figure 20. Results are shown in units of $cm^{-1}$.**

| μa | | | μs' | | |
|---|---|---|---|---|---|
| **685nm** | **780nm** | **830nm** | **685nm** | **780nm** | **830nm** |
| 0.0054 | 0.0267 | 0.0347 | 12.38 | 9.7597 | 9.4898 |

### 4.5.5 Calibrating multiple detectors using equidistant probe

The measured intensity of scattered light depends not only on the tissue properties, but also on the sensitivity of the Avalanche Photodiode (APD), the coupling to the detectors fibers, the transmission of the optical fibers and the gain of each detector block. The phase shift may be different in each channel because the optical and electrical signal delay depends on fiber length and coupling, the length of the RF coaxial cables, and any delays in the detector circuits. Instrument calibration is performed to allow us to separate variability due to the instrument hardware components from sample and measurement variability. The steps are as follows:

1. Create a Teflon probe with a geometry that allows the four detector fibers to be placed at the same distance (usually between 5-15 mm) from the source fiber.
2. Place the probe inside an Intralipid optical phantom (infinite geometry) or on the surface of an intralipid phantom (semi-infinite geometry).
3. Record amplitudes and phase measurements at each detector. Check that all measured amplitudes are within the linear range of each detector.
4. The difference in measured amplitude and phase for each detector reflects the different response of each detector to the same fluence of scattered light. Ideally, the amplitudes and phase shifts should be identical for all detectors. Create *amplitude correction coefficients* for the second, third, and fourth detectors relative to the first detector by dividing the measured amplitude from the 1st detector by the 2nd, 3rd, and 4th detector amplitudes.
5. Create *phase correction coefficients* for the second, third, and fourth detectors relative to the first detector by subtracting the 2nd, 3rd, and 4th detector phases from the measured phase from the 1st detector.

Subsequent experimental data obtained by the device will always be adjusted by multiplying the measured amplitudes by the amplitude correction coefficients, and by adding the phase correction coefficients to the measured phases. An example of the amplitudes and phase shifts obtained with an equidistant probe are shown in Table 3, and the correction coefficients that were derived from these data, are shown in Table 4.

**Table 3: Amplitude (in millivolts) and phase data (in radians) obtained using an equidistant probe (4 detector fibers equidistant from a single source fiber).**

| | Measured Amp - Equidistant probe | | | | Measured Phase - Equidistant probe | | | |
|---|---|---|---|---|---|---|---|---|
| | **Det1** | **Det2** | **Det3** | **Det4** | **Det1** | **Det2** | **Det3** | **Det4** |
| **685nm** | 6.0 | 87.8 | 18.7 | 12.2 | -1.114 | -0.986 | -0.948 | -0.940 |
| **780nm** | 7.0 | 101.0 | 22.2 | 13.8 | -1.213 | -1.002 | -0.961 | -0.957 |
| **830nm** | 5.0 | 73.0 | 16.0 | 9.5 | -1.146 | -1.557 | -1.540 | -1.509 |

**Table 4: Amplitude and phase correction coefficients derived from the data in Table 3.**

| | Amplitude Correction Coefficients | | | | Phase Correction Coefficients | | | |
|---|---|---|---|---|---|---|---|---|
| | **Det1** | **Det2** | **Det3** | **Det4** | **Det1** | **Det2** | **Det3** | **Det4** |
| **685nm** | 1.000 | 0.068 | 0.321 | 0.493 | 0.000 | -0.128 | -0.166 | -0.174 |
| **780nm** | 1.000 | 0.069 | 0.316 | 0.507 | 0.000 | -0.211 | -0.252 | -0.257 |
| **830nm** | 1.000 | 0.068 | 0.313 | 0.529 | 0.000 | 0.411 | 0.394 | 0.363 |

### *4.5.6 Measuring changes in $\mu_a$ and $\mu_s$' (intralipid and ink)*

Tests must be conducted to ensure that the DNIRS device can accurately measure changes in optical absorption and scattering. This can be done by creating optical phantoms with intralipid and ink (see Section 4.5.1 Optical Phantoms) in which one component (either intralipid or ink) is kept constant while the other component is varied in a stepwise fashion. The experimental results must demonstrate the linear dependence of the reduced scattering coefficient on intralipid concentrations, and the linear dependence of the absorption coefficient on ink concentration.

The procedure for testing changes in the absorption coefficient is as follows:

1. Create a 1% intralipid phantom in a 1-liter beaker according to Section 4.5.1 Optical Phantoms
2. Carefully place the DNIRS probe on the intralipid so that each fiber is resting on the surface
3. Record DNIRS data from the surface of the intralipid
4. Add 1ml of diluted black india ink (1:100 in DI water) to the intralipid phantom, mix thoroughly, and repeat steps 2-3.
5. Repeat steps 2-4 until the amplitude of the detected signal is below the detector's linear range.

Calculate the values of $\mu_a$ and $\mu'_s$ for each volume of ink, and plot the results. The absorption coefficient $\mu_a$ of these solutions is expected to show a linear dependence on ink concentration. The reduced scattering coefficient $\mu'_s$ of all solutions is expected to remain constant for all ink volumes. Figure 21 illustrates typical results for this experiment, which correspond to the expected trends.

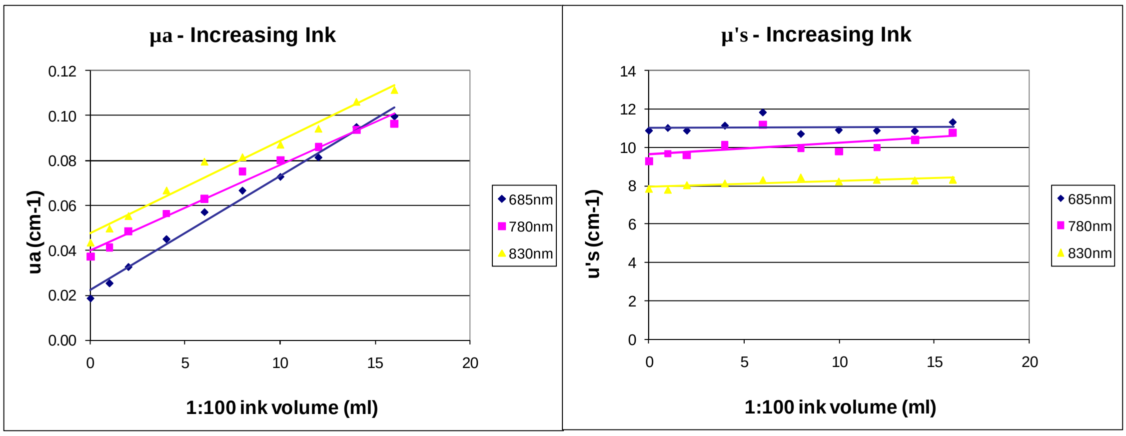

**Figure 21: Measured values of absorption coefficient $\mu a$ and reduced scattering coefficient $\mu_s'$ at various concentrations of black ink in intralipid solutions. The scattering coefficient remains constant, demonstrating the independence of determining absorption and scattering with our instrument.**

A similar procedure is used to test changes in the reduced scattering coefficient:

1. Create a 0.4% intralipid phantom (no ink) in a 1-liter beaker according to Section 4.5.1 Optical Phantoms
2. Carefully place the DNIRS probe on the intralipid so that each fiber is resting on the surface
3. Record DNIRS data from the surface of the intralipid
4. Repeat steps 1-3, using 0.8%, 1.2%, 1.6%, and 2.0% intralipid phantoms.

Calculate the values of $\mu_a$ and $\mu'_s$ for each volume of intralipid and plot the results. The reduced scattering coefficient $\mu'_s$ of these solutions is expected to show a linear dependence on intralipid concentration. The coefficient of absorption $\mu_a$ of all five solutions is expected to be constant and approximately equal to the absorption coefficient of water. Figure 22 illustrates typical results for this experiment, which correspond to the expected trends.

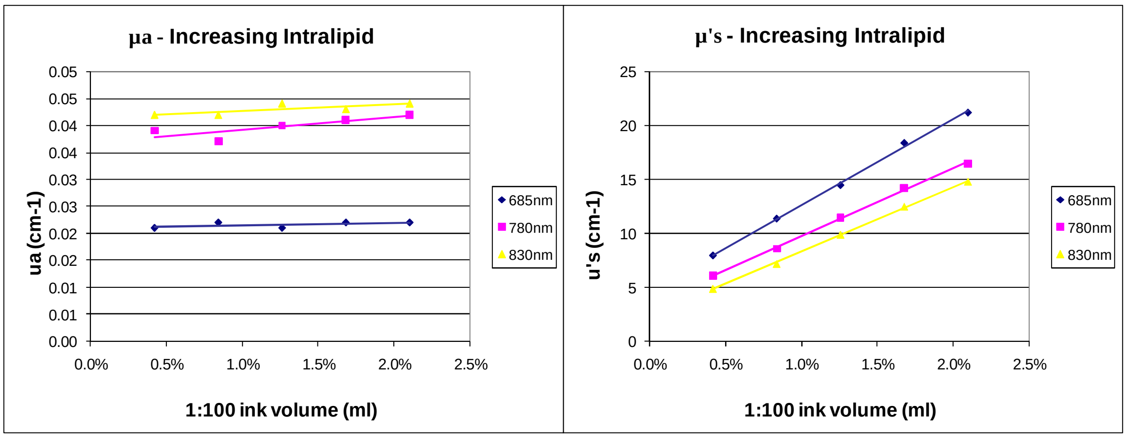

**Figure 22: Measured values of absorption coefficient µa and reduced scattering coefficient $\mu_s$' in various concentrations of intralipid - water solutions. The absorption coefficient remains constant, similar to the absorption of water, demonstrating the independence of determining absorption and scattering with our instrument.**

### *4.5.7 In-vivo cuff experiment*

The final method used to test the device before it is used for human or animal measurements is to measure oxygenation changes while an inflatable cuff is used to limit blood flow to the arm of a healthy volunteer. In this experiment, blood flow to the arm is occluded using an inflatable cuff for 5 minutes, and then the cuff is released. During the restriction phase, oxygenated hemoglobin cannot be delivered to the arm, while oxygen consumption continues. Therefore, the level of oxygenated hemoglobin is decreasing while the level of deoxygenated hemoglobin is increasing. Once the cuff is released, blood rushes to the previously occluded site, and oxygenated hemoglobin reaches normal levels after going through an abrupt increase (spike). This behavior has been documented by several methods and is a standard procedure to validate the ability to monitor levels of oxy and deoxy hemoglobin (Hamaoka, Katsumura et al. 2000; Yu, Durduran et al. 2005).

The results of a typical cuff experiment performed using the DNIRS system is shown in Figure 23. Optical measurements were taken continuously at 3-second intervals starting 1 minute before the cuff was inflated, 4 minutes and 45 seconds while the cuff was inflated to 180mmHg, and then 2 minutes after the cuff was deflated. This procedure was repeated for the same subject on three different days. The measured optical absorption coefficients were used to calculate the concentration of oxyhemoglobin, deoxyhemoglobin, total hemoglobin, and oxygen saturation.

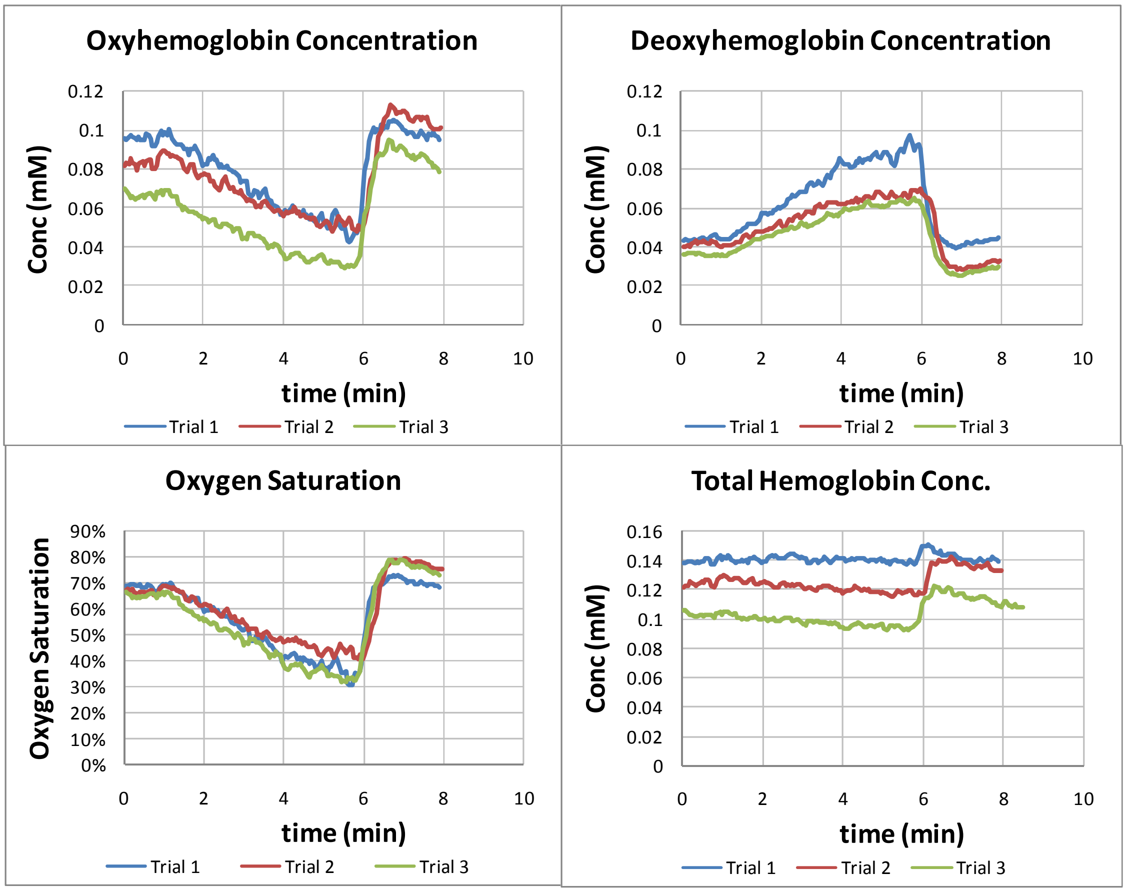

**Figure 23: Oxyhemoglobin concentration, deoxyhemoglobin concentration, total hemoglobin concentration, and oxygen saturation in human arm during cuff experiment. Measurements were acquired at 3-second intervals and 3-point averaging was used to smooth the curve. Trials represent different days of measurement.**

# CHAPTER 5: MONITORING IMPAIRED WOUND HEALING IN OBESE RATS WITH DIFFUSE NIR SPECTROSCOPY

## 5.1 Animal Study Description

### *5.1.1 Motivation*

The two main objectives of this study were to: (1) determine whether obese rats can be used as an impaired wound healing model that provides a slower rate of healing than lean hairless rats and streptozotocin-induced diabetic hairless rats, and (2) measure the optical properties of wounds throughout all phases of the wound healing process, including the remodeling phase.

In our previous animal studies of wound monitoring with DNIRS (Papazoglou, Weingarten et al. 2006; Papazoglou, Weingarten et al. 2008), a hairless rat wound model was used. Some of the rats were rendered diabetic by injection of streptozotocin to create a model of impaired diabetic wound healing. Non-diabetic hairless rats all healed within 18 days of wound surgery, while the diabetic rats healed within 21 days of the wound surgery. All rats were sacrificed immediately after their wounds had closed so that the healed tissue could be excised and analyzed using histological methods. It was impossible to observe the changes in wound optical properties that would occur during the remodeling phase of wound healing because the animals were sacrificed immediately after wound closure. In this paper, we describe a pilot study of healing in Zucker Diabetic Fatty (ZDF) obese rats in which the animals were continuously monitored with DNIRS for an extended period of time after wound closure to better understand the changes in optical properties that occur during the remodeling phase of wound healing.

### *5.1.2 Animal Study Procedures*

Animal procedures were conducted in accordance with the Guide for the Humane Care and Use of Laboratory Animals. The experimental protocol was approved by Drexel University's Institutional Animal Care and Use Committee (IACUC). Seven female obese Zucker Diabetic Fatty (ZDF) rats were purchased from Charles River Laboratories (Wilmington, MA). The rats were 7 weeks old at the start of the study. During the course of the study, all animals were supplied with food and water ad libitum and were housed in individual cages. DNIRS measurements were performed on the left and right dorsal areas of all rats every 3-4 days over a period of 97 days to establish baseline values of the optical absorption and reduced scattering coefficients ($\mu_a$ and $\mu'_s$). Animals were anesthetized using isoflurane and oxygen administered via facemask during all measurement sessions to eliminate motion artifact.

On day 100, full thickness wounds were made in the left dorsal area of each rat using a scalpel and a circular template with surface area 4.6 cm$^2$. A full thickness wound is a wound where the epidermis and dermis are removed to expose the underlying tissue. It is different from an incision wound and it heals by a combination of contraction and epithelialization. The right side of each animal remained unwounded to serve as a control for DNIRS measurements. Optical measurements were taken 2-3 times per week on the centers of the wounds, on intact skin adjacent to the edge of each wound, and on the unwounded right dorsal region of each animal, as illustrated in Figure 24. This measurement schedule was maintained until all wounds had closed (33 days after wound surgery). All wounds were covered with a Tegaderm (3M, Minneapolis, MN) sterile transparent dressing after wound surgery and between optical measurements. Weekly DNIRS measurements were continued for an additional 46 days past the date of closure, during the remodeling phase of the wound healing cycle. One obese animal was sacrificed by $CO_2$ asphyxiation on the 5th and 11th day after the wounds were inflicted. The five remaining animals were sacrificed on day 79.

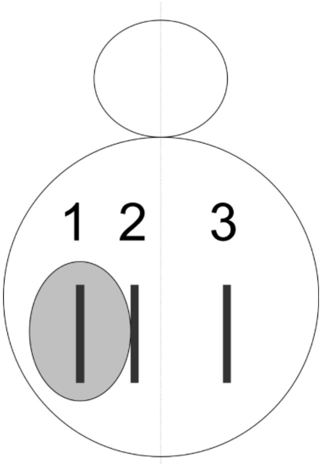

**Figure 24: Probe placement locations (dark rectangles) in animal model. Each animal was wounded on the left dorsum, and measurements were performed on (1) the center of the wound, (2) the edge of the wound, and (3) healthy tissue on the right dorsum, symmetric to the wound location.**

Wounds were digitally photographed using a Fujifilm Finepix s700 digital camera during each measurement session with cross-polarizing filters to reduce surface reflection. A ruler was held in the imaging plane of each photograph to allow the calculation of absolute wound area. The boundaries of each wound were manually traced using a computer mouse and Microsoft Paint software, and then wound areas were calculated from the traced photographs using an image analysis code developed with Matlab (Mathworks, Inc.) software. This image analysis code counts the number of pixels within the traced wound boundary, and then calculates the wound area by approximating the size of each pixel from the image of the ruler that was present in the imaging plane of each wound.

## 5.2 Animal Study Results

### 5.2.1 Wound size results

Normalized wound area was obtained for each wound on each measurement day by calculating the ratio of wound area each day to the initial wound area on the day of surgery (day 0). Average normalized wound areas on each measurement day are presented in **Figure 22**a. The wounds remained open for 33 days after wound surgery. **Figure 22**b compares the normalized wound areas obtained in this study with the data obtained from healthy hairless rats and STZ-induced diabetic hairless rats reported in our previous wound studies (Papazoglou, Weingarten et al. 2008; Weingarten, Papazoglou et al. 2008). The obese rat wounds exhibit a slower rate of healing than hairless rats with streptozotocin-induced diabetes. Figure 26 compares representative images from ZDF rats and hairless rats, and illustrates that the wounds on lean hairless rats healed primarily by contraction, while wounds from obese rats healed by a combination of contraction and epithelialization.

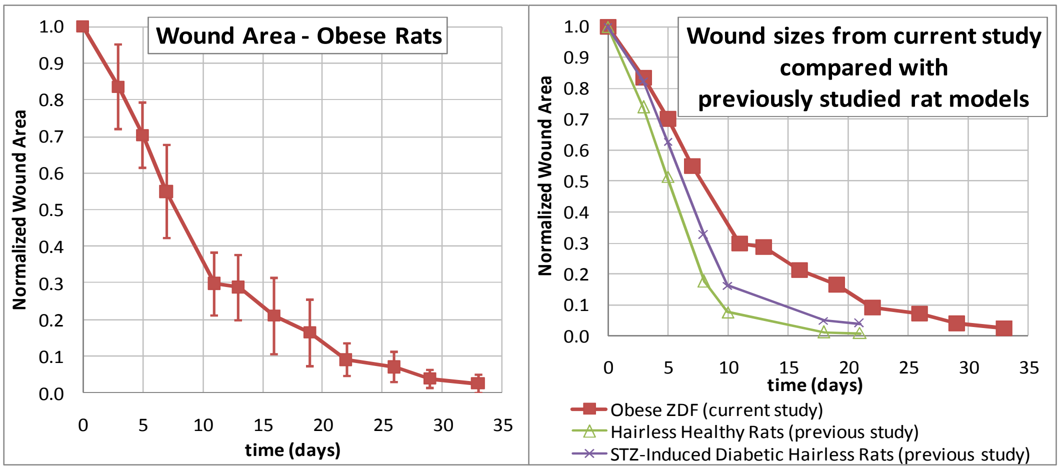

(a) (b)

**Figure 25: Normalized wound area from obese rats. (*a*) Normalized wound area (mean ± s.d.) from obese ZDF rats. (*b*) Normalized wound area from obese ZDF (current study), normal hairless [Weingarten 2008], and diabetic hairless rats [Weingarten 2008] are compared. Obese ZDF rats healed slower than normal hairless and diabetic hairless rats.**

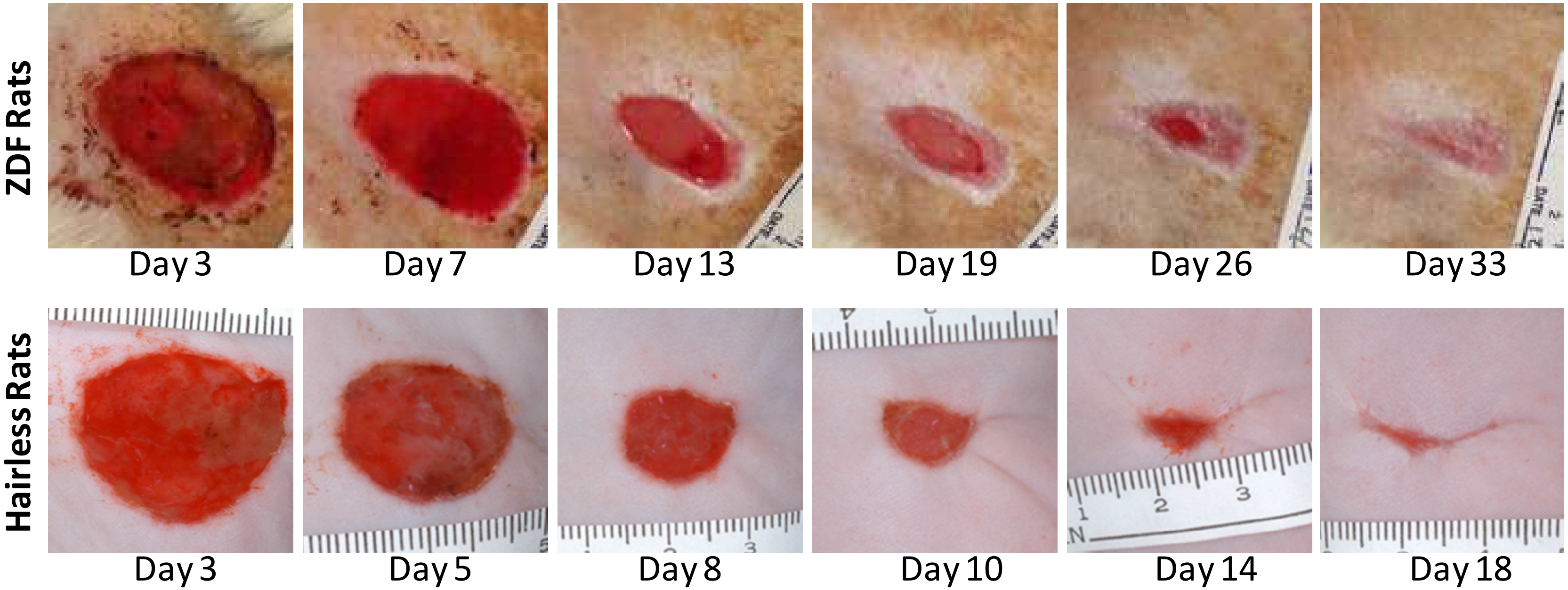

**Figure 26: Wound images from an obese ZDF rat (upper) and a healthy hairless Sprague-Dawley rat. The ZDF images show new epithelial tissue, which is visible beginning on Day 13 near the left edge of the wound, growing to cover the entire wound by Day 33. Images from hairless rats show that the wounds healed primarily by contraction, with skin striations clearly visible on days 10 and 14, and much less new epithelial tissue than the ZDF wounds.**

### *5.2.2 Optical results – Baseline Period*

The mean pre-wound baseline values of the optical absorption and reduced scattering coefficients at each measurement time point are shown in Figure 27, demonstrating the stability of *in-vivo* DNIRS measurements in animals over an extended period of time. The percent deviation for measurements made on different rats on the same day was less than 10%. The percent deviation for average measurements of $\mu_a$ and $\mu'_s$ across all baseline days ranges from 5-7%, or 4-5% if only the last 46 days of the baseline period are included. The greater day-to-day variability in $\mu_a$ and $\mu'_s$ during the first 51 days of the baseline period is apparent in Figure 27, and may be caused by DNIRS operator inconsistency when placing the probe on the skin during the first few measurement sessions. Additionally, the average weight of the rats increased 62% (from 210 to 340 grams) over the first 51 days of the study, but increased only 21% (from 340 to 410 grams) over the next 46 days of the baseline measurement period. The rapid growth of the animals may have contributed to the greater day-to-day variability during the first half of the baseline period.

A similar analysis was performed for baseline values of oxyhemoglobin concentration [$HbO_2$], deoxyhemoglobin concentration [Hb], and total hemoglobin concentration [Tot Hb]. The results are shown in Figure 28. The percent deviation for measurements made on different rats on the same day ranged from 8-16%. The percent deviation for average measurements of $\mu_a$ and $\mu'_s$ across all baseline days ranged from 5-10%, or 4-9% if only the last 46 days of the baseline period are included. The variability in hemoglobin concentrations is greater than the variability in optical absorption and scattering coefficients because the calculation of hemoglobin concentration (see Section **4.3 Calculation of hemoglobin concentration from** optical absorption) compounds any error present in the optical coefficients.

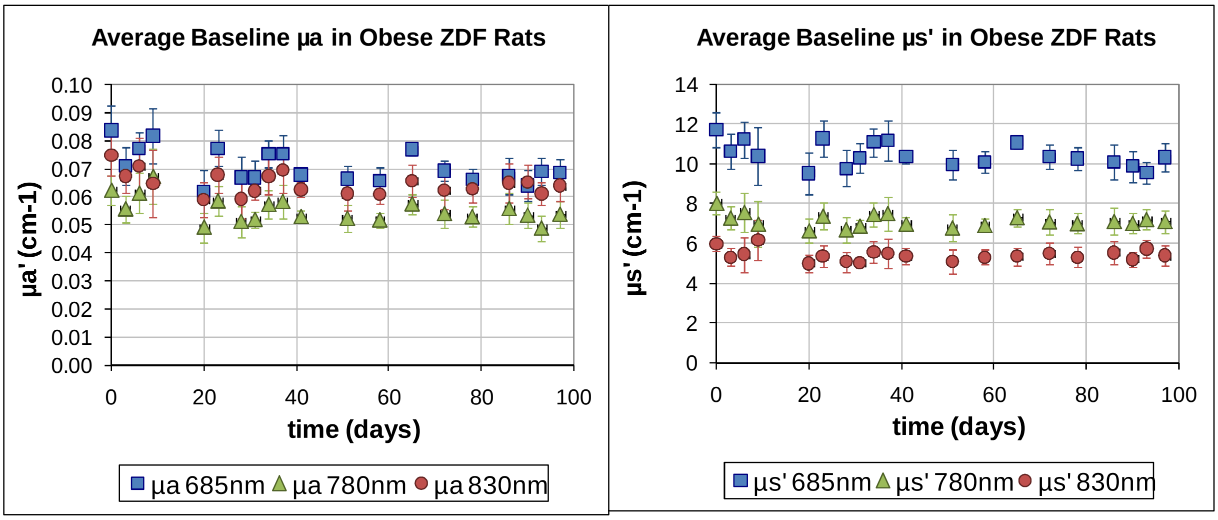

**Figure 27: Pre-wound baseline measurements of the optical absorption coefficient (µa) and reduced scattering coefficient (µs') from the dorsal skin of obese ZDF rats. Each marker represents the mean value obtained across all rats (n=7) on each measurement day. Error bars represent the standard deviation.**

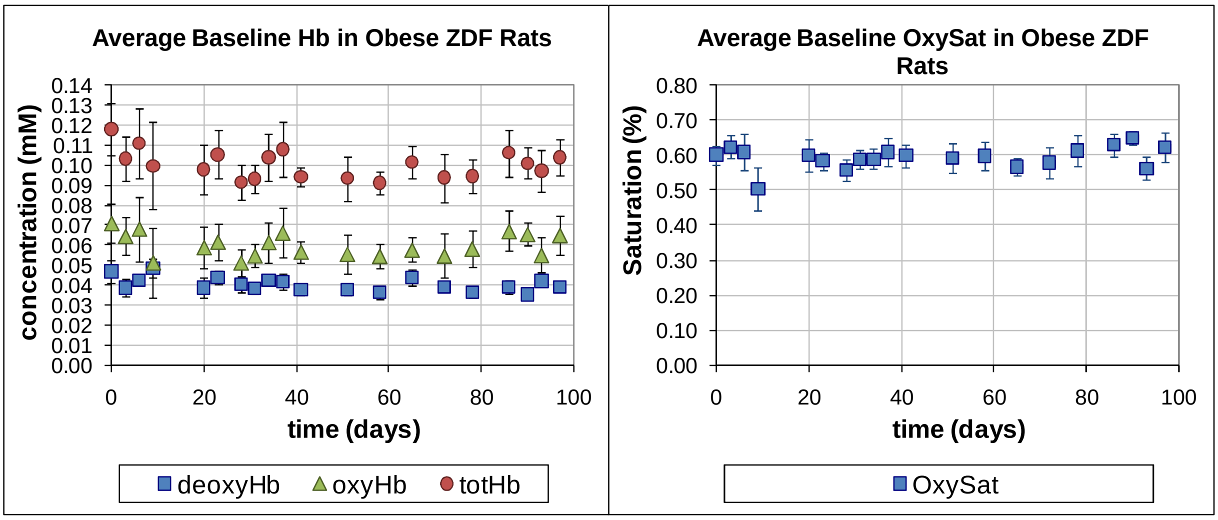

**Figure 28: Pre-wound baseline measurements of the hemoglobin concentration and oxygen saturation of the dorsal skin of obese ZDF rats. Each marker represents the mean value obtained across all rats (n=7) on each measurement day. Error bars represent the standard deviation.**

### *5.2.3 Optical results – Post-Wound Period*

The average values of the optical absorption coefficient ($\mu_a$) and the reduced scattering coefficient ($\mu'_s$) increased immediately after wound surgery and reached a plateau around the time of wound closure, as shown in Figure 29. This behavior is consistent with the changes in $\mu_a$ observed in previous studies with hairless rats, and may be correlated with increased vessel density beneath the wound surface during the proliferation phase of wound healing. After wound closure (days 34 to 79), the values of optical absorption decreased and approached their pre-wound baseline values. This may be correlated with a decrease in blood vessel density that occurs during the remodeling phase of wound healing.

The average values of [$HbO_2$], [Hb], [Tot Hb], and Oxygen Saturation from each measurement day are shown in Figure 30. The overall trends for [$HbO_2$] and [Tot Hb] show an increase immediately after wound surgery reaching a plateau around the time of wound closure, followed by a decreasing trend after wound closure. Deoxyhemoglobin concentration [Hb] at wound centers and wound edges showed an overall increasing trend, with Oxygen Saturation showed and overall decreasing trend throughout the study. However, the data measured at the control site (non-wounded skin) showed some instability over the course of the study, especially during the period after wound closure. To account for any systemic variation in the animals over the course of the study, control site values of [$HbO_2$], [Hb], [Tot Hb], and Oxygen Saturation were subtracted from data measured at the wound centers and wound edges. The resulting plots, shown in Figure 31, show elevated levels of [$HbO_2$] and [Tot Hb] immediately after wound surgery that decrease starting around the time of wound closure and converge with the levels measured in normal skin by the end of the study. Levels of [Hb] increased after wound surgery and remained elevated for several weeks after the wound had closed.

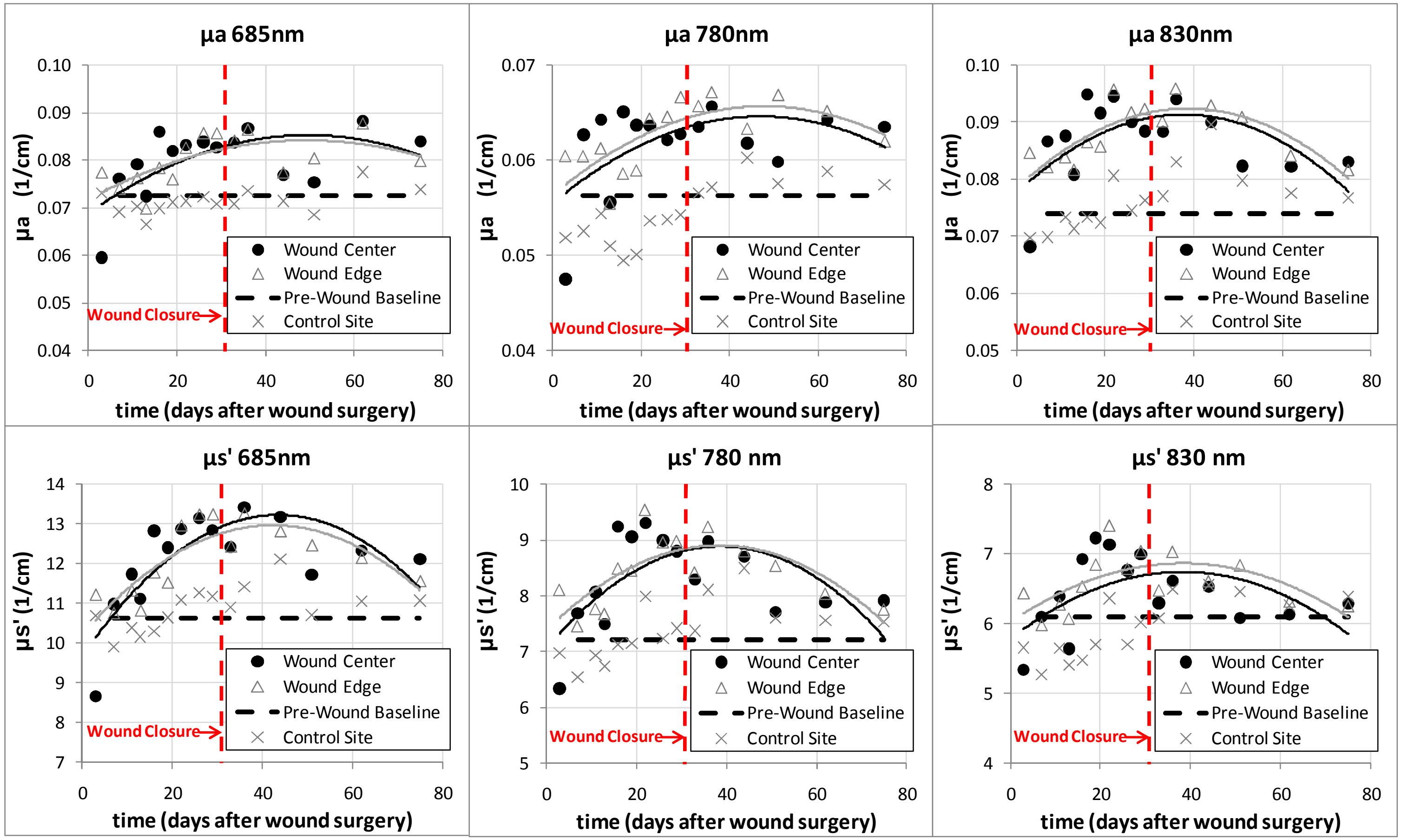

**Figure 29: Optical absorption coefficient (µa) and reduced scattering coefficient (µ's) at 685nm, 780nm, and 830nm from obese ZDF rats. Each marker represents the mean value across all rats. ● = Center of the wound (black line); Δ = Edge of the wound (gray line); x = Non-wound Control site; Dashed line = Pre-wound baseline.**

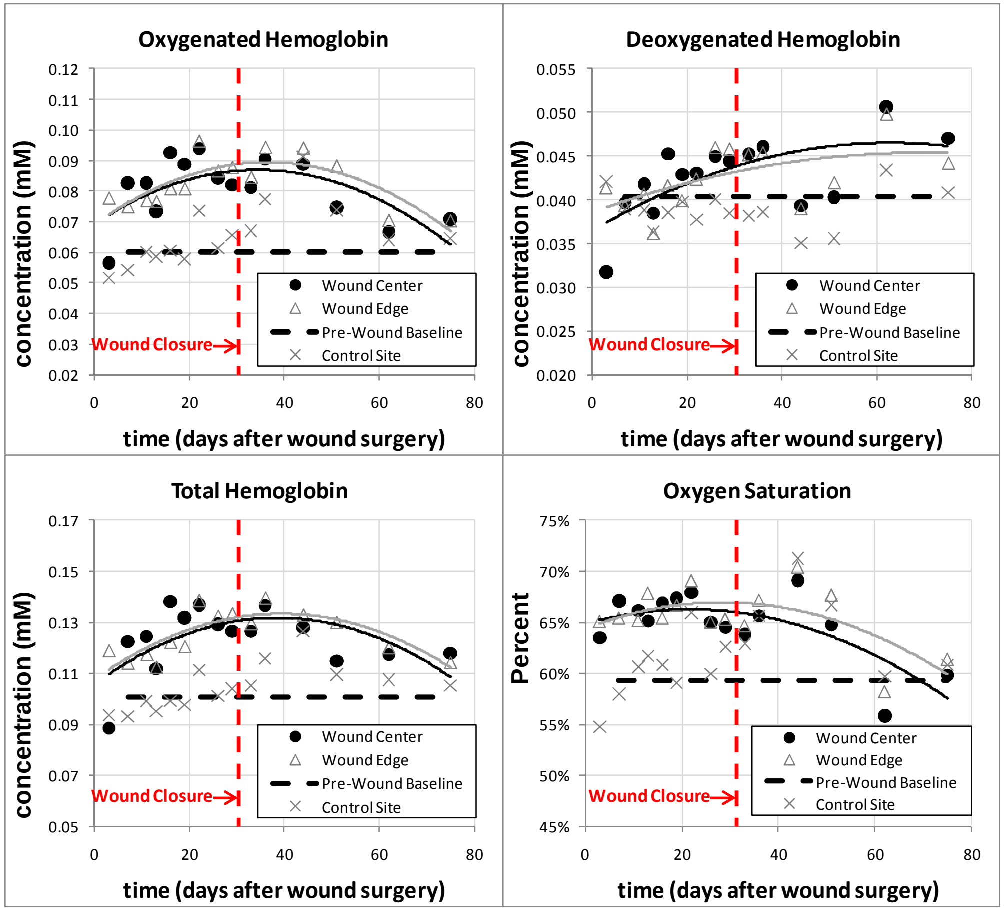

**Figure 30: Oxy-, deoxy-, and total hemoglobin concentrations, and oxygen saturation from obese ZDF rats. Each marker represents the mean value across all rats. ● = Center of the wound (black line); ∆ = Edge of the wound (gray line); x = Non-wound Control site; Dashed line = Pre-wound baseline.**

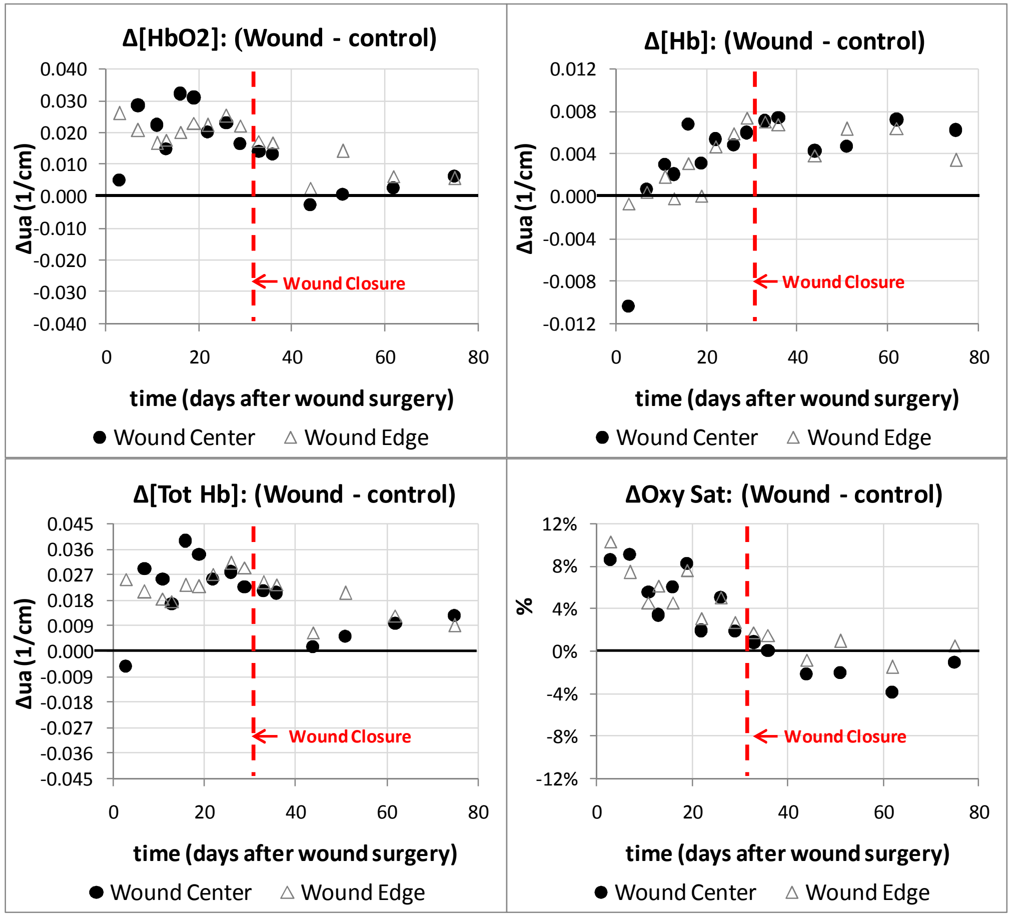

**Figure 31: Average difference (Δ) between wound and control measurements of oxy-, deoxy-, and total hemoglobin concentrations, and oxygen saturation on each measurement day. Each marker represents the mean value across all rats. ● = Center of the wound (black line); Δ = Edge of the wound (gray line).**

### 5.3 Animal Study Discussion

Streptozotocin-induced diabetic rats are often used in healing studies as models of impaired healing, even though they do not accurately represent human chronic wounds which often take months to heal. Although there are no animal models of truly chronic wounds (Davidson 1998), animals models of impaired healing are needed in order to complete the testing of novel wound therapies prior to the commencement of human trials. Because there is only a 3-day difference in the healing rates of STZ-induced diabetic rats and healthy hairless rats (see Figure 25b), any product that is intended to improve healing in STZ-diabetic rats has only a 3-day window to show improvement. ZDF rats may be a better model of impaired healing than chemically-induced diabetic hairless rats because they heal at a slower rate. This model may provide researchers with a larger time period over which the rate of healing can be improved, thus making it easier to show that a new wound therapy improves the rate of healing in animals.

In addition to having a slow rate of healing, the mechanism of wound healing in obese rats may be more similar to human chronic wounds than STZ-diabetic wounds. Healing in STZ-diabetic rats occurs primarily by contraction, where healthy tissue surrounding the wound is pulled over the wound, as is evident in Figure 26. In contrast, human skin (especially in the feet, where most diabetic wounds are located) heals primarily by epithelialization, which is much slower than contraction (Mogford and Mustoe 2001). Contraction is much more prominent in rodents than humans because rodent skin is much more loosely bound to underlying tissue than human skin (Dorsett-Martin 2004). However, obesity causes the skin of obese rats to be stretched tighter, so contraction contributes less to the healing process than in lean rats while epithelialization is more prominent, as illustrated in Figure 26.

Previously published animal studies of wound healing (Papazoglou, Weingarten et al. 2008; Weingarten, Papazoglou et al. 2008; Zhu 2008) demonstrated that increases in the optical absorption coefficient, and therefore hemoglobin concentration, in the period between wound surgery and wound closure correlate to increases in blood vessel density as measured by histological and immunohistochemical analysis of excised wound tissue. The elevated levels of total hemoglobin concentration in obese rat wounds that were measured by DNIRS between wound surgery and wound closure (Figure 31) are consistent with these earlier findings.

This study extends beyond our previous studies by measuring hemoglobin levels during a 42-day period after wound closure, during the remodeling phase of the wound healing process. Arterial and arteriolar blood that enters the new vessels formed during wound healing is expected to be high in oxygen. Hemoglobin in arterial blood is highly saturated with oxygen -- in healthy people arterial oxygen saturation is between 96-99% (Schutz 2001; Silverthorn, Ober et al. 2004). Therefore, changes in blood vessel density will be most strongly reflected by changes in oxy-hemoglobin concentration. During the late proliferation and remodeling stages of wound healing, angiogenesis stops and blood vessels begin to break down as a result of apoptosis (Singer and Clark 1999). This is consistent with the decreasing levels of [$HbO_2$] measured after wound closure and shown in Figure 31.

Deoxy-hemoglobin concentration is not affected as greatly as oxy-hemoglobin by changes in vessel density because only a small fraction of the arterial blood that enters a new vessel network is deoxygenated. Instead, changes in deoxy-hemoglobin concentration reflect increased oxygen consumption by the tissue surrounding the blood vessels (Wolff, Kolberg et al. 1998; Sowa, Matas et al. 2002). As blood passes through the microvasculature, oxygen diffuses out of arterioles and capillaries into the surrounding tissue along concentration gradients perpendicular to the blood vessels (Kuchenreuther, Adler et al. 1996). The oxygen gradient, and therefore the amount of oxygen that diffuses out of a blood vessel, is driven by the concentration of oxygen outside of the blood vessel (Kuchenreuther, Adler et al. 1996). When blood flows through a region of tissue that has low oxygen concentration due to high metabolic activity, more oxygen will be extracted from hemoglobin and deoxyhemoglobin concentration will increase. The cellular processes that occur during remodeling require oxygen in greater amounts than normal tissue as the extracellular matrix of the scar tissue is reorganized and strengthened (Singer and Clark 1999; Muncaster 2001). As a result, the amount of deoxyhemoglobin extracted from the vasculature remains greater than the levels of deoxyhemoglobin in healthy skin. This may be an explanation for the deoxy-hemoglobin measurements shown in Figure 31, which show that consistently elevated concentrations of deoxygenated hemoglobin [Hb] were observed throughout the 42 days of post-wound closure measurements.

The optical data measured in this study led us to the development of a hypothesis on the expected behavior of hemoglobin concentration during the course of healing. Our hypothesized model of the optical changes observed during healing is illustrated in Figure 32. The time dependence of oxy- and total hemoglobin concentration for human patients is expected to be different from that observed during the animal studies. Human patients are first seen when they have already developed chronic wounds, corresponding to an elevated yet constant absorption level (indicative of non-healing) in our healing model. Any progress in healing manifests itself by a decrease in the [$HbO_2$] and [Tot Hb], and a convergence to the value of non-wound tissue (Figure 32, dashed red lines). In wounds that do not heal, the levels of [$HbO_2$] and [Tot Hb] are not expected to converge with non-wound tissue (Figure 32, red markers). Levels of [Hb] in both healing and non-healing wounds are expected to remain elevated well after wound closure as the scar undergoes remodeling (Figure 32, blue markers).

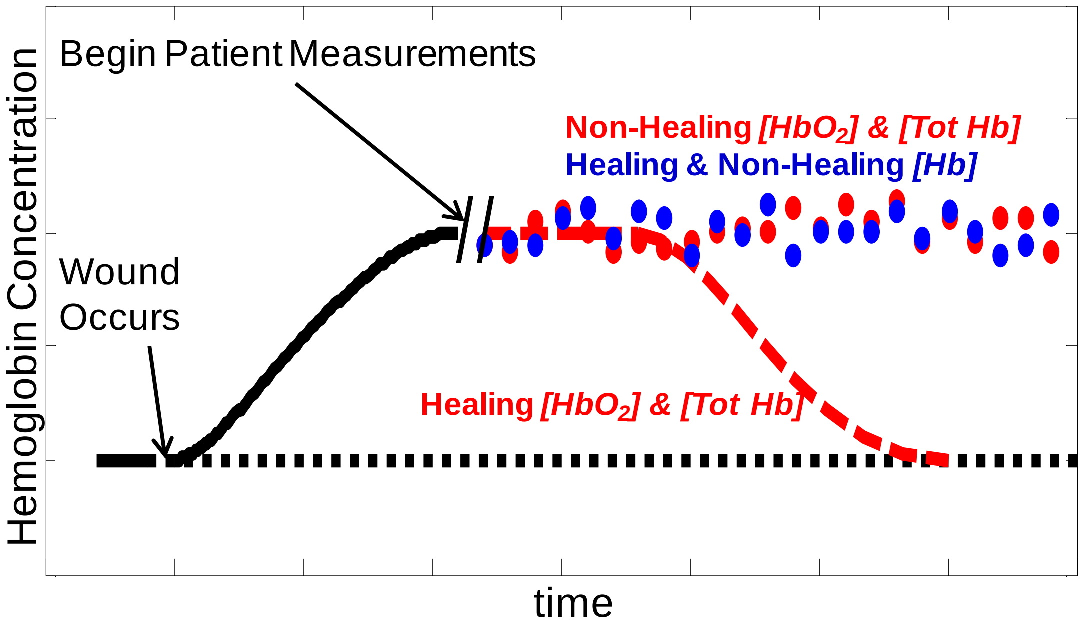

**Figure 32: Hypothesized wound healing curve for DNIRS measurements of hemoglobin concentration. The dotted black line represents normal (non-wound) tissue. The solid black line represents the increasing levels of [$HbO_2$], [Hb], and [Tot Hb] immediately after a wound occurs. The descending dashed lines represent the hypothesized curve for [$HbO_2$] and [Tot Hb] in healing wounds. The red markers represent [$HbO_2$] and [Tot Hb] measurements on non-healing wounds, and the blue markers represent [Hb] measurements on both healing and non-healing wounds.**

The next chapter of this thesis describes a clinical study of human chronic wounds that was undertaken in order to validate this hypothesized model of hemoglobin dynamics measured by DNIRS during wound healing.

# CHAPTER 6: MONITORING HUMAN DIABETIC FOOT ULCERS WITH DIFFUSE NIR SPECTROSCOPY

## 6.1 Human Study Description

### *6.1.1 Healthy Subject Enrollment and Study Procedures*

Before measuring diabetic foot ulcers, the optical properties of the feet of healthy subjects were measured using the DNRIS system. There were three aims to this study of healthy feet: (1) to assess the ability of the device to obtain measurements of optical absorption and scattering in human feet, (2) to assess the stability of optical measurements over time in feet, (3) to observe the effect of various measurement locations on optical properties.

Twelve healthy subjects were recruited for this study; eight subjects were male, and four were female. To be included in the study, all healthy subjects had to be 18-65 years of age, had no history of diabetes or vascular disease, and no open wounds on their feet. Enrolled subjects were asked to remove their footwear and DNIRS measurements were obtained at six different locations on the bottom of each foot: (1) the heel, (2) the ball of the foot under the 1st metatarsal, (3) the ball of the foot under the 5th metatarsal, (4) the big toe, (5) the arch of the foot, and (6) the center of the foot. Ten subjects were measured one time only. Two subjects were measured repeatedly every 2-3 days for over a period of 4-7 weeks.

### *6.1.2 Patient Enrollment and Study Procedures*

All procedures involving human subjects were conducted in compliance with human subjects protection guidelines and approved by the Drexel University College of Medicine Institutional Review Board (IRB). Thirty-nine subjects with diabetes and chronic wounds were recruited from the Drexel University Wound Healing Center in Philadelphia, PA. All subjects were between the ages of 30 to 65. All patients had a previous documented history of diabetes mellitus for at least 6 months. Areas evaluated were strictly ankle and foot wounds secondary to complications from diabetes that presented with a minimum surface area of 1 $cm^2$. Patients were only enrolled in the study if the Ankle-Brachial Index was greater than 0.75, indicating adequate blood supply to the wounded limb. All wounds were debrided of necrotic tissue before entering into the study. Patients diagnosed with osteomyelitis had excision of the infected bone and treatment with antibiotics before enrollment. All patients underwent a standard wound care routine for their foot ulcers, which consisted of weekly or biweekly debridement, offloading when possible, and treatment with moist wound healing protocols. When indicated, active wound healing modalities such as topical growth factors, hyperbaric oxygen, and active biosynthetic skin substitutes were used. The clinician was blinded to the results of DNIRS measurements, and no change in patient treatment occurred as a result of the DNIRS measurements.

Diffuse NIR measurements were conducted prior to wound debridement on a weekly or biweekly basis. During each measurement session, the wounds of each patient were interrogated using the NIR instrument in up to ten different locations. Measurement locations were chosen based on the geometry and size of each wound, and can be classified into four general locations: (1) directly on the wound, (2) on intact skin at the edge of the wound, (3) on non-wound tissue of the contralateral limb symmetric to the wound location if available, (4) on non-wound tissue on the ipsilateral limb at a distance of at least 2 cm from the wound. The measurement locations for a typical diabetic foot ulcer are shown in Figure 33. Tegaderm transparent sterile dressing (3M Health Care) was used to cover the fiber optic probe during all measurements. Our previous experience / results suggest that the presence of Tegaderm does not affect the measured NIR coefficients (Papazoglou, Weingarten et al. 2006).

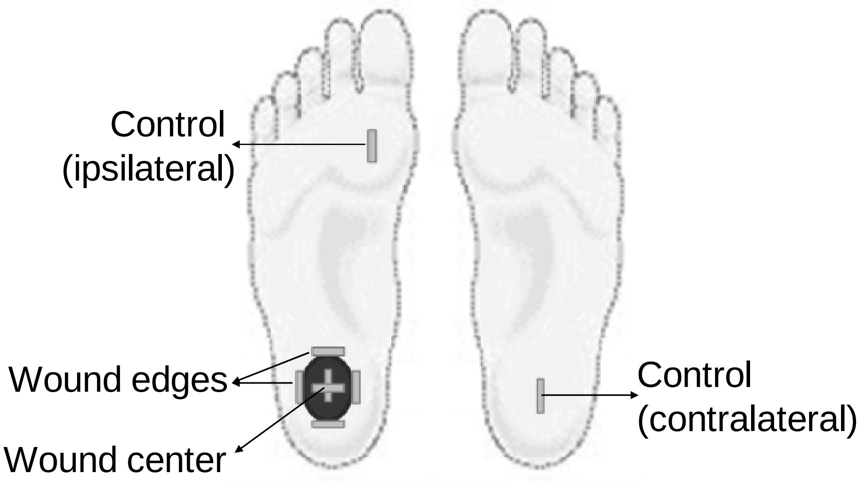

**Figure 33: Diagram of the positions at which NIR measurements were obtained from a representative subject. The dark oval on the heel represents a typical diabetic foot ulcer. Gray rectangles represent the eight different probe locations used during a measurement session.**

Some patients had multiple wounds, therefore a total of 44 wounds were enrolled in the study. Of the 44 wounds, 16 wounds were excluded from analysis because the wound was measured at fewer than four time points. Some of these patients were seen fewer than four times because they stopped coming to the wound clinic, or because they underwent a wound excision or amputation before four measurement sessions could be completed. Of the remaining 28 wounds that were analyzed, 14 wounds were classified as healing wounds and 14 wounds were classified as non-healing wounds. Healing wounds were defined as wounds that completely re-epithelialized and had no remaining open area. Non-healing wounds were defined as wounds that remained open after 20 measurement sessions or wounds that required amputation or wound excision prior to the completion of 20 measurement sessions. Details about the size of each wound, duration of measurements, and the active treatments used on each wound are shown in Table 5 and Table 6.

**Table 5: Size, duration, and active treatments used in healed wounds**

| Wound ID | Initial area (cm2) | Final area (cm2) | Number of Measurement Sessions | Number of weeks | Active treatment | Outcome |
|---|---|---|---|---|---|---|
| Healing #1 | 6.1 | 0.0 | 8 | 10 | Topical growth factor (Regranex) | Healed |
| Healing #2 | 11.1 | 0.0 | 15 | 41 | Hyperbaric oxygen | Healed |
| Healing #3 | 1.2 | 0.0 | 5 | 10 | Hyperbaric oxygen | Healed |
| Healing #4 | 4.6 | 0.0 | 7 | 17 | Hyperbaric oxygen | Healed |
| Healing #5 | 7.5 | 0.0 | 5 | 14 | Topical growth factor (Regranex) | Healed |
| Healing #6 | 3.0 | 0.0 | 4 | 12 | None | Healed |
| Healing #7 | 1.2 | 0.0 | 4 | 13 | None | Healed |
| Healing #8 | 21.0 | 0.0 | 11 | 15 | Hyperbaric oxygen | Healed |
| Healing #9 | 1.0 | 0.0 | 5 | 10 | None | Healed |
| Healing #10 | 1.4 | 0.0 | 4 | 6 | None | Healed |
| Healing #11 | 5.6 | 0.0 | 5 | 12 | Topical growth factor (Regranex) | Healed |
| Healing #12 | 1.9 | 0.0 | 6 | 13 | Bioengineered skin substitute (Apligraf) | Healed |
| Healing #13 | 3.6 | 0.0 | 4 | 9 | None | Healed |
| Healing #14 | 2.2 | 0.0 | 4 | 14 | None | Healed |

**Table 6: Size, duration, and active treatments used in non-healed wounds**

| Wound ID | Initial area (cm2) | Final area (cm2) | Number of Measurement Sessions | Number of weeks | Active treatment | Outcome |
|---|---|---|---|---|---|---|
| Non-Healing #1 | 17.3 | 10.3 | 12 | 35 | Bioengineered skin substitute (Dermagraft) | Below the knee amputation |
| Non-Healing #2 | 50.0 | 21.5 | 7 | 13 | None | Lisfranc amputation |
| Non-Healing #3 | 14.1 | 3.2 | 19 | 61 | Topical growth factor (Regranex) | Open after 20 visits |
| Non-Healing #4 | 1.0 | 4.4 | 5 | 14 | None | Below the knee amputation |
| Non-Healing #5 | 74.5 | 27.7 | 6 | 8 | Hyperbaric oxygen | Metatarsal amputation |
| Non-Healing #6 | 15.6 | 7.5 | 8 | 14 | Hyperbaric oxygen | Transmet amputation |
| Non-Healing #7 | 11.0 | 8.4 | 8 | 13 | None | Transmet amputation |
| Non-Healing #8 | 31.5 | 2.2 | 13 | 25 | Hyperbaric oxygen | Wound excision |
| Non-Healing #9 | 6.7 | 6.8 | 7 | 13 | None | Wound excision, cellulitis |
| Non-Healing #10 | 31.9 | 6.3 | 10 | 18 | None | Transmet revision |
| Non-Healing #11 | 1.9 | 1.1 | 6 | 7 | None | Removal of osteomyletic bone |
| Non-Healing #12 | 41.7 | 9.4 | 5 | 11 | None | Below the knee amputation |
| Non-Healing #13 | 4.8 | 2.7 | 3 | 6 | None | Wound excision |
| Non-Healing #14 | 5.2 | 5.3 | 5 | 12 | None | Transmet revision |

### *6.1.3 Validation of Optical Data*

*In-vivo* measurements on human patients in a busy clinical environment are subject to complications not found in the laboratory, such as motion by the patient (or operator) during a measurement or non-uniform contact between the optical fibers and the skin or wound. When these situations occur, unusable data may be recorded. To prevent invalid measurements from being included in data analysis, the following validation steps were performed on all DNIRS data:

1. The DNIRS device was configured to complete one measurement in approximately 3 seconds. At all measurement locations the probe was held in continuous contact with the wound or skin tissue long enough to obtain 8-10 successive measurements, over a period of approximately 30 seconds. The means and standard deviations of the detected amplitudes and phase shifts were computed at each measurement location, and measurements were discarded if the percent deviation was greater than 30% over the course of each 30 second measurement period. This was done to eliminate errors caused by motion artifacts from the patient or clinician.
2. Further validation was performed to ensure that uniform contact was made between each detector fiber and the wound or skin. The experimentally measured amplitude and phase were fit to the analytical solution of the diffusion approximation for semi-infinite geometry where the $log(I*r^2)$ and the phase show a linear dependence on $r$ ($r$ is the distance between source and detector, and $I$ is the intensity of scattered light registered by the detector). Measurements that did not exhibit good fitting were likely to have had non-uniform fiber / tissue contact and were discarded.
3. The wavelength dependence of the reduced scattering coefficient ($\mu_s'$) in suspensions of spherical particles can be approximated using a power law, where $\mu_s'$ is proportional to $\lambda^{-n}$, where $\lambda$ is wavelength and n ranges from 0.37 to 4 depending on the size of the particles

(Mourant, Fuselier et al. 1997). While the scattering environment of tissue is more complicated than that of particle suspensions, it is expected that the values of $\mu_s$' will decrease as a function of increasing wavelength. In this study, measurements where the reduced scattering coefficient ($\mu_s$') did not decrease as wavelength increased were discarded.

4. Measurements where the signal amplitude was outside of the linear range of the detectors, as described in Section 4.5.2 Detector linearity testing , were discarded.

### *6.1.4 Wound size assessment*

Wounds were digitally photographed using a Fujifilm Finepix s700 digital camera during each measurement session with cross-polarizing filters to reduce surface reflection. A ruler was held in the imaging plane of each photograph to allow the calculation of an absolute wound area. The boundaries of each wound were manually traced using a computer mouse and Microsoft Paint software, and then wound areas were calculated from the traced photographs using an image analysis code developed with Matlab (Mathworks, Inc.) software. This image analysis code counts the number of pixels within the traced wound boundary, and then calculates the wound area by approximating the size of each pixel from the image of the ruler that was present in the imaging plane of each wound.

## 6.2 Human Study Results

### *6.2.1 Results from Healthy Feet*

Figure 34 shows mean values of optical absorption at 780nm in twelve healthy volunteers at each measurement location. The standard deviation between subjects was approximately 25%, however it is clear that locations such as the sole and arch have greater optical absorption than locations such as the heel and balls of the feet. Similar results were obtained at all wavelengths. Understanding these trends may be important when interpreting data from foot ulcers located in a variety of locations.

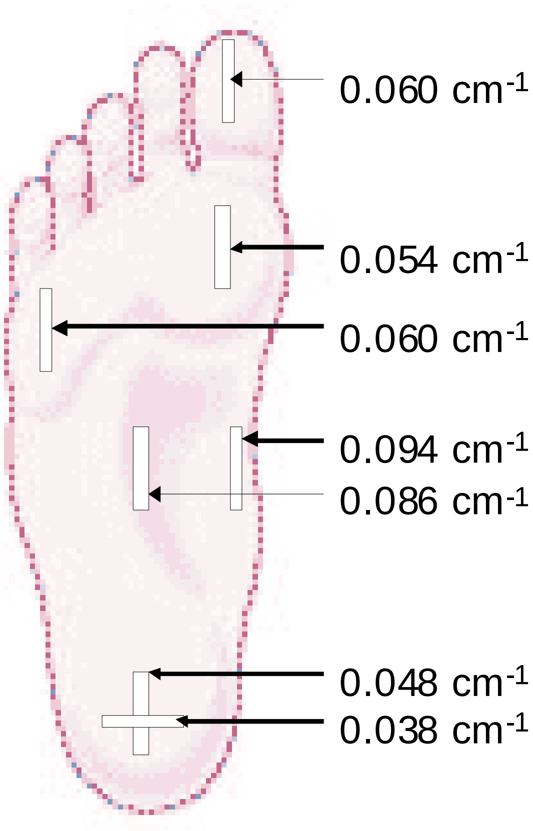

**Figure 34: Mean values of optical absorption at 780nm in 12 healthy subjects at different foot locations. Percent deviation across all subjects was approximately 25%.**

Figure 35 demonstrates the stability of optical absorption at 780nm in four locations on the foot of a healthy volunteer over a period of 49 days. The standard deviation is less than 10% at all locations. Similar results were obtained at all wavelengths.

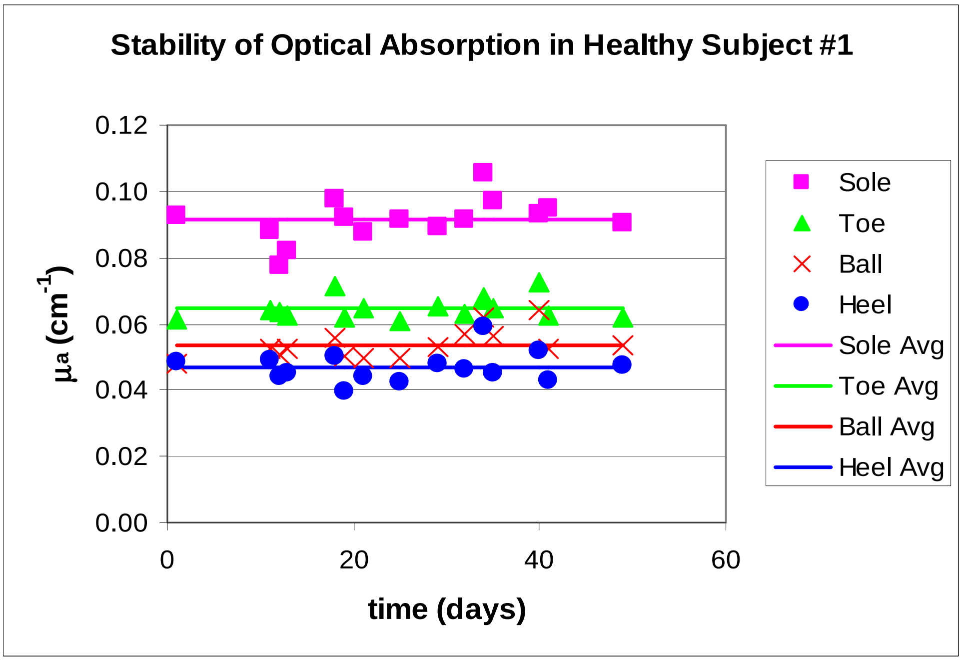

**Figure 35: Stability of optical absorption in a healthy volunteer over 49 days. Percent deviation was approximately 10% at all measurement locations.**

### *6.2.2 Hemoglobin concentration in healing vs. non-healing wounds*

In all wounds (healing and non-healing), values of the optical absorption coefficient ($\mu_a$), reduced scattering coefficient ($\mu'_s$), oxyhemoglobin concentration [$HbO_2$], deoxyhemoglobin concentration [*Hb*], and total hemoglobin concentration [*Tot Hb*] concentration were determined at the wound center, the wound edges, and at the selected and available control sites. A complete set of figures showing all optical results from each of the 28 wounds is given in Appendix A. In this section, results from representative wounds and interesting cases are highlighted, and summary statistics are given for the complete data set.

In all healing wounds the values of [$HbO_2$] and [*Tot Hb*] at the wound center and edge sites decreased and converged to the values measured at the control sites. This is illustrated in Figure 36, which shows plots of hemoglobin concentrations during the course of the study for a typical healing wound. The area of this wound was over 6 $cm^2$ at the beginning of the study, and closed after ten weeks of monitoring.

In contrast, values of [$HbO_2$] and [*Tot Hb*] in all non-healing wounds remained greater than the control sites and did not converge over the course of the study. This is illustrated in Figure 37, which shows plots of hemoglobin concentrations for a typical non-healing wound. The area of this particular wound decreased by only approximately 50% over the course of 35 weeks, after which a below-the knee amputation was performed.

Figure 38 shows results from a wound that appeared to be healing by clinical standards (i.e. a rapid decrease in wound size). However, the rates of change in [$HbO_2$] and [*Tot Hb*] were not converging with the control as is typical of non-healing wounds. Although the wound size decreased sharply by week 18, it never closed and required surgical excision after week 25, and ultimately led to a below the knee amputation several weeks later. In this case, the near infrared oxyhemoglobin measurements reflected the outcome of the wound more accurately and earlier than measurements of wound size.

Figure 39 shows how DNIRS can be used to monitor the effectiveness of a wound therapy. After 14 weeks of participation in the study, one subject underwent an application of a bioengineered skin substitute (Apligraf® ). During the first 14 weeks of NIR measurements, total and oxy-hemoglobin concentrations were not changing or were slightly increasing over time. After the treatment was applied, total and oxy-hemoglobin concentrations decreased until the wound was completely healed by week 31. The sharp decreases in [Total Hb] and [HbO2] slopes immediately after a treatment is applied may be an indication of a successful intervention.

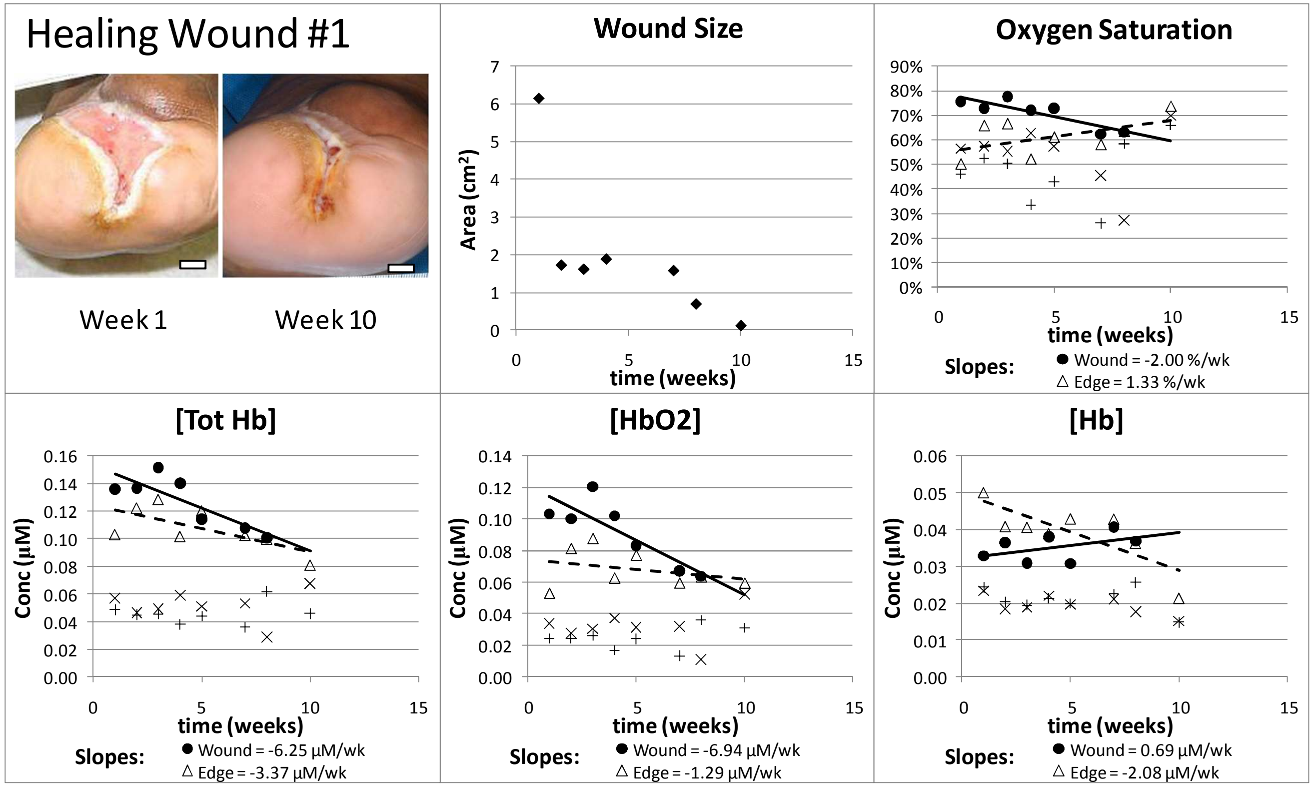

**Figure 36: Example of results from a Healing wound. Location: Transmetatarsal amputation site. Outcome: Wound healed week 10. *Upper left:* Digital photographs from selected time points. *Upper center:* Wound area as determined through analysis of digital photographs (♦). *Upper right*: Oxygen Saturation from each measurement day. *Lower:* Total hemoglobin concentration [*Tot Hb*], oxyhemoglobin concentration [*HbO$_2$*], and deoxyhemoglobin concentration [*Hb*] from each measurement day. Each data point represents the mean of measurements obtained from the center of the wound (●), the edges of the wound (Δ), a control site on the non-wounded foot (+), and a control site on the wounded foot (x). Solid lines are the linear trendlines associated with data obtained from the wound centers; dashed lines are the linear trendlines associated with data obtained from the wound edges.**

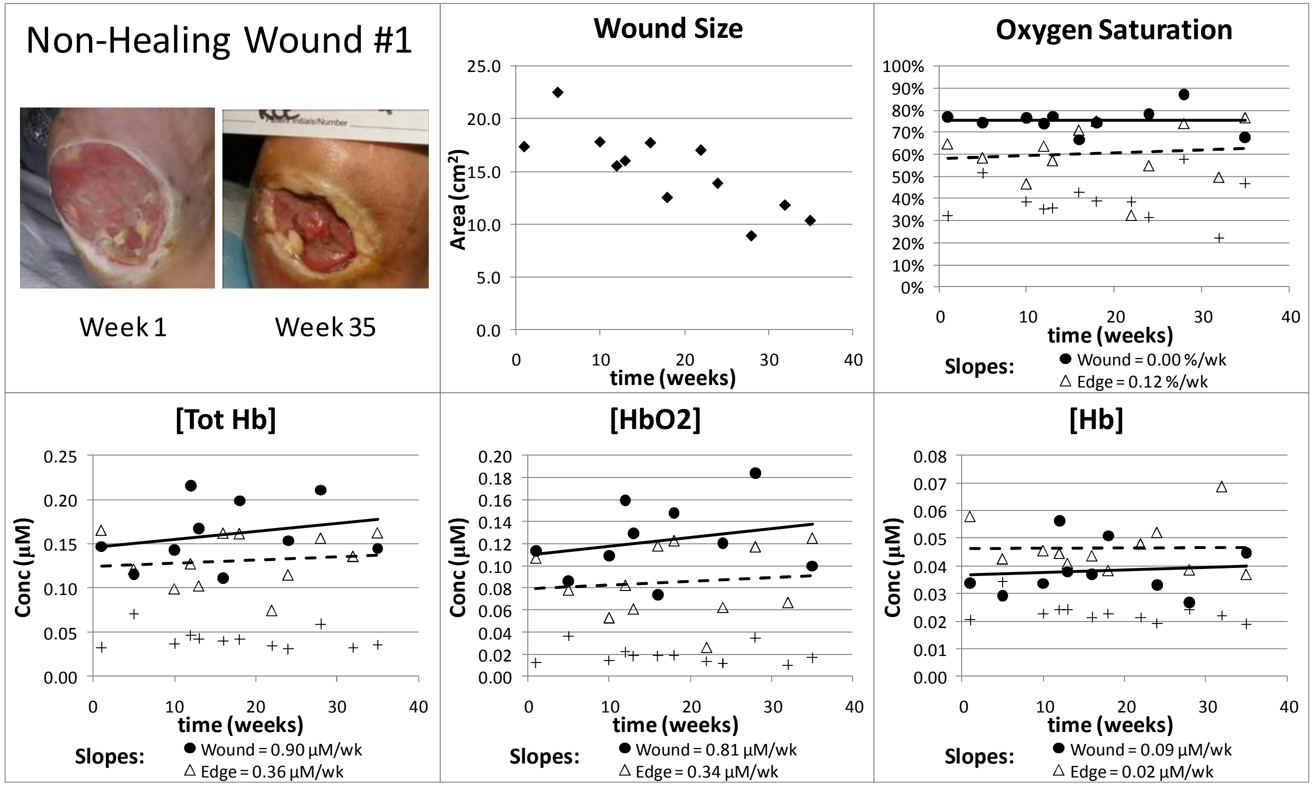

**Figure 37: Example of results from a Non-Healing wound. Location: Plantar surface. Outcome: Below the knee amputation week 38.** ***Upper left:*** **Digital photographs from selected time points.** ***Upper center:*** **Wound area as determined through analysis of digital photographs (♦).** ***Upper right*****: Oxygen Saturation from each measurement day.** ***Lower:*** **Total hemoglobin concentration [*Tot Hb*], oxyhemoglobin concentration [*$HbO_2$*], and deoxyhemoglobin concentration [*Hb*] from each measurement day. Each data point represents the mean of measurements obtained from the center of the wound (●), the edges of the wound (Δ), a control site on the non-wounded foot (+), and a control site on the wounded foot (x). Solid lines are the linear trendlines associated with data obtained from the wound centers; dashed lines are the linear trendlines associated with data obtained from the wound edges.**

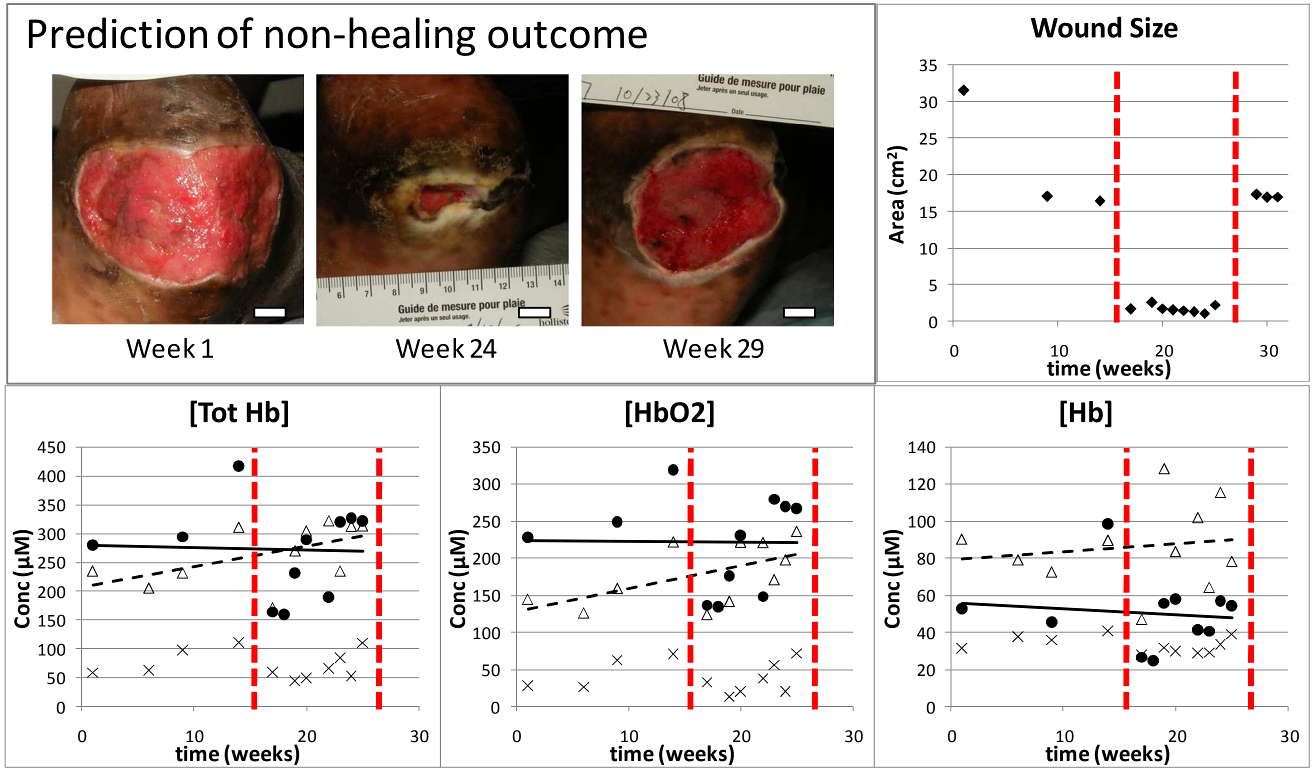

**Figure 38: Example of data obtained from a wound that was classified as non-healing by NIR measurements despite a sharp decrease in wound size. The wound required surgical excision after week 25 and ultimately resulted in amputation.** ***Upper left:*** **Digital photographs from selected time points. Scale bars represent 1 cm.** ***Upper right:*** **Wound area as determined through analysis of digital photographs (♦). A major debridement was performed prior to week 29, causing the observed increase in wound size.** ***Lower:*** **Total hemoglobin concentration [*Tot Hb*], oxyhemoglobin concentration [*HbO*$_2$], and deoxyhemoglobin concentration [*Hb*] from each measurement day. Each data point represents the mean of measurements obtained from the center of the wound (●), the edges of the wound (Δ), and a control site on the non-wounded foot (x). The solid lines are the linear trendlines associated with data obtained from the wound centers; the dashed lines are the linear trendlines associated with data obtained from the wound edges.**

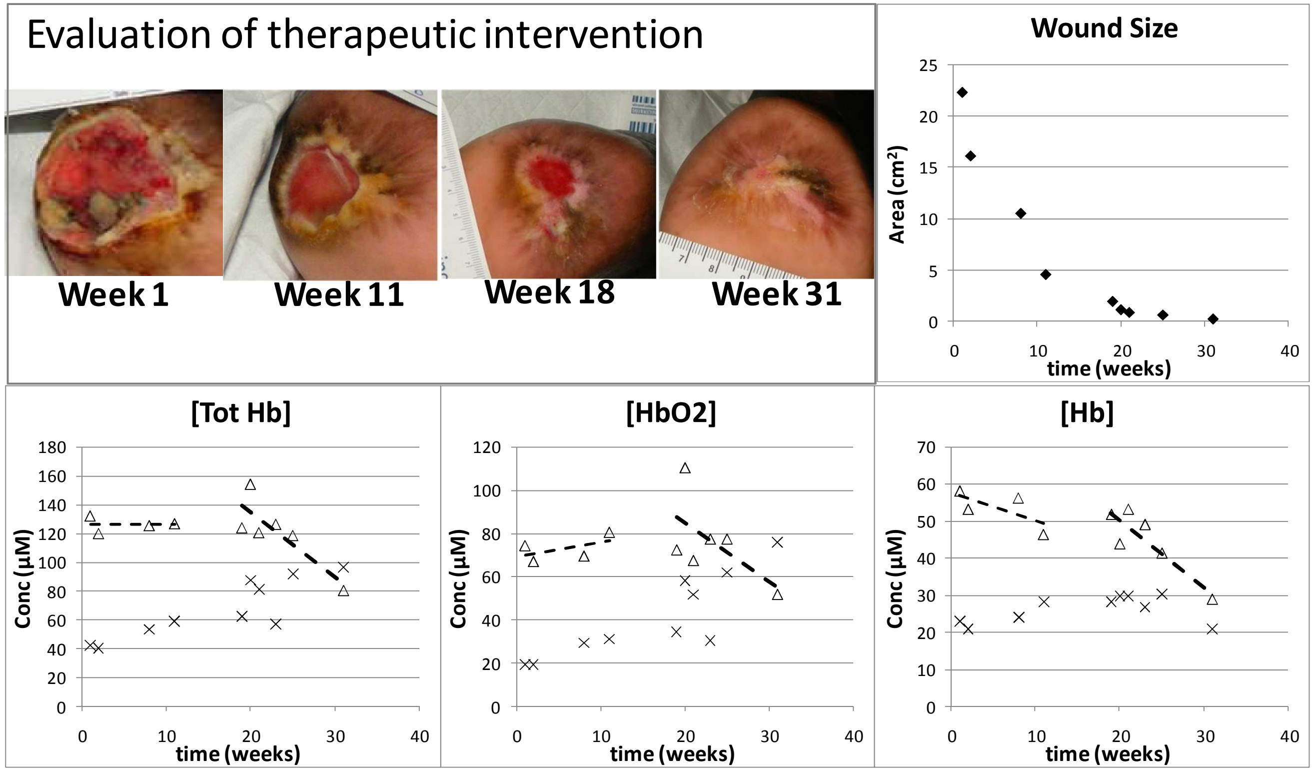

**Figure 39: Example of data obtained before and after application of an active wound healing therapy. In this example, a bioengineered skin substitute (Apligraf®) was applied after week 14 of the study. Upper left: Digital photographs from selected time points. Scale bars represent 1 cm. Upper right: Wound area as determined through analysis of digital photographs (♦). Lower: Total hemoglobin concentration [Tot Hb], oxyhemoglobin concentration [HbO2], and deoxyhemoglobin concentration [Hb] from each measurement day. Each data point represents the mean of measurements obtained from the edges of the wound (Δ) and a control site on the non-wounded foot (x). The dashed lines are the linear trendlines associated with data obtained from the wound edges. The slopes of total and oxy-hemoglobin trendlines prior to week 14 were -0.1 µM/wk and 0.7 µM/wk; the slopes of total and oxy-hemoglobin trendlines after week 14 were -4.5 µM/wk and -2.7 µM/wk.**

### *6.2.3 Rates of change in optical data*

The hypothesis of this research is that changes in blood vessel density and oxygen delivery beneath the surface of a wound can be measured using DNIRS, and that these changes may be used to quantitatively assess the healing status of a chronic wound. In this section, the temporal rate of change of hemoglobin concentration is estimated by fitting the data from each wound to a linear trend line. The slopes of these trend lines can be used as a quantitative indicator of the rate of change in hemoglobin concentration with time, and have proven useful in differentiating healing from non-healing wounds in our study. The slopes calculated from the hemoglobin concentration trend lines were calculated for the wound edge and wound center measurements of each wound. The sum of the edge slope and the center slope obtained from each wound is shown in Figure 40.

In all healing wounds negative rates of change were observed for [$HbO_2$] and [*Tot Hb*]. Values of [$HbO_2$] slopes in healing wounds ranged from -21.5 to -1.9 µM/wk, while [*Tot Hb*] slopes in healing wounds ranged from -20.8 to -3.8 µM/wk. In all non-healing wounds the rates of change for [$HbO_2$] and [*Tot Hb*] were close to zero or slightly positive. Values of [$HbO_2$] slopes in healing wounds ranged from -1.4 to 13.9 µM/wk, while [*Tot Hb*] slopes in healing wounds ranged from -1.3 to 10.0 µM/wk. The rate of change for [*Hb*] concentration was close to zero in both healing (ranged from -2.2 to 3.1 µM/wk) and non-healing wounds (ranged from -9.1 to 6.2 µM/wk). The mean rates of change in healing and non-healing wounds are compared for all hemoglobin concentrations ([*Tot Hb*], [$HbO_2$], and [*Hb*]) in Figure 41. A statistically significant difference ($p < 0.0001$) between the slopes of healing and non-healing wounds was observed for the total hemoglobin concentration and the oxy-hemoglobin concentration.

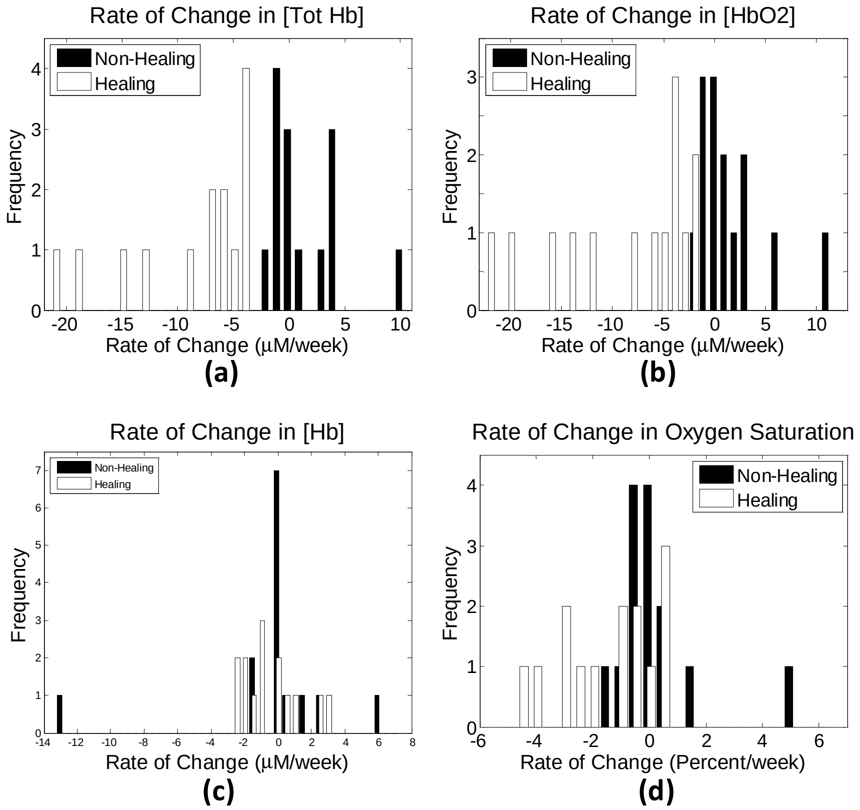

**(a)** **(b)** **(c)** **(d)**

**Figure 40: Rates of change in hemoglobin levels for all wound measurements. (a) Total hemoglobin concentration, (b) Oxy-hemoglobin concentration, (c) Deoxy-hemoglobin concentration, (d) Oxygen saturation. White bars represent data from healing wounds; black bars represent data from non-healing wounds. The rate of change in wound center measurements and wound edge measurements were calculated separately for each subject. The average of the wound center and wound edge rates of change are displayed.**

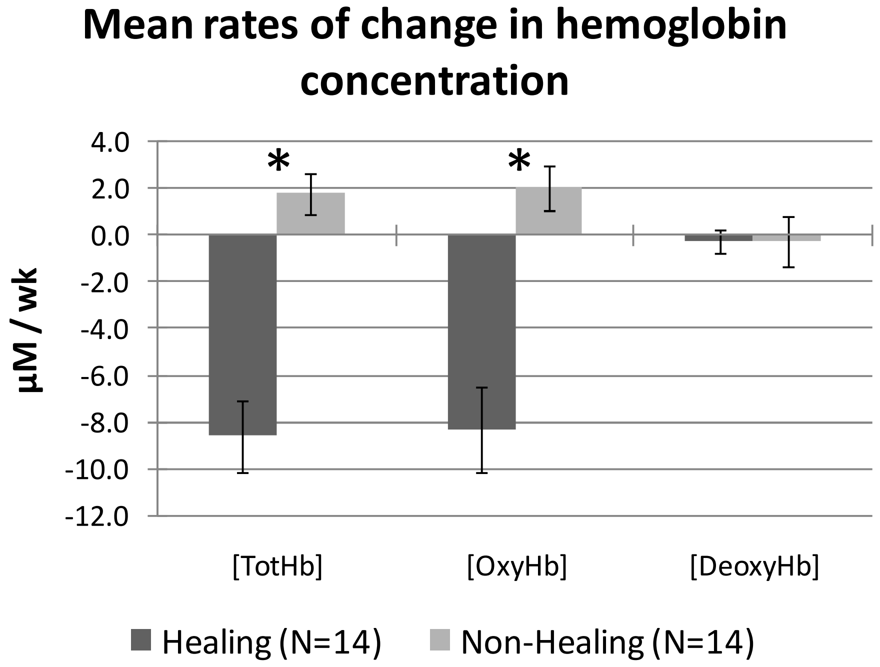

**Figure 41: Mean rates of change in hemoglobin concentration: healing vs. non-healing wounds. Error bars represent standard error. Two-tailed, heteroscedastic t-tests were used to test the difference between the rates of change in healing and non-healing wounds. *p < 0.0001**

### *6.2.4 Statistical Characterization of Healing and Non-Healing Wound Data*

In addition to the rate of change of hemoglobin concentration, the statistical dispersion or variability of hemoglobin concentration from a wound may provide an indicator of healing potential. Visual comparison of Figure 36 and Figure 37 reveals more week-to-week variability in the non-healing data than in the healing data. To quantify variability differences, the root mean square deviation (RMSD) of experimental data from the fitted linear trend line fitted for each wound was calculated using the following equation:

$$RMSD = \sqrt{\frac{\sum_{i=1}^{n}(x_{i,meas} - x_{i,fit})^2}{n}} \qquad \text{(Eq. 7)}$$

where *n* is the number of measurements, $x_{i,meas}$ are measured values, and $x_{i,fit}$ are the values predicted by the linear trend lines. The RMSD values were normalized by dividing by the mean of the experimental values obtained for each wound. Normalized RMSD values for [Total Hb], [$HbO_2$], and [Hb] data are shown in Figure 42. Figure 43 shows that the mean normalized RMSD was significantly greater in non-healing wounds than in healing wounds for total and oxy-hemoglobin concentrations obtained from the edges of wounds.

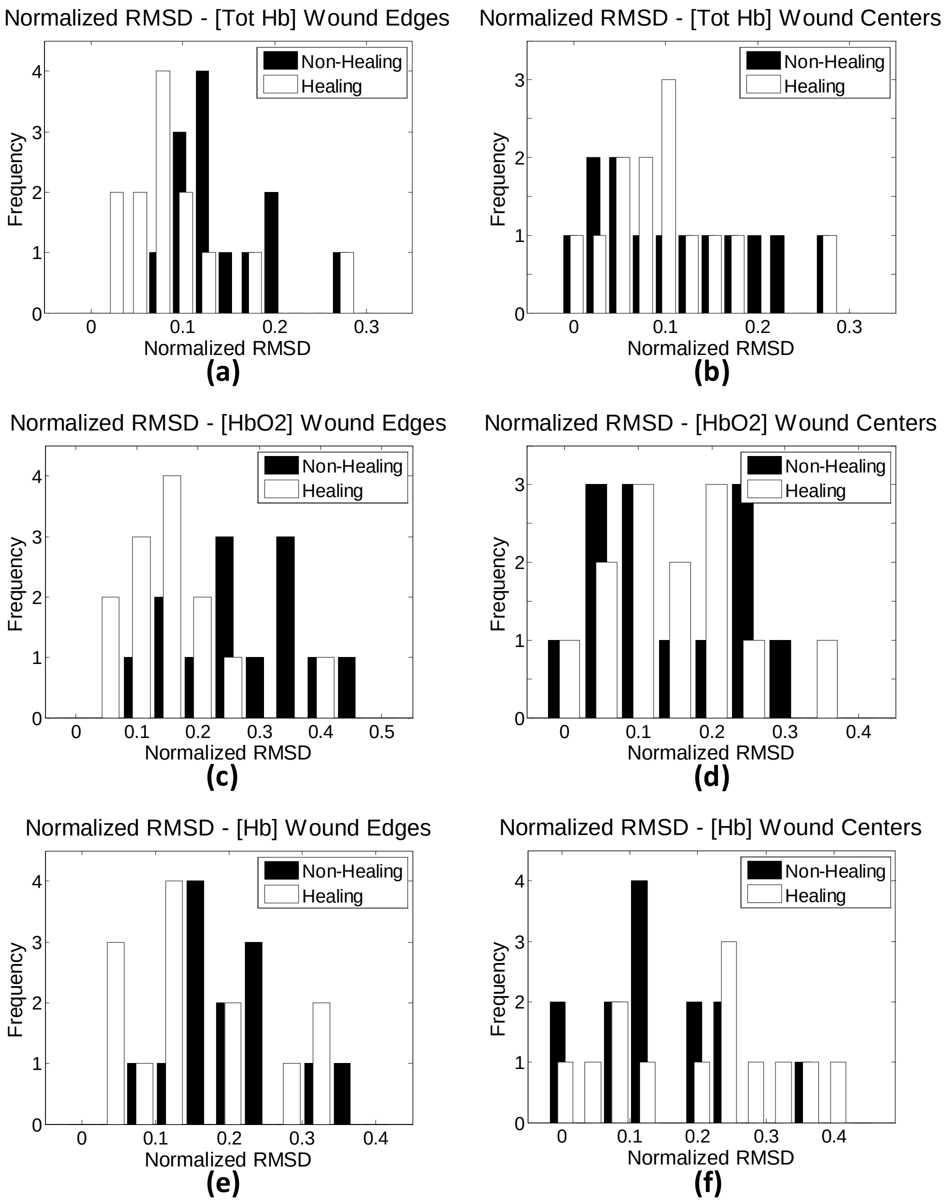

(a) (b) (c) (d) (e) (f)

**Figure 42: Normalized RMSD values for (a) total hemoglobin concentration measured at the edges of wounds, (b) total hemoglobin concentration measured at the centers of wounds, (c) oxyhemoglobin concentration measured at the edges of wounds, (d) oxyhemoglobin concentration measured at the centers of wounds, (e) deoxyhemoglobin concentration measured at the edges of wounds, (f) deoxyhemoglobin concentration measured at the centers of wounds.**

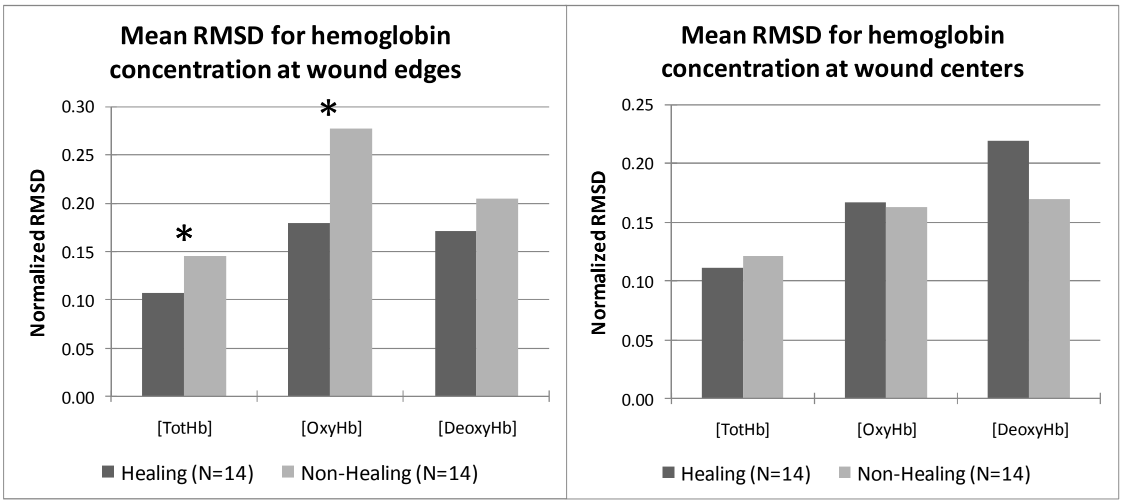

**Figure 43: Mean Normalized RMSD values for data obtained from (left) wound edges and (right) wound centers. *p<0.05, two-tailed t-test.**

### *6.2.5 Predictive capability of optical data*

The previous sections suggest that healing diabetic foot ulcers can be distinguished from non-healing ulcers by non-invasively measuring changes in hemoglobin concentration with DNIRS. It may be possible to use the rate of change of total- or oxy- hemoglobin concentration to predict whether or not a wound will heal. Using all of the [Total Hb] slopes shown in Figure 40a, healing wounds can be separated from non-healing wounds by selecting a threshold between -1.3 µM/wk and -3.4 µM/wk (i.e. all wounds with a [Total Hb] slope less than -3.4 µM/wk were classified as healing wounds, while all wounds with a [Total Hb] slope greater than -1.3 µM/wk were classified as non-healing wounds). For [$HbO_2$] slopes, a threshold between -1.4 µM/wk and -1.8 µM/wk could be used to separate all healing from non-healing wounds.

In a clinical environment, it will be necessary to be able to predict healing before the end points that were used in this study are reached (i.e. before a wound is completely healed or before a wound needs amputation). There are two factors that affect the clinical utility of using DNIRS to predict wound outcome: 1) the minimum time period needed to make an accurate prediction of wound outcome, and 2) the minimum number of measurements needed to make an accurate prediction of wound outcome. To address these factors, [Total Hb] and [$HbO_2$] slopes were calculated for each wound using sets of DNIRS data obtained over reduced time periods. Instead of using all available data from each wound, slopes were calculated using data obtained from a period of time ranging from the first 4 calendar weeks to the first 12 calendar weeks after a patient's first measurement session. The [Total Hb] and [$HbO_2$] slopes calculated for each reduced time period were used to classify each wound as healing or non-healing. This analysis was done using two different thresholds for separating a "healing" slope from a "non-healing" slope.

Table 7 summarizes the number and percent of healing and non-healing wounds that would have been correctly classified using the [Tot Hb] slopes calculated using reduced time periods. Note that slopes were calculated only if *at least three* measurements were taken over the reduced time period. This explains why there are fewer wounds in the 4-week analysis than in the 12-week analysis: only a small fraction of subjects were measured at least three times during the 4 week period immediately following their study enrollment. Table 7 shows that the number of correctly classified wounds increases as the measurement time period increases, as expected. When [Tot Hb] slopes are calculated for wounds that were measured *at least four* times during each reduced time period, the percentage of correctly classified healing and non-healing wounds increases, as shown in Table 8. This analysis was repeated for [$HbO_2$] slopes, and the results are summarized in Table 9 and Table 10.

**Table 7: Prediction capability of [*Tot Hb*] slopes calculated for reduced time periods ranging from the first 4 weeks to the first 12 weeks. Wounds were included only if *at least 3* DNIRS measurements were obtained during the measurement time period.**

| | Healing Wounds Correctly Classified | | Non-Healing Wounds Correctly Classified | |
|---|---|---|---|---|
| **Measurement Time Period (Weeks)** | **Threshold = -1 µM/wk** | **Threshold = -4 µM/wk** | **Threshold = -1 µM/wk** | **Threshold = -4 µM/wk** |
| 4 | 6 of 7 (86%) | 6 of 7 (86%) | 3 of 4 (75%) | 4 of 4 (100%) |
| 5 | 8 of 9 (89%) | 7 of 9 (78%) | 5 of 5 (100%) | 5 of 5 (100%) |
| 6 | 8 of 9 (89%) | 6 of 9 (67%) | 8 of 9 (89%) | 9 of 9 (100%) |
| 7 | 8 of 9 (89%) | 6 of 9 (67%) | 10 of 10 (100%) | 10 of 10 (100%) |
| 8 | 8 of 9 (89%) | 7 of 9 (78%) | 11 of 11 (100%) | 11 of 11 (100%) |
| 9 | 10 of 10 (100%) | 8 of 10 (80%) | 12 of 13 (92%) | 12 of 13 (92%) |
| 10 | 11 of 11 (100%) | 9 of 11 (82%) | 13 of 14 (93%) | 14 of 14 (100%) |
| 11 | 12 of 12 (100%) | 10 of 12 (83%) | 13 of 14 (93%) | 14 of 14 (100%) |
| 12 | 13 of 13 (100%) | 11 of 13 (85%) | 14 of 14 (100%) | 14 of 14 (100%) |

**Table 8: Prediction capability of [*Tot Hb*] slopes calculated for reduced time periods ranging from the first 4 weeks to the first 12 weeks. Wounds were included only if *at least 4* DNIRS measurements were obtained during the measurement time period.**

| | Healing Wounds Correctly Classified | | Non-Healing Wounds Correctly Classified | |
|---|---|---|---|---|
| **Measurement Time Period (Weeks)** | **Threshold = -1 µM/wk** | **Threshold = -4 µM/wk** | **Threshold = -1 µM/wk** | **Threshold = -4 µM/wk** |
| 4 | 0 of 1 (0%) | 0 of 1 (0%) | 1 of 2 (50%) | 2 of 2 (100%) |
| 5 | 3 of 3 (100%) | 2 of 3 (67%) | 2 of 2 (100%) | 2 of 2 (100%) |
| 6 | 7 of 7 (100%) | 5 of 7 (71%) | 2 of 3 (67%) | 3 of 3 (100%) |
| 7 | 7 of 7 (100%) | 5 of 7 (71%) | 6 of 6 (100%) | 6 of 6 (100%) |
| 8 | 7 of 7 (100%) | 6 of 7 (86%) | 8 of 8 (100%) | 8 of 8 (100%) |
| 9 | 9 of 9 (100%) | 7 of 9 (78%) | 9 of 9 (100%) | 9 of 9 (100%) |
| 10 | 9 of 9 (100%) | 8 of 9 (89%) | 10 of 10 (100%) | 10 of 10 (100%) |
| 11 | 9 of 9 (100%) | 8 of 9 (89%) | 10 of 10 (100%) | 10 of 10 (100%) |
| 12 | 11 of 11 (100%) | 10 of 11 (91%) | 12 of 12 (100%) | 12 of 12 (100%) |

**Table 9: Prediction capability of [$HbO_2$] slopes calculated for reduced time periods ranging from the first 4 weeks to the first 12 weeks. Wounds were included only if *at least 3* DNIRS measurements were obtained during the measurement time period.**

| | Healing Wounds Correctly Classified | | Non-Healing Wounds Correctly Classified | |
|---|---|---|---|---|
| **Measurement Time Period (Weeks)** | **Threshold = -1.5 µM/wk** | **Threshold = -3.5 µM/wk** | **Threshold = -1.5 µM/wk** | **Threshold = -3.5 µM/wk** |
| 4 | 6 of 7 (86%) | 6 of 7 (86%) | 3 of 4 (75%) | 3 of 4 (75%) |
| 5 | 6 of 9 (67%) | 5 of 9 (56%) | 4 of 5 (80%) | 4 of 5 (80%) |
| 6 | 5 of 9 (56%) | 4 of 9 (44%) | 7 of 9 (78%) | 7 of 9 (78%) |
| 7 | 6 of 9 (67%) | 5 of 9 (56%) | 7 of 10 (70%) | 8 of 10 (80%) |
| 8 | 6 of 9 (67%) | 5 of 9 (56%) | 8 of 11 (73%) | 8 of 11 (73%) |
| 9 | 7 of 10 (70%) | 6 of 10 (60%) | 9 of 13 (69%) | 9 of 13 (69%) |
| 10 | 10 of 11 (91%) | 8 of 11 (73%) | 13 of 14 (93%) | 14 of 14 (100%) |
| 11 | 11 of 12 (92%) | 9 of 12 (75%) | 10 of 14 (71%) | 12 of 14 (86%) |
| 12 | 12 of 13 (92%) | 9 of 13 (69%) | 9 of 14 (64%) | 12 of 14 (86%) |

**Table 10: Prediction capability of [$HbO_2$] slopes calculated for reduced time periods ranging from the first 4 weeks to the first 12 weeks. Wounds were included only if *at least 4* DNIRS measurements were obtained during the measurement time period.**

| | Healing Wounds Correctly Classified | | Non-Healing Wounds Correctly Classified | |
|---|---|---|---|---|
| **Measurement Time Period (Weeks)** | **Threshold = -1 µM/wk** | **Threshold = -4 µM/wk** | **Threshold = -1 µM/wk** | **Threshold = -4 µM/wk** |
| 4 | 0 of 1 (0%) | 0 of 1 (0%) | 1 of 2 (50%) | 1 of 2 (50%) |
| 5 | 2 of 3 (67%) | 0 of 3 (0%) | 2 of 2 (100%) | 2 of 2 (100%) |
| 6 | 5 of 7 (71%) | 3 of 7 (43%) | 3 of 3 (100%) | 3 of 3 (100%) |
| 7 | 6 of 7 (86%) | 4 of 7 (57%) | 5 of 6 (83%) | 6 of 6 (100%) |
| 8 | 6 of 7 (86%) | 4 of 7 (57%) | 6 of 8 (75%) | 7 of 8 (88%) |
| 9 | 7 of 9 (78%) | 5 of 9 (56%) | 7 of 9 (78%) | 8 of 9 (89%) |
| 10 | 9 of 9 (100%) | 7 of 9 (78%) | 7 of 10 (70%) | 9 of 10 (90%) |
| 11 | 9 of 9 (100%) | 7 of 9 (78%) | 8 of 10 (80%) | 9 of 10 (90%) |
| 12 | 11 of 11 (100%) | 8 of 11 (73%) | 11 of 12 (92%) | 12 of 12 (100%) |

These results indicate that although both [Tot Hb] and [$HbO_2$] slopes can be used to differentiate healing from non-healing wounds (Figure 41), it appears that the [Tot Hb] slopes in Table 7 and Table 8 consistently classify more wounds correctly than the [$HbO_2$] slopes in Table 9 and Table 10. This could indicate that changes in the total amount of blood in the wound environment are more important for predicting healing than its oxygenation status. In general, the percentage of correctly classified wounds increases as the measurement time period and the number of measurement sessions increase.

## 6.3 Human Study Discussion

The hypothesized model on the expected behavior of hemoglobin concentration during the course of healing that was explained in Section 5.3 Animal Study Discussion is illustrated in Figure 44. The data from human diabetic foot ulcers presented in previous section validate this hypothesized model of hemoglobin behavior. As expected, hemoglobin concentration in the wounds of all subjects was initially elevated over hemoglobin concentration at control sites. This is due to increased blood vessel density in the wound bed, as demonstrated in our previously published research on the application of DNIRS to assess wound healing in animal models (Papazoglou, Weingarten et al. 2006; Papazoglou 2008). The data from healing and non-healing wounds summarized in Section 6.2.3 Rates of change in optical data are in agreement with the hypothesized healing model, and demonstrate that [$HbO_2$] and [Tot Hb] decrease and converge to the values of non-wound tissue in healing wounds (Figure 44, dashed black line), but do not converge in non-healing wounds (Figure 44, gray markers). Furthermore, the healing model predicts that levels of [Hb] in both healing and non-healing wounds are expected to remain constant (Figure 44, gray markers), and this is the behavior of [Hb] in human diabetic foot ulcers shown in Figure 40 and Figure 41.

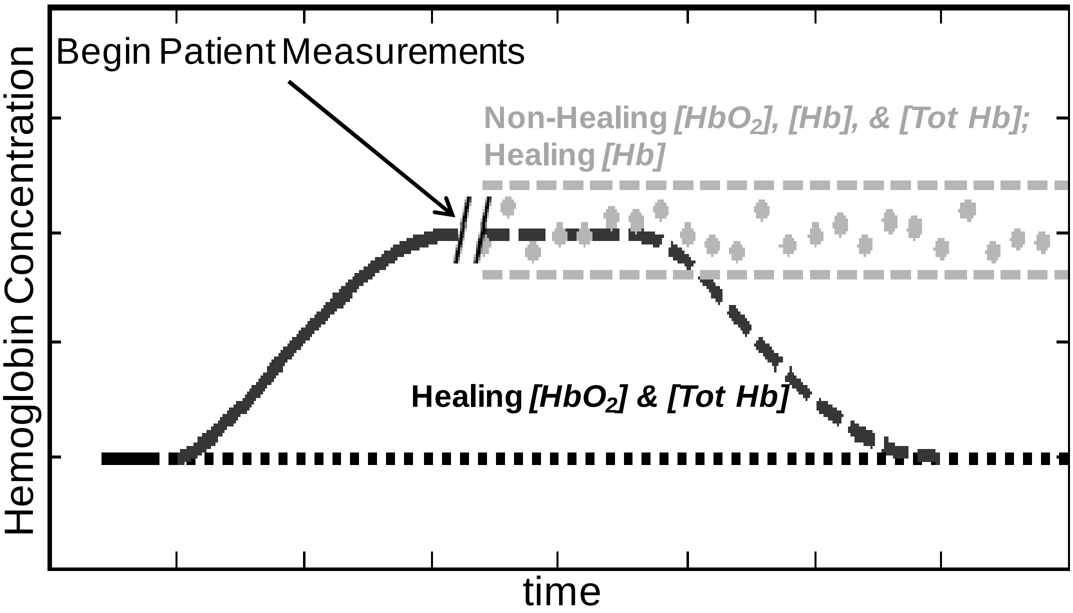

**Figure 44: Hypothesized wound healing curve for DNIRS measurements of hemoglobin concentration. The dotted black line represents normal (non-wound) tissue. The solid black line represents the increasing levels of [HbO$_2$], [Hb], and [Tot Hb] immediately after a wound occurs. The descending dashed black lines represent the hypothesized curve for [HbO$_2$] and [Tot Hb] in healing wounds. The gray markers represent [HbO$_2$] and [Tot Hb] measurements on non-healing wounds as well as [Hb] measurements on both healing and non-healing wounds.**

The data presented in Section 6.2.5 Predictive capability of optical data may provide an indication of how the rates of change in hemoglobin concentration could be used as a predictive “healing index”. From a clinical perspective, one could envision DNIRS being used to evaluate the effectiveness of a treatment regime on a particular wound. If a wound is classified as “Healing” after a few weeks of DNIRS measurements, the treatment would be continued. If the wound is classified as “Non-Healing,” the treatment would be discontinued and a different treatment would be prescribed. In this scenario, the result of misclassifying a “Non-Healing” wound is that an ineffective treatment would be continued for another week. However, the result of misclassifying a "Healing" wound is that an effective treatment would be discontinued and a new (possibly ineffective) treatment would be started. The tables in Section 6.2.4 indicate that choosing a threshold that is more negative (e.g. -4 µM/wk for [Tot Hb] slopes) increases the number of non-healing wounds that are correctly classified, while choosing a threshold that is less negative (e.g. -1 µM/wk for [Tot Hb] slopes) increases the number of correctly classified healing wounds. Therefore, when defining an algorithm for a predictive healing index, it may be best to choose a threshold close to -1 µM/wk in order to minimize the number of healing wounds that are misclassified. For example, if a Healing Index were based solely on [Tot Hb] slopes obtained after a measurement period of 5-weeks or more with at least 4 measurement sessions, 100% of healing wounds from our study would have been classified correctly, and all but one non-healing wound have been correctly classified. It is necessary to obtain data from more wounds than the 28 studied in this research before deciding on a final algorithm for a healing index.

The rate of change of oxygenated hemoglobin concentration in healing wounds is greater than the rate of change in deoxygenated hemoglobin concentration, as shown in Figure 41. There are three inter-related and overlapping phases of wound healing: first an inflammatory phase, then a proliferative phase which is characterized by increased cell growth and angiogenesis, and finally a remodeling phase in which collagen is deposited and organized to form scar tissue (Van Staveren, Moes et al. 1991). During the late inflammatory / early proliferation stage of wound healing, angiogenesis increases the supply of oxygenated blood to the wound resulting in increased levels of [$HbO_2$] and [Hb]. In the late proliferation stage, angiogenesis stops and blood vessels begin to break down as a result of apoptosis (Singer and Clark 1999). The resulting decrease in the supply of oxygenated hemoglobin to the wound may be reflected by the negative rate of change of [$HbO_2$] and [Tot Hb] observed in this study (Figure

41). Increased local cellular metabolic activity results in increased oxygen consumption which is reflected in elevated local concentrations of deoxygenated hemoglobin (Wolff, Kolberg et al. 1998; Sowa, Matas et al. 2002). In this study, levels of [Hb] measured in diabetic foot ulcers were greater than levels of [Hb] at the control sites, and showed very little change during the healing process, as demonstrated in Figure 41. These data may correspond to increased cellular metabolism that is required throughout the proliferation and remodeling phases of wound healing as the wounds reach complete closure and the extracellular matrix of the newly formed epithelial tissue is reorganized and strengthened, a process that has been shown to take many months (Singer and Clark 1999; Muncaster 2001). It is likely that if DNIRS measurements were continued after wound closure, levels of [Hb] in the scar tissue would decrease and converge with control levels of [Hb] over the course of wound remodeling.

It has been hypothesized that chronic diabetic wounds may be “stuck” in various phases of the healing process (Falanga 2005). The non-healing wounds observed in this study may have been “arrested” before reaching the end of the proliferative phase of healing, resulting in oxygenated hemoglobin concentrations that were always greater than normal tissue and did not decrease like healing wounds. Furthermore, there is evidence that neuropathy and a prolonged inflammatory response in diabetic patients are important factors in the etiology of diabetic foot ulcers (Loots, Lamme et al. 1998; Falanga 2005). Diabetic neuropathy is associated with microcirculatory dysfunction in the foot, even in patients who have normal large-vessel blood flow to the foot, like the patients enrolled in our study (Veves, Akbari et al. 1998). It has been hypothesized that repeated ischemia and reperfusion within the microvasculature of the foot may lead to cycles of inflammation in foot ulcers, further impairing the wound healing process (Driver, Feather et al. 1989; Mustoe, O'Shaughnessy et al. 2006). The high degree of week-to-week variability in non-healing wounds compared to healing wounds shown in Figure 43 supports this hypothesis and could be an indication of cyclical inflammation in these wounds.

# CHAPTER 7: CONCLUSIONS AND FUTURE WORK

Diffuse near infrared spectroscopy (DNIRS) is a method of non-invasively measuring the optical absorption and reduced scattering coefficients of tissue at depths ranging from several millimeters to several centimeters. Measured values of the optical absorption coefficient reflect the concentrations of oxyhemoglobin and deoxyhemoglobin within the probed tissue volume. The purpose of this research was to determine whether DNIRS could be used to monitor changes in wound physiology during the healing process, whether the measured changes could be used to differentiate healing from non-healing wounds, and whether DNIRS data could be used to predict a healing/non-healing outcome in human chronic wounds. A study of healing in an obese rat wound model and a study of human diabetic foot ulcers were conducted in order to meet these goals.

To summarize the results of the animal study, obese rats may provide a model of healing that is more similar to human chronic wound healing than lean, chemically-induced diabetic rats. The obese Zucker Diabetic Fatty rats used in this study exhibited a significantly slower healing rate than lean diabetic rats (33 days vs. 21 days), and epithelialization appeared to contribute more to the healing of obese rat wounds than lean diabetic rat wounds. DNIRS wound monitoring was used to quantify changes in wound vascularization and oxygenation that occurred during all phases of healing, including the remodeling phase. A model of the expected behavior of hemoglobin concentration during wound healing was developed based on the results of the animal study. In this model, increasing levels of hemoglobin concentration (oxy-, deoxy-, and total hemoglobin concentrations) were seen immediately after wound surgery. Decreasing levels of [Tot Hb] and [$HbO_2$] were observed after wound closure, consistent with blood vessel apoptosis during late proliferation and remodeling stages of wound healing. Elevated [Hb] levels were observed for 7 weeks after wound closure, and may reflect increased cellular metabolism required for remodeling phase of wound healing.

To summarize the study of human wound healing, 14 healing and 14 non-healing diabetic foot ulcers were measured using DNIRS on a weekly or biweekly basis. Hemoglobin concentration measured in wounds was greater than hemoglobin concentrations measured at control sites on the feet of each patient. Levels of oxyhemoglobin [$HbO_2$] and total hemoglobin [Tot Hb] concentration decrease over time in healing wounds, but remain constant in non-healing wounds. There was a statistically significant difference ($p<0.0001$) between healing and non-healing wounds in the temporal rates of change of [Total Hb] and [Oxy-Hb]. Deoxyhemoglobin concentration [Hb] remained relatively constant over time in both healing and non-healing wounds. This behavior is consistent with the model of hemoglobin behavior during wound healing that was developed from our animal studies. Furthermore, the results demonstrate that week-to-week variability of [$HbO_2$] and [Tot Hb] in non-healing wounds is significantly ($p<0.05$) greater than in healing wounds.

Our human data suggest that [Tot Hb] slopes can predict wound outcome with nearly 100% specificity and sensitivity when at least 4 measurements are made over a period of 5 weeks or more. Measurements on more patients are needed to better determine the minimum time period needed to accurately predict healing with DNIRS wound monitoring, however, our results indicate that DNIRS wound monitoring may be able to supplement and improve upon traditional evaluation methods for predicting wound healing.

Future work with the DNIRS wound monitor may include: (1) the assessment of other types of tissue damage such as venous leg ulcers, pressure ulcers, surgical wounds, burns. The human study described here was limited to diabetic foot ulcer in order to achieve some uniformity between subjects. However, DNIRS should be able to monitor many types of wounds. (2) The development of a non-contact probe that uses lenses to deliver light to and from a wound rather than optical fibers could allow DNIRS measurements without causing any patient discomfort or risk of contamination. (3) Simultaneous measurement of microcirculatory blood perfusion using diffuse correlation spectroscopy (DCS). A combined DNIRS/DCS system could be developed with a shared fiber optic probe and integrated software control. The addition of microcirculatory blood perfusion to measurements of oxy-, deoxy-, and total hemoglobin may provide additional information about the healing status of a wound. (4) Monitoring healing during pre-clinical and clinical trials of novel wound therapies. Non-invasive DNIRS measurements can provide quantitative information on subsurface improvements in the wound bed caused by a treatment without the need for biopsies. (5) Improved modeling of photon transport in tissue at small source-detector separation distances. This would be especially valuable when using DNIRS for rodent wound studies, because rodent skin tends to be thin and a more superficial measurement depth may be desirable.

## REFERENCES

Ambrozy, E., I. Waczulikova, et al. (2009). "Microcirculation in mixed arterial/venous ulcers and the surrounding skin: clinical study using a laser Doppler perfusion imager and capillary microscopy." Wound Repair and Regeneration **17**(1): 19.

Armstrong, D. G., L. A. Lavery, et al. (1997). "Infrared dermal thermometry for the high-risk diabetic foot." Physical Therapy **77**(2): 169.

Bader, M. (2008). "Diabetic foot infection." American family physician **78**(1): 71-79.

Bagavathiappan, S., T. Saravanan, et al. (2008). "Investigation of peripheral vascular disorders using thermal imaging." The British Journal of Diabetes & Vascular Disease **8**(2): 102.

Basu, H. (2007). A novel method for calibration of a functional near infrared spectroscopy (fNIRS) instrument used in the assessment of wound healing. Philadelphia, PA, Drexel University. **M.S.**

Baugh, N., H. Zuelzer, et al. (2007). "Wounds in surgical patients who are obese." AJN The American Journal of Nursing **107**(6): 40-50.

Baum, C. and C. Arpey (2005). "Normal cutaneous wound healing: clinical correlation with cellular and molecular events." Dermatologic Surgery **31**(6): 674-686.

Beckert, S., M. B. Witte, et al. (2004). "The Impact of the Micro-Lightguide O2C for the Quantification of Tissue Ischemia in Diabetic Foot Ulcers." Diabetes care **27**(12): 2863-2867.

Boas, D. A. (1996). Diffuse photon probes of structural and dynamical properties of turbid media: theory and biomedical applications, Ph.D. Thesis, University of Pennsylvania.

Brem, H., P. Sheehan, et al. (2004). "Protocol for treatment of diabetic foot ulcers." The American journal of surgery **187**(5A): 1-10.

Christ, F., A. Bauer, et al. (2002). "Different optical methods for clinical monitoring of the microcirculation." Eur Surg Res **34**: 145-151.

Cobb, M. J., Y. Chen, et al. (2006). "Noninvasive assessment of cutaneous wound healing using ultrahigh-resolution optical coherence tomography." Journal of Biomedical Optics **11**: 064002.

Cross, K. M., L. Leonardi, et al. (2007). "Clinical utilization of near-infrared spectroscopy devices for burn depth assessment." Wound Repair & Regeneration **15**(3): 332.

Cullum, N., E. A. Nelson, et al. (2001). "Systematic reviews of wound care management:(5) beds;(6) compression;(7) laser therapy, therapeutic ultrasound, electrotherapy and electromagnetic therapy." Health Technol Assess **5**(9): 1-221.

Davidson, J. M. (1998). "Animal models for wound repair." Archives of Dermatological Research **290**(14): 1-11.

Diegelmann, R. and M. Evans (2004). "Wound healing: an overview of acute, fibrotic and delayed healing." Front Biosci **9**(1): 283-289.

Dorsett-Martin, W. A. (2004). "Rat models of skin wound healing: A review." Wound Repair & Regeneration **12**(6): 591.

Driver, I., J. Feather, et al. (1989). "The optical properties of aqueous suspensions of Intralipid, a fat emulsion." Physics in Medicine and Biology **34**(12): 1927-1930.

Dunsby, C. and P. M. W. French (2003). "Techniques for depth-resolved imaging through turbid media including coherence-gated imaging." J. Phys. D: Appl. Phys **36**: R207-R227.

Falanga, V. (2005). "Wound healing and its impairment in the diabetic foot." The Lancet **366**(9498): 1736-1743.

Farrell, T., M. Patterson, et al. (1992). "A diffusion theory model of spatially resolved, steady-state diffuse reflectance for the noninvasive determination of tissue optical properties in vivo." Medical physics **19**(4): 879-888.

Fauci, M. A., R. Breiter, et al. (2001). "Medical infrared imaging–differentiating facts from fiction, and the impact of high precision quantum well infrared photodetector camera systems, and other factors, in its reemergence." Infrared Physics and Technology **42**(3-5): 337-344.

Flock, S., S. Jacques, et al. (1992). "Optical properties of Intralipid: a phantom medium for light propagation studies." Lasers in Surgery and Medicine **12**(5): 510-519.

Fridolin, I., K. Hansson, et al. (2000). "Optical non-invasive technique for vessel imaging: II. A simplified photon diffusion analysis." Phys Med Biol **45**(12): 3779-3792.

Gallagher, S. and J. L. Gates (2003). "Obesity, Panniculitis, Panniculectomy, and Wound Care: Understanding the Challenges." Journal of Wound, Ostomy and Continence Nursing **30**(6): 334.

Gambichler, T., G. Moussa, et al. (2005). "Applications of optical coherence tomography in dermatology." Journal of Dermatological Science **40**(2): 85-94.

Gillies, R., J. E. Freeman, et al. (2003). "Systemic effects of shock and resuscitation monitored by visible hyperspectral imaging." Diabetes Technology & Therapeutics **5**(5): 847-855.

Goldman, R. J. and R. Salcido (2002). "More than One Way to Measure a Wound: An Overview of Tools and Techniques." Advances in Skin & Wound Care **15**(5): 236-243.

Greenman, R. L., S. Panasyuk, et al. (2005). "Early changes in the skin microcirculation and muscle metabolism of the diabetic foot." The Lancet **366**(9498): 1711-1717.

Groner, W., J. W. Winkelman, et al. (1999). "Orthogonal polarization spectral imaging: a new method for study of the microcirculation." Nature Medicine **5**: 1209-1213.

Gschwandtner, M. E., E. Ambrozy, et al. (1999). "Microcirculation in venous ulcers and the surrounding skin: findings with capillary microscopy and a laser Doppler imager." European Journal of Clinical Investigation **29**(8): 708.

Gschwandtner, M. E., E. Ambrózy, et al. (2001). "Microcirculation is similar in ischemic and venous ulcers." Microvascular Research **62**(3): 226-235.

Gschwandtner, M. E., E. Ambrózy, et al. (1999). "Laser Doppler imaging and capillary microscopy in ischemic ulcers." Atherosclerosis **142**(1): 225-232.

Hale, G. M. and M. R. Querry (1973). "Optical constants of water in the 200-nm to 200-micrometer wavelength region." Applied Optics **12**(3): 555.

Hamaoka, T., T. Katsumura, et al. (2000). "Quantification of ischemic muscle deoxygenation by near infrared time-resolved spectroscopy." Journal of Biomedical Optics **5**(1): 102-105.

Harding, J. R., D. F. Wertheim, et al. (1998). Infrared imaging in diabetic foot ulceration. Proceedings of the 20th Annual International Conference of the IEEE Engineering in Medicine and Biology Society., Hong Kong, China.

Haskell, R. C., L. O. Svaasand, et al. (1994). "Boundary conditions for the diffusion equation in radiative transfer." JOURNAL-OPTICAL SOCIETY OF AMERICA A **11**: 2727-2727.

Humeau, A., W. Steenbergen, et al. (2007). "Laser Doppler perfusion monitoring and imaging: novel approaches." Medical and Biological Engineering and Computing **45**(5): 421-435.

Jacques, S. L. and B. W. Pogue (2008). "Tutorial on diffuse light transport." Journal of Biomedical Optics **13**: 041302.

Jeffcoate, W. and K. Harding (2003). "Diabetic foot ulcers." The Lancet **361**(9368): 1545-1551.

Jessup, R. L. (2006). "What is the Best Method for Assessing the Rate of Wound Healing?: A Comparison of 3 Mathematical Formulas." Advances in skin wound care **19**(3): 138 -146.

Jones, B. F. (1998). "A reappraisal of the use of infrared thermal image analysis inmedicine." IEEE transactions on medical imaging **17**(6): 1019-1027.

Jones, B. F. and P. Plassmann (2002). "Digital infrared thermal imaging of human skin." IEEE Engineering in Medicine and Biology Magazine **21**(6): 41-48.

Jünger, M., T. Klyscz, et al. (1996). "Disturbed blood flow regulation in venous leg ulcers." Int J Microcirc **16**: 259-265.

Khan, F. and D. J. Newton (2003). "Laser Doppler Imaging in the Investigation of Lower Limb Wounds." The International Journal of Lower Extremity Wounds **2**(2): 74.

Khaodhiar, L., T. Dinh, et al. (2007). "The use of medical hyperspectral technology to evaluate microcirculatory changes in diabetic foot ulcers and to predict clinical outcomes." Diabetes care **30**(4): 903-910.

King, H. (1998). "Global burden of diabetes, 1995-2025: prevalence, numerical estimates, and projections." Diabetes care **21**(9): 1414-1431.

Kuchenreuther, S., J. Adler, et al. (1996). "The Erlanger Microlightguioe Photometer: A new concept for monitoring intracapillary oxygen supply of tissue—First results and a review of the physiological basis." Journal of Clinical Monitoring and Computing **12**(3): 211-224.

Lamorte, W. (2002). "Basics of Wound Closure and Healing." Retrieved October 20, 2010, from http://www.bumc.bu.edu/generalsurgery/technical-training/suturing-basics/.

Langer, S., F. Born, et al. (2002). "Orthogonal Polarization Spectral Imaging Versus Intravital Fluorescent Microscopy for Microvascular Studies in Wounds." Annals of plastic surgery **48**(6): 646.

Levasseur, M., L. Leonardi, et al. (2005). "Near infrared hyperspectral imaging: the road traveled to a clinical burn application." Proc. SPIE **5969**: 59691O59691-59699.

Li, X. (1998). Fluorescence and diffusive wave diffraction tomographic probes in turbid media, Ph.D. Thesis, University of Pennsylvania.

Loots, M., S. Kenter, et al. (2002). "Fibroblasts derived from chronic diabetic ulcers differ in their response to stimulation with EGF, IGF-I, bFGF and PDGF-AB compared to controls." European journal of cell biology **81**(3): 153-160.

Loots, M. A. M., E. N. Lamme, et al. (1998). "Differences in Cellular Infiltrate and Extracellular Matrix of Chronic Diabetic and Venous Ulcers Versus Acute Wounds." Journal of Investigative Dermatology **111**(5): 850-857.

Margolis, D. J., L. Allen-Taylor, et al. (2002). "Diabetic Neuropathic Foot Ulcers: The association of wound size, wound duration, and wound grade on healing." Diabetes Care **25**(10): 1835.

Martin, P. (1997). "Wound healing--aiming for perfect skin regeneration." Science **276**(5309): 75-81.

Martinez, L. (2002). A Non-Invasive Spectral Reflectance Method for Mapping Blood Oxygen Saturation in Wounds. Proceedings of the 31st Applied Imagery Pattern Recognition Workshop.

Meaume, S., D. Couilliet, et al. (2005). "Prognostic factors for venous ulcer healing in a non-selected population of ambulatory patients." Journal of wound care **14**(1): 31-34.

Milner, S. M., S. Bhat, et al. (2005). "Observations on the microcirculation of the human burn wound using orthogonal polarization spectral imaging." Burns **31**(3): 316-319.

Mlacak, B., A. Blinc, et al. (2005). "Microcirculation disturbances in patients with venous ulcer before and after healing as assessed by laser Doppler flux-metry." Archives of medical research **36**(5): 480-484.

Mobley, J. and T. Vo-Dinh (2003). Optical properties of tissue. Biomedical Photonics Handbook. T. Vo-Dinh, CRC Press**:** 1-75.

Mogford, J. E. and T. A. Mustoe (2001). "Experimental models of wound healing." Cutaneous wound healing. London: Martin Dunitz: 109-122.

Mourant, J. R. and I. J. Bigio (2003). Elastic-scattering spectroscopy and diffuse reflectance. Biomedical Photonics Handbook. T. Vo-Dinh, CRC Press.

Mourant, J. R., T. Fuselier, et al. (1997). "Predictions and measurements of scattering and absorption over broad wavelength ranges in tissue phantoms." Applied Optics **36**(4): 949-957.

Muncaster, D. (2001). "The physiology of wound healing and wound assessment." British journal of perioperative nursing: the journal of the National Association of Theatre Nurses **11**(8): 362-370.

Mustoe, T. (March 17-18, 2005). Dermal ulcer healing: Advances in understanding. Tissue repair and ulcer/wound healing: molecular mechanisms, therapeutic targets and future directions, Paris, France.

Mustoe, T. A., K. O'Shaughnessy, et al. (2006). "Chronic Wound Pathogenesis and Current Treatment Strategies: A Unifying Hypothesis." Plastic and Reconstructive Surgery **117**(7S): 35S.

Nabuurs-Franssen, M. H., M. S. P. Huijberts, et al. (2005). "Health-related quality of life of diabetic foot ulcer patients and their caregivers." Diabetologia **48**(9): 1906-1910.

Nelzen, O. (2000). "Leg ulcers: Economic aspects." Phlebology **15**(3-4): 110-114.

Newman, P. and N. H. Davis (1981). "Thermography as a predictor of sacral pressure sores." Age and Ageing **10**(1): 14-18.

Newton, D., G. Leese, et al. (2001). "Microvascular abnormalities in diabetic foot ulcers." The Diabetic Foot **4**(3): 141-146.

Oh, J. T., S. W. Lee, et al. (2006). "Quantification of the wound healing using polarization-sensitive optical coherence tomography." Journal of Biomedical Optics **11**: 041124.

Papazoglou, E. S., M.S. Weingarten, L. Zubkov, M. Neidrauer, L. Zhu, S. Tyagi, K. Pourrezaei (2008). "Changes in optical properties of tissue during acute wound healing in an animal model." Journal of Biomedical Optics **13**(4): In Press.

Papazoglou, E. S., M. S. Weingarten, et al. (2008). "Changes in optical properties of tissue during acute wound healing in an animal model." Journal of Biomedical Optics **13**: 044005.

Papazoglou, E. S., M. S. Weingarten, et al. (2006). "Optical properties of wounds: diabetic versus healthy tissue." IEEE Transactions on Biomedical Engineering **53**(6): 1047-1055.

Papazoglou, E. S., M. S. Weingarten, et al. (2006). "Optical properties of wounds: diabetic versus healthy tissue." IEEE Trans Biomed Eng **53**(6): 1047-1055.

Park, B. H., C. Saxer, et al. (2001). "In vivo burn depth determination by high-speed fiber-based polarization sensitive optical coherence tomography." Journal of Biomedical Optics **6**: 474.

Payette, J. R., E. Kohlenberg, et al. (2005). "Assessment of Skin Flaps Using Optically Based Methods for Measuring Blood Flow and Oxygenation." Plastic and Reconstructive Surgery **115**(2): 539.

Pham, T. H., O. Coquoz, et al. (2000). "Broad bandwidth frequency domain instrument for quantitative tissue optical spectroscopy." Review of Scientific Instruments **71**: 2500.

Pierce, M. C., R. L. Sheridan, et al. (2004). "Collagen denaturation can be quantified in burned human skin using polarization-sensitive optical coherence tomography." Burns **30**(6): 511-517.

Prahl, S. (1999). "Optical absorption of hemoglobin." Oregon Medical Laser Center, Portland, Oreg Retrieved May 15, 2009, from http://omlc.ogi.edu/spectra/hemoglobin/index.html.

Prahl, S. (1999). "Optical absorption of hemoglobin." see http://omlc.ogi.edu/spectra/hemoglobin/, Oregon Medical Laser Center.

Querry, M. R., P. G. Cary, et al. (1978). "Split-pulse laser method for measuring attenuation coefficients of transparent liquids: application to deionized filtered water in the visible region." Applied Optics **17**(22): 3587-3592.

Rajan, V., B. Varghese, et al. (2009). "Review of methodological developments in laser Doppler flowmetry." Lasers in Medical Science **24**(2): 269-283.

Rajbhandari, S. M. (1999). "Early identification of diabetic foot ulcers that may require intervention using the micro lightguide spectrophotometer." Diabetes care **22**(8): 1292-1295.

Reiber, G. E., B. A. Lipsky, et al. (1998). "The burden of diabetic foot ulcers." Am J Surg **176**(2A Suppl): 5S-10S.

Samson, D. J., F. Lefevre, et al. (2004). Wound-healing Technologies: Low-level Laser and Vacuum-assisted Closure. Evidence Report/Technology Assessment No. 111. (Prepared by the Blue Cross and Blue Shield Association Technology Evaluation Center Evidence-based Practice Center, under Contract No. 290-02-0026) Agency for Healthcare Research and Quality, Rockville, MD.

Sayre, E. K., T. J. Kelechi, et al. (2007). "Sudden increase in skin temperature predicts venous ulcers: A case study." Journal of Vascular Nursing **25**(3): 46-50.

Schmidt, W. D., K. Liebold, et al. (2001). "Contact-Free Spectroscopy of Leg Ulcers: Principle, Technique, and Calculation of Spectroscopic Wound Scores." Journal of Investigative Dermatology **116**: 531-535.

Schmitt, J. M. (1999). "Optical coherence tomography (OCT): a review." IEEE Journal of selected topics in quantum electronics **5**(4): 1205-1215.

Schutz, S. (2001). "Oxygen saturation monitoring by pulse oximetry." AACN procedure manual for critical care **Chapter 14**: 77-82.

Shah, N., A. E. Cerussi, et al. (2004). "Spatial variations in optical and physiological properties of healthy breast tissue." Journal of Biomedical Optics **9**: 534-540.

Sibbald, R. G., H. L. Orsted, et al. (2007). "Best Practice Recommendations for Preparing the Wound Bed: Update 2006." Advances in Skin & Wound Care **20**(7): 390-405.

Silverthorn, D., W. Ober, et al. (2004). Human physiology: an integrated approach, Pearson/Benjamin Cummings.

Singer, A. J. and R. A. F. Clark (1999). "Cutaneous wound healing." New England journal of medicine **341**(10): 738-746.

Singer, A. J., Z. Wang, et al. (2007). "Optical coherence tomography: a noninvasive method to assess wound reepithelialization." Academic Emergency Medicine **14**(5): 387-391.

Singh, N., D. G. Armstrong, et al. (2005). Preventing Foot Ulcers in Patients With Diabetes, Am Med Assoc. **293:** 217-228.

Skyler, J. S. and C. Oddo (2002). "Diabetes trends in the USA." Diabetes Metab Res Rev **18**(3): S21-26.

Sowa, M., A. Matas, et al. (2002). "Spectroscopic assessment of cutaneous hemodynamics in the presence of high epidermal melanin concentration." Clinica Chimica Acta **317**(1-2): 203-212.

Sowa, M. G., L. Leonardi, et al. (2001). "Near infrared spectroscopic assessment of hemodynamic changes in the early post-burn period." Burns **27**(3): 241-249.

Srinivas, S. M., J. F. de Boer, et al. (2004). "Determination of burn depth by polarization-sensitive optical coherence tomography." Journal of Biomedical Optics **9**: 207.

Stamatas, G. N. and N. Kollias (2007). "In vivo documentation of cutaneous inflammation using spectral imaging." Journal of Biomedical Optics **12**: 051603.

Stamatas, G. N., B. Z. Zmudzka, et al. (2004). "Non-Invasive Measurements of Skin Pigmentation In Situ." Pigment Cell Research **17**(6): 618.

Svensson, T., S. Andersson-Engels, et al. (2007). "In vivo optical characterization of human prostate tissue using near-infrared time-resolved spectroscopy." Journal of Biomedical Optics **12**: 014022.

Timar-Banu, O., H. Beauregard, et al. (2001). "DEVELOPMENT OF NONINVASIVE AND QUANTITATIVE METHODOLOGIES FOR THE ASSESSMENT OF CHRONIC ULCERS AND SCARS IN HUMANS." Wound Repair and Regeneration **9**(2): 123-132.

Ueno, C., T. Hunt, et al. (2006). "Using physiology to improve surgical wound outcomes." Plastic and Reconstructive Surgery **117**(7S): 59S-71S.

Van Staveren, H., C. Moes, et al. (1991). "Light scattering in Intralipid-10% in the wavelength range of 400–1100 nm." Appl. Opt **30**(31): 4507–4514.

Verhonick, P. J., D. W. Lewis, et al. (1972). "Thermography in the study of decubitus ulcers: preliminary report." Nursing Research **21**(3): 233.

Veves, A., C. M. Akbari, et al. (1998). "Endothelial dysfunction and the expression of endothelial nitric oxide synthetase in diabetic neuropathy, vascular disease, and foot ulceration." Diabetes **47**(3): 457.

Virgini-Magalhães, C. E., C. L. Porto, et al. (2006). "Use of microcirculatory parameters to evaluate chronic venous insufficiency." Journal of Vascular Surgery **43**(5): 1037-1044.

Vo-Dinh, T. (2003). Biomedical Photonics, CRC Press, Boca Raton.

Vo-Dinh, T. (2004). "A hyperspectral imaging system for in vivo optical diagnostics." IEEE Engineering in Medicine and Biology Magazine **23**(5): 40-49.

Wang, Z., H. Pan, et al. (2008). "Assessment of dermal wound repair after collagen implantation with optical coherence tomography." Tissue Engineering Part C: Methods **14**(1): 35-45.

Weingarten, M., E. Papazoglou, et al. (2008). "Correlation of near infrared absorption and diffuse reflectance spectroscopy scattering with tissue neovascularization and collagen concentration in a diabetic rat wound healing model." Wound Repair and Regeneration **16**(2): 234-242.

Weiss, G. H., R. Nossal, et al. (1989). "Statistics of Penetration Depth of Photons Re-emitted from Irradiated Tissue." Journal of Modern Optics **36**(3): 349-359.

Wilson, J. A. and J. J. Clark (2003). "Obesity: Impediment to Wound Healing." Critical Care Nursing Quarterly **26**(2): 119-132.

Wilson, J. A. and J. J. Clark (2004). "Obesity: Impediment to Postsurgical Wound Healing." Advances in Skin & Wound Care **17**(8): 426.

Wolff, K., A. Kolberg, et al. (1998). "Cutaneous hemoglobin oxygenation of different free flap donor sites." Plastic and Reconstructive Surgery **102**(5): 1537-1543.

Wollina, U., K. Liebold, et al. (2002). "Biosurgery supports granulation and debridement in chronic wounds-clinical data and remittance spectroscopy measurement." International journal of dermatology **41**(10): 635.

Yeong, E. K., T. C. Hsiao, et al. (2005). "Prediction of burn healing time using artificial neural networks and reflectance spectrometer." Burns **31**(4): 415-420.

Yu, G., T. Durduran, et al. (2005). "Time-dependent blood flow and oxygenation in human skeletal muscles measured with noninvasive near-infrared diffuse optical spectroscopies." Journal of Biomedical Optics **10**(2): 24027-24027.

Zhu, L. C. (2008). Non-invasive optical technologies to monitor wound healing, Drexel University. **Ph.D. Thesis**.

Zuzak, K. J., T. J. Perumanoor, et al. (2007). A Multimodal Reflectance Hyperspectral Imaging System for Monitoring Wound Healing in Below Knee Amputations. IEEE Engineering in Medicine and Biology Workshop, Dallas, TX.

# APPENDIX A: OPTICAL DATA FROM ALL HUMAN DIABETIC FOOT ULCERS

In this section, optical data are shown for all 28 of the human diabetic foot ulcers described in Chapter 6. The data are divided into two figures per wound: (1) wound photographs, wound sizes, oxygen saturation, total, oxy-, and deoxy-hemoglobin concentrations are given in the first figure for each wound, while (2) optical absorption and optical scattering coefficients are given in the second figure for each wound. The 14 wound that were classified as “Healing” are given first (Figure 45 through Figure 72) and the 14 “Non-Healing” wounds are shown in Figure 73 through Figure 100.

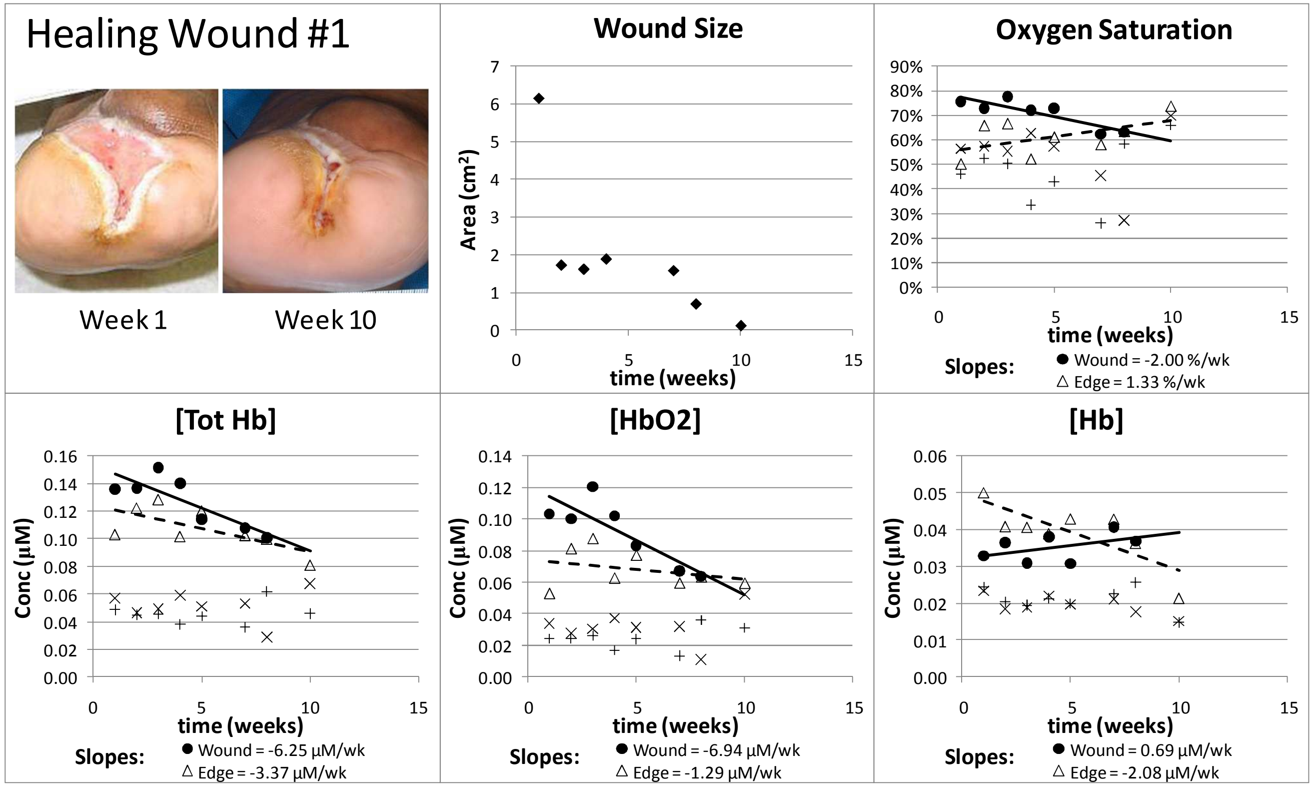

**Figure 45: Healing Wound #1 - Wound size and hemoglobin data. Location: Transmetatarsal amputation site. Outcome: Wound healed week 10. *Upper left:* Digital photographs from selected time points. *Upper center:* Wound area as determined through analysis of digital photographs (♦). *Upper right*: Oxygen Saturation from each measurement day. *Lower:* Total hemoglobin concentration [*Tot Hb*], oxyhemoglobin concentration [*HbO$_2$*], and deoxyhemoglobin concentration [*Hb*] from each measurement day. Each data point represents the mean of measurements obtained from the center of the wound (●), the edges of the wound (Δ), a control site on the non-wounded foot (+), and a control site on the wounded foot (x). Solid lines are the linear trendlines associated with data obtained from the wound centers; dashed lines are the linear trendlines associated with data obtained from the wound edges.**

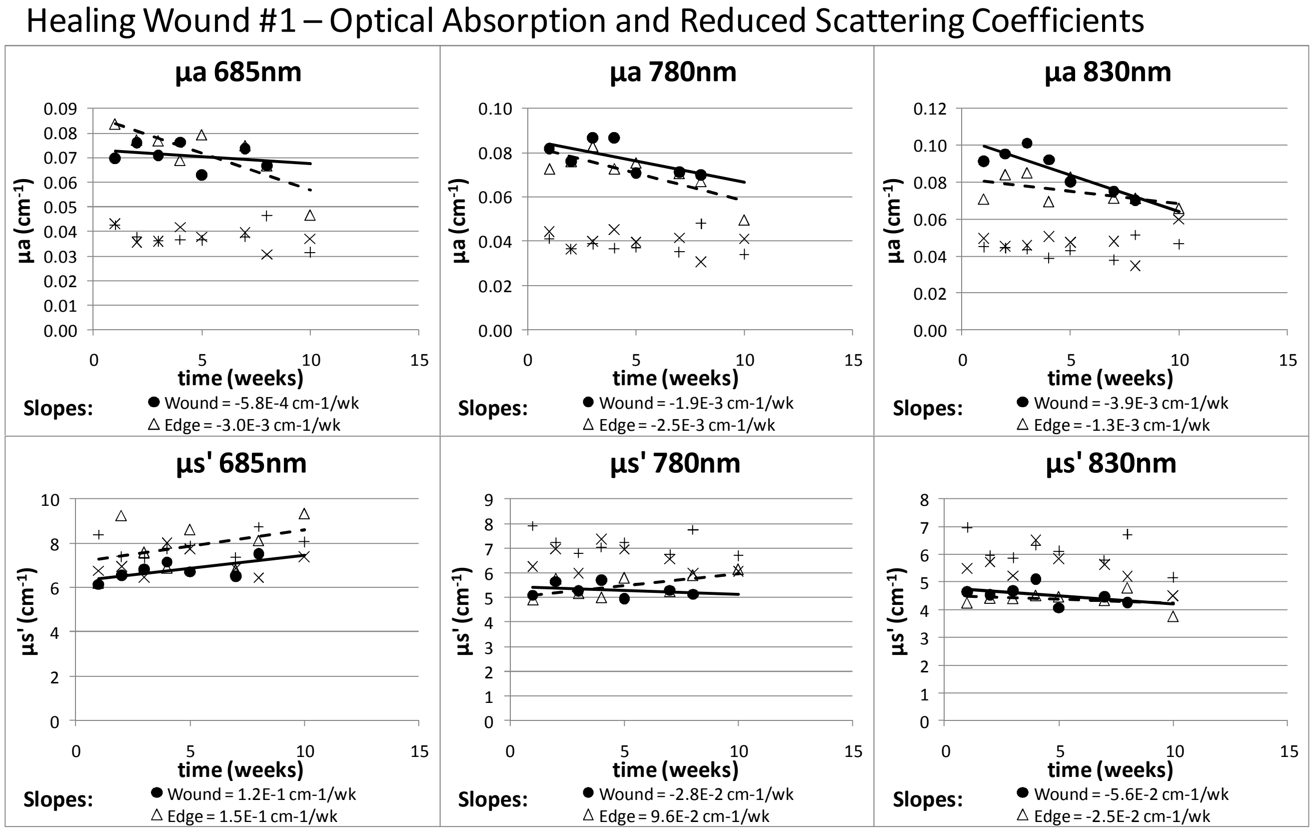

**Figure 46: Healing Wound #1 - Optical aborption (μa) and reduced scattering coefficients (μs’). Location: Transmetatarsal amputation site. Outcome: Wound healed week 10. Each data point represents the mean of measurements obtained on each measurement day from the center of the wound (●), the edges of the wound (Δ), a control site on the non-wounded foot (+), and a control site on the wounded foot (x). Solid lines are the linear trendlines associated with data obtained from the wound centers; dashed lines are the linear trendlines associated with data obtained from the wound edges.**

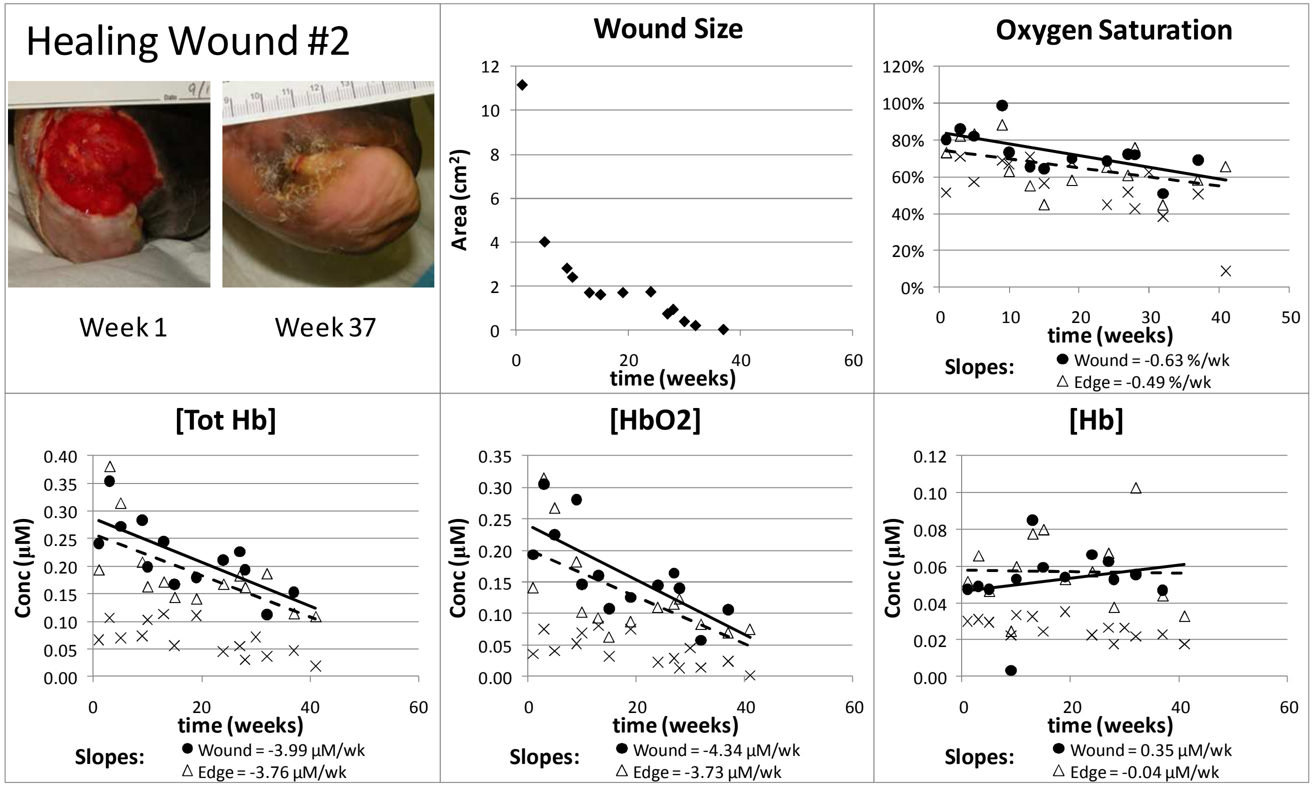

**Figure 47: Healing Wound #2 - Wound size and hemoglobin data. Location: Transmetatarsal amputation site. Outcome: Wound healed week 37.** ***Upper left:*** **Digital photographs from selected time points.** ***Upper center:*** **Wound area as determined through analysis of digital photographs (♦).** ***Upper right*****: Oxygen Saturation from each measurement day.** ***Lower:*** **Total hemoglobin concentration [*****Tot Hb*****], oxyhemoglobin concentration [*****HbO*****$_2$], and deoxyhemoglobin concentration [*****Hb*****] from each measurement day. Each data point represents the mean of measurements obtained from the center of the wound (●), the edges of the wound (Δ), and a control site on the wounded foot (x). Solid lines are the linear trendlines associated with data obtained from the wound centers; dashed lines are the linear trendlines associated with data obtained from the wound edges.**

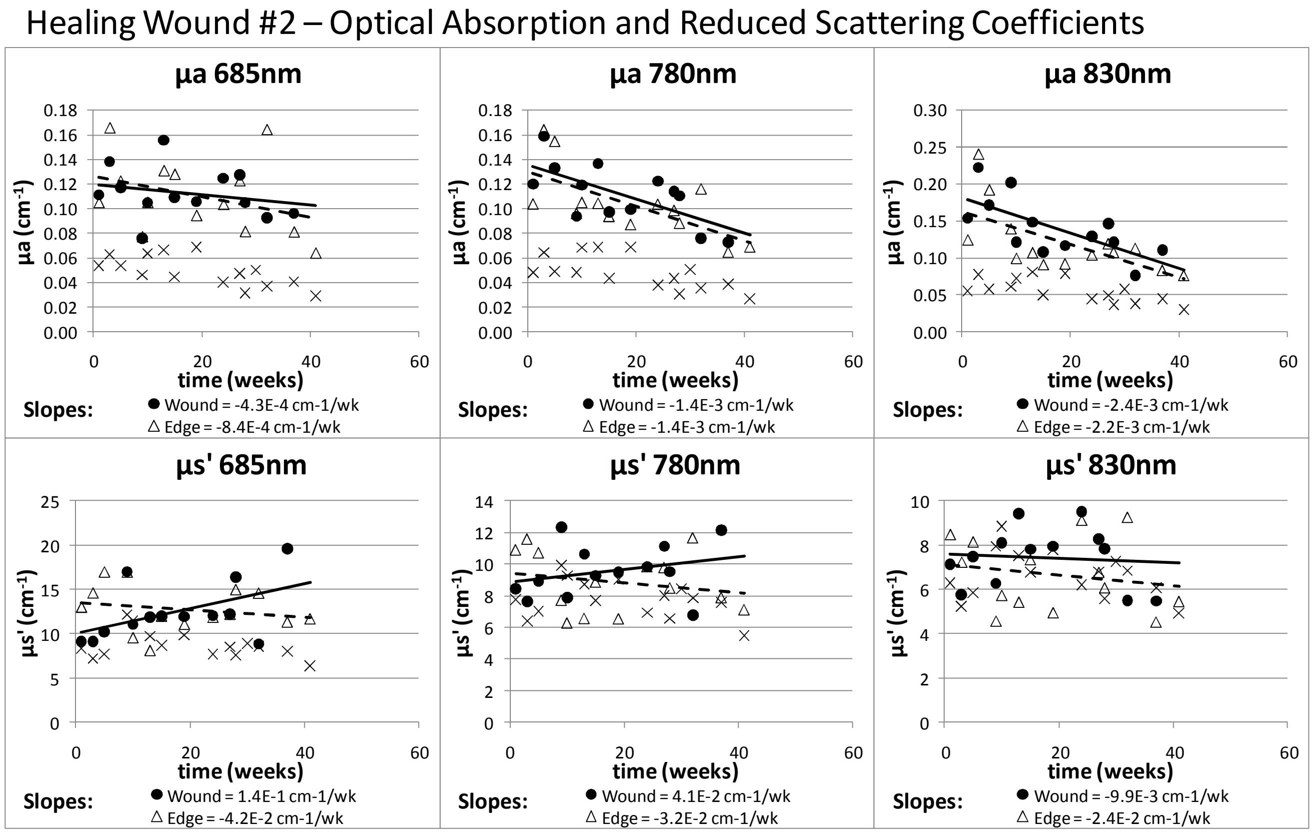

**Figure 48: Healing Wound #1 - Optical aborption (µa) and reduced scattering coefficients (µs'). Location: Transmetatarsal amputation site. Outcome: Wound healed week 37. Each data point represents the mean of measurements obtained on each measurement day from the center of the wound (●), the edges of the wound (Δ), and a control site on the wounded foot (x). Solid lines are the linear trendlines associated with data obtained from the wound centers; dashed lines are the linear trendlines associated with data obtained from the wound edges.**

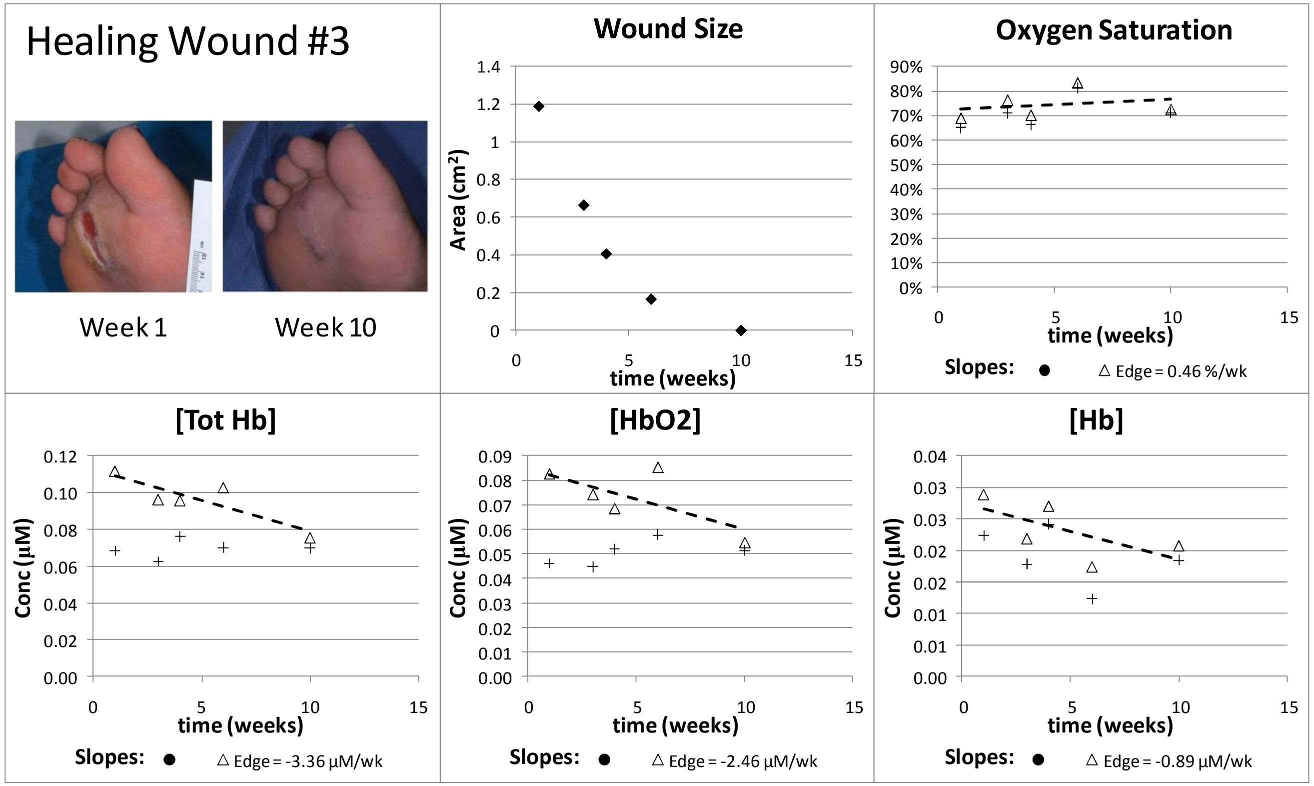

**Figure 49: Healing Wound #3 - Wound size and hemoglobin data. Location: Plantar surface. Outcome: Wound healed week 10. *Upper left:* Digital photographs from selected time points. *Upper center:* Wound area as determined through analysis of digital photographs (♦). *Upper right*: Oxygen Saturation from each measurement day. *Lower:* Total hemoglobin concentration [*Tot Hb*], oxyhemoglobin concentration [$HbO_2$], and deoxyhemoglobin concentration [*Hb*] from each measurement day. Each data point represents the mean of measurements obtained from the edges of the wound (Δ), and a control site on the non-wounded foot (+). Measurements could not be obtained from the wound center due to the size and geometry of the wound. Dashed lines are the linear trendlines associated with data obtained from the wound edges.**

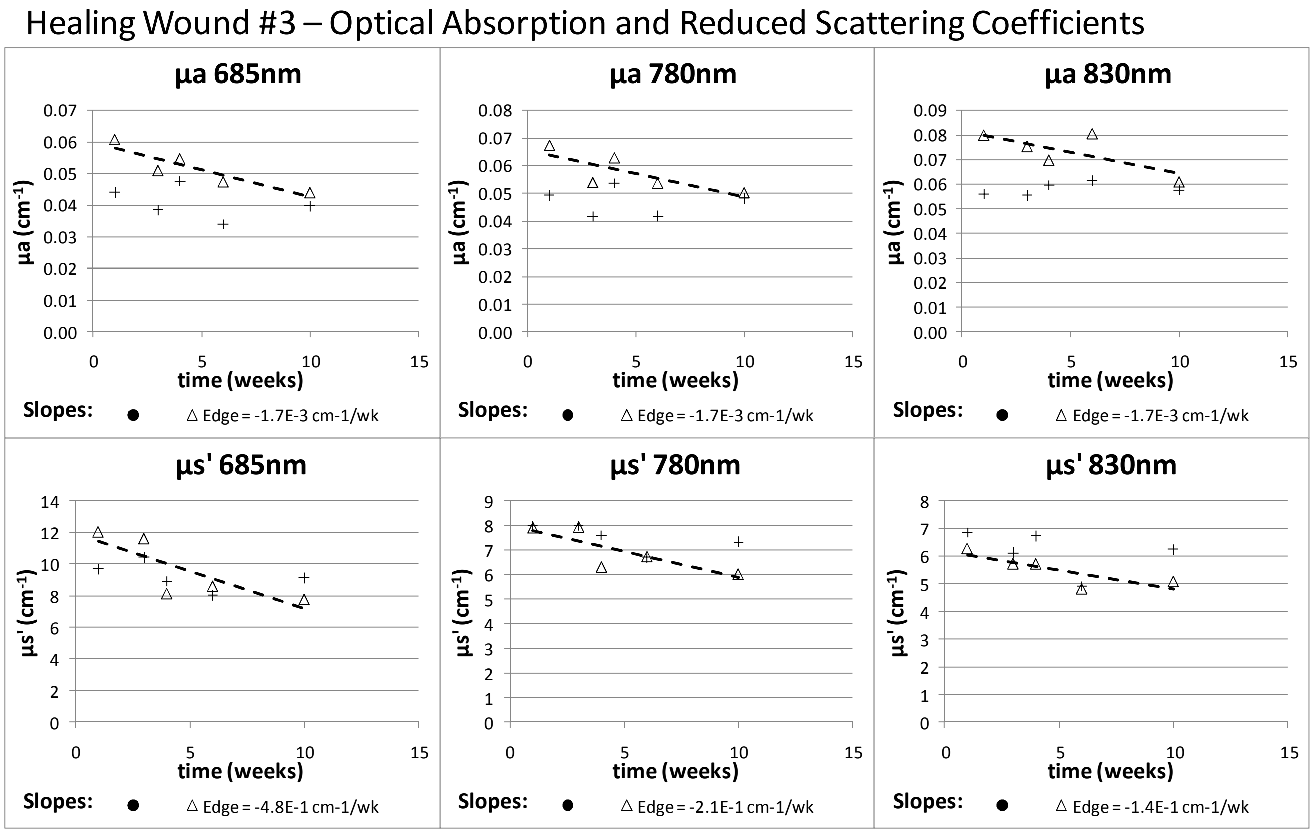

**Figure 50: Healing Wound #3 - Optical aborption (µa) and reduced scattering coefficients (µs'). Location: plantar surface. Outcome: Wound healed week 10. Each data point represents the mean of measurements obtained on each measurement day from the edges of the wound (Δ), and a control site on the non-wounded foot (+). Measurements could not be obtained from the wound center due to the size and geometry of the wound. Dashed lines are the linear trendlines associated with data obtained from the wound edges.**

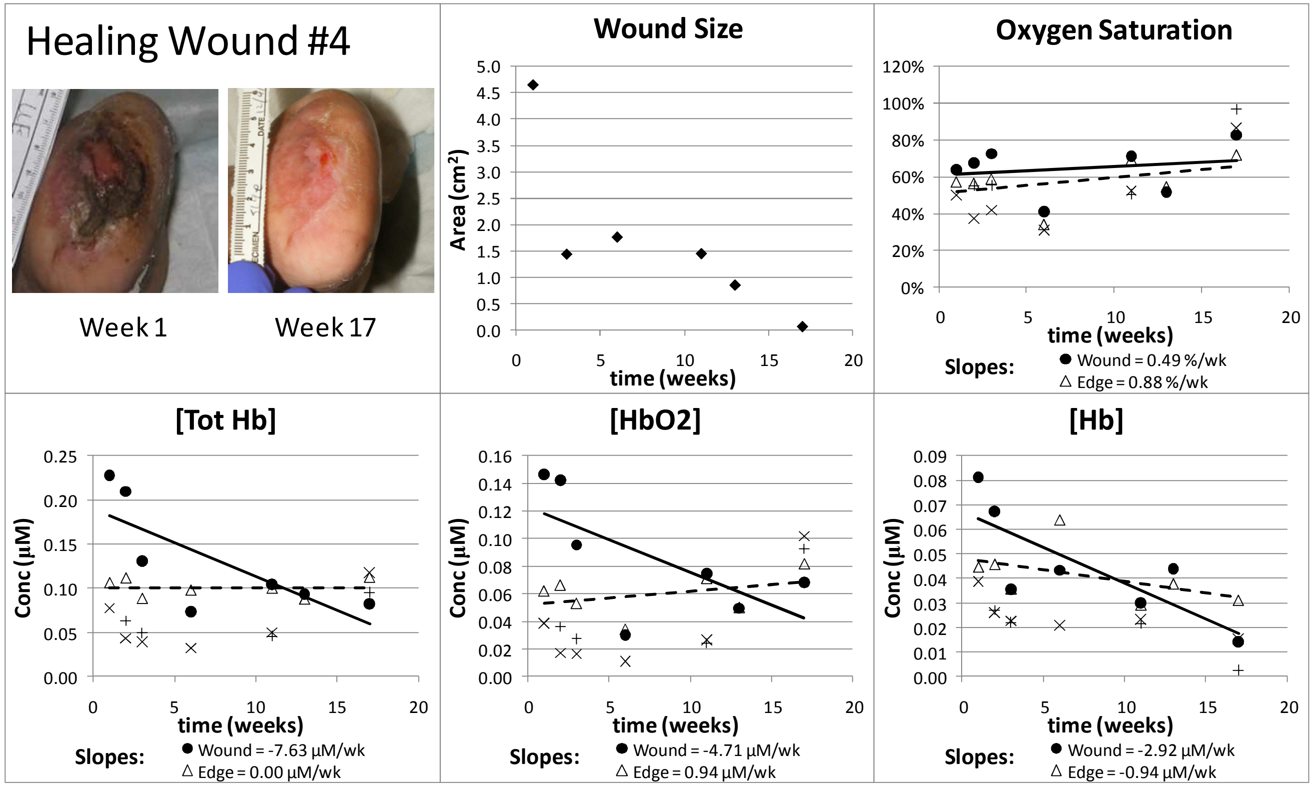

**Figure 51: Healing Wound #4 - Wound size and hemoglobin data. Location: Transmetatarsal amputation site. Outcome: Wound healed week 17.** ***Upper left:*** **Digital photographs from selected time points.** ***Upper center:*** **Wound area as determined through analysis of digital photographs (♦).** ***Upper right*****: Oxygen Saturation from each measurement day.** ***Lower:*** **Total hemoglobin concentration [*Tot Hb*], oxyhemoglobin concentration [*HbO$_2$*], and deoxyhemoglobin concentration [*Hb*] from each measurement day. Each data point represents the mean of measurements obtained from the center of the wound (●), the edges of the wound (Δ), a control site on the non-wounded foot (+), and a control site on the wounded foot (x). Solid lines are the linear trendlines associated with data obtained from the wound centers; dashed lines are the linear trendlines associated with data obtained from the wound edges.**

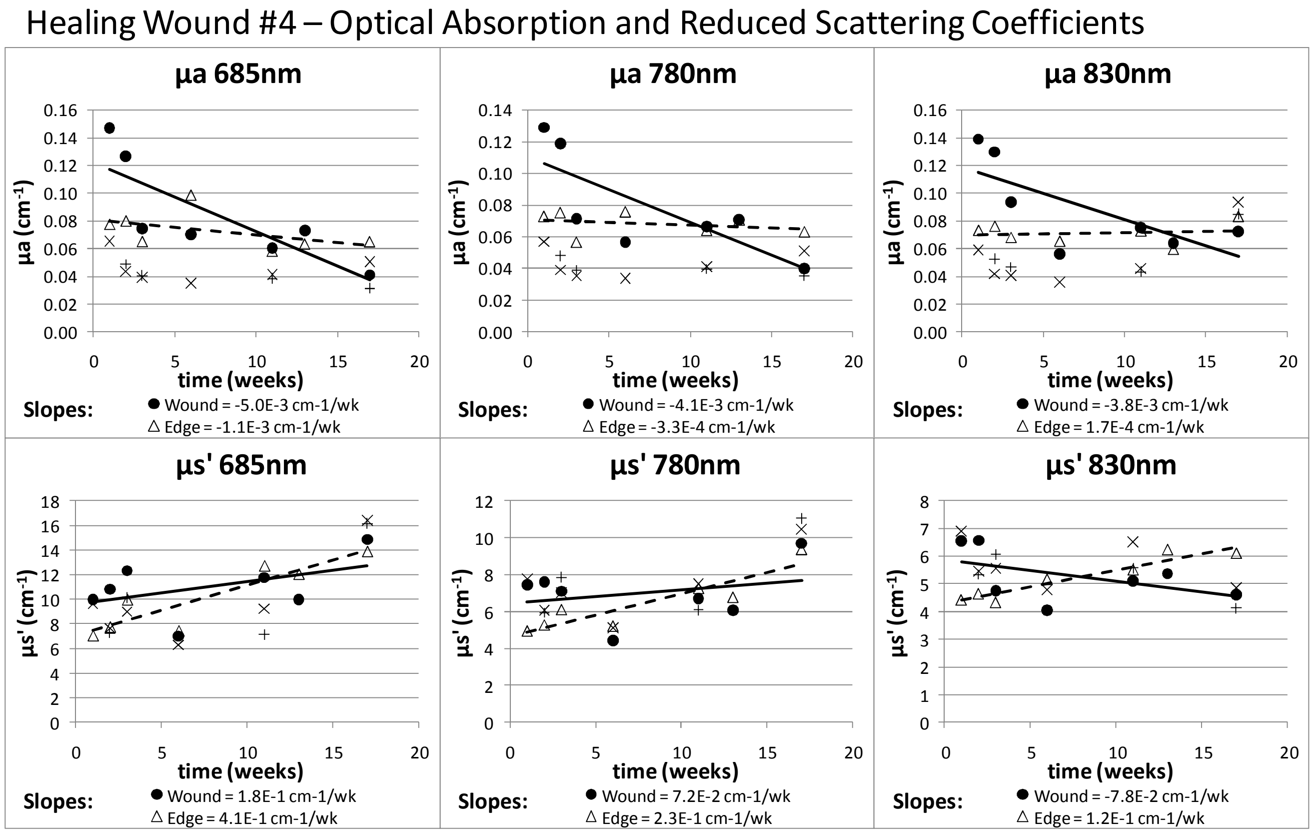

**Figure 52: Healing Wound #4 - Optical aborption (µa) and reduced scattering coefficients (µs'). Location: Transmetatarsal amputation site. Outcome: Wound healed week 17. Each data point represents the mean of measurements obtained on each measurement day from the center of the wound (●), the edges of the wound (Δ), a control site on the non-wounded foot (+), and a control site on the wounded foot (x). Solid lines are the linear trendlines associated with data obtained from the wound centers; dashed lines are the linear trendlines associated with data obtained from the wound edges.**

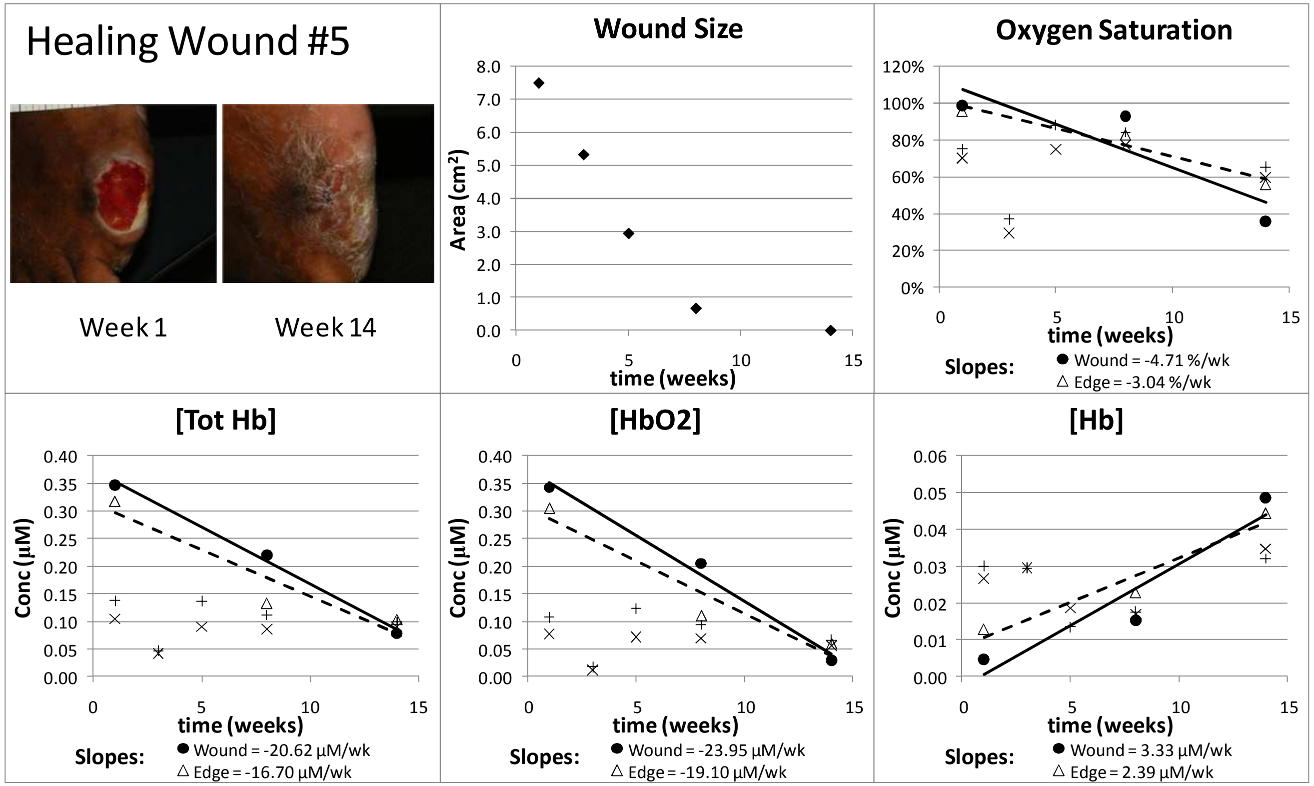

**Figure 53: Healing Wound #5 - Wound size and hemoglobin data. Location: Fifth toe amputation site. Outcome: Wound healed week 14. *Upper left:* Digital photographs from selected time points. *Upper center:* Wound area as determined through analysis of digital photographs (♦). *Upper right*: Oxygen Saturation from each measurement day. *Lower:* Total hemoglobin concentration [*Tot Hb*], oxyhemoglobin concentration [*HbO$_2$*], and deoxyhemoglobin concentration [*Hb*] from each measurement day. Each data point represents the mean of measurements obtained from the center of the wound (●), the edges of the wound (Δ), a control site on the non-wounded foot (+), and a control site on the wounded foot (x). Solid lines are the linear trendlines associated with data obtained from the wound centers; dashed lines are the linear trendlines associated with data obtained from the wound edges.**

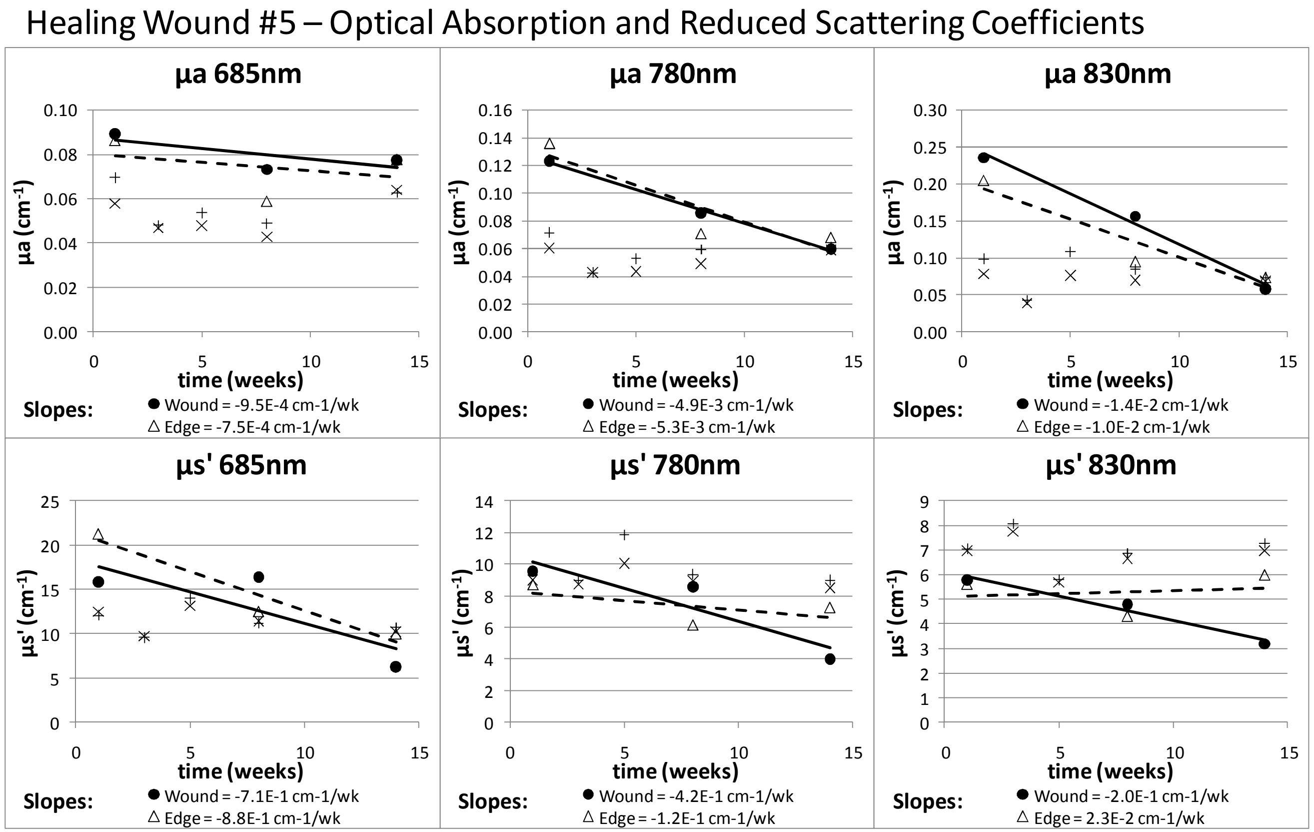

**Figure 54: Healing Wound #5 - Optical aborption (µa) and reduced scattering coefficients (µs'). Location: Fifth toe amputation site. Outcome: Wound healed week 14. Each data point represents the mean of measurements obtained on each measurement day from the center of the wound (●), the edges of the wound (Δ), a control site on the non-wounded foot (+), and a control site on the wounded foot (x). Solid lines are the linear trendlines associated with data obtained from the wound centers; dashed lines are the linear trendlines associated with data obtained from the wound edges.**

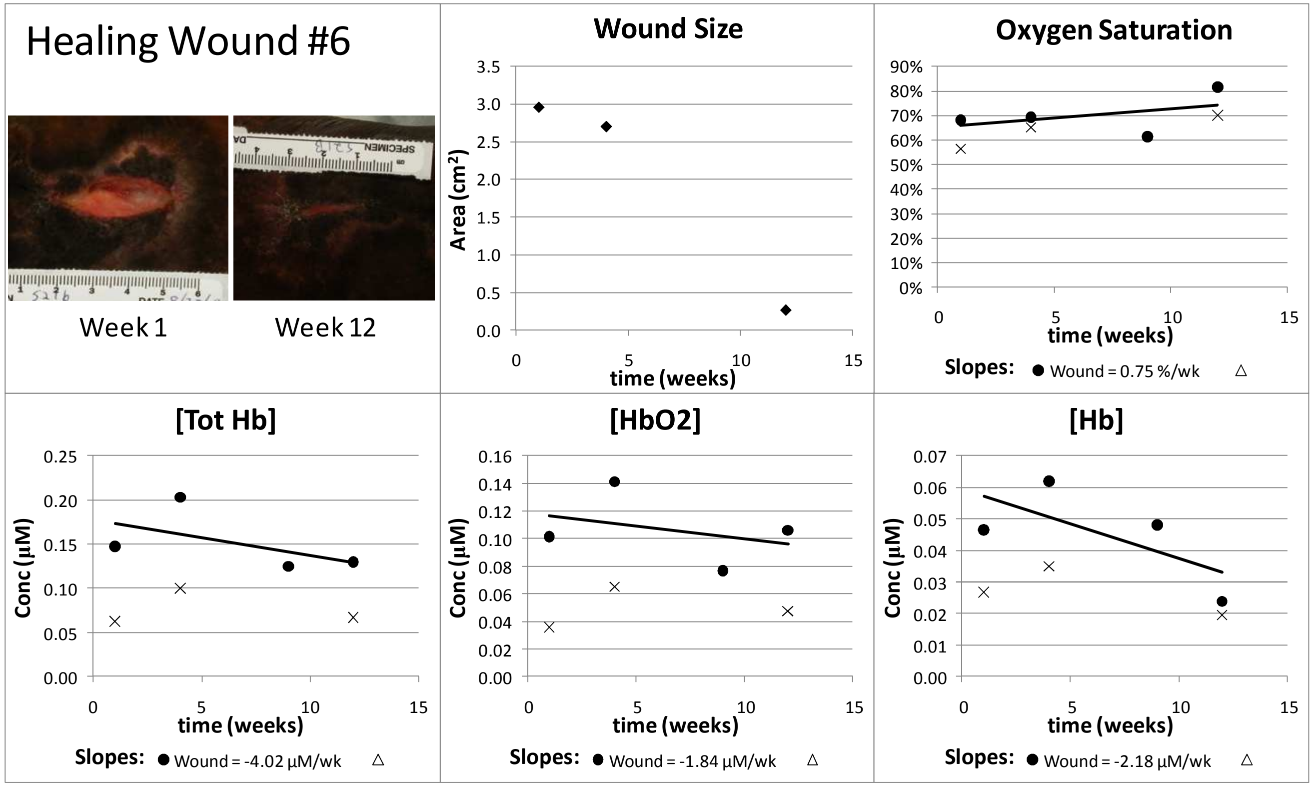

**Figure 55: Healing Wound #6 - Wound size and hemoglobin data. Location: Lateral aspect of ankle. Outcome: Wound healed week 12.** ***Upper left:*** **Digital photographs from selected time points.** ***Upper center:*** **Wound area as determined through analysis of digital photographs (♦).** ***Upper right*****: Oxygen Saturation from each measurement day.** ***Lower:*** **Total hemoglobin concentration [*****Tot Hb*****], oxyhemoglobin concentration [*****$HbO_2$*****], and deoxyhemoglobin concentration [*****Hb*****] from each measurement day. Each data point represents the mean of measurements obtained from the center of the wound (●), and a control site on the wounded foot (x). Measurements could not be obtained at the edges of the wound because of hyperpigmentation. The signal intensity was too low. Solid lines are the linear trendlines associated with data obtained from the wound centers.**

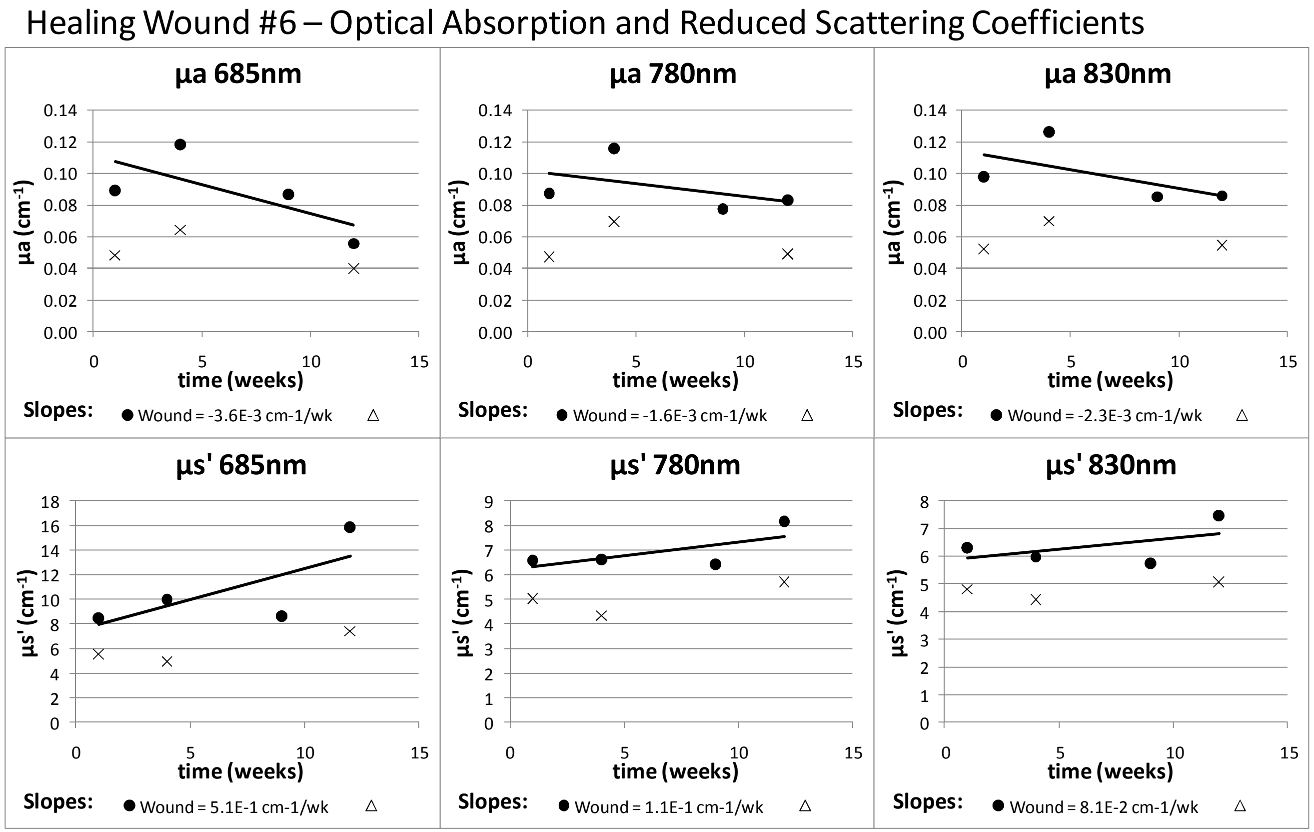

**Figure 56: Healing Wound #6 - Optical aborption (µa) and reduced scattering coefficients (µs').  Location: lateral aspect of ankle.  Outcome: Wound healed week 12.  Each data point represents the mean of measurements obtained on each measurement day from the center of the wound (●), and a control site on the wounded foot (x).  Measurements could not be obtained at the edges of the wound because of hyperpigmentation.  The signal intensity was too low.   Solid lines are the linear trendlines associated with data obtained from the wound centers.**

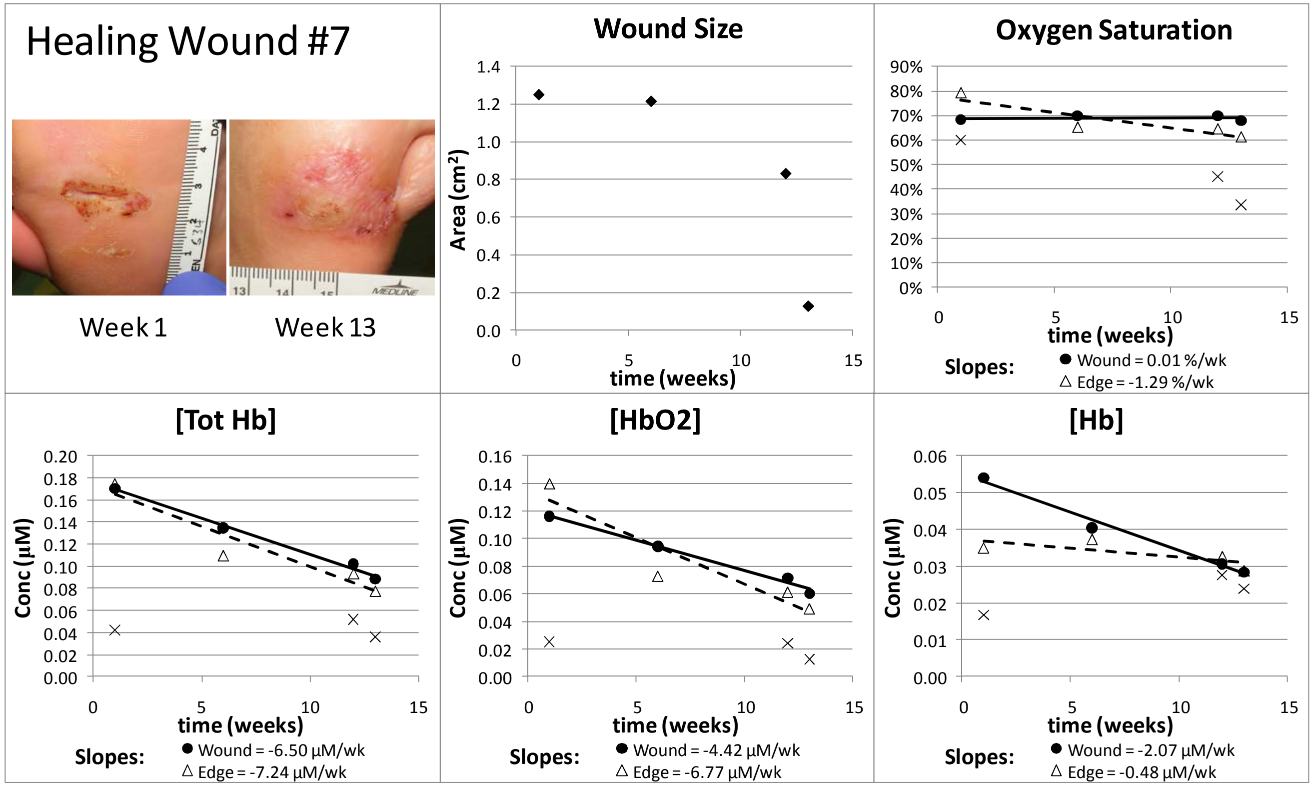

**Figure 57: Healing Wound #7 - Wound size and hemoglobin data. Location: Plantar surface. Outcome: Wound healed week 13. *Upper left:* Digital photographs from selected time points. *Upper center:* Wound area as determined through analysis of digital photographs (♦). *Upper right*: Oxygen Saturation from each measurement day. *Lower:* Total hemoglobin concentration [*Tot Hb*], oxyhemoglobin concentration [*HbO$_2$*], and deoxyhemoglobin concentration [*Hb*] from each measurement day. Each data point represents the mean of measurements obtained from the center of the wound (●), the edges of the wound (Δ), and a control site on the wounded foot (x). Solid lines are the linear trendlines associated with data obtained from the wound centers; dashed lines are the linear trendlines associated with data obtained from the wound edges.**

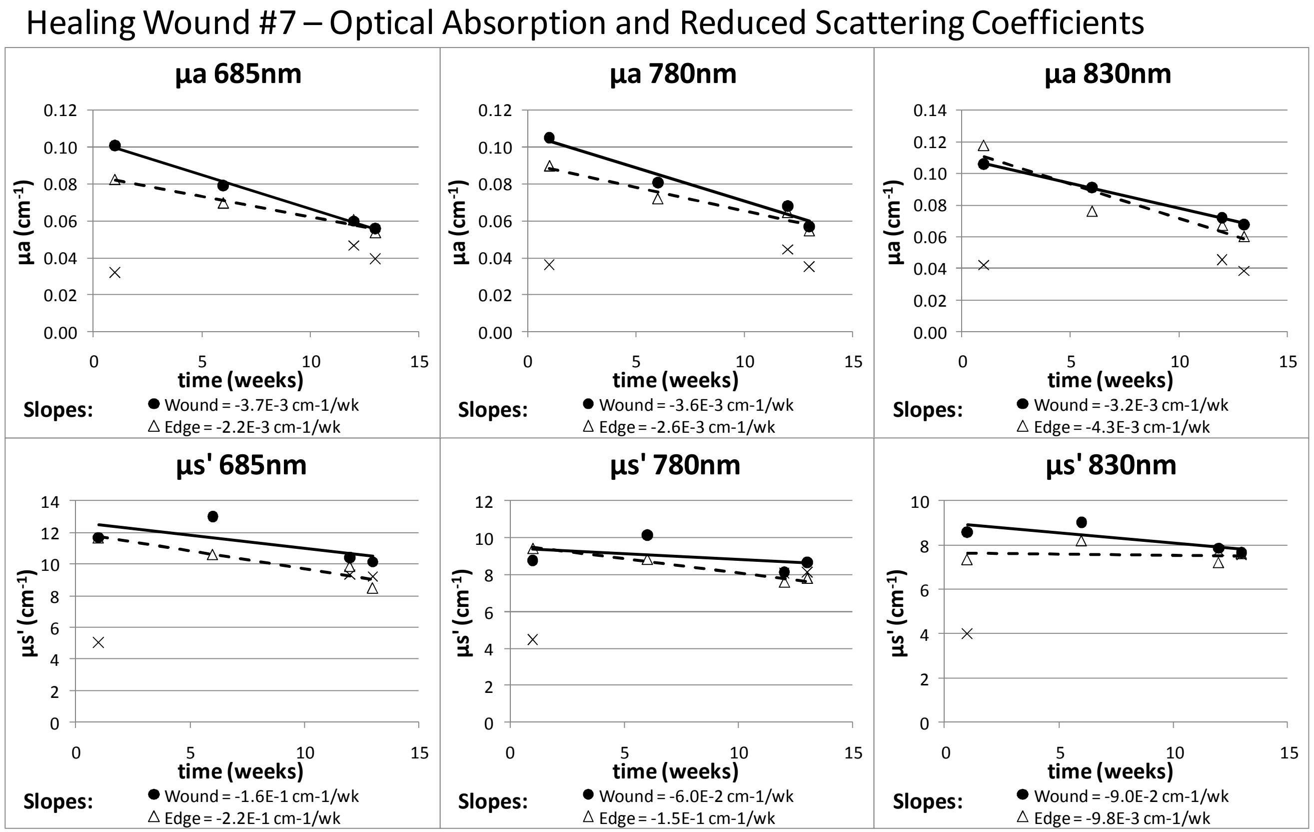

**Figure 58: Healing Wound #7 - Optical aborption (µa) and reduced scattering coefficients (µs'). Location: plantar surface. Outcome: Wound healed week 13. Each data point represents the mean of measurements obtained on each measurement day from the center of the wound (●), the edges of the wound (Δ), and a control site on the wounded foot (x). Solid lines are the linear trendlines associated with data obtained from the wound centers; dashed lines are the linear trendlines associated with data obtained from the wound edges.**

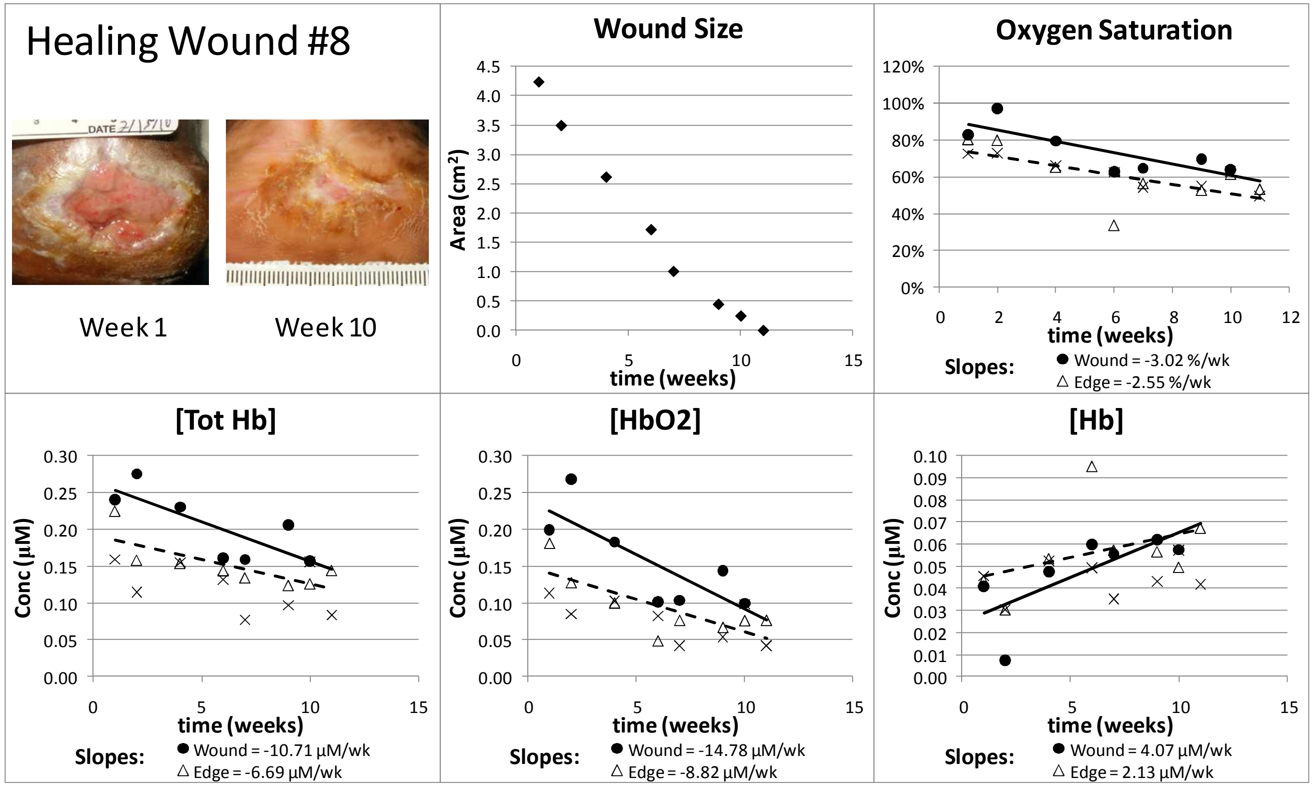

**Figure 59: Healing Wound #8 - Wound size and hemoglobin data. Location: Partial calcanectomy site. Outcome: Wound healed week 11. (Week 11 photograph not available) *Upper left:* Digital photographs from selected time points. *Upper center:* Wound area as determined through analysis of digital photographs (♦). *Upper right*: Oxygen Saturation from each measurement day. *Lower:* Total hemoglobin concentration [*Tot Hb*], oxyhemoglobin concentration [$HbO_2$], and deoxyhemoglobin concentration [*Hb*] from each measurement day. Each data point represents the mean of measurements obtained from the center of the wound (●), the edges of the wound (Δ), and a control site on the wounded foot (x). Solid lines are the linear trendlines associated with data obtained from the wound centers; dashed lines are the linear trendlines associated with data obtained from the wound edges.**

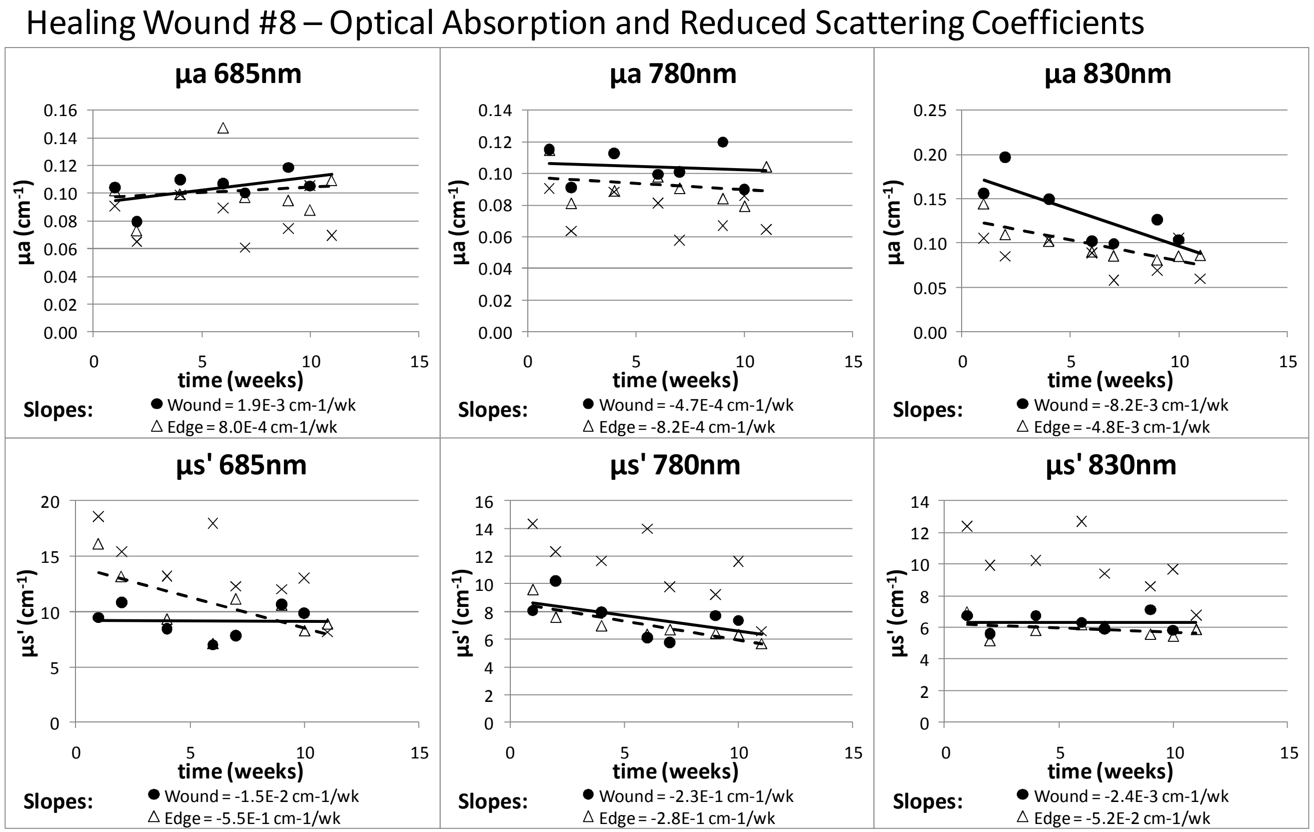

**Figure 60: Healing Wound #8 - Optical aborption (µa) and reduced scattering coefficients (µs'). Location: Partial calcanectomy site. Outcome: Wound healed week 11. Each data point represents the mean of measurements obtained on each measurement day from the center of the wound (•), the edges of the wound (Δ), and a control site on the wounded foot (x). Solid lines are the linear trendlines associated with data obtained from the wound centers; dashed lines are the linear trendlines associated with data obtained from the wound edges.**

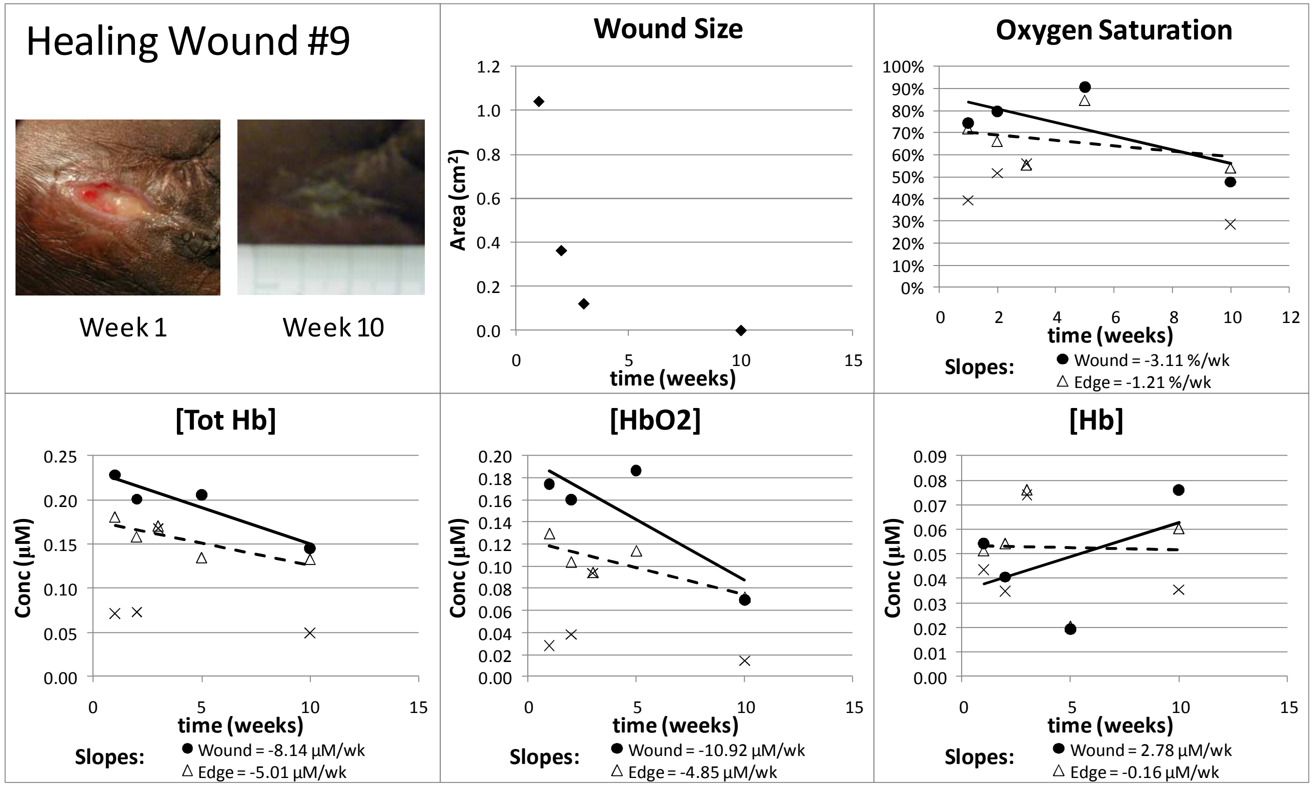

**Figure 61: Healing Wound #9 - Wound size and hemoglobin data. Location: Dorsal surface. Outcome: Wound healed week 10. *Upper left:* Digital photographs from selected time points. *Upper center:* Wound area as determined through analysis of digital photographs (♦). *Upper right*: Oxygen Saturation from each measurement day. *Lower:* Total hemoglobin concentration [*Tot Hb*], oxyhemoglobin concentration [$HbO_2$], and deoxyhemoglobin concentration [*Hb*] from each measurement day. Each data point represents the mean of measurements obtained from the center of the wound (●), the edges of the wound (Δ), and a control site on the wounded foot (x). Solid lines are the linear trendlines associated with data obtained from the wound centers; dashed lines are the linear trendlines associated with data obtained from the wound edges.**

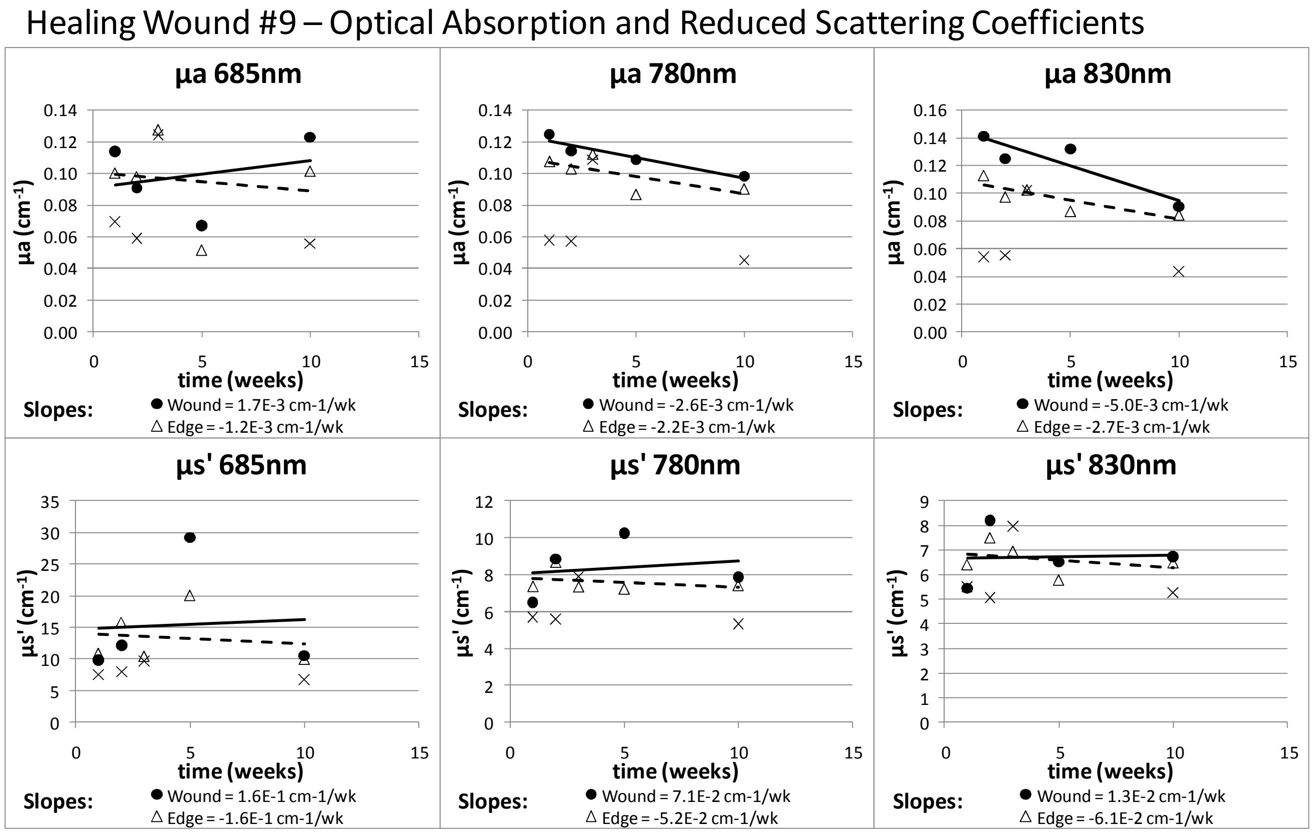

**Figure 62: Healing Wound #9 - Optical aborption (µa) and reduced scattering coefficients (µs'). Location: Dorsal surface. Outcome: Wound healed week 10. Each data point represents the mean of measurements obtained on each measurement day from the center of the wound (●), the edges of the wound (Δ), and a control site on the wounded foot (x). Solid lines are the linear trendlines associated with data obtained from the wound centers; dashed lines are the linear trendlines associated with data obtained from the wound edges.**

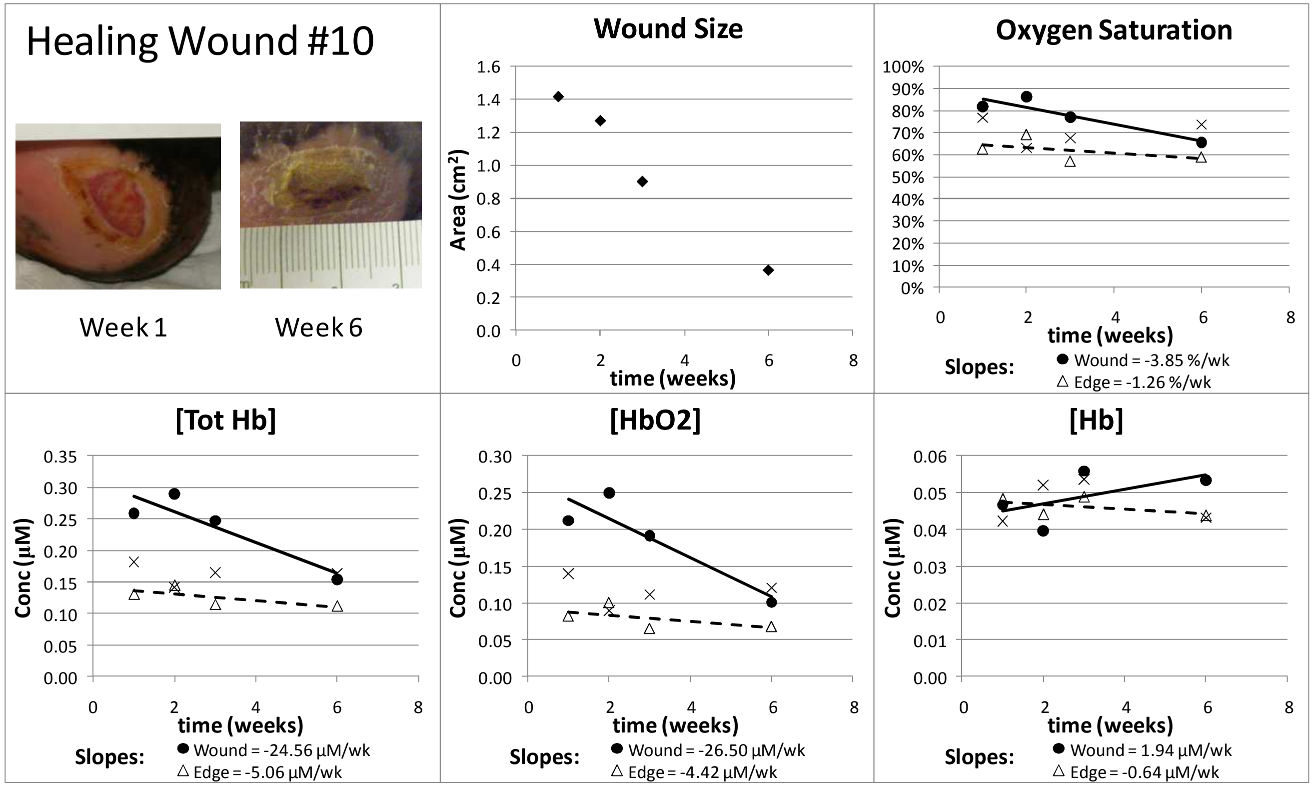

**Figure 63: Healing Wound #10 - Wound size and hemoglobin data. Location: Plantar surface of heel. Outcome: Wound healed by week 10, but no optical data is available for week 10. *Upper left:* Digital photographs from selected time points. *Upper center:* Wound area as determined through analysis of digital photographs (♦). *Upper right*: Oxygen Saturation from each measurement day. *Lower:* Total hemoglobin concentration [*Tot Hb*], oxyhemoglobin concentration [*HbO$_2$*], and deoxyhemoglobin concentration [*Hb*] from each measurement day. Each data point represents the mean of measurements obtained from the center of the wound (●), the edges of the wound (Δ), and a control site on the wounded foot (x). Solid lines are the linear trendlines associated with data obtained from the wound centers; dashed lines are the linear trendlines associated with data obtained from the wound edges.**

Healing Wound #10 – Optical Absorption and Reduced Scattering Coefficients

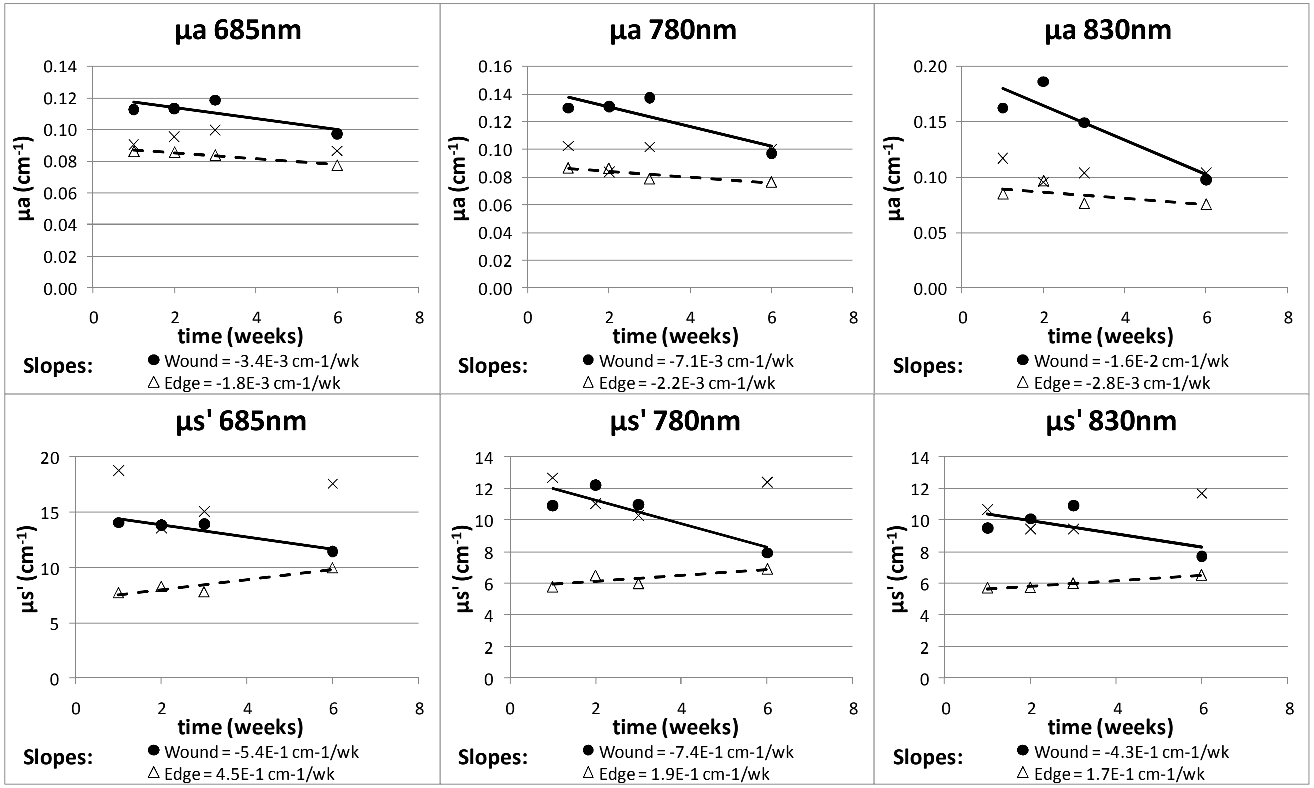

**Figure 64: Healing Wound #10 - Optical aborption (µa) and reduced scattering coefficients (µs'). Location: Plantar surface of heel. Outcome: Wound healed by week 10, but no optical data is available for week 10. Each data point represents the mean of measurements obtained on each measurement day from the center of the wound (●), the edges of the wound (Δ), a control site on the non-wounded foot (+), and a control site on the wounded foot (x). Solid lines are the linear trendlines associated with data obtained from the wound centers; dashed lines are the linear trendlines associated with data obtained from the wound edges.**

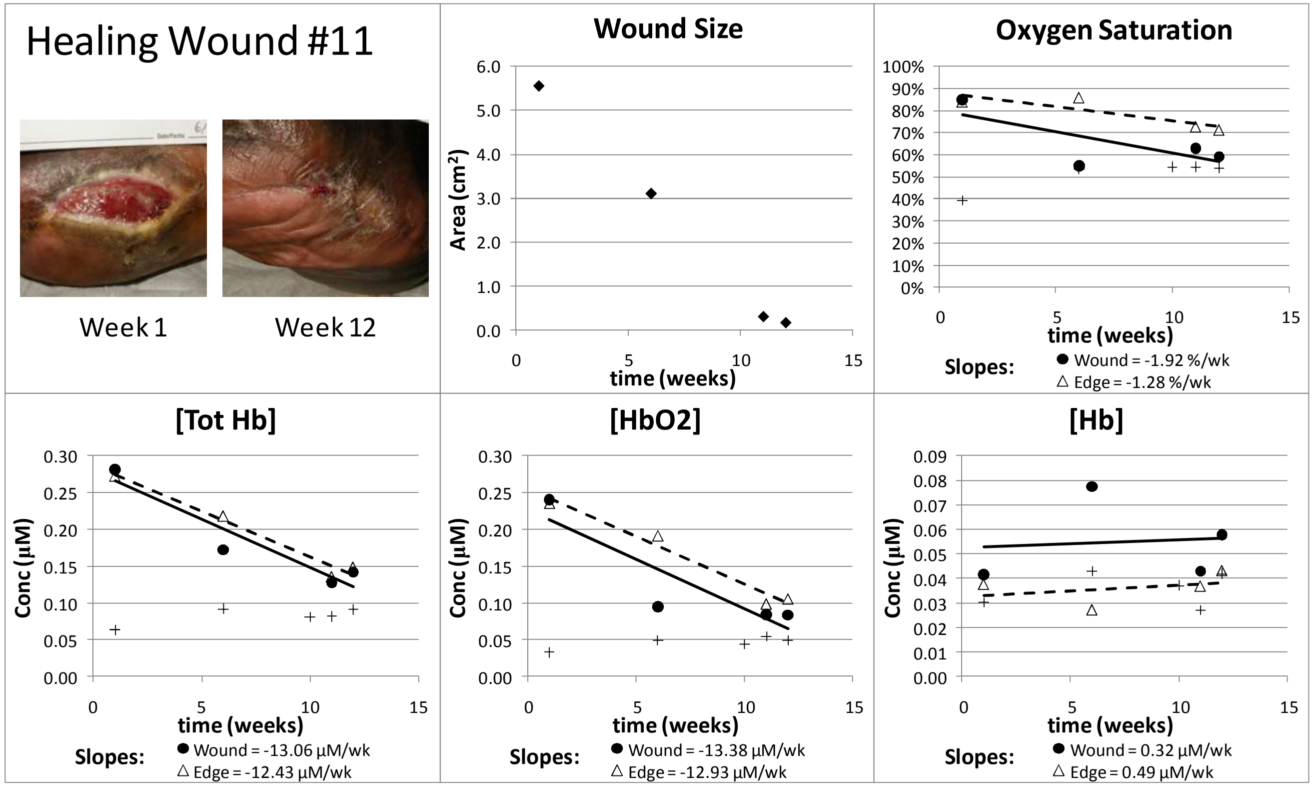

**Figure 65: Healing Wound #11 - Wound size and hemoglobin data. Location: Transmetatarsal amputation site. Outcome: Wound healed by week 12. *Upper left:* Digital photographs from selected time points. *Upper center:* Wound area as determined through analysis of digital photographs (♦). *Upper right*: Oxygen Saturation from each measurement day. *Lower:* Total hemoglobin concentration [*Tot Hb*], oxyhemoglobin concentration [*$HbO_2$*], and deoxyhemoglobin concentration [*Hb*] from each measurement day. Each data point represents the mean of measurements obtained from the center of the wound (●), the edges of the wound (Δ), and a control site on the wounded foot (x). Solid lines are the linear trendlines associated with data obtained from the wound centers; dashed lines are the linear trendlines associated with data obtained from the wound edges.**

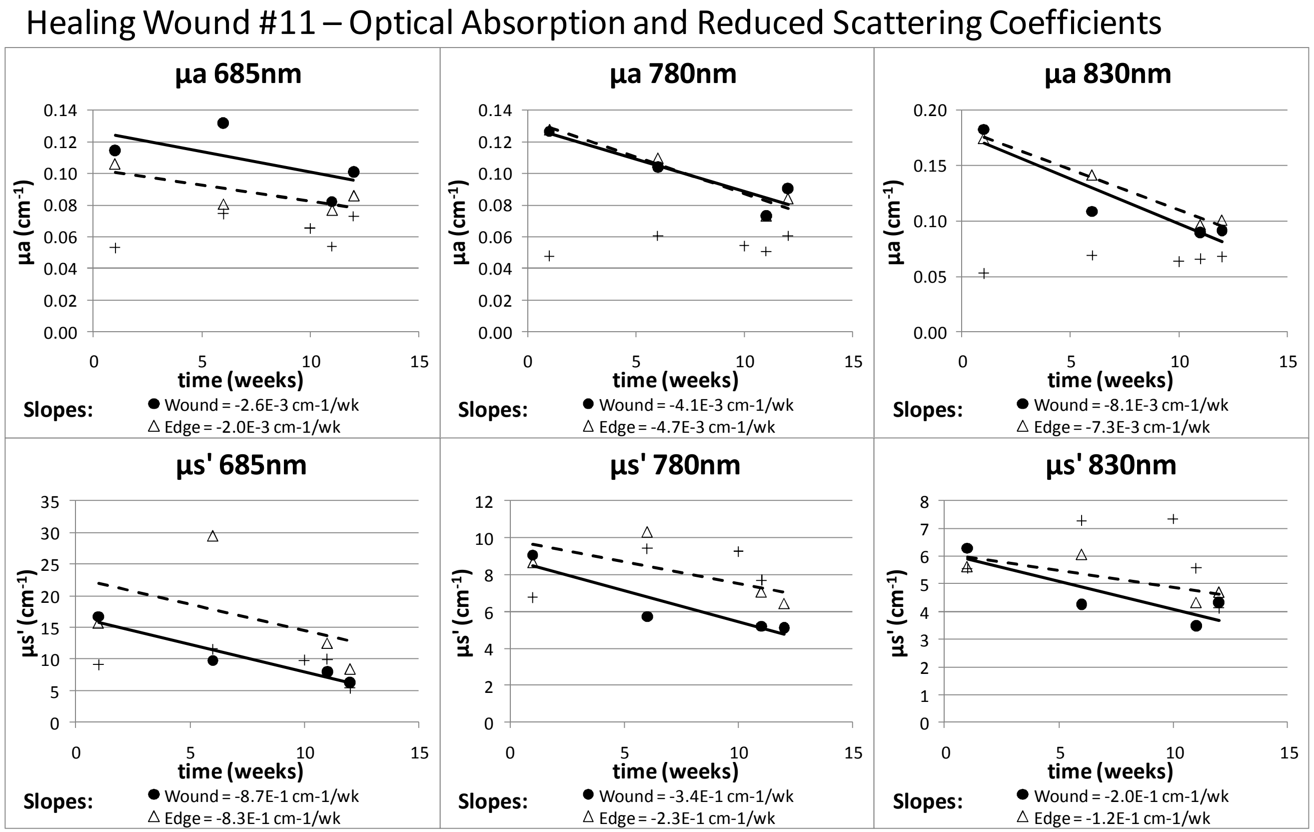

**Figure 66: Healing Wound #11 - Optical aborption (µa) and reduced scattering coefficients (µs'). Location: Transmetatarsal amputation site. Outcome: Wound healed by week 12. Each data point represents the mean of measurements obtained on each measurement day from the center of the wound (●), the edges of the wound (Δ), a control site on the non-wounded foot (+), and a control site on the wounded foot (x). Solid lines are the linear trendlines associated with data obtained from the wound centers; dashed lines are the linear trendlines associated with data obtained from the wound edges.**

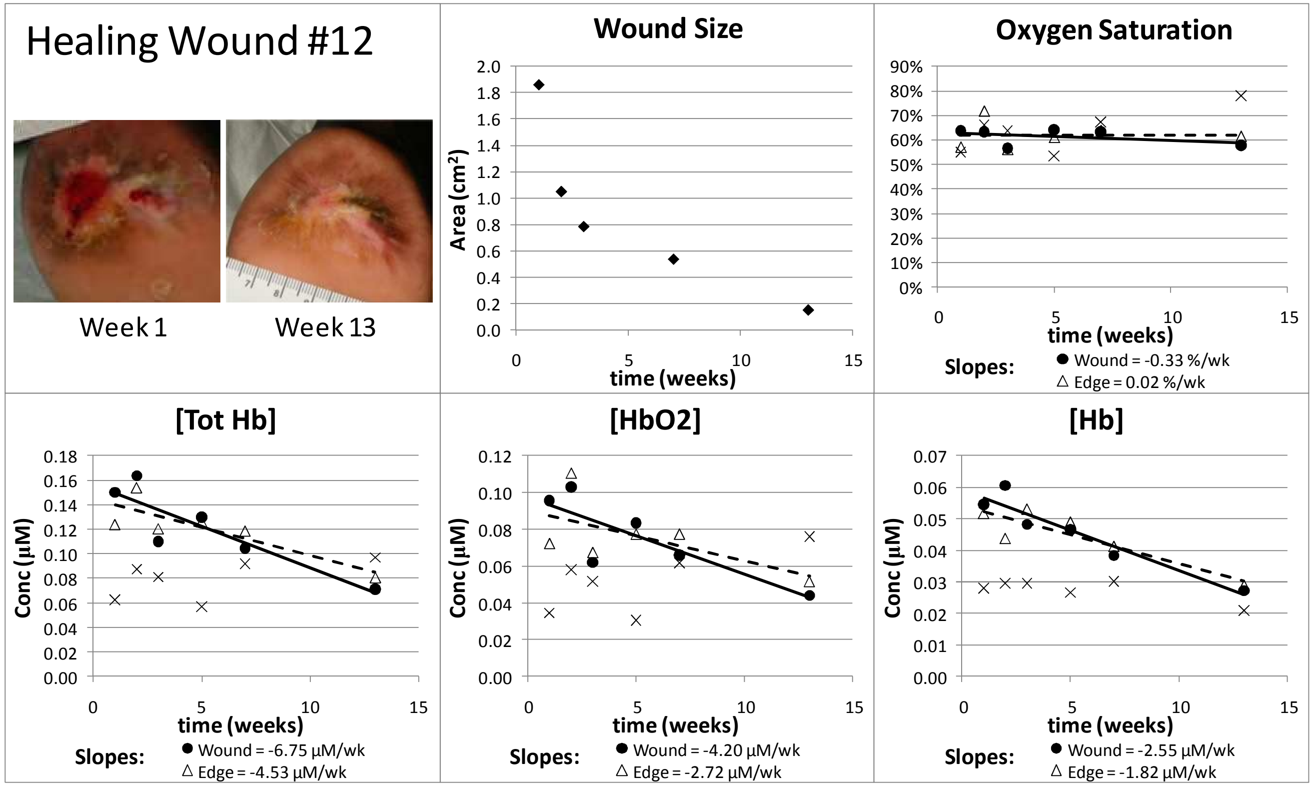

**Figure 67: Healing Wound #12 - Wound size and hemoglobin data. Location: Heel. Outcome: Wound was healed week 13.** ***Upper left:*** **Digital photographs from selected time points.** ***Upper center:*** **Wound area as determined through analysis of digital photographs (♦).** ***Upper right*****: Oxygen Saturation from each measurement day.** ***Lower:*** **Total hemoglobin concentration [*Tot Hb*], oxyhemoglobin concentration [*$HbO_2$*], and deoxyhemoglobin concentration [*Hb*] from each measurement day. Each data point represents the mean of measurements obtained from the center of the wound (●), the edges of the wound (Δ), and a control site on the wounded foot (x). Solid lines are the linear trendlines associated with data obtained from the wound centers; dashed lines are the linear trendlines associated with data obtained from the wound edges.**

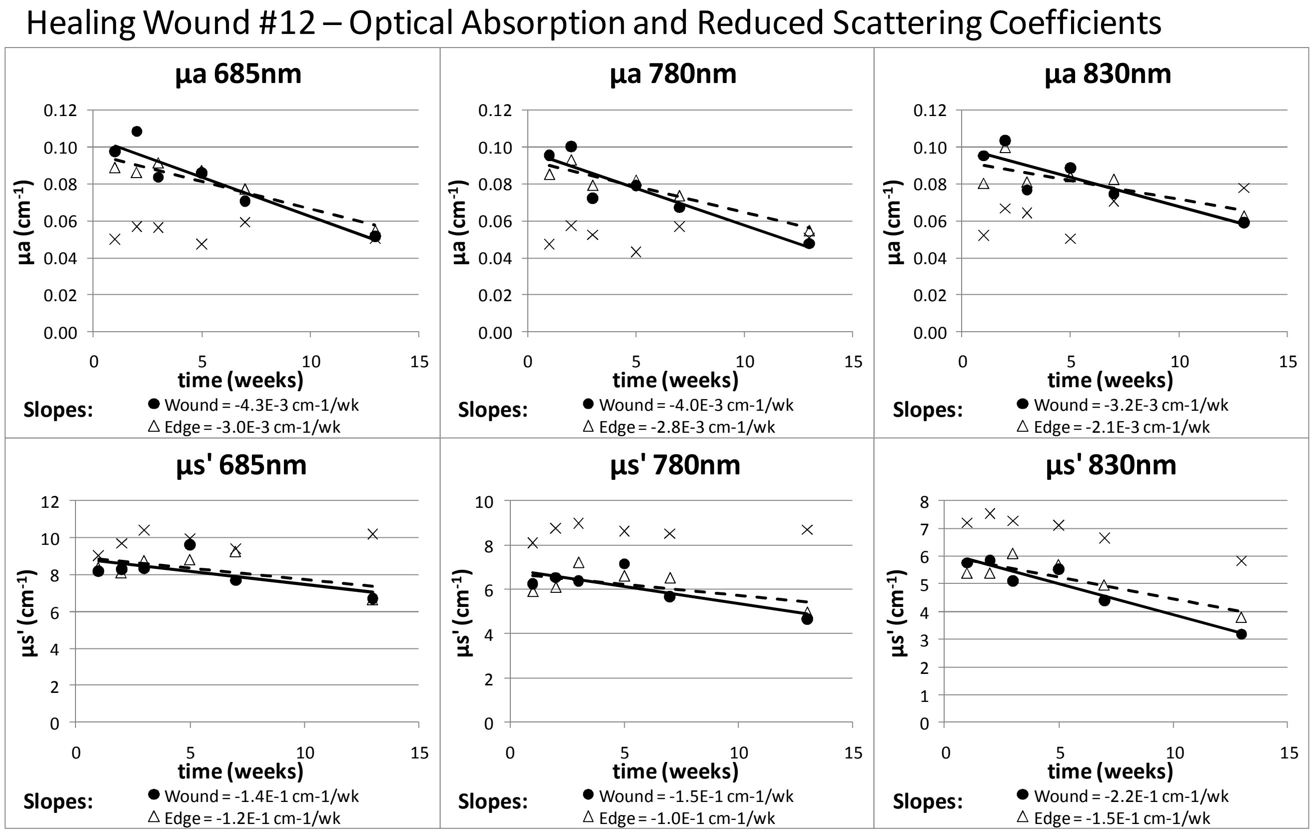

**Figure 68: Healing Wound #12 - Optical aborption (µa) and reduced scattering coefficients (µs'). Location: Heel. Outcome: Wound healed by week 13. Each data point represents the mean of measurements obtained on each measurement day from the center of the wound (●), the edges of the wound (Δ), a control site on the non-wounded foot (+), and a control site on the wounded foot (x). Solid lines are the linear trendlines associated with data obtained from the wound centers; dashed lines are the linear trendlines associated with data obtained from the wound edges.**

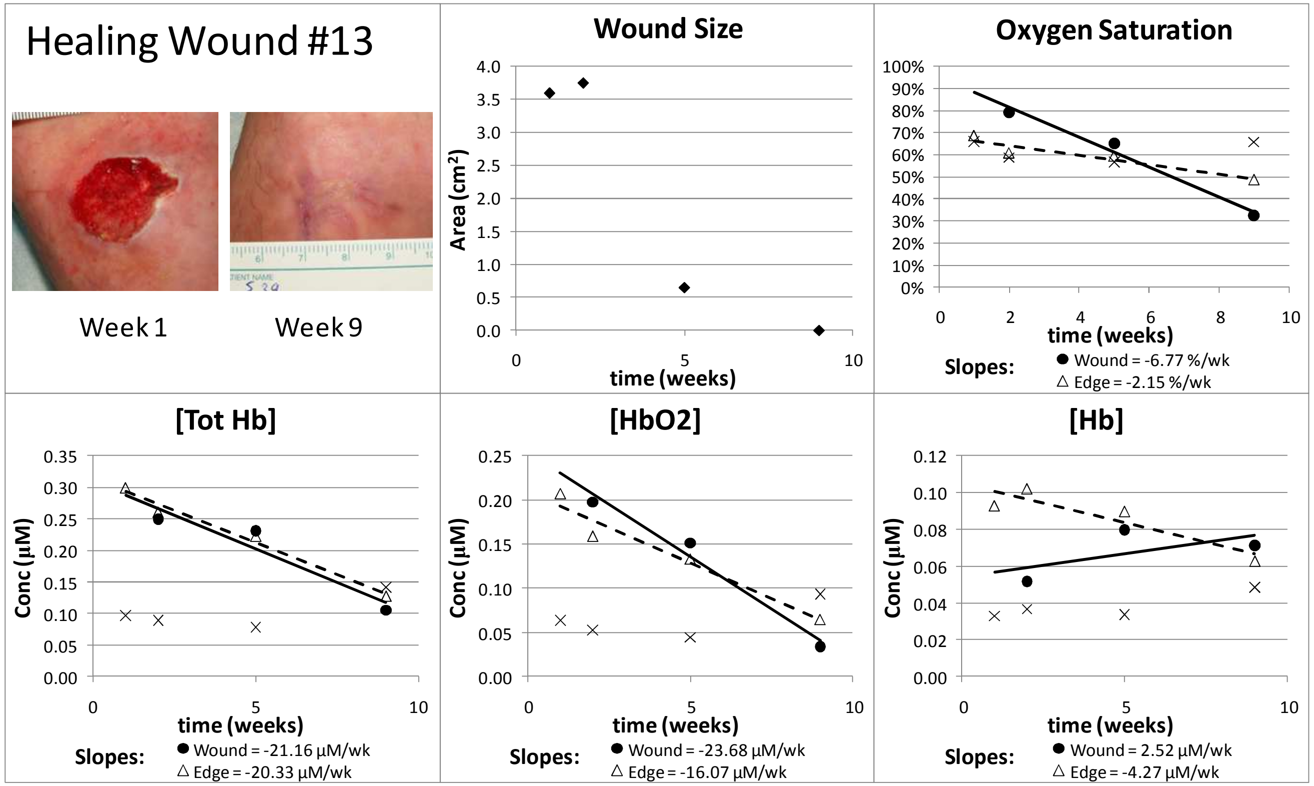

**Figure 69: Healing Wound #13 - Wound size and hemoglobin data. Location: Dorsum. Outcome: Wound was healed week 9.** ***Upper left:*** **Digital photographs from selected time points.** ***Upper center:*** **Wound area as determined through analysis of digital photographs (♦).** ***Upper right*****: Oxygen Saturation from each measurement day.** ***Lower:*** **Total hemoglobin concentration [*Tot Hb*], oxyhemoglobin concentration [*HbO$_2$*], and deoxyhemoglobin concentration [*Hb*] from each measurement day. Each data point represents the mean of measurements obtained from the center of the wound (●), the edges of the wound (Δ), and a control site on the wounded foot (x). Solid lines are the linear trendlines associated with data obtained from the wound centers; dashed lines are the linear trendlines associated with data obtained from the wound edges.**

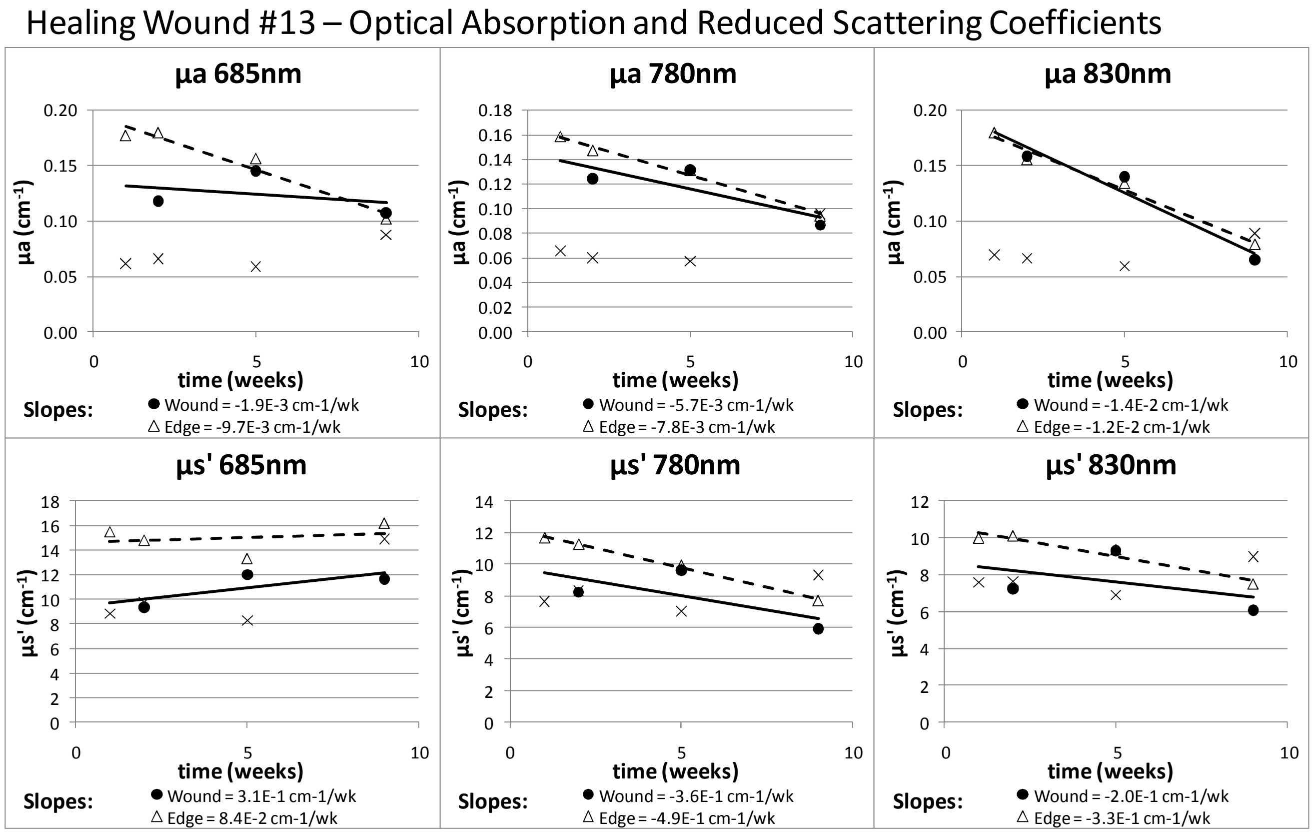

**Figure 70: Healing Wound #13 - Optical aborption (μa) and reduced scattering coefficients (μs'). Location: Dorsum. Outcome: Wound healed by week 9. Each data point represents the mean of measurements obtained on each measurement day from the center of the wound (●), the edges of the wound (Δ), a control site on the non-wounded foot (+), and a control site on the wounded foot (x). Solid lines are the linear trendlines associated with data obtained from the wound centers; dashed lines are the linear trendlines associated with data obtained from the wound edges.**

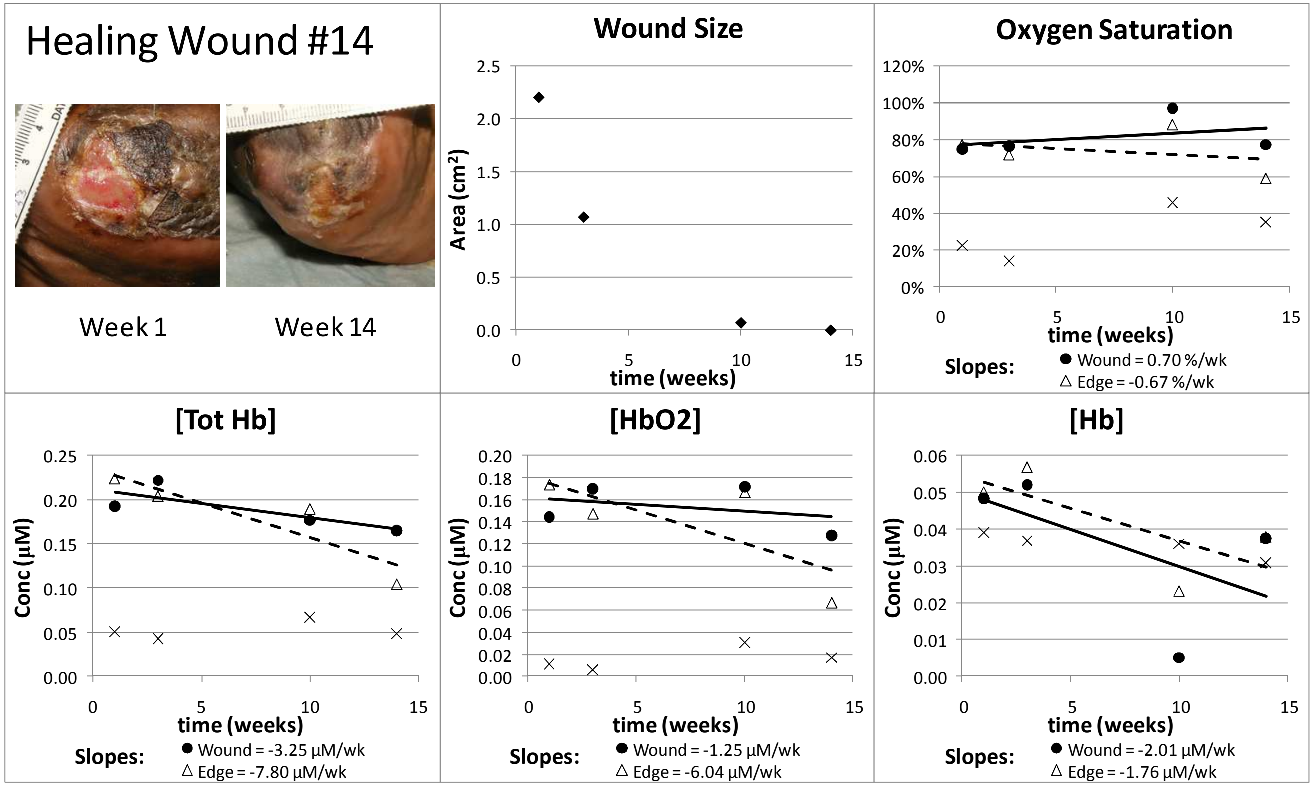

**Figure 71: Healing Wound #14 - Wound size and hemoglobin data. Location: Transmetatarsal amputation site. Outcome: Wound was healed week 14. *Upper left:* Digital photographs from selected time points. *Upper center:* Wound area as determined through analysis of digital photographs (♦). *Upper right*: Oxygen Saturation from each measurement day. *Lower:* Total hemoglobin concentration [*Tot Hb*], oxyhemoglobin concentration [*HbO$_2$*], and deoxyhemoglobin concentration [*Hb*] from each measurement day. Each data point represents the mean of measurements obtained from the center of the wound (●), the edges of the wound (Δ), and a control site on the wounded foot (x). Solid lines are the linear trendlines associated with data obtained from the wound centers; dashed lines are the linear trendlines associated with data obtained from the wound edges.**

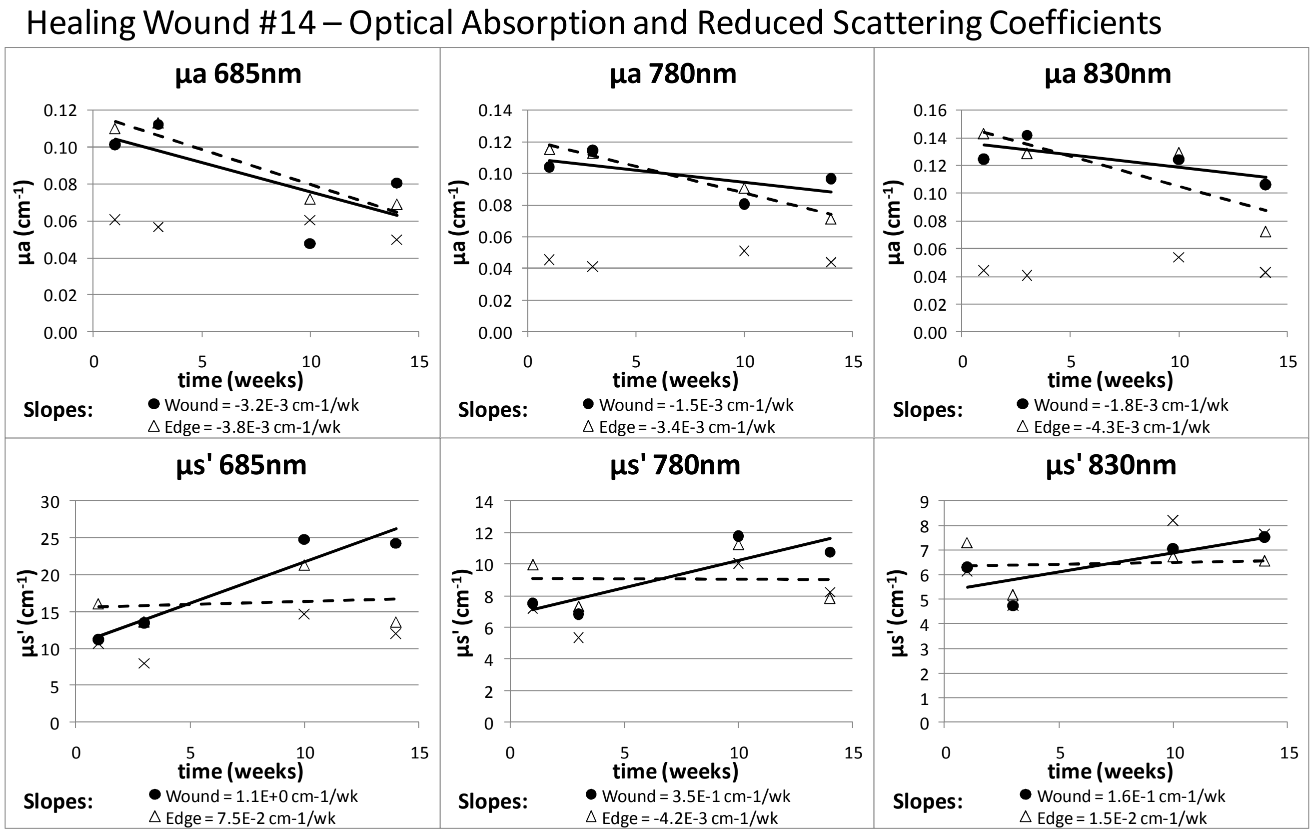

**Figure 72: Healing Wound #14 - Optical aborption (µa) and reduced scattering coefficients (µs'). Location: Transmetatarsal amputation site. Outcome: Wound was healed week 14. Each data point represents the mean of measurements obtained on each measurement day from the center of the wound (●), the edges of the wound (Δ), a control site on the non-wounded foot (+), and a control site on the wounded foot (x). Solid lines are the linear trendlines associated with data obtained from the wound centers; dashed lines are the linear trendlines associated with data obtained from the wound edges.**

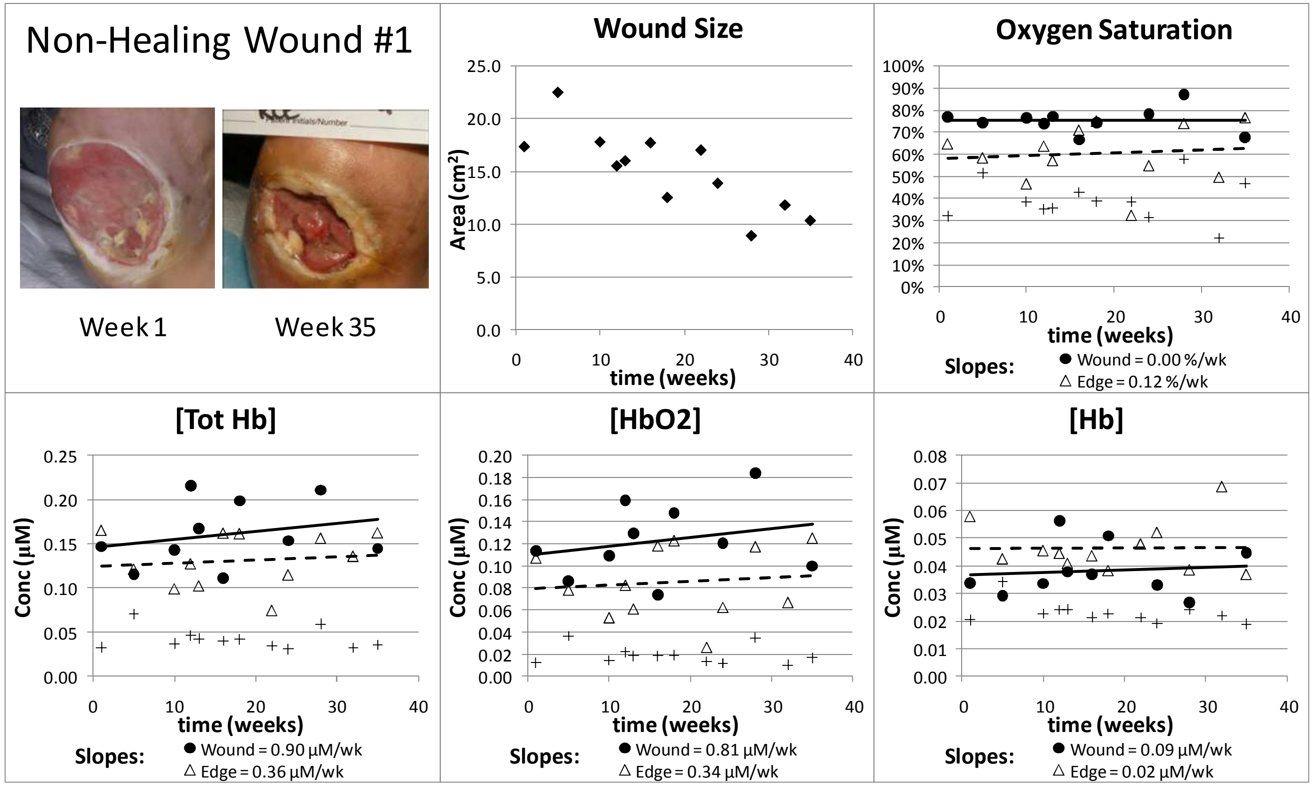

**Figure 73: Non-Healing Wound #1 - Wound size and hemoglobin data. Location: Plantar surface. Outcome: Below the knee amputation week 38. *Upper left:* Digital photographs from selected time points. *Upper center:* Wound area as determined through analysis of digital photographs (♦). *Upper right*: Oxygen Saturation from each measurement day. *Lower:* Total hemoglobin concentration [*Tot Hb*], oxyhemoglobin concentration [$HbO_2$], and deoxyhemoglobin concentration [*Hb*] from each measurement day. Each data point represents the mean of measurements obtained from the center of the wound (●), the edges of the wound (Δ), a control site on the non-wounded foot (+), and a control site on the wounded foot (x). Solid lines are the linear trendlines associated with data obtained from the wound centers; dashed lines are the linear trendlines associated with data obtained from the wound edges.**

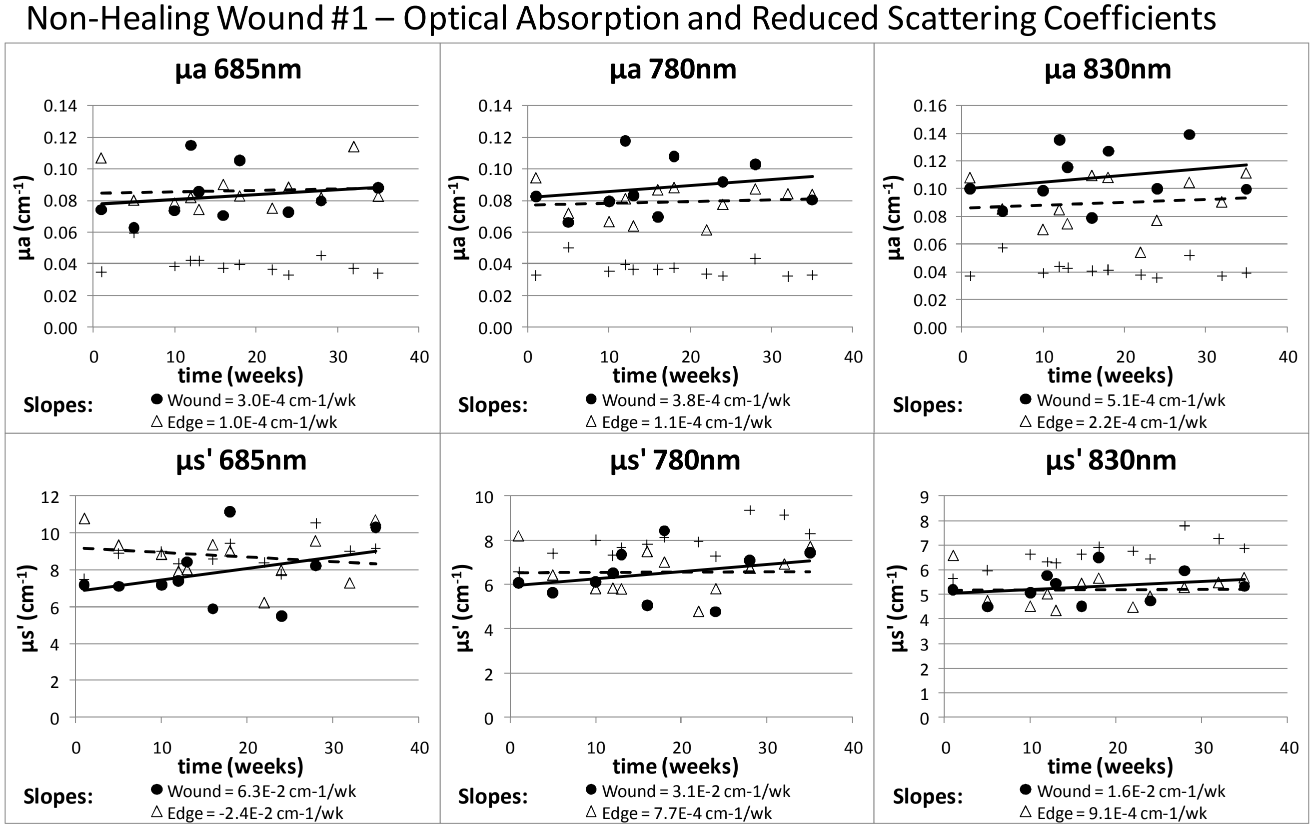

**Figure 74: Non-Healing Wound #1 - Optical aborption (µa) and reduced scattering coefficients (µs'). Location: Plantar surface. Outcome: Below the knee amputation week 38. Each data point represents the mean of measurements obtained on each measurement day from the center of the wound (•), the edges of the wound (Δ), a control site on the non-wounded foot (+), and a control site on the wounded foot (x). Solid lines are the linear trendlines associated with data obtained from the wound centers; dashed lines are the linear trendlines associated with data obtained from the wound edges.**

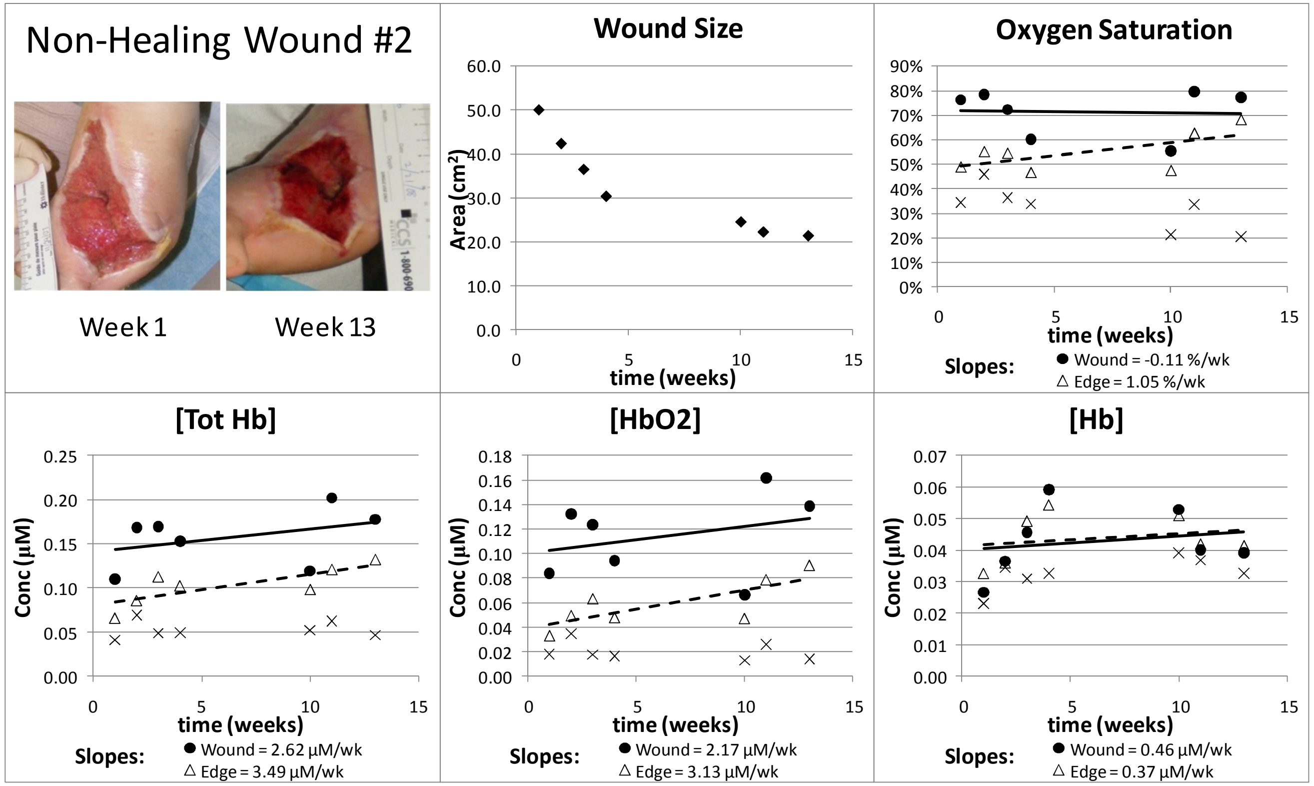

**Figure 75: Non-Healing Wound #2 - Wound size and hemoglobin data. Location: Dorsum. Outcome: Lisfranc amputation week 16. *Upper left:* Digital photographs from selected time points. *Upper center:* Wound area as determined through analysis of digital photographs (♦). *Upper right*: Oxygen Saturation from each measurement day. *Lower:* Total hemoglobin concentration [*Tot Hb*], oxyhemoglobin concentration [*$HbO_2$*], and deoxyhemoglobin concentration [*Hb*] from each measurement day. Each data point represents the mean of measurements obtained from the center of the wound (●), the edges of the wound (Δ), and a control site on the wounded foot (x). Solid lines are the linear trendlines associated with data obtained from the wound centers; dashed lines are the linear trendlines associated with data obtained from the wound edges.**

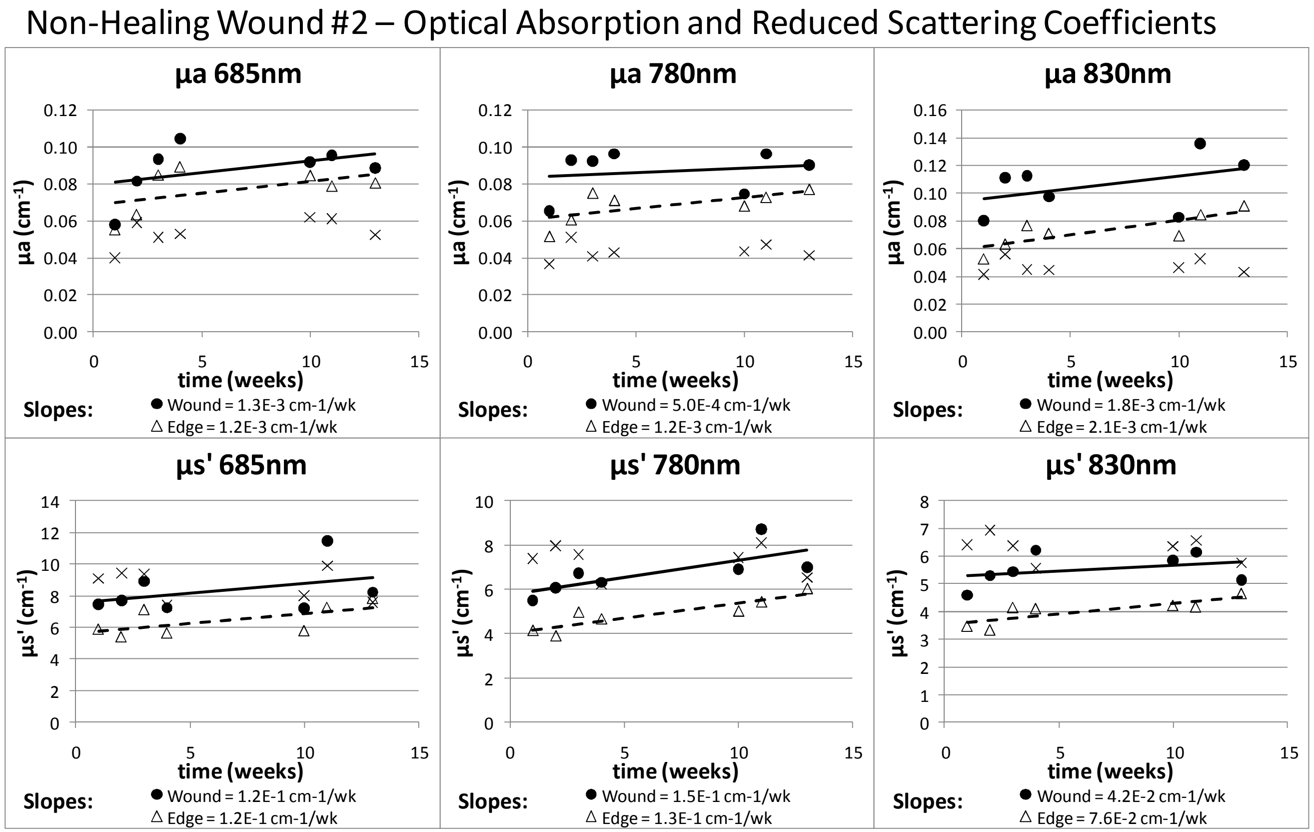

**Figure 76: Non-Healing Wound #2 - Optical aborption (μa) and reduced scattering coefficients (μs'). Location: Dorsum. Outcome: Lisfranc amputation week 16. Each data point represents the mean of measurements obtained on each measurement day from the center of the wound (●), the edges of the wound (Δ), and a control site on the wounded foot (x). Solid lines are the linear trendlines associated with data obtained from the wound centers; dashed lines are the linear trendlines associated with data obtained from the wound edges.**

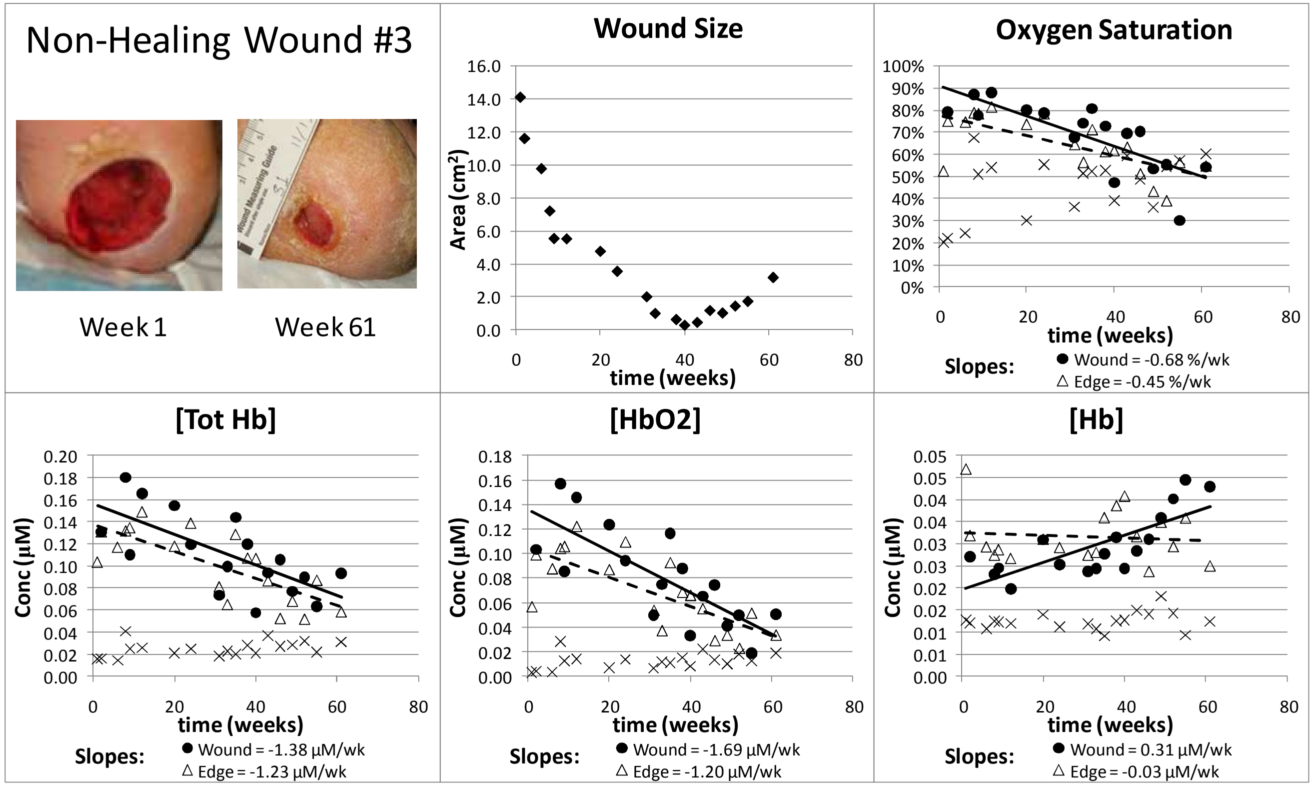

**Figure 77: Non-Healing Wound #3 - Wound size and hemoglobin data. Location: Heel. Outcome: Wound remained open after 20 measurement sessions.** ***Upper left:*** **Digital photographs from selected time points.** ***Upper center:*** **Wound area as determined through analysis of digital photographs (♦).** ***Upper right*****: Oxygen Saturation from each measurement day.** ***Lower:*** **Total hemoglobin concentration [*Tot Hb*], oxyhemoglobin concentration [*HbO$_2$*], and deoxyhemoglobin concentration [*Hb*] from each measurement day. Each data point represents the mean of measurements obtained from the center of the wound (●), the edges of the wound (Δ), and a control site on the wounded foot (x). Solid lines are the linear trendlines associated with data obtained from the wound centers; dashed lines are the linear trendlines associated with data obtained from the wound edges.**

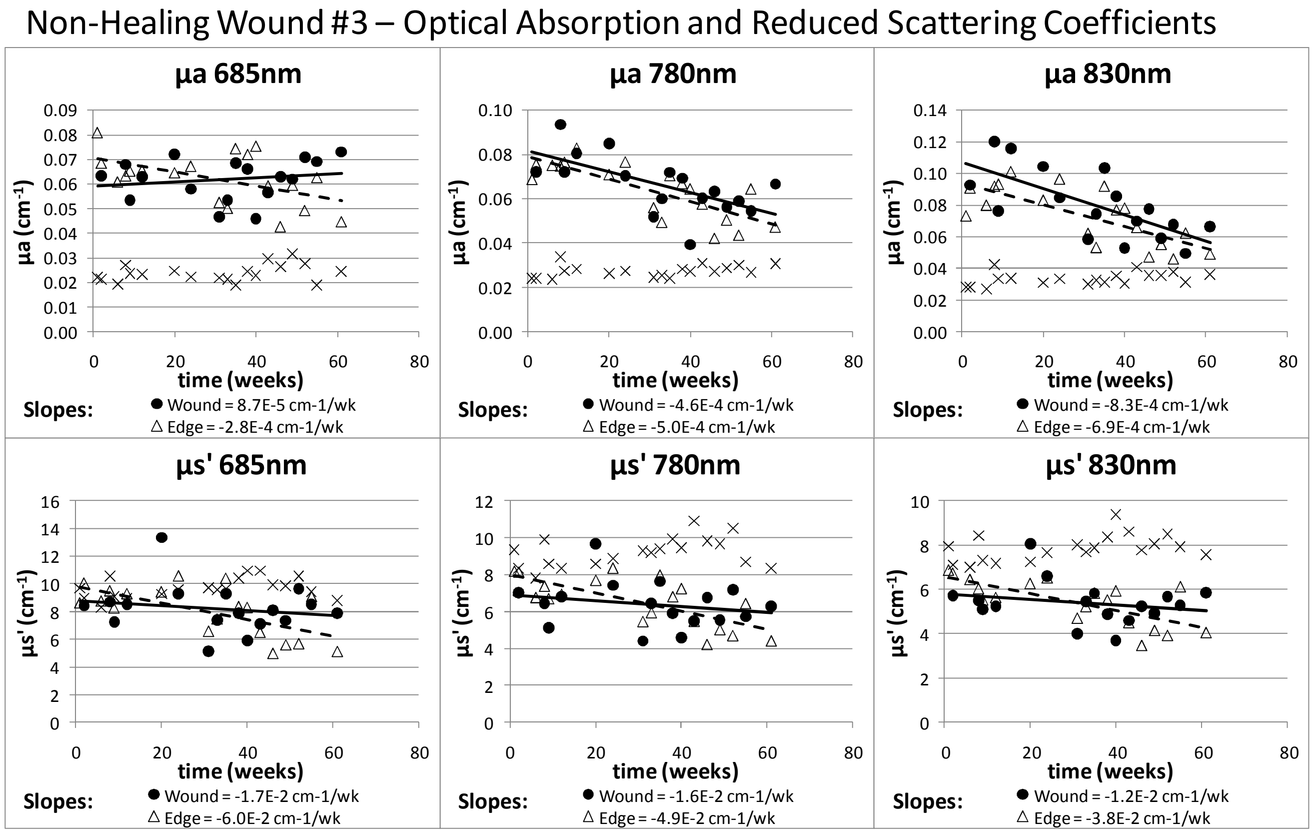

**Figure 78: Non-Healing Wound #3 - Optical aborption (µa) and reduced scattering coefficients (µs'). Location: Heel. Outcome: Wound remained open after 20 measurement sessions. Each data point represents the mean of measurements obtained on each measurement day from the center of the wound (●), the edges of the wound (Δ), and a control site on the wounded foot (x). Solid lines are the linear trendlines associated with data obtained from the wound centers; dashed lines are the linear trendlines associated with data obtained from the wound edges.**

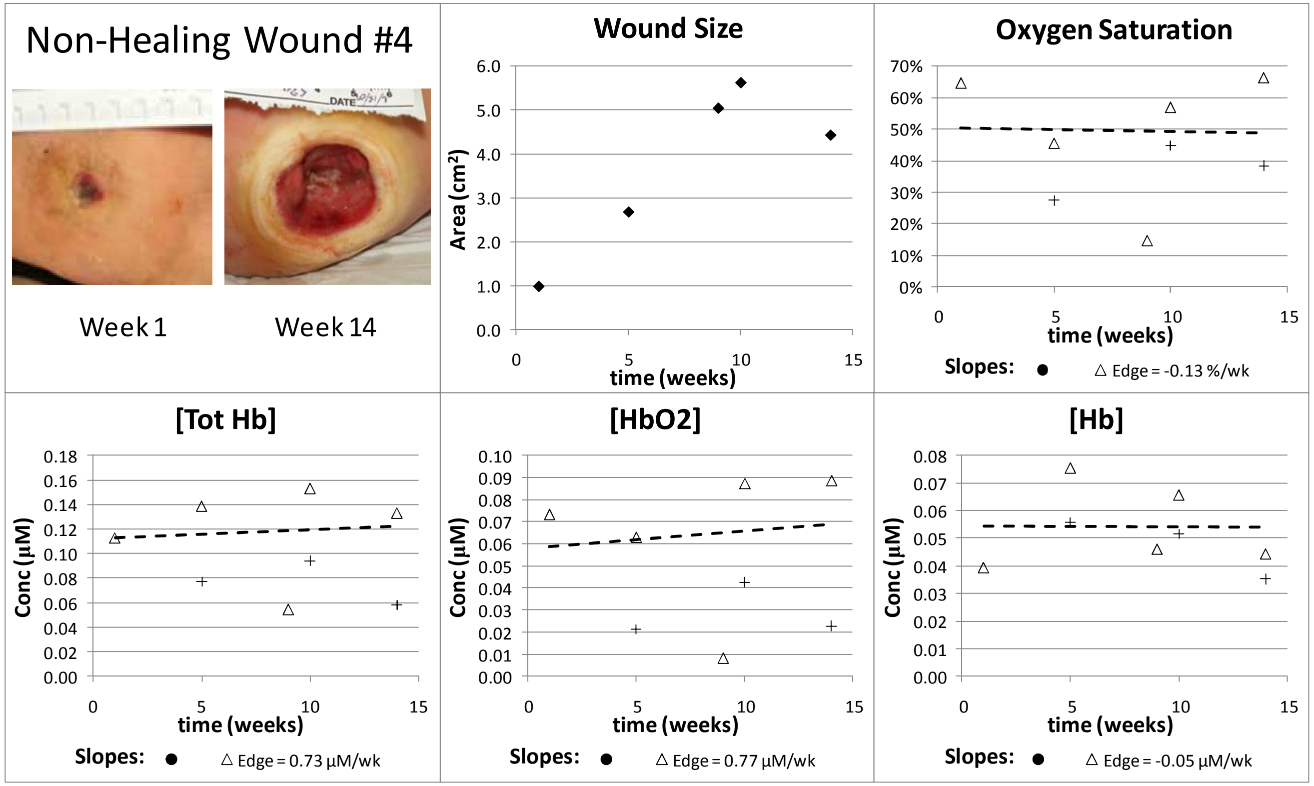

**Figure 79: Non-Healing Wound #4 - Wound size and hemoglobin data. Location: Plantar surface. Outcome: Below the knee amputation week 18. *Upper left:* Digital photographs from selected time points. *Upper center:* Wound area as determined through analysis of digital photographs (♦). *Upper right*: Oxygen Saturation from each measurement day. *Lower:* Total hemoglobin concentration [*Tot Hb*], oxyhemoglobin concentration [$HbO_2$], and deoxyhemoglobin concentration [*Hb*] from each measurement day. Each data point represents the mean of measurements obtained from the edges of the wound (Δ), and a control site on the non-wounded foot (+). Wound center measurements are not available due to the size and geometry of the wound. Dashed lines are the linear trendlines associated with data obtained from the wound edges.**

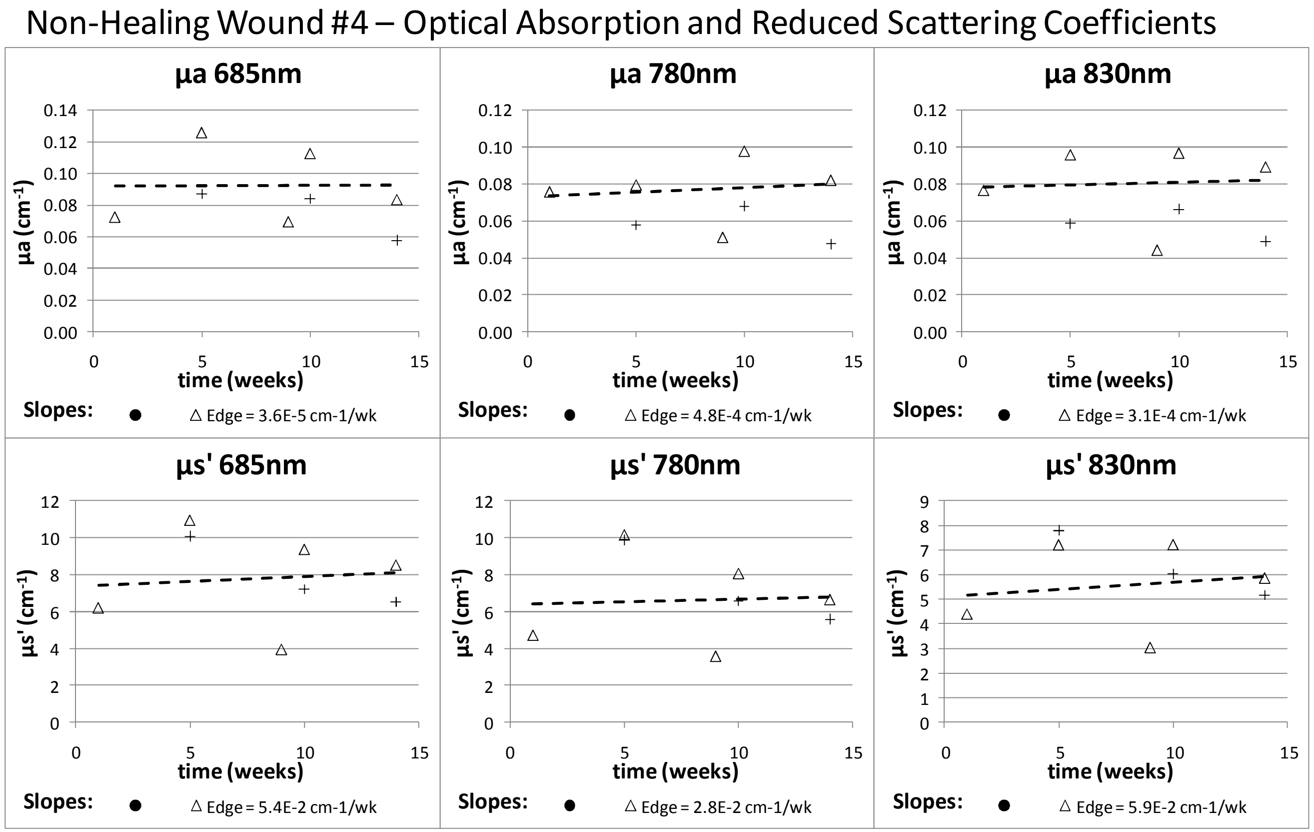

**Figure 80: Non-Healing Wound #4 - Optical aborption (µa) and reduced scattering coefficients (µs'). Location: Plantar surface. Outcome: Below the knee amputation week 18. Each data point represents the mean of measurements obtained from the edges of the wound (Δ), and a control site on the non-wounded foot (+). Wound center measurements are not available due to the size and geometry of the wound. Dashed lines are the linear trendlines associated with data obtained from the wound edges.**

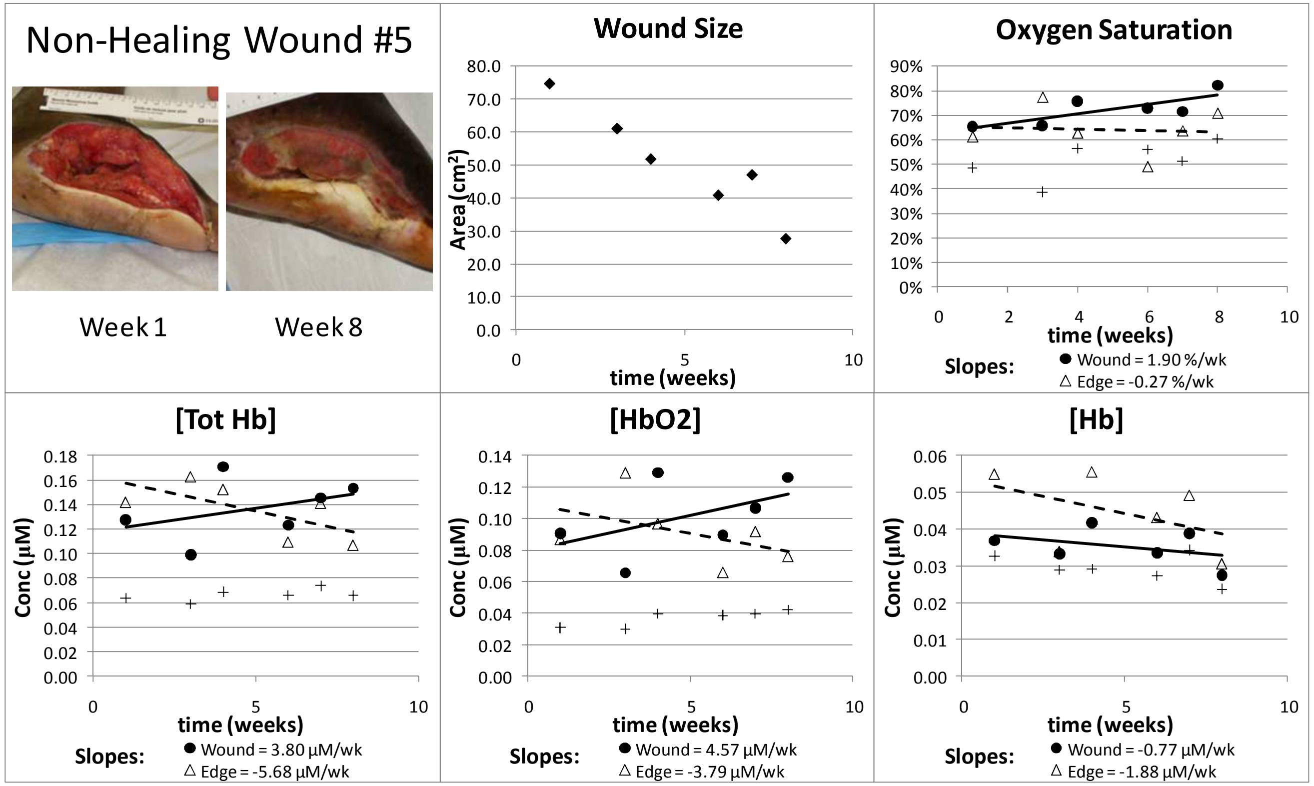

**Figure 81: Non-Healing Wound #5 - Wound size and hemoglobin data. Location: Lateral surface of foot. Outcome: Transmetatarsal amputation week 10. *Upper left:* Digital photographs from selected time points. *Upper center:* Wound area as determined through analysis of digital photographs (♦). *Upper right*: Oxygen Saturation from each measurement day. *Lower:* Total hemoglobin concentration [*Tot Hb*], oxyhemoglobin concentration [*$HbO_2$*], and deoxyhemoglobin concentration [*Hb*] from each measurement day. Each data point represents the mean of measurements obtained from the center of the wound (●), the edges of the wound (Δ), and a control site on the non-wounded foot (+). Solid lines are the linear trendlines associated with data obtained from the wound centers; dashed lines are the linear trendlines associated with data obtained from the wound edges.**

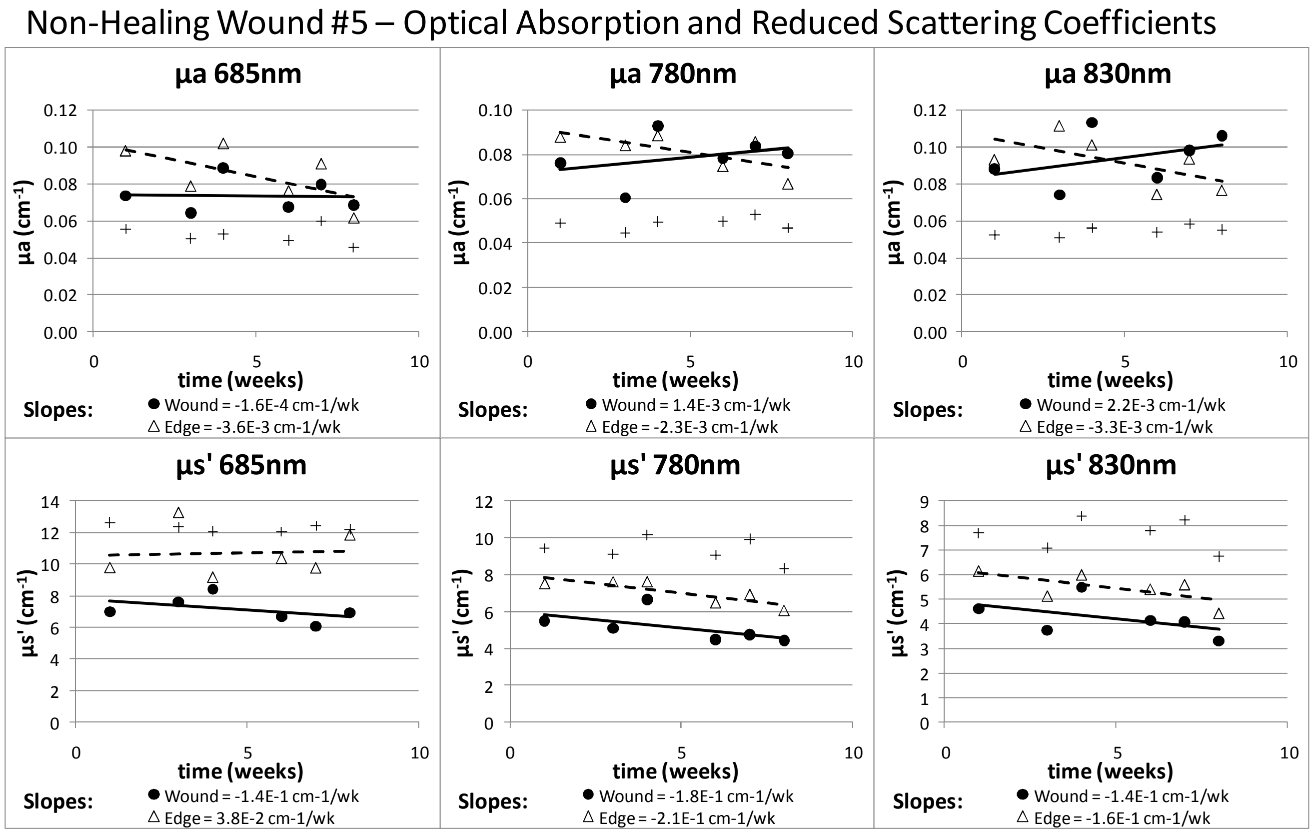
Non-Healing Wound #5 – Optical Absorption and Reduced Scattering Coefficients

**Figure 82: Non-Healing Wound #5 - Optical aborption (µa) and reduced scattering coefficients (µs'). Location: Lateral surface of foot. Outcome: Transmetatarsal amputation week 10. Each data point represents the mean of measurements obtained on each measurement day from the center of the wound (●), the edges of the wound (Δ), and a control site on the non-wounded foot (+). Solid lines are the linear trendlines associated with data obtained from the wound centers; dashed lines are the linear trendlines associated with data obtained from the wound edges.**

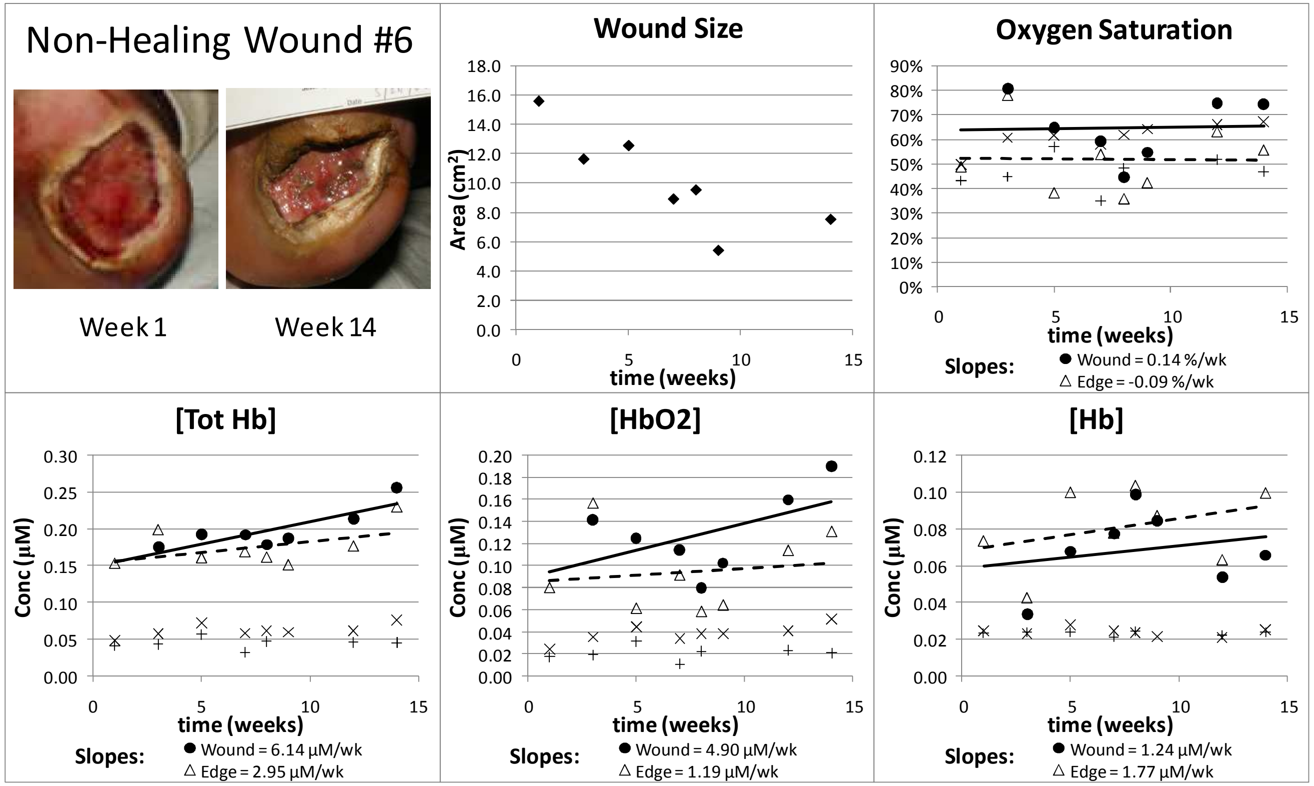

**Figure 83: Non-Healing Wound #6 - Wound size and hemoglobin data. Location: Transmetatarsal amputation site. Outcome: Wound excision and revision of transmetatarsal stump during week 15. *Upper left:* Digital photographs from selected time points. *Upper center:* Wound area as determined through analysis of digital photographs (♦). *Upper right*: Oxygen Saturation from each measurement day. *Lower:* Total hemoglobin concentration [*Tot Hb*], oxyhemoglobin concentration [*HbO$_2$*], and deoxyhemoglobin concentration [*Hb*] from each measurement day. Each data point represents the mean of measurements obtained from the center of the wound (●), the edges of the wound (Δ), a control site on the non-wounded foot (+), and a control site on the wounded foot (x). Solid lines are the linear trendlines associated with data obtained from the wound centers; dashed lines are the linear trendlines associated with data obtained from the wound edges.**

Non-Healing Wound #6 – Optical Absorption and Reduced Scattering Coefficients

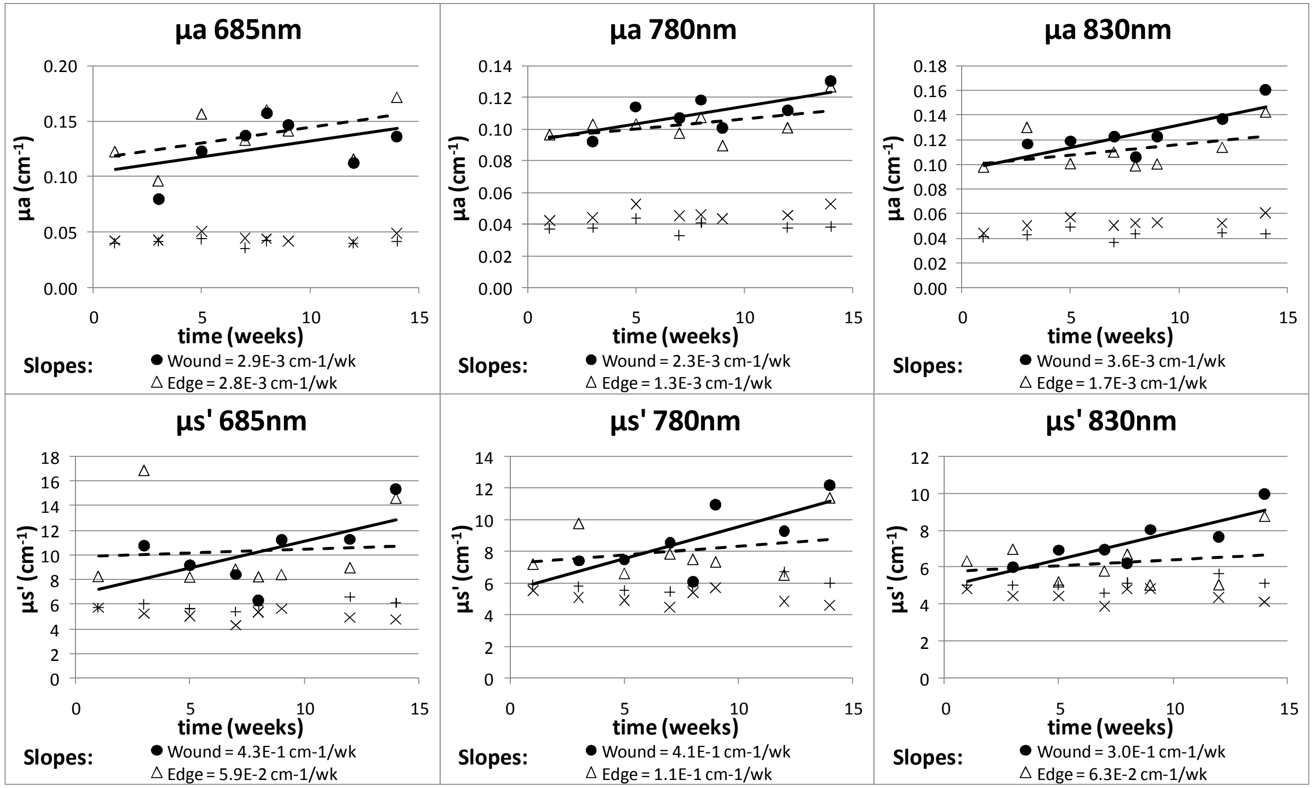

**Figure 84: Non-Healing Wound #6 - Optical aborption (µa) and reduced scattering coefficients (µs'). Location: Transmetatarsal amputation site. Outcome: Wound excision and revision of transmetatarsal stump during week 15. Each data point represents the mean of measurements obtained on each measurement day from the center of the wound (●), the edges of the wound (Δ), a control site on the non-wounded foot (+), and a control site on the wounded foot (x). Solid lines are the linear trendlines associated with data obtained from the wound centers; dashed lines are the linear trendlines associated with data obtained from the wound edges.**

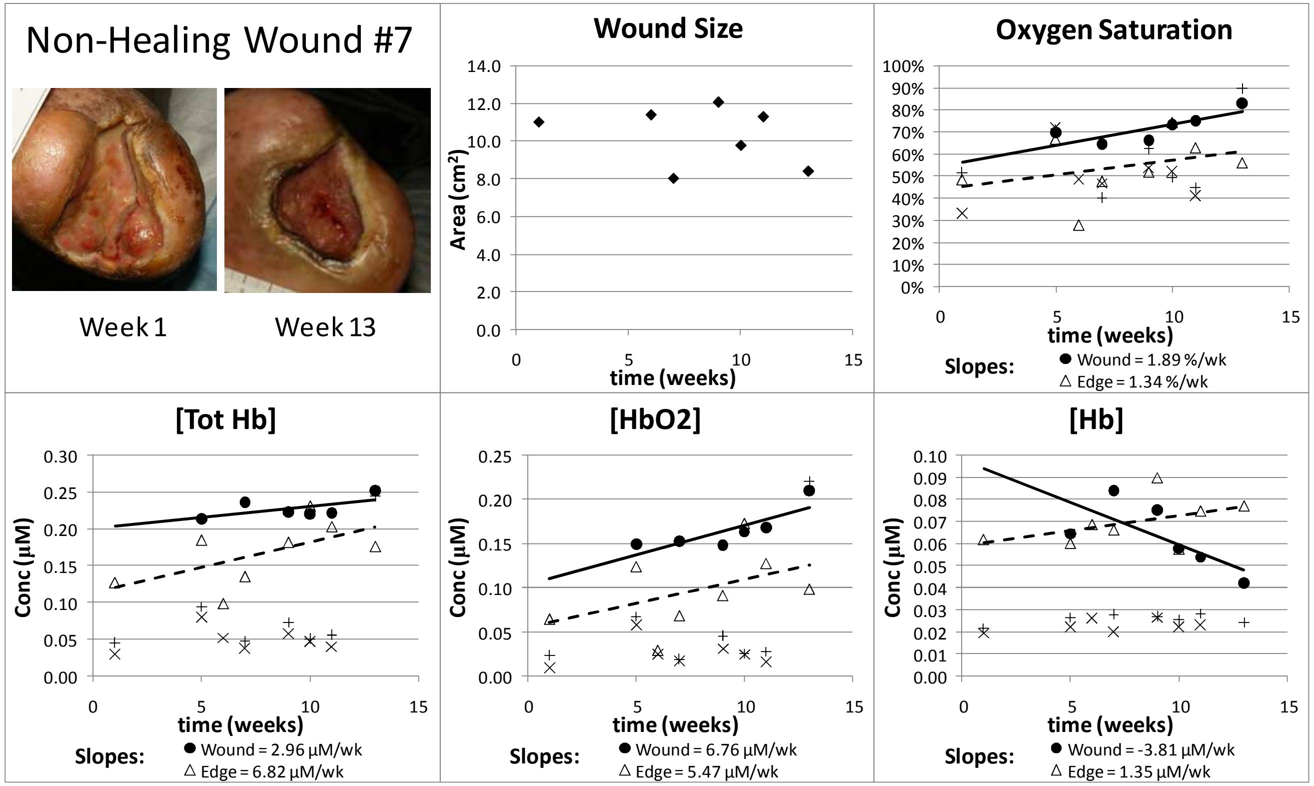

**Figure 85: Non-Healing Wound #7 - Wound size and hemoglobin data. Location: Transmetatarsal amputation site. Outcome: Wound excision and revision of transmetatarsal stump during week 14. *Upper left:* Digital photographs from selected time points. *Upper center:* Wound area as determined through analysis of digital photographs (♦). *Upper right*: Oxygen Saturation from each measurement day. *Lower:* Total hemoglobin concentration [*Tot Hb*], oxyhemoglobin concentration [$HbO_2$], and deoxyhemoglobin concentration [*Hb*] from each measurement day. Each data point represents the mean of measurements obtained from the center of the wound (●), the edges of the wound (Δ), a control site on the non-wounded foot (+), and a control site on the wounded foot (x). Solid lines are the linear trendlines associated with data obtained from the wound centers; dashed lines are the linear trendlines associated with data obtained from the wound edges.**

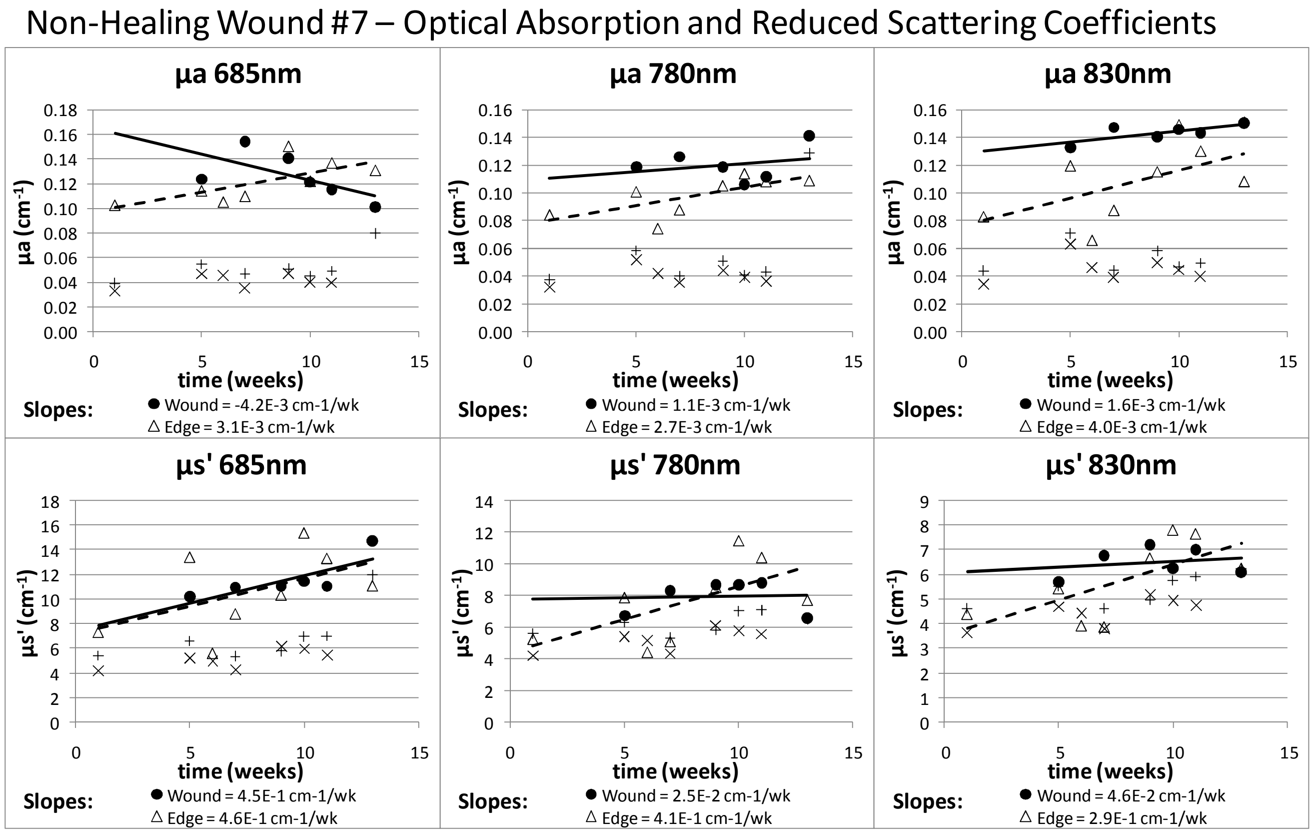

**Figure 86: Non-Healing Wound #7 - Optical aborption (µa) and reduced scattering coefficients (µs'). Location: Transmetatarsal amputation site. Outcome: Wound excision and revision of transmetatarsal stump during week 14. Each data point represents the mean of measurements obtained on each measurement day from the center of the wound (●), the edges of the wound (Δ), a control site on the non-wounded foot (+), and a control site on the wounded foot (x). Solid lines are the linear trendlines associated with data obtained from the wound centers; dashed lines are the linear trendlines associated with data obtained from the wound edges.**

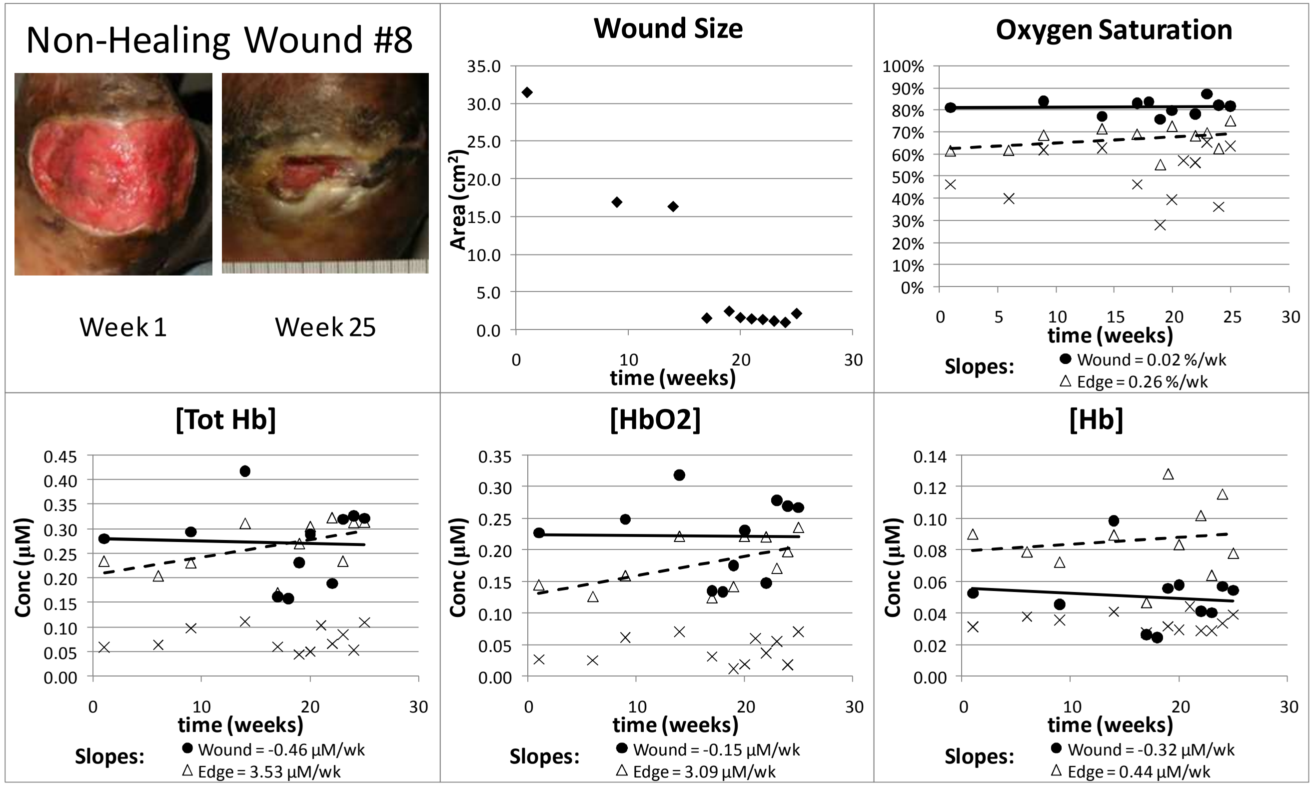

**Figure 87: Non-Healing Wound #8 - Wound size and hemoglobin data. Location: Plantar and lateral surfaces. Outcome: Wound excision during week 26. *Upper left:* Digital photographs from selected time points. *Upper center:* Wound area as determined through analysis of digital photographs (♦). *Upper right*: Oxygen Saturation from each measurement day. *Lower:* Total hemoglobin concentration [*Tot Hb*], oxyhemoglobin concentration [*HbO$_2$*], and deoxyhemoglobin concentration [*Hb*] from each measurement day. Each data point represents the mean of measurements obtained from the center of the wound (●), the edges of the wound (Δ), and a control site on the wounded foot (x). Solid lines are the linear trendlines associated with data obtained from the wound centers; dashed lines are the linear trendlines associated with data obtained from the wound edges.**

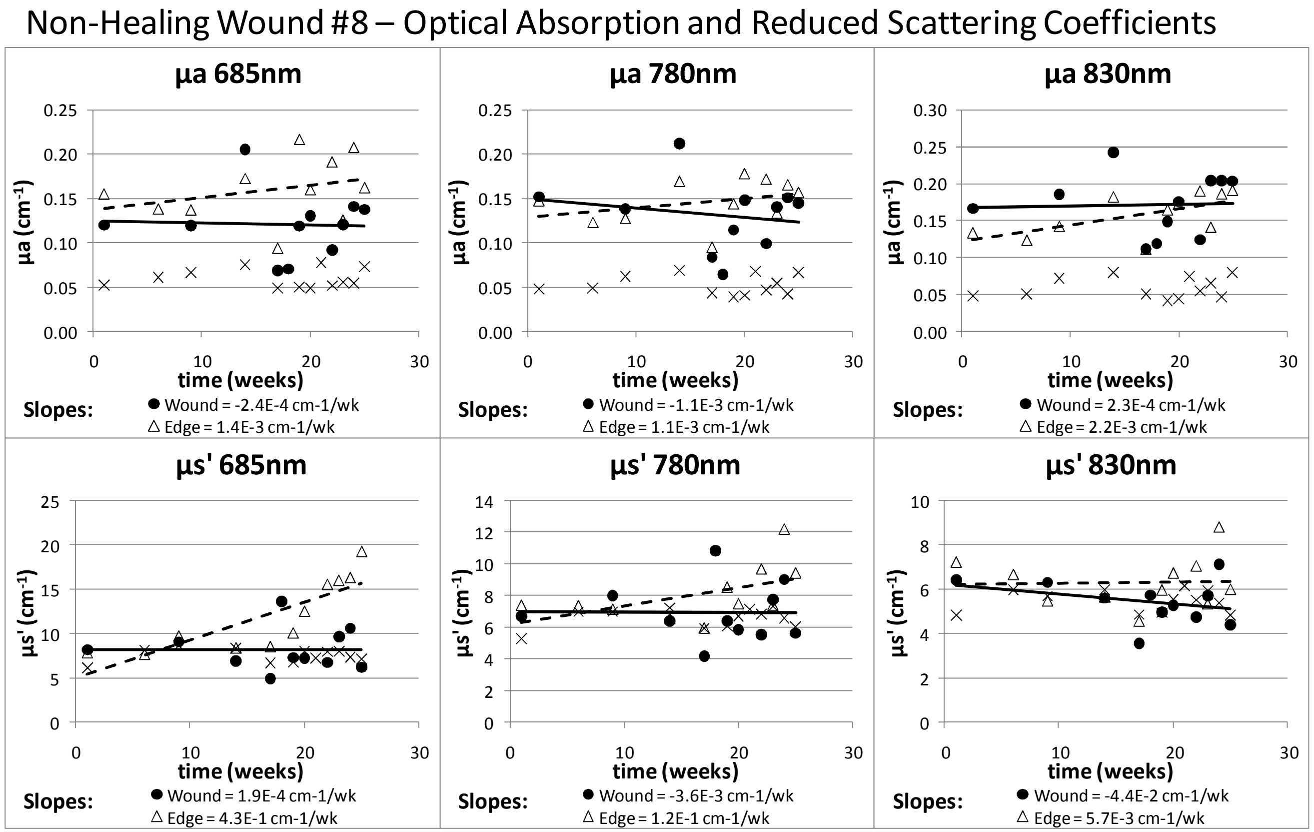

**Figure 88: Non-Healing Wound #8 - Optical aborption (µa) and reduced scattering coefficients (µs'). Location: Plantar and lateral surfaces. Outcome: Wound excision during week 26. Each data point represents the mean of measurements obtained on each measurement day from the center of the wound (●), the edges of the wound (Δ), and a control site on the wounded foot (x). Solid lines are the linear trendlines associated with data obtained from the wound centers; dashed lines are the linear trendlines associated with data obtained from the wound edges.**

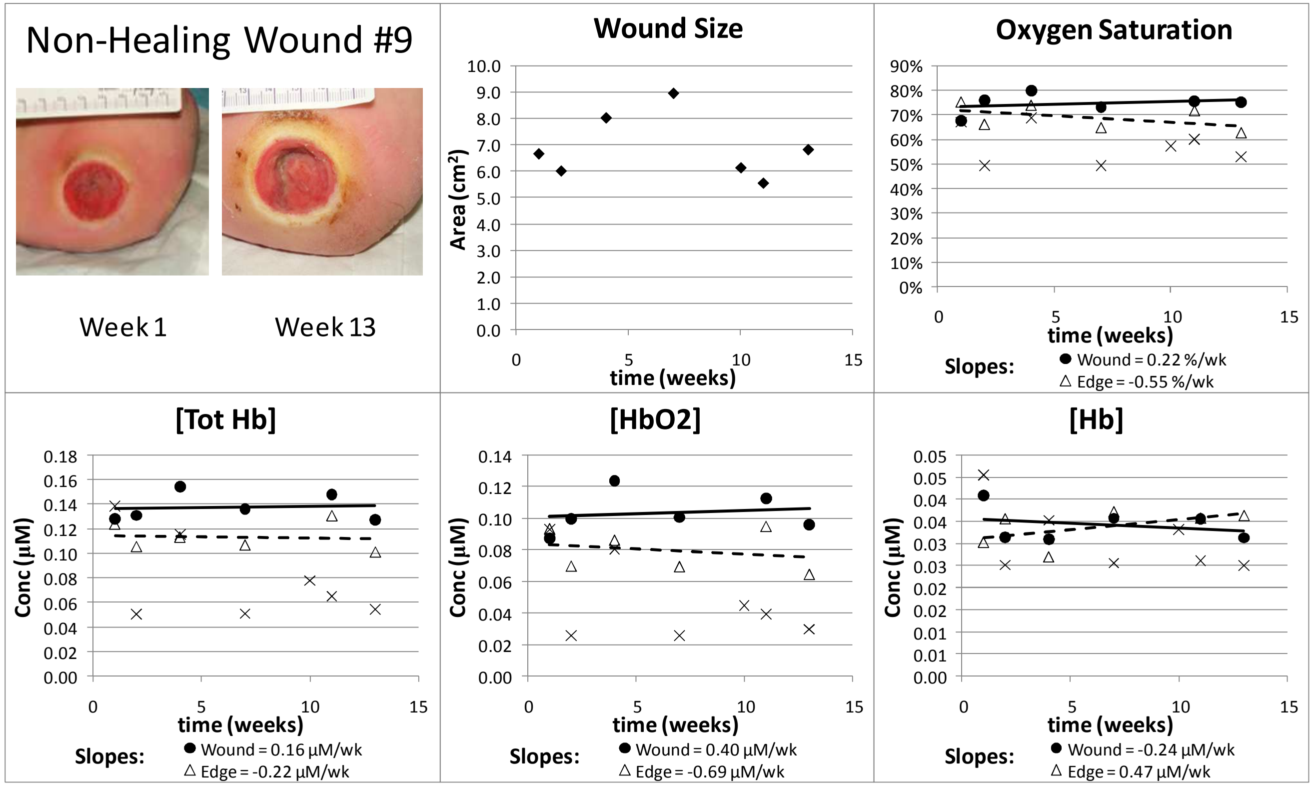

**Figure 89: Non-Healing Wound #9 - Wound size and hemoglobin data. Location: Plantar surface. Outcome: Cellulitis and wound excision during week 14. *Upper left:* Digital photographs from selected time points. *Upper center:* Wound area as determined through analysis of digital photographs (♦). *Upper right*: Oxygen Saturation from each measurement day. *Lower:* Total hemoglobin concentration [*Tot Hb*], oxyhemoglobin concentration [*HbO$_2$*], and deoxyhemoglobin concentration [*Hb*] from each measurement day. Each data point represents the mean of measurements obtained from the center of the wound (●), the edges of the wound (Δ), and a control site on the wounded foot (x). Solid lines are the linear trendlines associated with data obtained from the wound centers; dashed lines are the linear trendlines associated with data obtained from the wound edges.**

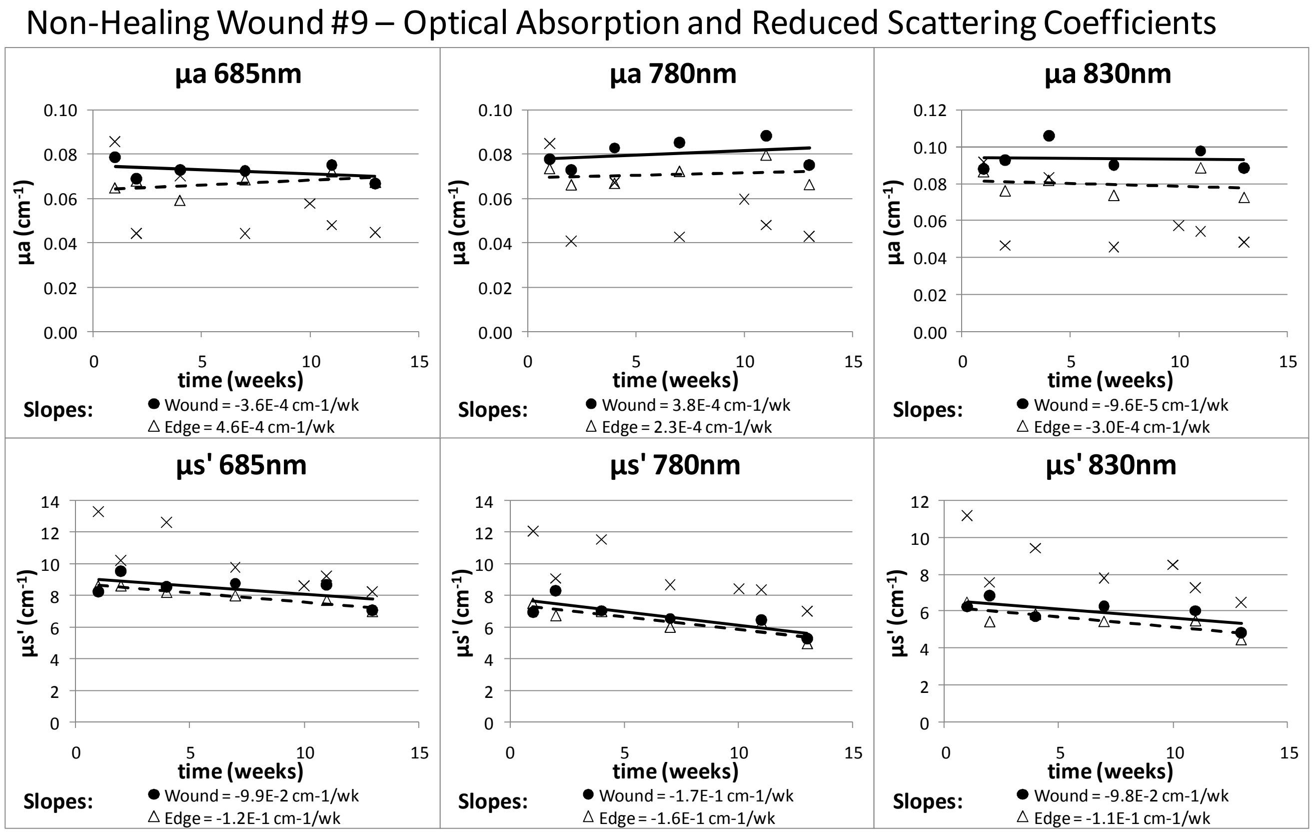

**Figure 90: Non-Healing Wound #9 - Optical aborption (µa) and reduced scattering coefficients (µs'). Location: Plantar surface. Outcome: Cellulitis and wound excision during week 14. Each data point represents the mean of measurements obtained on each measurement day from the center of the wound (●), the edges of the wound (Δ), and a control site on the wounded foot (x). Solid lines are the linear trendlines associated with data obtained from the wound centers; dashed lines are the linear trendlines associated with data obtained from the wound edges.**

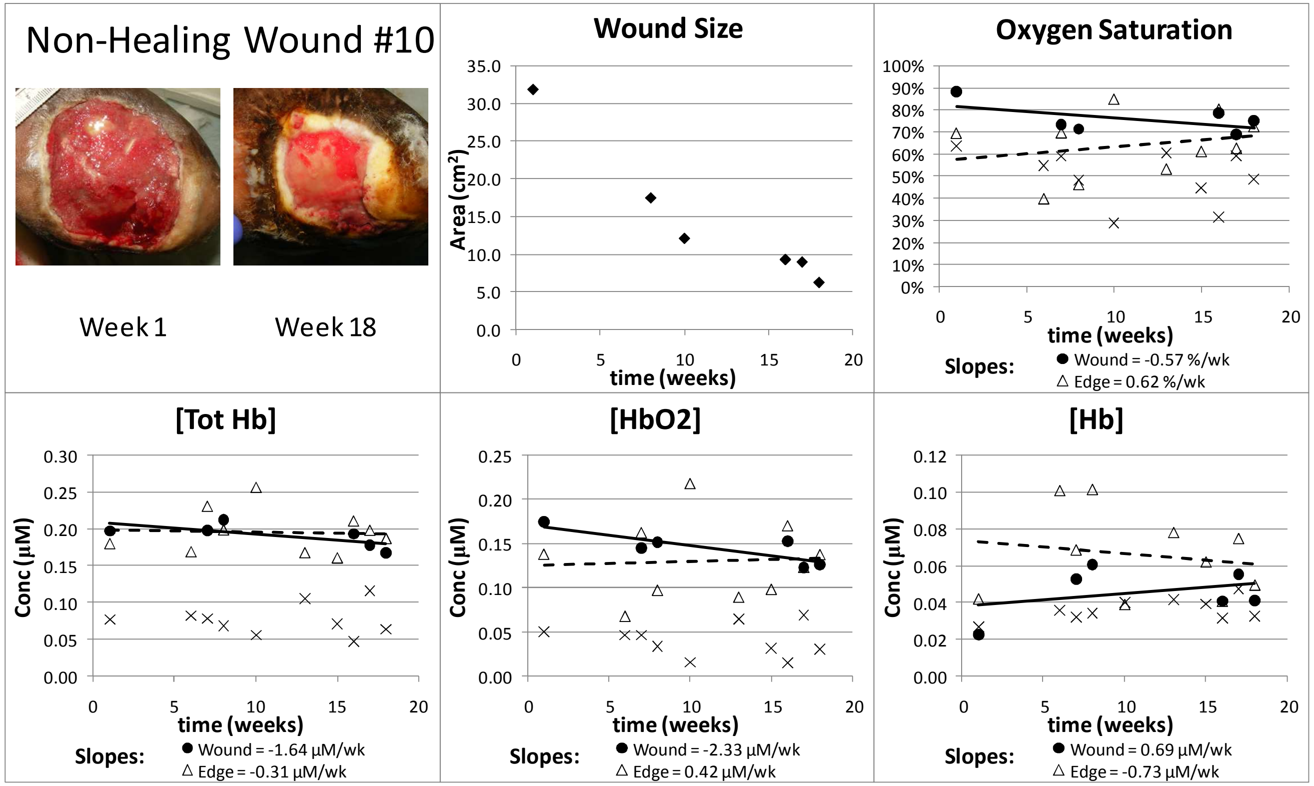

**Figure 91: Non-Healing Wound #10 - Wound size and hemoglobin data. Location: Transmetatarsal amputation site. Outcome: Wound excision and stump revision during week 19. *Upper left:* Digital photographs from selected time points. *Upper center:* Wound area as determined through analysis of digital photographs (♦). *Upper right*: Oxygen Saturation from each measurement day. *Lower:* Total hemoglobin concentration [*Tot Hb*], oxyhemoglobin concentration [*HbO*$_2$], and deoxyhemoglobin concentration [*Hb*] from each measurement day. Each data point represents the mean of measurements obtained from the center of the wound (●), the edges of the wound (Δ), and a control site on the wounded foot (x). Solid lines are the linear trendlines associated with data obtained from the wound centers; dashed lines are the linear trendlines associated with data obtained from the wound edges.**

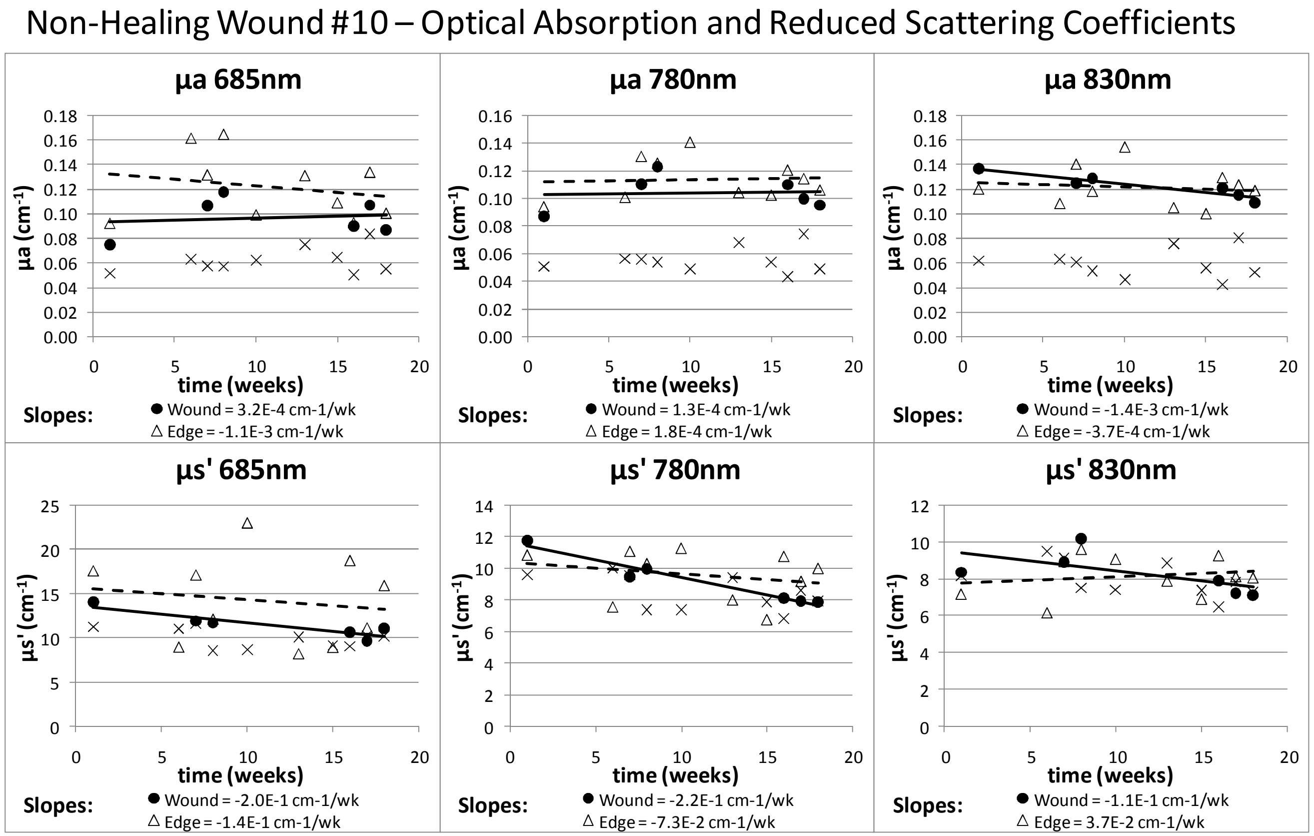

**Figure 92: Non-Healing Wound #10 - Optical aborption (µa) and reduced scattering coefficients (µs’). Location: Transmetatarsal amputation site. Outcome: Wound excision and stump revision during week 19. Each data point represents the mean of measurements obtained on each measurement day from the center of the wound (●), the edges of the wound (Δ), and a control site on the wounded foot (x). Solid lines are the linear trendlines associated with data obtained from the wound centers; dashed lines are the linear trendlines associated with data obtained from the wound edges.**

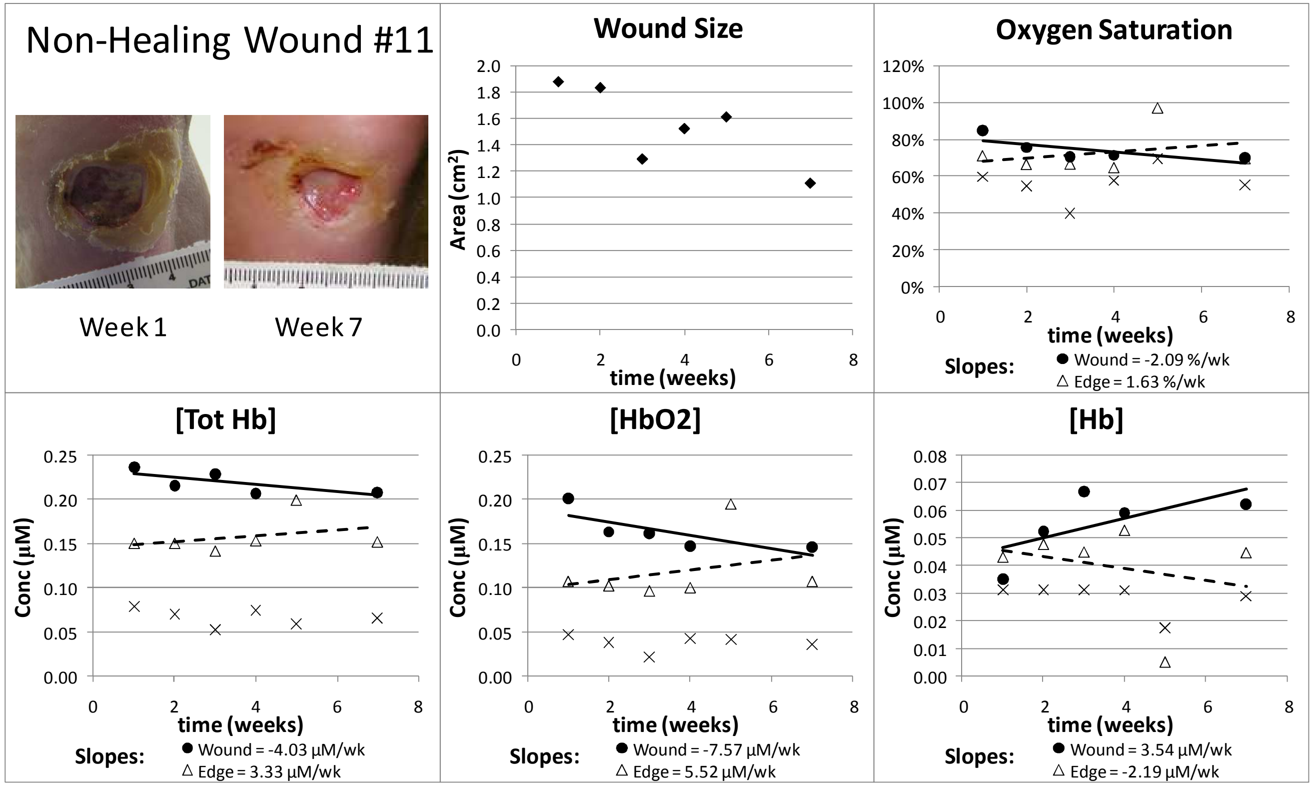

**Figure 93: Non-Healing Wound #11 - Wound size and hemoglobin data. Location: Plantar surface. Outcome: Removal of osteomyelitic bone during week 8. *Upper left:* Digital photographs from selected time points. *Upper center:* Wound area as determined through analysis of digital photographs (♦). *Upper right*: Oxygen Saturation from each measurement day. *Lower:* Total hemoglobin concentration [*Tot Hb*], oxyhemoglobin concentration [*HbO$_2$*], and deoxyhemoglobin concentration [*Hb*] from each measurement day. Each data point represents the mean of measurements obtained from the center of the wound (●), the edges of the wound (Δ), and a control site on the wounded foot (x). Solid lines are the linear trendlines associated with data obtained from the wound centers; dashed lines are the linear trendlines associated with data obtained from the wound edges.**

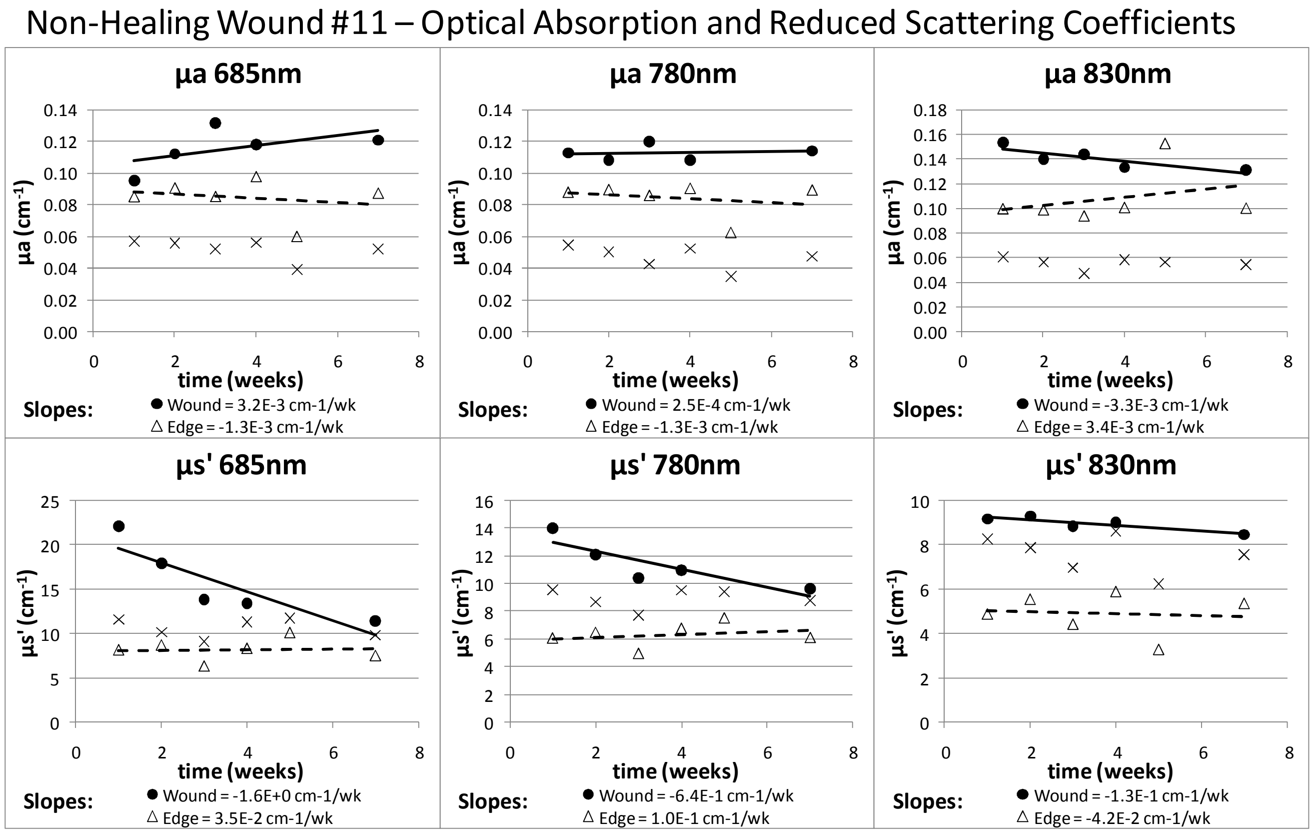

**Figure 94: Non-Healing Wound #11 - Optical aborption (µa) and reduced scattering coefficients (µs'). Location: Plantar surface. Outcome: Removal of osteomyelitic bone during week 8. Each data point represents the mean of measurements obtained on each measurement day from the center of the wound (●), the edges of the wound (Δ), and a control site on the wounded foot (x). Solid lines are the linear trendlines associated with data obtained from the wound centers; dashed lines are the linear trendlines associated with data obtained from the wound edges.**

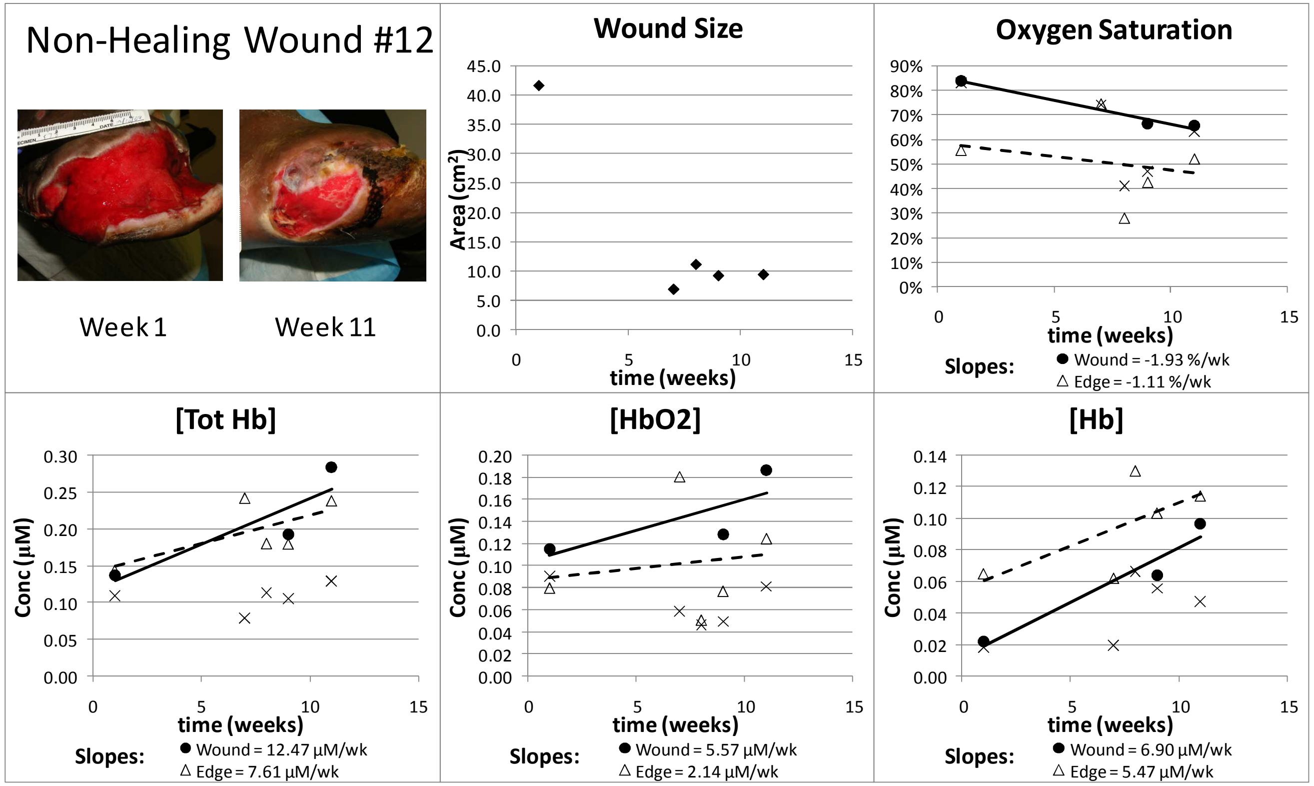

**Figure 95: Non-Healing Wound #12 - Wound size and hemoglobin data. Location: Transmetatarsal amputation site. Outcome: Below the knee amputation during week 12. *Upper left:* Digital photographs from selected time points. *Upper center:* Wound area as determined through analysis of digital photographs (♦). *Upper right*: Oxygen Saturation from each measurement day. *Lower:* Total hemoglobin concentration [*Tot Hb*], oxyhemoglobin concentration [$HbO_2$], and deoxyhemoglobin concentration [*Hb*] from each measurement day. Each data point represents the mean of measurements obtained from the center of the wound (●), the edges of the wound (Δ), and a control site on the wounded foot (x). Solid lines are the linear trendlines associated with data obtained from the wound centers; dashed lines are the linear trendlines associated with data obtained from the wound edges.**

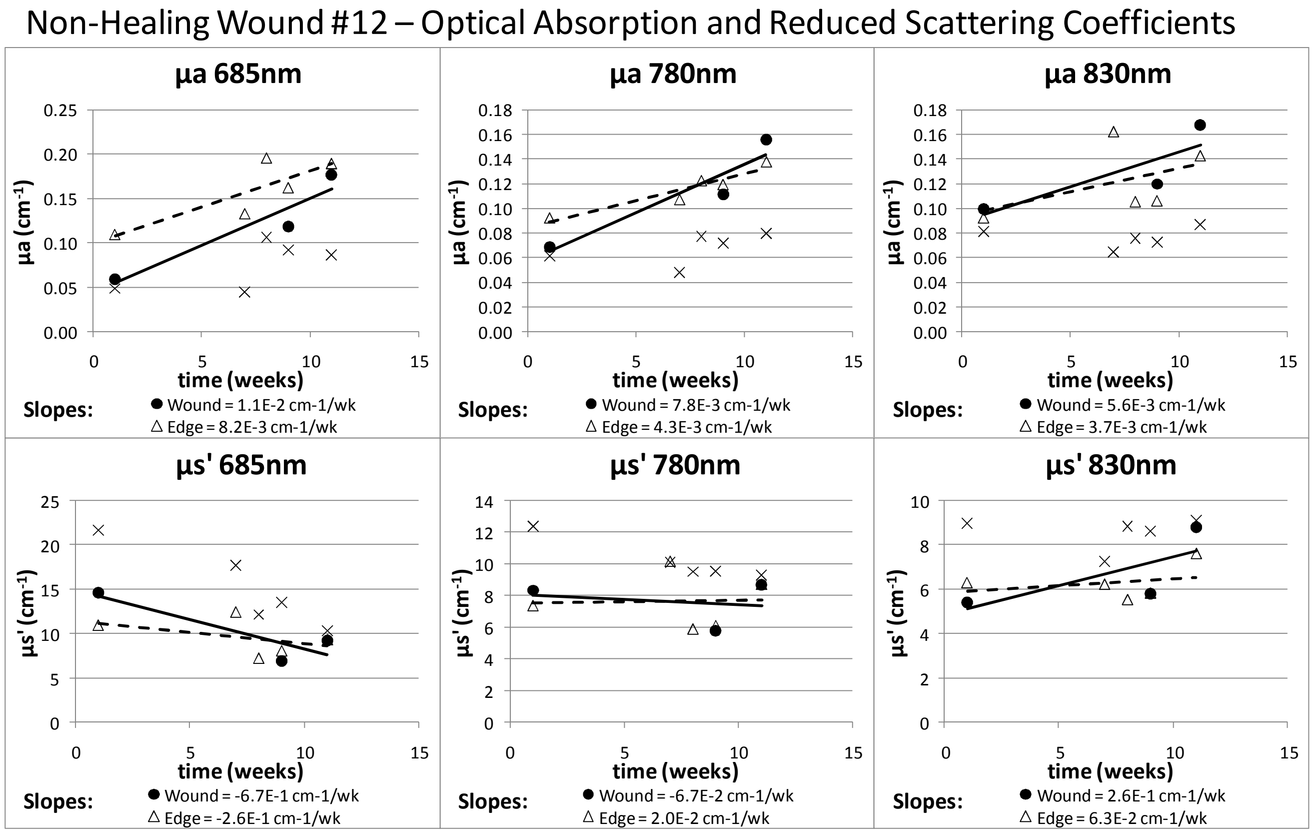

**Figure 96: Non-Healing Wound #12 - Optical aborption (µa) and reduced scattering coefficients (µs'). Location: Transmetatarsal amputation site. Outcome: Below the knee amputation during week 12. Each data point represents the mean of measurements obtained on each measurement day from the center of the wound (●), the edges of the wound (Δ), and a control site on the wounded foot (x). Solid lines are the linear trendlines associated with data obtained from the wound centers; dashed lines are the linear trendlines associated with data obtained from the wound edges.**

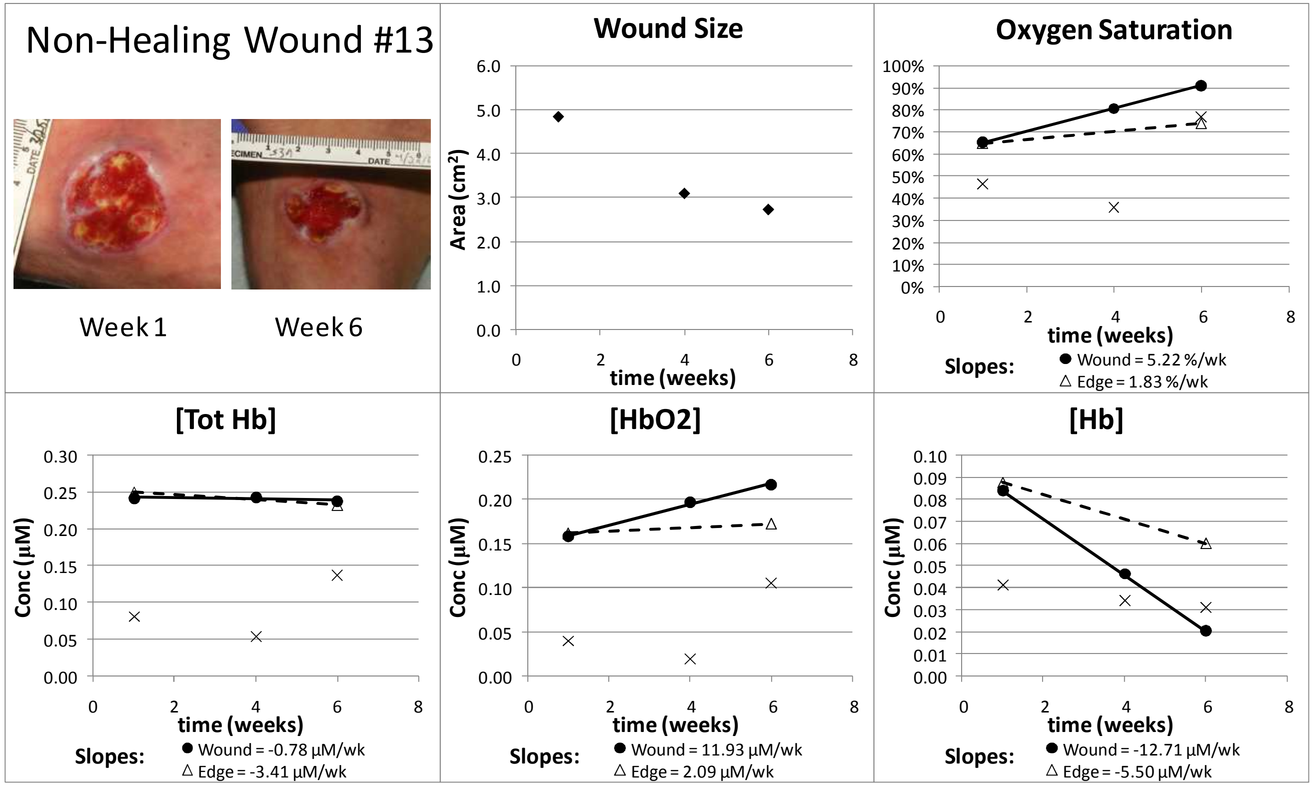

**Figure 97: Non-Healing Wound #13 - Wound size and hemoglobin data. Location: Dorsum. Outcome: Wound excision during week 8. *Upper left:* Digital photographs from selected time points. *Upper center:* Wound area as determined through analysis of digital photographs (♦). *Upper right*: Oxygen Saturation from each measurement day. *Lower:* Total hemoglobin concentration [*Tot Hb*], oxyhemoglobin concentration [*HbO$_2$*], and deoxyhemoglobin concentration [*Hb*] from each measurement day. Each data point represents the mean of measurements obtained from the center of the wound (●), the edges of the wound (Δ), and a control site on the wounded foot (x). Solid lines are the linear trendlines associated with data obtained from the wound centers; dashed lines are the linear trendlines associated with data obtained from the wound edges.**

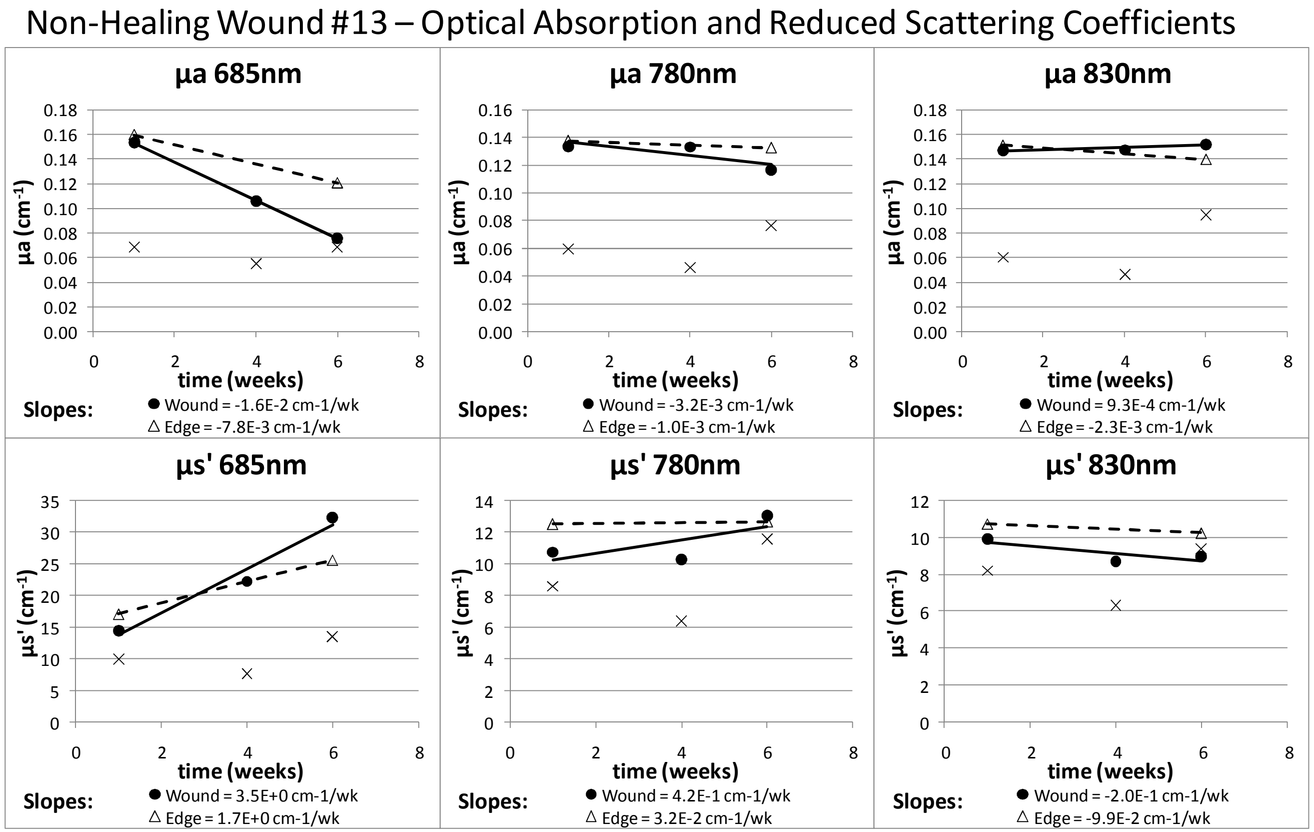

**Figure 98: Non-Healing Wound #13 - Optical aborption (μa) and reduced scattering coefficients (μs'). Location: Dorsum. Outcome: Wound excision during week 8. *Upper left:* Digital photographs from selected time points. Each data point represents the mean of measurements obtained on each measurement day from the center of the wound (●), the edges of the wound (Δ), and a control site on the wounded foot (x). Solid lines are the linear trendlines associated with data obtained from the wound centers; dashed lines are the linear trendlines associated with data obtained from the wound edges.**

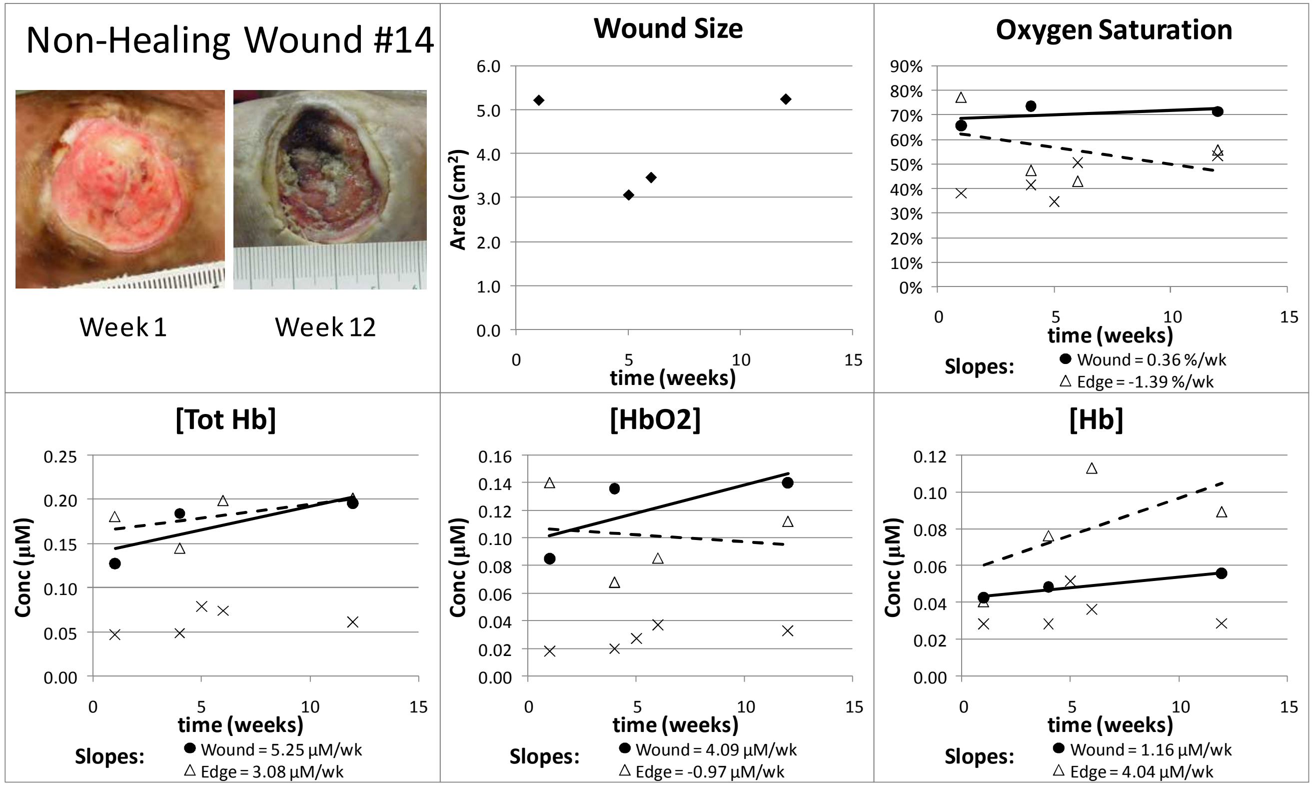

**Figure 99: Non-Healing Wound #14 - Wound size and hemoglobin data. Location: Plantar surface. Outcome: Transmetatarsal amputation week 13. *Upper left:* Digital photographs from selected time points. *Upper center:* Wound area as determined through analysis of digital photographs (♦). *Upper right*: Oxygen Saturation from each measurement day. *Lower:* Total hemoglobin concentration [*Tot Hb*], oxyhemoglobin concentration [*HbO₂*], and deoxyhemoglobin concentration [*Hb*] from each measurement day. Each data point represents the mean of measurements obtained from the center of the wound (●), the edges of the wound (Δ), and a control site on the wounded foot (x). Solid lines are the linear trendlines associated with data obtained from the wound centers; dashed lines are the linear trendlines associated with data obtained from the wound edges.**

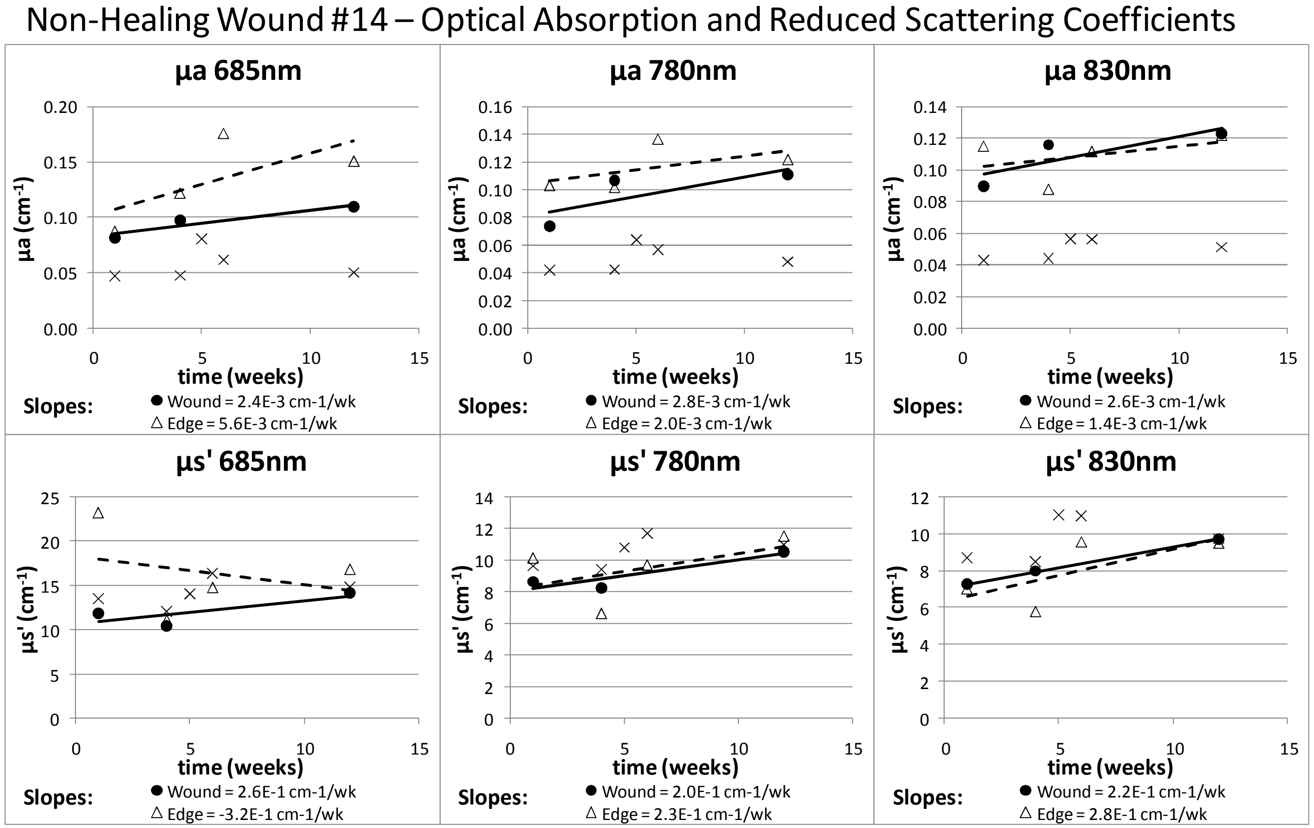

**Figure 100: Non-Healing Wound #14 - Optical aborption (μa) and reduced scattering coefficients (μs'). Location: Plantar surface. Outcome: Transmetatarsal amputation week 13. Each data point represents the mean of measurements obtained on each measurement day from the center of the wound (●), the edges of the wound (Δ), and a control site on the wounded foot (x). Solid lines are the linear trendlines associated with data obtained from the wound centers; dashed lines are the linear trendlines associated with data obtained from the wound edges.**